Environmental Tracers

Edited by

Trevor Elliot

Printed Edition of the Special Issue Published in *Water*

www.mdpi.com/journal/water

Trevor Elliot (Ed.)

Environmental Tracers

This book is a reprint of the special issue that appeared in the online open access journal *Water* (ISSN 2073-4441) in 2013 (available at: http://www.mdpi.com/journal/water/special_issues/environ_tracers).

Guest Editor
Trevor Elliot
Environmental Tracers Laboratory (ETL)
Environmental Engineering Research Centre (EERC)
School of Planning, Architecture & Civil Engineering (SPACE)
Queen's University Belfast
David Keir Building, Stranmillis Road
Belfast. BT9 5AG. Northern Ireland
UK

Editorial Office
MDPI AG
Klybeckstrasse 64
Basel, Switzerland

Publisher
Shu-Kun Lin

Managing Editor
Cherry Gong

1. Edition 2014

MDPI • Basel • Beijing

ISBN 978-3-906980-92-8

Dear Colleagues,

Aquifer resources continue to be overexploited, leaving the world's most impoverished (or vulnerable) populations and/or the aquatic environment at an ever increasing risk from climate change. Adaptation strategies demand detailed evaluation and management of water as a resource, requiring an understanding of the chemical, geological (hydrogeological/geohydrological) and biological interactions that waters effect or undergo in the hydrologic cycle. Environmental tracers are ambient natural or man-made compounds widely distributed in the Earth's near-surface. They may be injected into the hydrological system from the atmosphere at recharge and/or are added/lost/exchanged inherently as waters flow over and through materials. Variations in their chemical abundances and isotopic compositions can be used as tracers to determine sources (provenance), pathways (of reaction or interaction) and also timescales (dating) of environmental processes. Water dating may invoke their characteristic decay or accumulation functions, (*cf.* radioactive and radiogenic compounds and isotopes) in a system or the characteristic injection of sources. Environmental tracers in groundwater systems can give information both on current and past flow conditions independently of hydraulic analyses and modelling. Thus, environmental tracers generically are important tools for developing sustainable management policies for the protection of water resources and the aquatic environment.

Recent overviews have highlighted how most environmental tracer systematics have become well-established through proof-of-concept studies in geochemically and hydraulically simple aquifers. The challenge now lies in enhancing the way they are put to use by the hydrologic community and water resource managers in more complex systems (e.g., inter- and intra-aquifer mixing; aquifers as distributed water systems – water coming in at one point is going somewhere, and pumping of water represents an interception) and how they may be used to address issues of vulnerability, sustainability, and uncertainty in water resource systems (including resource, flooding, drought, climate justice, water and food security, water footprints, *etc.*).

Therefore we would like to call for papers to disseminate and share findings especially on the robustness or fitness-for-purpose of the application and use of environmental tracers in water resource systems in addressing problems and opportunities scientifically. Papers are selected by a rigorous peer review procedure with the aim of rapid and wide dissemination of research results, development and application in the wide area of environmental tracers. Original research papers or critical reviews are invited.

Guest Editor
Trevor Elliot, PhD

Biographical Sketch - Guest Editor

Dr. Elliot is a Reader in Environmental Engineering at Queen's University Belfast (QUB). His training was in Geophysics & Planetary Physics (Newcastle University, 1983); his PhD in Groundwater Geochemistry (Bath University, 1990) under the guidance of the late John N. Andrews. After research positions at Exeter (Geology), Cambridge (Earth Sciences), and Newcastle (Water Resources Systems Research Laboratory, Civil Engineering), in 1999 he joined QUB and established the Environmental Tracers Laboratory (ETL) in the School of Civil Engineering (now SPACE) as a component laboratory of the Environmental Engineering Research Centre. The ETL aims to: advance the use of natural and applied tracers and intelligent tracing (*i.e.*, specifically utilising the physico-chemical properties of particular tracers to target system characteristics) approaches in geohydrology; investigate and & characterise environmental and engineering systems, so as to promote sustainable use and practice and to increase fundamental understanding of gas and dissolved phase bio/geochemical processes; mathematically model and predict fate and transport processes for compounds of environmental concern. His research interests to date cover: intelligent tracers for environmental & engineering systems; geohydrology; isotope hydrology; groundwater dating; aquifer sustainability issues. He has worked on a number of major aquifer systems: single porosity media in Algeria (sandstone), China (gravel) and Germany (gravel/sands); dual-porosity Chalks (southern England; East Yorkshire); dual-permeability, fissured sandstone (Northern Ireland); a swallow-hole karst system (Republic of Ireland); and the local/regional hydrology of a sabkha system (Saudi Arabia). As well as promoting the use of noble gases for the direct-measurement gas evasion technique to study reaeration in rivers, in engineering systems focus has been particularly on tracing subsurface, permeable reactive barriers (PRB's), mixing dynamics for pumped minewater systems, and the carbon isotope fractionation of chlorofluorocarbons (CFCs) during degradation.

Table of Contents

List of Contributors

Mark Baskaran: Department of Geology, Wayne State University, Detroit, MI 48202, USA
Timothy E. Becker: Department of Earth Science, University of California, Santa Barbara, CA 93106, USA
Andrew Benson: Program of Environmental Studies, University of California, Santa Barbara, CA 93106, USA
Nikolaus H. Buenning: Department of Earth Sciences, University of Southern California, Zumberge Hall of Science (ZHS), 3651 Trousdale Pkwy, Los Angeles, CA 90089, USA
Frederic Brunet: Laboratory of Functional Ecology and Environment (EcoLab), UPS, INPT, University of Toulouse,118 route de Narbonne, Toulouse F-31062, France; Laboratory of Functional Ecology and Environment (EcoLab), CNRS, 118 route de Narbonne, Toulouse F-31062, France
Jordan F Clark: Department of Earth Science, University of California, Santa Barbara, CA 93106, USA; Program of Environmental Studies, University of California, Santa Barbara, CA 93106, USA
Jean François Comanducci: International Atomic Energy Agency (IAEA)–Environment Laboratories, 98000 Monaco
Rory Cowie: Institute of Arctic and Alpine Research, University of Colorado Boulder, Boulder, CO 80309, USA
Jason Dadakis: Orange County Water District, Fountain Valley, CA 92728, USA
Elizabeth DeRubeis: Department of Earth and Environmental Sciences, California State University East Bay, Hayward, CA 94542, USA
Marco Doveri: National Research Council of Italy, Institute of Geosciences and Earth Resources, Via G. Moruzzi 1 56124, Pisa, Italy
Christopher J. Eastoe: Geosciences Department, University of Arizona, Tucson, AZ 85721, USA
Brian D. Edwards: U.S. Geological Survey, Menlo Park, CA 94025, USA
Trevor Elliot: Environmental Tracers Laboratory (ETL), Environmental Engineering Research Centre (EERC), School of Planning, Architecture & Civil Engineering (SPACE), Queen's University Belfast, David Keir Building, Stranmillis Road, Belfast, BT9 5AG Northern Ireland, UK
Bradley K. Esser: Chemical Science Division, Lawrence Livermore National Laboratory, Livermore, CA 94551, USA
Roy Herndon: Orange County Water District, Fountain Valley, CA 92728, USA
Adam Hutchinson: Orange County Water District, Fountain Valley, CA 92728, USA
Naoki Kabeya: Kyushu Research Centre, Forestry and Forest Product Research Institute, 4-11-16 Kurokami, Kumamoto 860-0862, Japan

Lisa Kanner: Department of Earth Sciences, University of Southern California, Zumberge Hall of Science (ZHS), 3651 Trousdale Pkwy, Los Angeles, CA 90089, USA
Kay Knoeller: Helmholtz-Centre for Environmental Research–UFZ, Leipzig 04318, Germany
Luc Lambs: Laboratory of Functional Ecology and Environment (EcoLab), UPS, INPT, University of Toulouse,118 route de Narbonne, Toulouse F-31062, France; Laboratory of Functional Ecology and Environment (EcoLab), CNRS, 118 route de Narbonne, Toulouse F-31062, France
Cheng-Haw Lee: Department of Resources Engineering, National Cheng Kung University, Tainan 701, Taiwan
Kuo-Chin Hsu: Department of Resources Engineering, National Cheng Kung University, Tainan 701, Taiwan
Michael Land: U.S. Geological Survey, San Diego, CA 92101, USA
Hung-I Lin: Department of Resources Engineering, National Cheng Kung University, Tainan 701, Taiwan
Ulf Mallast: Helmholtz-Centre for Environmental Research–UFZ, Leipzig 04318, Germany
Jean E. Moran: Department of Earth and Environmental Sciences, California State University East Bay, Hayward, CA 94542, USA
Sheila Morrissey: Department of Earth Science, University of California, Santa Barbara, CA 93106, USA
Issam Moussa: Laboratory of Functional Ecology and Environment (EcoLab), UPS, INPT, University of Toulouse,118 route de Narbonne, Toulouse F-31062, France; Laboratory of Functional Ecology and Environment (EcoLab), CNRS, 118 route de Narbonne, Toulouse F-31062, France
Mario Mussi: National Research Council of Italy, Institute of Geosciences and Earth Resources, Via G. Moruzzi 1 56124, Pisa, Italy
Tatsuhiko Nobuhiro: Hokkaido Research Centre, Forestry and Forest Product Research Institute, 7 Hitsujigaoka, Toyohira, Sapporo, Hokkaido 062-8516, Japan
Mai Khanh Pham: International Atomic Energy Agency (IAEA)–Environment Laboratories, 98000 Monaco
Robert J. Rosenbauer: U.S. Geological Survey, Santa Cruz, CA 95060, USA
Ryan Rodney: Newmont Mining Corporation, 1655 Mountain City Highway, Elko, NV 89801, USA
Robert L. Runkel: U.S. Geological Survey, 3215 Marine St., Boulder, CO 80303, USA
Axel Schmidt: German Federal Institute of Hydrology, Koblenz 56068, Germany; Helmholtz-Centre for Environmental Research–UFZ, Leipzig 04318, Germany
Jan Scholten: Institute of Geosciences, University Kiel, Kiel 24118, Germany
Michael Schubert: Helmholtz-Centre for Environmental Research–UFZ, Leipzig 04318, Germany
Akira Shimizu: Kyushu Research Centre, Forestry and Forest Product Research Institute, 4-11-16 Kurokami, Kumamoto 860-0862, Japan

Lowell Stott: Department of Earth Sciences, University of Southern California, Zumberge Hall of Science (ZHS), 3651 Trousdale Pkwy, Los Angeles, CA 90089, USA
Peter W. Swarzenski: U.S. Geological Survey, Santa Cruz, CA 95060, USA
Stephanie H. Uriostegui: Department of Earth Science, University of California, Santa Barbara, CA 93106, USA; Chemical Science Division, Lawrence Livermore National Laboratory, Livermore, CA 94551, USA
Ate Visser: Chemical Science Division, Lawrence Livermore National Laboratory, Livermore, CA 94551, USA
Mark W. Williams: Institute of Arctic and Alpine Research, University of Colorado Boulder, Boulder, CO 80309, USA
Mike Wireman: U.S. Environmental Protection Agency, Region 8, Denver, CO 80202, USA
Chi-Shin Wu: Department of Resources Engineering, National Cheng Kung University, Tainan 701, Taiwan
Hsin-Fu Yeh: Department of Resources Engineering, National Cheng Kung University, Tainan 701, Taiwan
Kei Yoshimura: Atmosphere and Ocean Research Institute, University of Tokyo, General Research Building 211a, 5-1-5 Kashiwanoba, Kashiwa Chiba 277-8568, Japan
Matthew Zane: Department of Earth Science, University of California, Santa Barbara, CA 93106, USA
Jian-Jun Zhang: College of Soil and Water Conservation, Beijing Forestry University, No. 35 Qinghuadong Road, Haidian District, Beijing 100083, China

Preface

Environmental Tracers are ambient, natural or man-made compounds. They are widely distributed in the Earth's near-surface and can be both (i) added/lost/exchanged inherently (as waters flow over and through materials) and (ii) discriminated, determined analytically, and tracked sensitively.

They can also be applied (injected) deliberately at levels higher than the ambient background to characterize environmental (and indeed engineering) systems. Environmental Tracers, including their stable and radioactive isotopic signatures, when considered alongside elemental abundances, generically provide important tools for understanding the source, flow, and mixing dynamics of water resource systems through their imprint on the system or their sensitivity to alteration within it, and especially for subsurface waters (groundwaters).

Since the pioneering work of the 1950's and 1960's, isotopic signatures of waters in the hydrological cycle have been well-characterized in terms of stable isotopes (oxygen and hydrogen—^{18}O; ^{2}H) of the water molecule itself as a natural, environmental tracer. Carbon (^{13}C -) isotopes of dissolved compounds also started to be investigated around this period; the range of elements covered (isotopic signatures of ^{15}N, ^{34}S, compounds, etc.) and the techniques available for analyzing them in various, dissolved compounds has subsequently increased rapidly over the ensuing decades; elements covered now include radioactive environmental isotopes (*cf.* the radioactive isotope of hydrogen occurring in water itself—tritium, ^{3}H). Over the decades, researchers have investigated and characterized many water resource systems with these tools in their hydrogeological arsenal. Whilst the effectiveness (and weaknesses, as necessary) of these tracers in discriminating aquifer dynamics and processes has been corroborated in proof of concept studies, their uptake as a standard hydrogeological, geohydrological or water resource tool by the professions is still disappointing. This Special Issue focuses therefore particularly on the robustness or fitness-for-purpose of the application and use of Environmental Tracers in addressing problems and opportunities scientifically, to promote their wider use, and to address substantive issues of vulnerability, sustainability, and uncertainty in (ground)water resources systems and their management.

The Special Issue arose as an open call to the *Water* community, with rigorous peer-review applied to selected and published papers. Eleven papers from researchers, based in seven different countries, are included in this Special Issue. The papers reflect global research in this area. My hope then is that the collation of these papers contributes to piquing further interest and action in how Environmental Tracers can contribute and be used to address the substantive issues of vulnerability, sustainability, and uncertainty in (ground)water resources systems and their management.

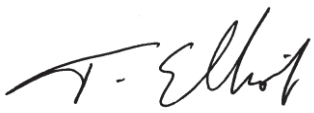

Trevor Elliot
Guest Editor

School of Planning, Architecture and Civil Engineering (SPACE), Queen's University Belfast, UK.

5 November, 2014

Environmental Tracers

Trevor Elliot

Abstract: Environmental tracers continue to provide an important tool for understanding the source, flow and mixing dynamics of water resource systems through their imprint on the system or their sensitivity to alteration within it. However, 60 years or so after the first isotopic tracer studies were applied to hydrology, the use of isotopes and other environmental tracers are still not routinely necessarily applied in hydrogeological and water resources investigations where appropriate. There is therefore a continuing need to promote their use for developing sustainable management policies for the protection of water resources and the aquatic environment. This Special Issue focuses on the robustness or fitness-for-purpose of the application and use of environmental tracers in addressing problems and opportunities scientifically, to promote their wider use and to address substantive issues of vulnerability, sustainability, and uncertainty in (ground)water resources systems and their management.

Reprinted from *Water*. Cite as: Elliot, T. Environmental Tracers. *Water* **2014**, *6*, 3264-3269.

1. Introduction

Environmental tracers are ambient, natural or man-made compounds widely distributed in the Earth's near-surface. They may be injected naturally into the hydrological system from the atmosphere at recharge and/or are added/lost/exchanged inherently as waters flow over and through materials. Because of possible issues of chemical equivalence in sampled groundwater signatures, to screen hypotheses and identify contributing processes typically detailed and/or quantitative groundwater investigations require consideration of multiple tracers of chemical reactions: ion ratios/correlations, minor/trace element determinands, mineralogy and reaction-path simulations, isotopic compositions, *etc.* These tracers separately or in conjunction may suggest a unique solution in detailing the hydrogeochemical processes operating. As for trace elements, environmental isotopic signatures of dissolved compounds, and the water molecule itself, can prove particularly sensitive tracers, as they occur generally at low levels of concentration and can be affected by chemical and physical fractionation effects shifting their signatures. Variations then in groundwater chemical abundances and isotopic compositions can be used as natural tracers to determine sources (provenance), pathways (of reaction or interaction), and also timescales (dating) of environmental processes. Dating may invoke their characteristic decay or accumulation functions (*i.e.*, radioactive *vs.* radiogenic compounds and isotopes) in a system, or the characteristic injection of sources. This then provides a handhold on timescales of processes and water residence times to be considered critically alongside hydraulic transit (flowthrough) and system turnover times. Moreover, environmental tracers in groundwater systems can give information both on current and past flow conditions independently of hydraulic analyses and groundwater modelling. Thus, generically environmental tracers are important tools for developing sustainable management policies for the protection of water resources (quantity and quality) and the aquatic environment. For example, where investigations are taking place in groundwater systems in which mixing is a potentially important

process (*cf.* pumping flooded mines (see below) or even pumped public supply wells), the addition of even modest amounts of additional sampling and analysis for isotopic environmental tracers can greatly expand understanding of the flow and geochemical/water quality (mixing) dynamics of pumped groundwater systems [1].

Recent overviews (e.g., [2]) have highlighted how most environmental tracers systematics have now become well-established through proof-of-concept studies in geochemically and hydraulically simple aquifers. The challenge now lies in enhancing the way they are put to use by the hydrologic community and water resource managers in more complex systems, and how they may be used to address issues of vulnerability, sustainability, and uncertainty of water resources and their systems. Therefore the aim of this Special Issue is to disseminate and share findings especially on the robustness or fitness-for-purpose of the application and use of environmental tracers in water resource systems in addressing problems and opportunities scientifically. Original research papers were selected by rigorous peer-review process with the aim of rapid, accessible and wide dissemination of results.

2. Contributions

The selected papers presented in the Special Issue are highlighted in this section. They fall broadly into three categories: those focused particularly on the stable oxygen- and hydrogen-isotopes and also the radioactive hydrogen-isotope (tritium) of the water molecule to characterise its source(s), fractionation effects, and dating young groundwater systems (five papers); those focused on multi-isotope approaches (including the use of other radioisotopes, and significantly natural Uranium- and Thorium-series radionuclides) (three papers); and those using natural environmental tracers alongside or as applied tracers introduced into groundwater systems (three papers).

2.1. Stable Isotopes of Water (δ^2H, $\delta^{18}O$)

Three articles [3–5] look at the start of the hydrological cycle, at the origin of rainfall and its selection in groundwater recharge using characteristic, naturally-occurring δ^2H and $\delta^{18}O$ signatures in monthly samples. The concept of "deuterium excess", originally defined by Dansgaard [6] as $d = \delta^2H - 8.\delta^{18}O$, is used in case studies by Lambs *et al.* [3] in France and Yeh *et al.* [4] in Taiwan, to identify the predominance of different air masses contributing to rainfall patterns seasonally and the groundwater recharge at the regional/catchment scale. Buenning *et al.* [5] model specifically the $\delta^{18}O$ of annual rainfall across the western USA to identify mechanisms controlling interannual variations in isotopic signatures. Such signatures feed into groundwater systems and might be used as climate proxy for various surface archives and potentially [5] to monitor storm track changes. Overall, isotope mapping and monitoring on multiple spatial and temporal scales is helping recognise and characterise isoscapes, of use in a wide range of hydrological and other contexts [7].

A fourth contribution by Kabeya *et al.* [8] links a storm event over a 48-h. period to sediment production and transport in a forested headwater catchment in Japan. Their correlation is used to identify the source area for sediment, which might be linked potentially with mobilisation of radioactive caesium deposited following the recent Fukushima Daiichi nuclear power plant incident.

Doveri and Mussi [9] use both the stable isotopes (δ^2H, δ^{18}O) of water and its radioactive isotope (tritium, ^{3}H, with a half-life of 12.3 years) monitored in springs and wells (up to six times over a 2-year period) as natural environmental tracers to suggest a conceptual model of groundwater flow in the Scansano-Magliano region of southern Tuscany (Italy). The local sandstone aquifer here may provide a strategic alternative source for water supply given the overexploitation and contamination of known, local alluvial aquifers, and for supplying isolated villages on the Toscana ridge in this semiarid area.

2.2. Multi-Isotope Studies

In another regional aquifer study, and alongside the water isotopes (δ^2H, δ^{18}O, ^{3}H), Eastoe and Rodney [10] additionally utilise natural C-isotope systematics (stable δ^{13}C, and radioactive ^{14}C—this latter with a half-life of 5730 years) of dissolved inorganic carbon, and the S-isotope signature of dissolved sulfate (δ^{34}S). The environmental tracers are used to date groundwater residence times (^{3}H, ^{14}C) and to identify winter recharge at high-elevation in the Sacramento Mountains (USA) as the source of groundwaters in the regional carbonate aquifer and flanking basins. The authors highlight therefore that if winter rainfall decreases e.g., as a result of global climate change then aquifer recharge also will be affected. However, the authors also show that the use of stable isotopes of water equivocally here of themselves cannot help discriminate sources of groundwater for the more distant Roswell basin.

Swarzenski *et al.* [11] also combine stable and radioactive tracers alongside hydrochemistry in a coastal Los Angeles County (USA) study to investigate the complex groundwater scenario associated with a historical scheme to inject freshwater at three locations as a hydraulic barrier to saline intrusion. Here groundwater may be a "complex mixture of native groundwater, intruded seawater, non-native injected water, and oil-field brine water." The baseline geochemical study to discriminate sources and characterise groundwater dynamics and mixing included looking at natural Uranium- and Thorium-series radiogenic nuclides (^{223}Ra, ^{224}Ra, ^{226}Ra, ^{228}Ra, ^{222}Rn) particularly to study potential controls on the adsorption-desorption rates for dissolved cations. Schubert *et al.* [12] evaluate the use of the stable isotopes of water alongside natural radium isotopic ratios (^{224}Ra/^{228}Ra, ^{228}Ra/^{226}Ra) and radon (^{222}Rn) contents to detect submarine groundwater discharge (SGD) in a submarine cave near Monaco. They found ^{222}Rn contents the most robust indicator in context and δ^2H, δ^{18}O suitable. They propose particularly therefore utilising ^{222}Rn contents alongside salinity for the investigation of offshore fresh groundwater reserves. Such SGD and offshore groundwater reserves have recently been highlighted as a global phenomenon potentially to be exploited [13]. Elsewhere, other authors [14] have used dissolved uranium and ^{234}U/^{238}U activity ratios and natural Uranium- and Thorium-series radiogenic nuclides, alongside dissolved noble gases (including ^{4}He, the stable by-product of U- and Th-series radioactive decay) to attest to the "fossil" water (palaeowater) status of groundwaters in the regional Continental Intercalaire aquifer of Algeria and Tunsia. Their abstraction is therefore akin to mining this groundwater resource. Where a freshwater/saline water interface is identifiable, even the use of scavenger well technology (e.g., [15,16]) must take into account the potential paleowater status of at least a component of the pumped water and the effect on the movement of the interface.

2.3. Investigations Using Natural Tracers in Combination with Applied Tracers

In complex hydrogeological settings the use of applied tracers to analyse system flow-through (transit) times and hydraulic connections can be problematic as the tracers can be diluted out, or if the mixing reservoir is overestimated there can be tracer breakthrough at concentrations exceeding environmental or analytical specifications.

Three further USA case studies [17–19] deploy applied tracers alongside ambient tracers. Cowie *et al.* [17] use a two-tier investigative approach in a flooded, abandoned, underground hard-rock mine system (USA). They monitored natural environmental tracers of water (δ^2H, $\delta^{18}O$, ^3H) to gain a conceptual understanding of the hydrogeology, and then injected applied tracers (here ionic and fluorescent tracers) at specific locations to focus their investigations. Remediation efforts for acid mine drainage (AMD) then can be targetted at separating and isolating or preventing sources of poor quality water. This approach then essentially follows the philosophy of Source-Pathway-Receptor (SPR) risk management (for Contaminated Land investigations) rather than a traditional end-of-pipe remedial solution for such waters. Elsewhere [1], monitoring of natural environmental tracers during pumping of AMD waters to control the water table in the system and prevent environmental impacts is used to characterise the sources, dynamics and evolution of mixing of waters and their water quality for flooded, abandoned coal mines.

Benson *et al.* [18] use injected, applied gas tracers (SF_6 and Xe) as nonpolar, partitioning tracers for the air-water interface in streams to monitor gas loss downstream and oxygen reaeration (K_{DO} or K_2, mass transfer coefficients). The link with environmental tracing is twofold, both because these two tracer gases are already present in the environment sourced from the atmosphere (albeit at very low ambient, dissolved concentrations which allows significant enhancement of dissolved concentrations for tracing), and because the loss rate for these gases could be used also for interpretation of ^{222}Rn measurements in the streams to study then groundwater-surface water interactions. Especially noble gases (like Xe) are perceived as "environmentally-friendly" tracers for stream reaeration and gas evasion/mass transfer (K) studies, as well as for characterising hydrodynamic properties [20].

Finally, Clark *et al.* [19] have applied (injected) the environmental gas tracers SF_6 and Xe in groundwater to characterise hydraulic connections between recharge facilities and production wells of a Managed Aquifer Recharge (MAR) site. MAR involves a strategy of injecting "surface waters into aquifers for storage and later extraction". Each tracer was injected separately and following an intervening period of a decade between the two tests to assess whether operation of the MAR facility (including any changes in recharge conditions) therefore had impacted the system response.

3. Conclusions

Eleven original research articles have been selected for this Special Issue. The research findings are novel and timely in informing the hydrological and water resources management communities on up-to-date research and practice. Sixty years or so after the first isotopic tracer studies applied to hydrology the use of isotopes and other environmental tracers are still not necessarily routinely applied in hydrogeological and water resources investigations where appropriate. We trust that the

collation of these papers contributes to piquing further interest in how environmental tracers can contribute and be used to address substantive issues of vulnerability, sustainability, and uncertainty in (ground)water resources systems and their management.

Acknowledgments

The Guest Editor (TE) thanks both the research community for offering and contributing a wide range of valuable papers, and the publisher MDPI for allocating resources and support towards this Special Issue.

Conflicts of Interest

The author declares no conflict of interest.

References

1. Elliot, T.; Younger, P.L. Detection of Mixing Dynamics during Pumping of a Flooded Coal Mine. *Groundwater* **2014**, *52*, 251–263.
2. Sanford, W.E.; Aeschbach-Hertig, W.; Herczeg, A.L. Preface: Insights from Environmental Tracers in Groundwater Systems. *Hydrogeol. J.* **2011**, *19*, 1–3.
3. Lambs, L.; Moussa, I.; Brunet, F. Air Masses Origin and Isotopic Tracers: A Study Case of the Oceanic and Mediterranean Rainfall Southwest of France. *Water* **2013**, *5*, 617–628.
4. Yeh, H.F.; Lin, H.I.; Lee, C.H. Identifying Seasonal Groundwater Recharge Using Environmental stable isotopes. *Water* **2014**, *6*, 2849–2861.
5. Buenning, N.H.; Stott, L.; Kanner, L.; Yoshimura, K. Diagnosing Atmospheric Influences on the Interannual $^{18}O/^{16}O$ Variations in Western U.S. Precipitation. *Water* **2013**, *5*, 1116–1140.
6. Dansgaard, W. Stable Isotopes in Precipitation. *Tellus* **1964**, *16*, 436–468.
7. West, J.B., Bowen, G.J., Dawson, T.E., Tu, K.P., Eds. *Isoscapes: Understanding Movement, Pattern and Process on Earth through Isotope Mapping*; Springer: New York, NY, USA, 2010; ISBN 978-90-481-3353-6; pp. 1–487.
8. Kabeya, N.; Shimizu, A.; Zhang, J.J.; Nobuhiro, T. Effect of Hydrograph Separation on Suspended Sediment Concentration Predictions in a Forested Headwater with Thick Soil and Weathered Gneiss Layers. *Water* **2014**, *6*, 1671–1684.
9. Doveri, M.; Mussi, M. Water Isotopes as Environmental Tracers for Groundwater Flow Understanding: An Application on Fractured Aquifer Systems in the Scansano-Magliano in Toscana area (southern Tuscany-Italy). *Water* **2014**, *6*, 2255–2277.
10. Eastoe, C.J.; Rodney, R. Isotopes as Tracers of Water Origin in and Near a Regional Carbonate Aquifer: The Southern Sacramento Mountains, New Mexico. *Water* **2014**, *6*, 301–323.
11. Swarzenski, P.W.; Baskaran, M.; Rosenbauer, R.J.; Edwards, B.D.; Land, M. A Combined Radio- and Stable-Isotopic Study of a California Coastal Aquifer System. *Water* **2013**, *5*, 480–504.

12. Schubert, M.; Scholten, J.; Schmidt, A.; Comanducci, J.F.; Pham, M.K.; Mallast, U.; Knoeller, K. Submarine Groundwater Discharge at a Single Spot Location: Evaluation of Different Detection Approaches. *Water* **2014**, *6*, 584–601.
13. Post, V.E.A.; Groen, J.; Kooi, H.; Person, M.; Ge, S.; Edmunds, W.M. Offshore Fresh Groundwater Reserves as a Global Phenomenon. *Nature* **2013**, *504*, 71–78.
14. Elliot, T.; Bonotto, D.M.; Andrews, J.N. Uranium, Radium and Radon evolution in the Continental Intercalaire aquifer, Algeria and Tunisia. *J. Environ. Radioac.* **2014**, *137*,150–162.
15. Stoner, R.F.; Bakiewicz, W. Scavenger Wells-1-Historic Development. In *Study and Modelling of Saltwater Intrusion into Aquifers*, Proceedings of the 12th Saltwater Intrusion Meeting, Barcelona, Spain, 1–6 November 1992; Custodio, E., Galofr, A., Eds.; CIMNE: Barcelona, Spain; pp. 545–556.
16. Aliewi, A.S.; Mackay, R.; Jayyousi, A.; Nasereddin, K.; Mushtaha, A.; Yaqubi, A. Numerical Simulation of the Movement of Saltwater Under Skimming and Scavenger Pumping in the Pleistocene Aquifer of Gaza and Jericho Areas, Palestine. *Transp. Porous Media* **2001**, *43*, 195–212.
17. Cowie, R.; Williams, M.W.; Wireman, M.; Runkel, R.L. Use of Natural and Applied Tracers to Guide Targeted Remediation Efforts in an Acid Mine Drainage System, Colorado Rockies, USA. *Water* **2014**, *6*, 745–777.
18. Benson, A.; Zane, M.; Becker, T.E.; Visser, A.; Uriostegui, S.H.; DeRubeis, E.; Moran, J.E.; Esser, B.K.; Clark, J.F. Quantifying Reaeration Rates in Alpine Streams Using Deliberate Gas Tracer Experiments. *Water* **2014**, *6*, 1013–1027.
19. Clark, J.F.; Morrissey, S.; Dadakis, J.; Hutchinson, A.; Herndon, R. Investigation of Groundwater Flow Variations near a Recharge Pond with Repeat Deliberate Tracer Experiments. *Water* **2014**, *6*, 1826–1839.
20. Semuwemba, J.; Elliot, T.; Mackinnon, P.A. Determining the Reaeration Coefficient and Hydrodynamic Properties of Rivers Using Inert Gas Tracers. In Proceedings of the Second International Conference on Advances in Engineering and Technology (AET 2011), Entebbe, Uganda, 30 January–2 Febuary 2011; Mwakali, J.A., Alinaitwe, H.M., Eds.; Macmillan Publishers: Kampala, Uganda, 2011; ISBN 978-214-00-7; pp. 670–676.

Section 1: *Stable Isotopes of Water (δ^2H, $\delta^{18}O$)*

Air Masses Origin and Isotopic Tracers: A Study Case of the Oceanic and Mediterranean Rainfall Southwest of France

Luc Lambs, Issam Moussa and Frederic Brunet

Abstract: Aquifers recharge mainly by local rainfall, which depend on the air mass humidity and orographic lifting, causing rain. The stable isotopes of the water molecule, *i.e.*, oxygen-18 and deuterium, are useful tracers to determine the water source origin. Moreover, the calculation of the deuterium excess enables one to differentiate between the air masses from the Atlantic Ocean or the Mediterranean Sea. A transect from one coast to the other one and going through the city of Toulouse have been made to sample the groundwater and determine their isotopic characteristic. A monthly rainfall sampling has also been done over one year, close to the city Toulouse, to see how the d-excess values range over the season. The discussion replaces these results in available isotopic data.

Reprinted from *Water*. Cite as: Lambs, L.; Moussa, I.; Brunet, F. Air Masses Origin and Isotopic Tracers: A Study Case of the Oceanic and Mediterranean Rainfall Southwest of France. *Water* **2013**, *5*, 617-628.

1. Introduction

France presents a wide range of coasts and is influenced by both the Atlantic Ocean and the Mediterranean Sea. The morphology of this country, which impacts the rainfall pattern, is complex, with the Massif Central in the center, the Alps to the east and the Pyrenees to the south. The main processes controlling the $\delta^{18}O$ and δD isotopic signatures in precipitations were summarized by Rozanski *et al.* [1]; *i.e.*, the rainfall amount, continental and altitude effects and the origin of air masses. For France, some pioneer works have studied the isotopic pattern of rainfall, such as Celle *et al.*, Celle-Jeanton *et al.*, Ladouche *et al.* and Millot *et al.* [2–5], but still, some areas lack for valuable data, like the Southwest area. It is, therefore, important to constrain the signature of the atmospheric signal in these geographical and geomorphological contexts by means of a rainfall-monitoring network and groundwater measurements.

The Southwest of France presents the characteristics of having two major winds blowing in an opposite direction. For instance, in Toulouse, the northwest wind (280° to 340°), called “Cers”, blows during 43% of the year, bringing the moisture from the Atlantic Ocean, and the southeast wind (120° to 180°), called “Autan”, blows during 29% of the year, bringing the Mediterranean influences. Therefore the airport runways are oriented N-W/S-E, the planes taking them from one end or the other depending on the wind origin.

The Autan wind is a föhn-type wind deriving from the Marin wind from the Mediterranean and blowing over the Languedoc into the Tarn and the Garonne valleys, affecting the Lauragais (the hilly area between Castelnaudary and Toulouse) and the Toulouse area. Channeled and intensified by the narrowing lowlands between the Pyrenees and the south of the Massif Central, it undergoes sudden

acceleration between the Corbières and the Montagne Noire (Venturi effect). Gusts can exceed twice the mean speed, possibly enhanced by lee-wave activity.

To understand the Atlantic Ocean and the Mediterranean Sea on the southwest rainfall of France, the present work summarizes over 75 isotopic measurements of shallow groundwater, used as rainfall natural gauges, located between these two coasts. This study is completed by an 18 months' rainfall survey near Toulouse in view to follow the air masses origin for the rainfall over the season and the influence of the Mediterranean income mainly through the Autan wind.

2. Experimental Section

2.1. Study Area

The Southwest of France stretches between the Atlantic and the Mediterranean coast over 350 km; see Figures 1 and 5. For the groundwater, the sampling places were taken in alluvial plains, *i.e.*, along the Garonne and Adour valley at the west and along the Aude valley at the east. The connection between the two basins is *Seuil de Naurouze* (189 m) located 40 km southeast of Toulouse. Farm wells or piezometers, if available, were used for the shallow groundwater sampling. Typical water depth ranges between 2 and 12 m. The longer groundwater survey has been made near Verdun sur Garonne, 35 km downstream (northwest) of Toulouse, in a farm well (depth 2–4 m), one km away from the Garonne River. It is located in the middle of the Garonne Channel and would be classified as mixed bedrock-alluvial stream [6], and the valley contains a classic flight of clay terraces that represent an episodic bedrock valley deepening and punctuated by lateral migration of the deposition of coarse gravels and sands.

Figure 1. The Southwest of France with the localization of the sample sites with the typical $\delta^{18}O$ value of the groundwater (in white) and the upstream basin (in red). The resulting isovalue contour for $\delta^{18}O = -5‰$, $-6‰$ and $-7‰$ are given with a white line, and the two dominant wind directions are given by both arrows.

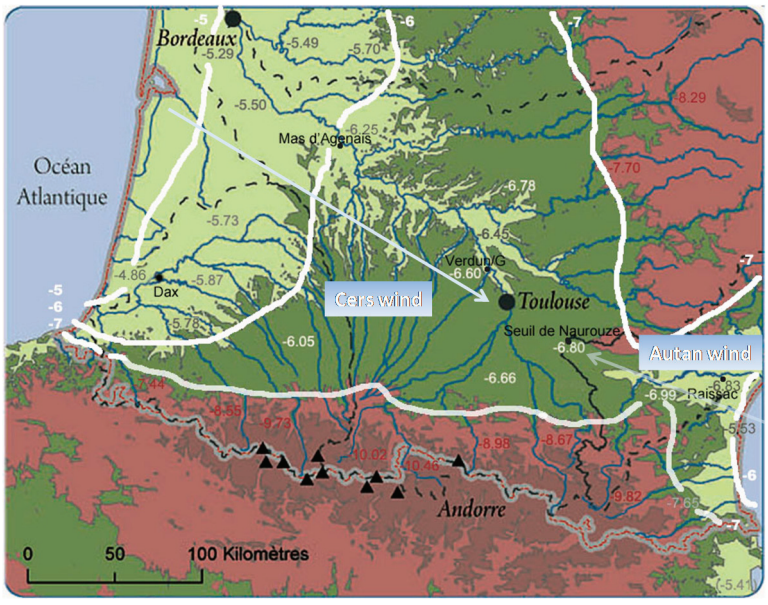

Along the west to east transect, the rainfall cumulates at the feet of the Western Pyrenees, with 1156 mm per year in Dax and a little less for Cestas-Pierroton, located north of Bordeaux with 920 mm. After, the rainfall amounts lower along the Garonne Valley with 763 mm in Agen and 660 mm in Toulouse. It increases slowly in the area of Carcasonne 736 mm, due to the proximity of the mountains, before slowing down again in the direction of the Mediterranean Sea: 609 mm in Narbonne, 549 mm in Perpignan and 605 mm in Sète. On the contrary, the evaporation enhance from west to east due to the increasing insulation.

2.2. Rainfall Sampling

Close to our isotopic laboratory in Auzeville, 8 km southeast of Toulouse, a rainfall sampling was installed during June 2011. Its consist of a polypropylene funnel (22 cm diameter) covering a 5 L polypropylene jerrycan, containing 300 mL of paraffin oil to avoid any evaporation process. The rainfall aliquots were sampled monthly, between July 2011 and December 2012. The meteorological data used were obtained from the close INRA station (less than 1 km) and compared with the long-term Toulouse airport station, Blagnac, where the record started in 1809, and located northwest, at 18 km. For each monthly sample, 10 mL were used for $\delta^{18}O$ and δD determination.

2.3. Groundwater Sampling

The shallow groundwater survey started in 1997 at Monbequi near Verdun sur Garonne in farm wells and piezometers to follow the influence of the Garonne River in this meander area [7,8]. The upper well was chosen as the local ground water reference and samplings were made over 6 years. To get a wider understanding of the alluvial groundwater characteristic, complementary samplings were done along the Garonne Valley between 2004 and 2007, for the Adour Valley between 2005 and 2006 and at the Seuil de Naurouze and Aude Valley in 2010.

2.4. Isotopic Measurements

Glass vial of 10 mL with tight caps were used for water sampling. The vials were kept at stable temperature before the measurement of the $\delta^{18}O$ and δD determination on a continuous flow isotope ratio mass spectrometer. Before 2007, the water samples were send to an iso-analytical laboratory in England (ANCA-GSL and GEO 20–20 IRMS, Europa Scientific, Crewe UK). Each water sample was measured in triplicate for each isotope ratio. The overall mean standard deviation (SD) for the $\delta^{18}O$ values was around ±0.15‰, and the mean SD for the $\delta^{2}H$ values was ±1.7‰. From 2010, the measurements were done on our own isotopic platform, Shiva (Isoprim 100 and Geo-multi-flow, Elementar, Hamburg, Germany). Each water sample was measured in duplicate. The mean standard deviation (SD) for the rainfall measurements was around ±0.29‰ for $\delta^{18}O$, and the overall mean SD was ±2.5‰ for $\delta^{2}H$.

The results are given relative to V-SMOW standards from IAEA. The deuterium excess was calculated using the Global Meteorological Water Line (GMWL), as defined by Craig [9] and completed by Dansgaard [10]:

$$\text{d-excess} = \delta D - 8 \times \delta^{18}O \quad (1)$$

A value of d-excess around 10 or below, *i.e.*, similar to the GMWL, was taken as originating from Atlantic moisture and a value around 14 [2] as moisture with water recycling as one coming from the close West Mediterranean basin.

3. Results and Discussion

3.1. Rainfall Results

The data were obtained between July 2011 and December 2012. The annual amount of rainfall for 2011 was 538 mm, and for 2012 it was 548 mm in the INRA station and around 20% over the amount values from Blagnac Airport station. These numbers are under the 30 years mean (CLINO period 1961–1990 [11]), 671 ± 121 mm per year monthly, as since 2003, the Toulouse area is in a dry period. The obtained isotopic value for $\delta^{18}O$ ranges from −10.7‰ to −4.0‰, showing the continental influence, with a mean monthly temperature ranging from −2.5 °C (February 2012) for the minimum to +30.4 °C (August 2012) for the maximum. Table 1 reports the obtained isotopes values for the monthly rainfall, with the meteorological data from the nearby INRA station.

In Figure 2, both years are plotted along a whole year and present a similar pattern. The $\delta^{18}O$ signal presents the more depleted values in winter and the less depleted in summer, following the temperature shift. The negative peak from February 2012 corresponds to a cold period, until −12.5 °C on February 9, with one week of snow. The d-excess displays more erratic variations, perhaps with some evaporative process in summer (July) and a possible Mediterranean influence in October.

Figure 3 gives the representation of $\delta^{18}O$ *versus* $\delta^{2}H$ for both years. For 2011, the regression gives in 2011 a slope of 7.70 and a d-excess of 11.28 with $R^2 = 0.979$, and in 2012, the slope is equal to 7.70 and a d-excess of 9.85 with a $R^2 = 0.909$. Both sets are very close with the Global Meteorological Water Line (GMWL) defined by Craig 1961 [9]. The point above the GMWL ($\delta^{18}O$ = −7.83‰, d-excess = +22.12) corresponds to a possible Autan wind influence with the incoming of Mediterranean rain. The weighted mean (w-mean) of $\delta^{18}O$ or the d-excess can be calculated by summing the monthly amount of rainfall (rainfall $\text{amount}_{\text{month}}$) relative to the total rainfall for one year and multiplying both monthly isotopic values, according to the following equation:

$$\delta^{18}O_{\text{w-mean}} = \Sigma^{\,i = 1 \text{ to } 12}\, \delta^{18}O_{\text{month}} \times \text{Rainfall amount}_{\text{month}} \div \text{Rainfall amount}_{\text{year}} \quad (2)$$

The obtained value for the 2012 values is $\delta^{18}O_{\text{w-mean}}$ = −6.32‰ ± 0.25‰ and a $\text{d-excess}_{\text{w-mean}}$ = 11.76 ± 0.59.

Table 1. Isotopic results, calculated d-excess and meteorological conditions for the rainfall samples near Toulouse.

Month	$\delta^{18}O$ (‰)	$\delta^{2}H$ (‰)	d-excess	Rainfall (mm)	Min. T (°C)	Max. T (°C)
July 2011	−4.48	−28.15	7.69	86.5	14.9	25.7
August 2011	−4.00	−19.02	12.98	21.5	16.3	29.0
September 2011	−5.18	−27.18	14.24	73.5	14.8	27.2
October 2011	−6.59	−36.73	15.98	24.5	9.6	21.7
November 2011	−10.71	−72.56	13.12	31.0	9.6	15.9
December 2011	−5.62	−30.45	14.51	53.0	5.0	12.1
January 2012	−6.55	−40.87	11.53	39.0	3.8	10.3
February 2012	−10.22	−71.81	9.95	4.0	−2.5	6.0
March 2012	−5.80	−32.00	14.40	22.0	4.1	17.5
April 2012	−6.71	−44.17	9.51	69.0	7.6	16.2
May 2012	−4.80	−24.84	13.56	75.5	11.6	22.2
June 2012	−4.67	−27.23	10.10	53.5	15.0	26.5
July 2012	−4.53	−29.61	6.63	58.0	14.7	27.5
August 2012	−6.28	−39.35	10.89	48.5	17.5	30.4
September 2012	−5.25	−28.96	13.05	26.0	13.9	24.7
October 2012	−7.83	−40.53	22.12	53.0	11	20.5
November 2012	−8.89	−55.92	15.20	49.5	6.8	14
December 2012	−8.09	−59.80	4.93	50.5	4.6	11.6

Figure 2. Monthly variation of (**a**) $\delta^{18}O$ and (**b**) d-excess with error bars for the rainfall in 2011 (dotted line, no symbol) and 2012 (plain line, cross symbol) near Toulouse.

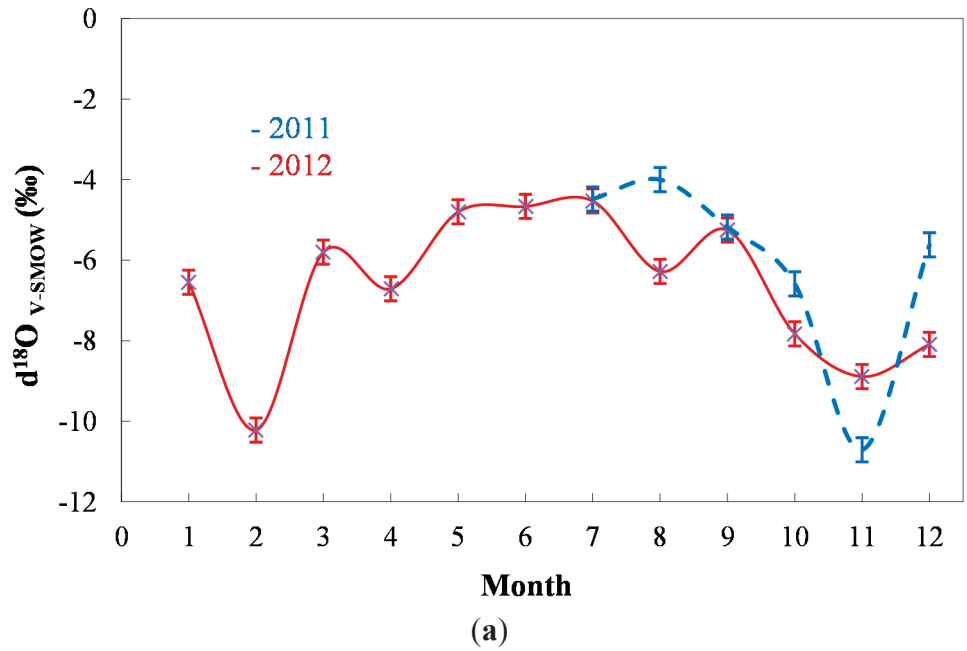

(**a**)

Figure 2. *Cont.*

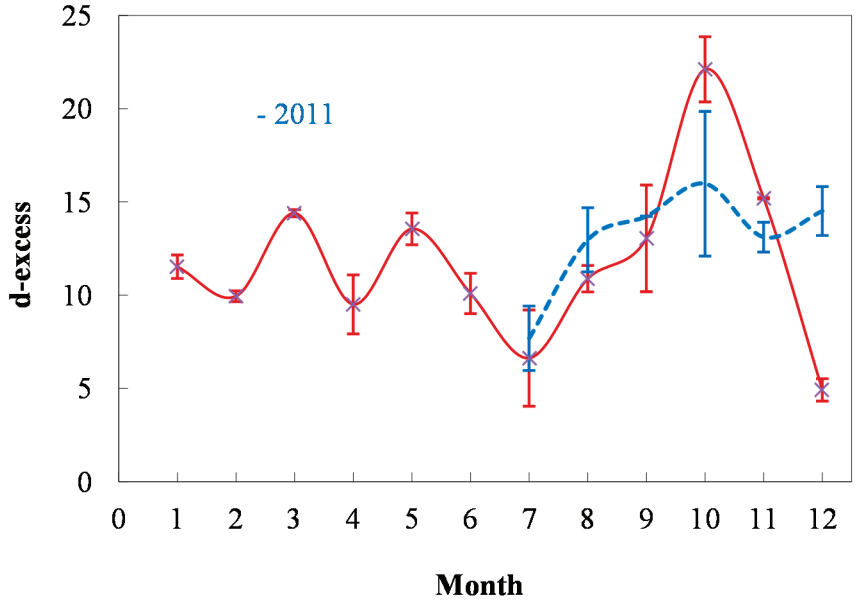

(b)

Figure 3. Relationship between the $\delta^{18}O$ and $\delta^{2}H$ rainfall values for 2011 and 2012 compared to the GMWL line (dotted line).

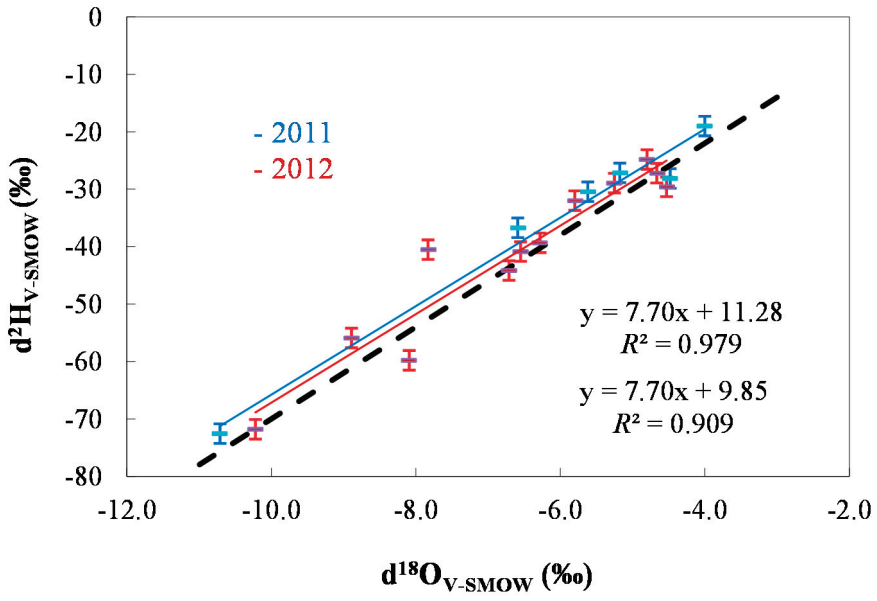

3.2. Groundwater Results

3.2.1. Reference Well

The survey of the reference well for the groundwater over six years (see Figure 4) reveals that the $\delta^{18}O$ values range from −6.18‰ to −7.10‰.The overall mean value of $\delta^{18}O$= −6.60‰ ± 0.24‰ (n = 31), whereas the annual mean values range from −6.43‰ to −6.86‰. The seasonal pattern appears very reduced ($\Delta\delta^{18}O$ = 0.2 units) for these 31 samples, with a slight depletion in spring. This dampened isotopic amplitude (A_{GW}) response compared to the rainfall isotopic amplitude ($A_{rainfall}$)

can be used to calculate the mean residence time (t_{mr}) according to the exponential model equation of Stichler and Herrmann [12]:

$$t_{mr} = 0.5\pi \times (A_{rainfall}^2/A_{GW}^2 - 1)^{0.5} \quad (3)$$

This calculation gives a residence time of about five years.

Figure 4. Variation of the $\delta^{18}O$ values of the reference groundwater well near Verdun sur Garonne (between 1997 and 2003) over the season. The solid line represents the polynomial regression line.

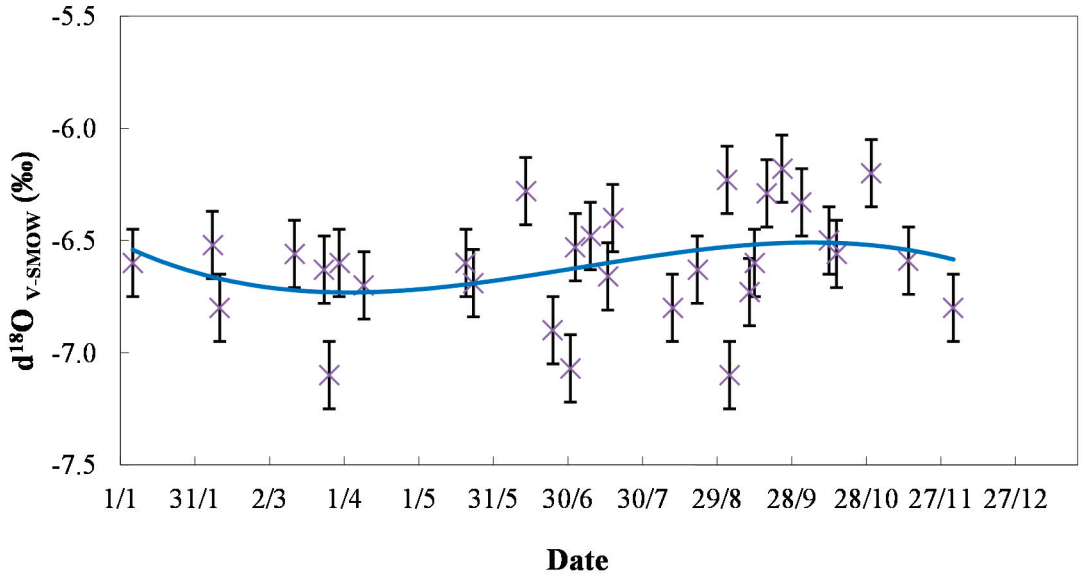

3.2.2. Groundwater between Atlantic and Mediterranean Coasts

The numerous alluvial ground water sample along the Garonne, Adour and Aude Valleys shows that there is a gradient from around $\delta^{18}O = -5.0‰$ close to the Atlantic coast (−4.6‰ in Dax and −5.4‰ in Bordeaux) and slowly becoming more depleted when coming more inland. At Verdun/Garonne, 50 km downstream of Toulouse, and until Seuil de Naurouze, the highest point (189 m) where the water flux divides itself between the Atlantic and the Mediterranean slope, the $\delta^{18}O$ reaches −6.6‰. The continental effect continues on the east slope until Raissac, 25 km before the Mediterranean Sea, with a value of $\delta^{18}O$ around −6.8‰. Along this sea coast, the isotopic values become less depleted, with $\delta^{18}O$ value close to −5.5‰.

On the contrary, the d-excess starts close to 10 (*i.e.*, the value of GMWL) along the Atlantic coast, before dropping inland, until Toulouse, around 6. From Seuil de Naurouze, the d-excess increases from 8.2, to 9.8 in Raissac, before reaching 12.6 at La Franqui. The Mediterranean Sea is a closed system and displays a higher d-excess value, around 14 [2]. The effect of the Mediterranean Sea through the Autan wind affects the d-excess, meaning that the water vapor recycles until Seuil de Naurouze, but the isotopic signal of the of the Continental effect coming from the Atlantic coast stops only a few ten km before reaching the Mediterranean coast, see Figure 5.

Figure 5. Continental gradient from the west Atlantic coast to east Mediterranean coast: mean isotopic values ($\delta^{18}O$, d-excess) for the different alluvial ground water stations along the Garonne, Adour and Aude Valleys. The altitude of the station is given between brackets.

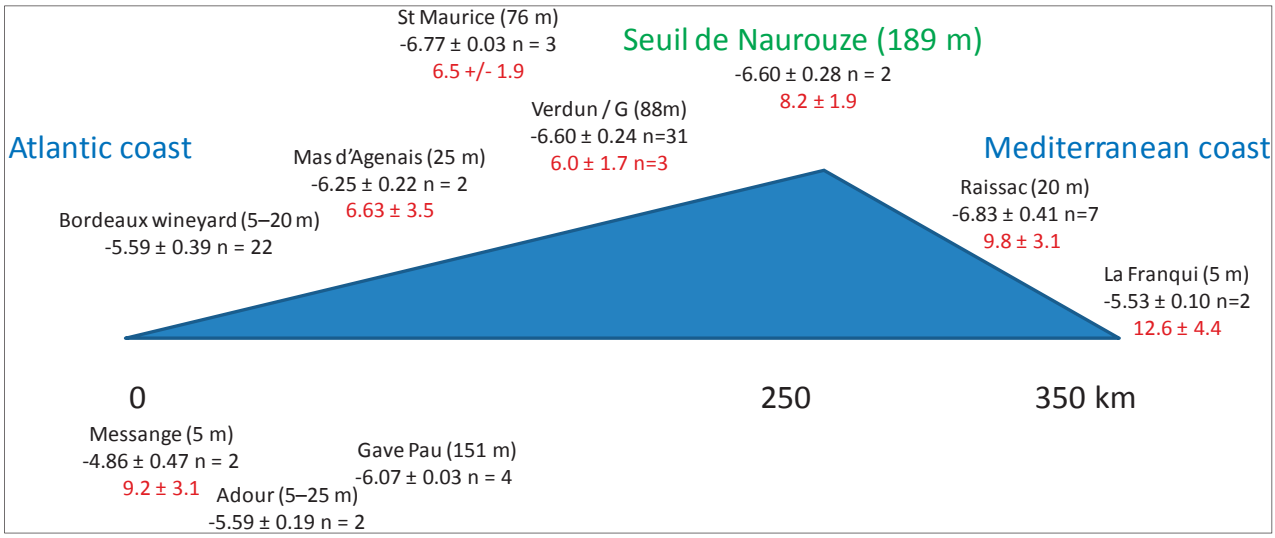

3.3. Discussion

Most shallow groundwater is of meteoric, *i.e.*, atmospheric origin. Rainwater directly infiltrates the ground or indirectly via the inflow of surface water or from bank storage in streams [13]. Shallow and locally-derived ground waters are often used to characterize the isotopic content of meteoric waters, due to the conservative nature of the stable isotope composition of water in an aquifer [14].

Unconsolidated sediments, like in a river valley, are excellent and most efficient aquifers. Their porosity and permeability are usually high [13]. We have measured the groundwater velocity in Verdun near our reference well, and the velocity ranges from 2.1 to 3.2 m/day [15]. Such alluvial plains present high precipitation response to rainfall, and the residence time of ground water is short. In general, alluvial shallow groundwaters are known to be two to 50 years old [16]. In our case, with the equation of Stichler [12], we found a resident time of five years for our groundwater reference well.

On the contrary, deeper groundwater in the Adour-Garonne basin is characterized by more depleted values than the actual mean isotopic rainfall, with values ranging from $\delta^{18}O = -5.6‰$ to $-10.6‰$ [17]. For instance, in the Southwest of France, we found isotopic values ranging from $\delta^{18}O = -7.2‰$ to $-7.8‰$, (Lambs, unpublished results) for many tens of meters-depth bore wells. Such heterogeneity in the $\delta^{18}O$ signature for a Paleocene aquifer reflects a variable recharge, either in space and time. The most depleted values correspond to a water recharged with a colder climate than the present one [17].

From the isotopic results around Toulouse, there is very good agreement between the Verdun groundwater annual average value ($\delta^{18}O_{mean} = -6.60‰ \pm 0.25‰$) and the rainfall ($\delta^{18}O_{mean} = -6.63‰ \pm 1.81‰$). For the calculated d-excess, there is a small shift with a mean value of $d\text{-excess}_{mean} = 6.0 \pm 1.7$ for the groundwater and $d\text{-excess}_{mean} = 11.8 \pm 4.43$ for the rainfall. Notice also that the groundwater

taken at the Naurouze pass in 2010 gives similar values ($\delta^{18}O = -6.80‰ \pm 0.28‰$, d-excess = 8.2 ± 1.9) compared to Verdun groundwater sampled between 1997 and 2003.

On a wider scale, the isotopic fractionation with the altitude is around −0.28 $\delta^{18}O$ per mil for 100 m of elevation [2]. Along our transect, as the mean values of the groundwater around Bordeaux are $\delta^{18}O = -5.6‰$, at the highest point, Seuil de Naurouze (189 m), the altitude isotopic should at least be −6.2‰, but as the mean Lauragais hill is around 290 m, a correct value would be −6.5‰. Another way is to calculate the continental effect with the ratio of −3.2 $\delta^{18}O$ per mil for 1000 km inland [5]. From the Atlantic coast at the level of Bordeaux until Seuil de Naurouze, there is 330 km, which should give a fractionation of −1.06, *i.e.*, around −6.66‰, which is in better accordance with the measured values. If one calculates the continental fractionation until Raissac, 420 km from the Atlantic coast, the new $\delta^{18}O$ would become −6.94‰, a value more depleted than the observed mean value of −6.83‰.

Rainfall coming from the western Mediterranean basin is known to present less depleted $\delta^{18}O$ values, but with a higher d-excess value, around +14 [3,18]. Such an influence is seen on groundwater $\delta^{18}O$ values of la Franqui and perhaps also in the higher d-excess of the Raissac area. Even in Toulouse, in October 2012, the abnormal d-excess of the rainfall could come from this Mediterranean inflow. In general, the Mediterranean rainfall seems to be located much closer to the coast, a few tens of kilometers wide. Only the black Autan wind, a particular case of the Autan wind blowing northwest, can bring Mediterranean moisture more inland. However, the amount of this East Mediterranean rainfall remains low compared to the West Atlantic rainfall. The Autan wind is a continental high pressure wind bringing heat and dryness and is influenced by the local orography. Even if different meteorological models try to understand this particular wind [19–21], it is often not announced in the weather forecast.

Table 2 reports the rainfall isotopic data available in the Global Network of Isotopes in Precipitation (GNIP) database from IAEA [22]. For Toulouse, the data is from the present work (year 2012), as there is no other data on the GNIP database. However, it is possible to get the calculated interpolated data from the area of Toulouse [23], which is $\delta^{18}O = -6.2‰ \pm 0.3‰$. This value is a little less than our mean value ($\delta^{18}O_{mean} = -6.6‰ \pm 1.8‰$), but equal to our weighted mean: $\delta^{18}O_{w\text{-}mean} = -6.32‰ \pm 0.25‰$. For the slope between the $\delta^{18}O$ and δD values, only Toulouse presents a value close to the GMWL (respectively, 7.70 and 8.00). All the other places on both coasts display a lower slope, due to a smaller $\delta^{18}O$. It is not necessarily a problem of coastal influence or the evaporation process. In fact, the GMWL as a global line is made of many small local lines with slopes that are often smaller than eight. There is a good correspondence between the calculated $\delta^{18}O$ weighted mean of Bordeaux (in fact, Cestas-Pierroton) and our mean groundwater of this area (respectively, −5.69‰ and −5.59‰) and also the calculated $\delta^{18}O$ weighted mean of Dax and our mean groundwater of this area (respectively, −4.59‰ and −4.86‰). With these $\delta^{18}O$ weighted means, the continental effect from west to east between Bordeaux and Toulouse is around one unit and the latitude effect between Bordeaux and Dax, also one unit of $\delta^{18}O$. One can also notice the equivalent of $\delta^{18}O$ weight mean values of Dax and Montpellier (respectively, −4.59‰ and −4.17‰), nearly on the same latitude, but on a different sea coast. The calculated weighted d-excess mean is always high, *i.e.*, between nine and 12, and only in Avignon, it drops at around eight.

The study of the West Mediterranean influence is complex, as it is a transition zone between the cool North Atlantic air masses and the warm and wet air flowing from the Mediterranean basin. The isotopic signal of the air masses from these different origins crossing the Mediterranean may be modified by water vapor produced in the Mediterranean [3]. The d-excess value of the water vapor of the Mediterranean region results from the intensive evaporation near the coast, under conditions of a large humidity deficit [24]. All these particular features from the Mediterranean water vapor reveal the importance of the study to understand the local climate by monitoring numerous and long-term rainfall and groundwater sampling.

Table 2. Comparison of the isotopic features of the GNIP stations and our Toulouse station.

City	Slope	d-excess	R^2	$\delta^{18}O_{w\ mean}$ (‰)	d-excess$_w$	$\delta^{18}O$ range (‰)	Rainfall (mm)	Year
Dax	6.09	0.32	0.948	−4.59 ± 0.95	9.71 ± 1.24	−6.84–−2.25	1156	1999–2005
Bordeaux	6.90	3.90	0.925	−5.69 ± 0.65	10.18 ± 0.32	−7.16–−4.33	920	2007–2009
Toulouse	7.70	9.86	0.909	−6.32 ± 0.25	11.76 ± 0.59	−10.71–−4.00	548	2012
Montpellier	6.49	3.07	0.825	−4.17 ± 0.14	9.07 ± 2.07	−6.65–−1.79	595	1997–1998
Avignon	7.19	2.31	0.984	−5.49 ± 1.20	7.39 ± 2.95	−7.83–−2.23	619	1997–2009

4. Conclusions

The present study is the first one to provided isotopic rainfall data for the Toulouse area in connection with numerous alluvial groundwater sampling over the Southwest of France. These results reveal that this area is influenced by both the Atlantic and the Mediterranean climate, but also, a continental effect is perceptible through the wide isotopic range. The Mediterranean influence is mainly brought by the Autan wind, but the isotopic composition of the groundwater is only influenced closer to a few tens of kilometers from the Mediterranean shore. Only some d-excess higher value can reveal it. More sampling of rainfall at the month scale still needs to be done for this area to better understand this specific climate. Furthermore, sampling of individual special rain events, like after the Autan wind, is now also performed for trying to refine these possible Mediterranean moisture inflows.

Acknowledgments

We would like to thank Florent Barbecot (University of Paris Sud) and Stephan Terzer (IAEA, Vienna) for their advice for the rainfall isotope sampling, Romain Walker (Ecolab) for Figure 1 and Daniel Dalger (Ecolab) for help with the isotopic analysis. For the meteorological data, we are grateful to Pierre Perrin (INRA Auzeville) and Meteofrance (Blagnac airport), and for the two anonymous reviewers for their valuables comments.

References

1. Rozanski, K.; Araguas-Araguas, L.; Gonfiantini, R. Isotopic patterns in modern global precipitation. In *Climate Change in Continental Isotopic Records*; Geophysical Monograph Series Volume 78; Swart, P.K., Lohmann, K.C., Mckenzie, J., Savin, S., Eds.; American Geophysical Union: Washington, DC, USA, 1993; pp. 1–36.
2. Celle, H.; Daniel, M.; Mudry, J.; Blavoux, B. Signal pluie et traçage par les isotopes stables en Méditerranée occidentale: Exemple de la région avignonnaise (Sud-Est de la France) [in French]. *C. R. d'Acad. Sci. Ser. IIA Earth Planet. Sci.* **2000**, *331*, 647–650.
3. Celle-Jeanton, H.; Travi, Y.; Blavoux, B. Isotopic typology of the precipitation in the Western Mediterranean region at three different time scales. *Geophys. Res. Lett*. **2001**, *28*, 1215–1218.
4. Ladouche, B.; Aquilina, L.; Dörfliger, N. Chemical and isotopic investigation of rainwater in Southern France (1996–2002): Potential use as input signal for karst functioning investigation. *J. Hydrol.* **2009**, *367*, 150–164.
5. Millot, R.; Petelet-Giraud, E.; Guerrot, C.; Négrel, Ph. Multi-isotopic composition (Li, B, D, O) of rainwaters in France: Origin and spatio-temporal characteristization. *Appl. Geochem.* **2010**, *25*, 1510–1524.
6. Howard, A.D.; Dietrich, W.E.; Seidl, M.A. Modeling fluvial erosion on regional to continental scales. *J. Geophys. Res. Solid Earth* **1994**, *99*, 13971–13986.
7. Lambs, L. Correlation of conductivity and stable isotope ^{18}O for the assessment of water origin in river system. *Chem. Geol.* **2000**, *164*, 161–170.
8. Lambs, L. Interactions between groundwater and surface water at river banks and the confluence of rivers. *J. Hydrol.* **2004**, *288*, 312–326.
9. Craig, H. Isotopic variation in meteoric waters. *Science* **1961**, *133*, 1702–1703.
10. Dansgaard, W. Stable isotopes in precipitation. *Tellus* **1964**, *16*, 436–468.
11. Word Meteorological Organization (WMO). *Climatological Normals (CLINO) for the Period 1961–1990*; Secretariat of the Word Meteorological Organization: Geneva, Switzerland, 1996.
12. Stichler, W.; Herrmann, A. Application of Environmental Isotope Techniques in Water Balance Studies of Small Basins. In *New Approaches in Water Balance Computations*, Proceedings of the 18th General Assembly of the International Union of Geodesy and Geophysics, Hamburg, Germany, August 1983; IAHS Publication 148: Oxfordshire, UK; pp. 93–112.
13. Geyh, M. Groundwater. In *Environmental Isotopes in the Hydrological Cycle*; Mook, W.G., Ed.; International Hydrological Programme: Paris, France; International Atomic Energy Agency: Vienna, Austria, 2000; Volume 4, pp. 1–193.
14. Longinelli, A.; Selmo, E. Isotope geochemistry and the water cycle: A short review with special emphasis on Italy. *Mem. Descr. Carta Geol. d'It*. **2010**, *90*, 153–164.
15. Bats-Landalle, G. Analyse Géomorphologique de la Plaine d'Inondation de la Garonne [in French]. Ph.D. Thesis, University of Toulouse, Toulouse, France, September 1998.
16. Weisman, G.S.; Zhang, Y.; LaBolle, E.M.; Fogg, G.E. Dispersion of groundwater age in an alluvial aquifer system. *Water Resour. Res.* **2002**, *38*, 1–13.

17. Negrel, Ph.; Petelet-Giraud, E. Isotopes in groundwater: Indicators of climate changes. *Trends Anal. Chem.* **2011**, *30*, 1279–1290.
18. Gat, J.R.; Carmi, I. Effect of Climate Changes on the Precipitation Patterns and Isotopic Composition of Water in a Climatic Transition Zone: Case of the Eastern Mediterranean Sea Area. In *The Influence of Climate Change and Climatic Variability on the Hydrologic Regime and Water Resources*, Proceedings of the Vancouver Symposium, Vancouver, Canada, 9–22 August 1987; IAHS Publication 168: Oxfordshire, UK; pp. 513–523.
19. Von der Emde, K.; Bougeault, Ph. High resolution simulation of a flow past the Pyrenees. *Meteorol. Atmos. Phys*. **1997**, *62*, 1–8.
20. Benech, B.; Koffi, E.; Druilhet, A.; Durand, P. Dynamic characteristics of regional flows around the Pyrenees in view of the Pyrex experiment. *J. Appl. Meteorol.* **1998**, *37*, 32–51.
21. Aouzerats, B.; Tulet, P.; Pigean, G.; Masson, V.; Gomes, L. High resolution modeling of aerosol dispersion regimes during the Capitoul field experiment: From regional to local scale interactions. *Atmos. Chem. Phys. Discuss*. **2010**, *10*, 29569–29598.
22. International Atomic Energy Agency Web Page. Global Network of Isotopes in Precipitation. Available online: http://www-naweb.iaea.org/napc/ih/IHS_resources_gnip.html (accessed on 9 May 2013).
23. Bowen, G.J. *The Online Isotopes in Precipitation Calculator*, Version 2.2. Available online: http://www.waterisotopes.org (accessed on 13 May 2013)
24. Gat, J.R.; Klein, B.; Kushnir, Y.; Roether, W.; Wernli, H.; Yam, R.; Shemesh, A. Isotope composition of air moisture over the Mediterranean Sea: An index of the air-sea interaction pattern. *Tellus* **2003**, *55*, 953–965.

Identifying Seasonal Groundwater Recharge Using Environmental Stable Isotopes

Hsin-Fu Yeh, Hung-I Lin, Cheng-Haw Lee, Kuo-Chin Hsu and Chi-Shin Wu

Abstract: In this study, the stable isotope values of oxygen and hydrogen were used to identify the seasonal contribution ratios of precipitation to groundwater recharge in the Hualien River basin of eastern Taiwan. The differences and correlations of isotopes in various water bodies were examined to evaluate the groundwater recharge sources for the Hualian River basin and the interrelations between groundwater and surface water. Proportions of recharge sources were calculated based on the results of the mass balance analysis of the isotope composition of hydrogen and oxygen in the basin. Mountain river water accounted for 83% and plain rainfall accounted for 17% of the groundwater recharge in the Huanlian River basin. Using the mean *d*-values, a comparison of *d*-values of precipitation and groundwater indicates the groundwater consists of 75.5% wet seasonal sources and 24.5% dry seasonal sources, representing a distinct seasonal variation of groundwater recharge in the study area. Comparisons between hydrogen and oxygen isotopes in rainwater showed that differences in the amount of rainfall resulted in depleted oxygen and hydrogen isotopes for precipitation in wet seasons as compared to dry seasons. The river water contained more depleted hydrogen and oxygen isotopes than was the case for precipitation, implying that the river water mainly came from the upstream catchment. In addition, the hydrogen and oxygen isotopes in the groundwater slightly deviated from the hydrogen and oxygen isotopic meteoric water line in Huanlian. Therefore, the groundwater in this basin might be a mixture of river water and precipitation, resulting in the effect of the river water recharge being greater than that of rainfall infiltration.

Reprinted from *Water*. Cite as: Yeh, H.-F; Lin, H.-I; Lee, C.-H; Hsu, K.-C; Wu, C.-S. Identifying Seasonal Groundwater Recharge Using Environmental Stable Isotopes. *Water* **2014**, *6*, 2849-2861.

1. Introduction

Oxygen and hydrogen isotopes of water are widely used as tracers to understand hydrogeological processes such as precipitation, groundwater recharge, groundwater-surface water interactions, and basin hydrology [1–6]. A comparison of the oxygen and hydrogen isotopic compositions of precipitation and groundwater provides an excellent tool for evaluating the recharge mechanism [7–11]. Determining the sources of groundwater recharge is important for the effective management of groundwater resources.

In hydrology, fractionation of $\delta^{18}O$ and δD is driven by kinetic processes during evaporation and condensation [12]. In the process of oceanic water evaporation becoming inland rainfall, a sequence of isotope fractionations causes variations in the composition of the isotope values of oxygen and hydrogen in continental meteoric water. Since this fractionation process is based on the equilibrium processes of the isotopes of evaporation and condensation, there is a specific relationship that governs the distributions of isotope values of oxygen and hydrogen in rainfall.

The empirical equation was found by Craig [13] when he used a linear regression method to analyze the composition of the isotopes of oxygen and hydrogen in samples of precipitation, snow water, and river water from all over the world. His finding is known as the Global Meteoric Water Line (GMWL):

$$\delta D = 8\,\delta^{18}O + 10 \quad (1)$$

A later study by the IAEA (International Atomic Energy Agency), water samples from rainfall stations were collected globally showing a similar result [12,14]:

$$\delta D = (8.17 \pm 0.08)\,\delta^{18}O + (10.56 \pm 0.64) \quad (2)$$

Most of the precipitation in the world follows this relationship. However, some specific areas that have different evaporation and condensation conditions (e.g., temperature and humidity), or that have a unique terrain environment, create their own special local meteoric water line with a different slope and intercept [12,15]. In the meteoric water line of oxygen and hydrogen isotopes, the slope represents the ratio of the temperature relationship between δD and $\delta^{18}O$ when condensation occurs; the value of the intercept is based on the evaporative conditions in the water source region.

The intercept is also called deuterium excess or *d*-excess ($d = \delta D - 8\delta^{18}O$) [14]. The intercepts in most places around the world are about 10‰. However, areas may have different slopes and intercepts due to different rainfall evaporation conditions or source evaporation conditions in various air mass sources. For example, North America: $\delta D = 7.95\,\delta^{18}O + 6.03$ [12]; Tropical Island area: $\delta D = 6.17\,\delta^{18}O + 3.97$ [12]; Japan: $\delta D = 8\,\delta^{18}O + 17.5$ [16]. Generally speaking, if evaporation is faster, or if rainfall evaporation occurs, intercepts are higher. Some studies have used *d*-excess to identify the air mass source of meteoric water and to define the seasonal recharge of groundwater [4,5,7,17].

Taiwan is located in the West Pacific Ocean monsoon climate area. The air mass of the Northeast monsoon prevalent in winter originates from the Antarctic Continent. The air mass of the Southwest monsoon prevalent in summer originates from the equator in the Pacific Ocean and from the North Pacific Ocean tropical marine air mass. Rainfall in Taiwan is related to these three air masses. The summer rainfall in Taiwan is mostly typhoon cloudbursts and afternoon rainfall caused by thermal convection. Due to the effects of the Central Mountain Range, Northern Taiwan faces the Northeast monsoon [18]. During the winter, southward cold fronts bring plentiful water vapor from the East China Sea which results in rainfall. Although Eastern Taiwan is to the east of the Central Mountain Range, rainfall is low because the Northeast monsoon moves parallel to the coast. In addition, Western Taiwan, protected by the Central Mountain Range, is not obviously affected by the Northeast monsoon, causing winter drought [18].

The purpose of this study is to use oxygen and hydrogen isotopes as natural tracers to identify the possible sources of groundwater and the seasonal variations in groundwater recharge in the eastern Taiwan Huanlian River basin. The results provide useful information about hydrological processes, such as the interaction of precipitation, river water, and groundwater.

2. Study Area

The Huanlian River is located in the Huatung Valley in Hualian County, Eastern Taiwan. To the north, this river connects with the Taroko River system basin; to the west, it is adjacent to the Chuoshui River; to the south, it is next to the Xiuguluan River basin; and to the east, it is next to the Fengping River system basin (Figure 1). The Hualian River originates from Bazi Mountain, which is a sub-range of the Dan Mountain. The main stream is approximately 57.28 km long, with a basin area of 1507 km^2 and an annual runoff of 3813 million m^3. The Hualian River basin water resources are primarily used for agriculture irrigation, followed by domestic and industrial water use. Despite the rich amount of surface water offered by the Huanlian River, the surface runoff during wet and dry seasons fluctuates significantly. Each year's high-flow period starts from May to October, which accounts for 70% of the runoff of the entire year. After October, the flow declines significantly, and the driest period occurs in February and March. From November to April of the following year, the runoff in the drought period accounts for approximately 30% of the annual runoff.

The main stream of the Huanlian River exits the valley from Dafong Mountain and enters the plains areas. It flows along Huatung Valley from southwest to northeast. The primary sub-ranges include the Guangfu River, the Maan River, the Wanli River, the Shoufeng River, and the Mugua River. These rivers run into the ocean near Hualian Mountain, at the north of the Coastal Range. The hydrogeology of the Hualian River basin can be divided into three areas based on location: the Central Mountain Range, Huatung Valley, and the Coastal Range. Depending on the terrain, Hualian can be divided into two sections, Hualian Plain and Huatung Valley Plain. Hualian Plain is located to the north of Huatung Valley. Good gravel aquifers can be found at depths of 80–90 m underground. The width of the Huatung Valley's shallow gravel layer tends to become thinner from the top to the bottom of the alluvial fan, whereas the deeper layer is characterized by coarse sands and occasional mud layers. With respect to geological characteristics, Huatung Valley is located at the line of collision between the Eurasian Plate and the Philippine Sea Plate. The two sides of the valley are delimited by upthrust with high angles.

Hualian River is abundant in runoff and high in sediment transport capacity. Most surface water is utilized for agricultural purposes, whereas domestic and industrial water rely on the copious amount of available groundwater. To understand the use of water resources in this basin, the fundamental characteristics and recharge sources of the groundwater need to be analyzed. Based on the effective fractional porosity volume in the alluvium, it can be determined that the groundwater reserve in the Hualian River basin is approximately 5 billion m^3, 370 million m^3 of which can be exploited per year [19]. Based on water balance, the river infiltration recharge for the whole region is 1.45 billion m^3 [20]. A report published by the Taiwan Water Resource Agency [21] shows a simulation of the hydraulic characteristics of regional groundwater using the MODFLOW model in the Groundwater Modeling System (GMS). According to the results of the groundwater budget in the Hualian River basin, 27% of the infiltration is direct rainfall, 18% of the recharge is the lateral flow of boundary, and 55% of the groundwater recharge comes from river water.

Figure 1. The location of the study region. Precipitation sampling sites (circles), river water (squares), and groundwater (triangles) samples are shown.

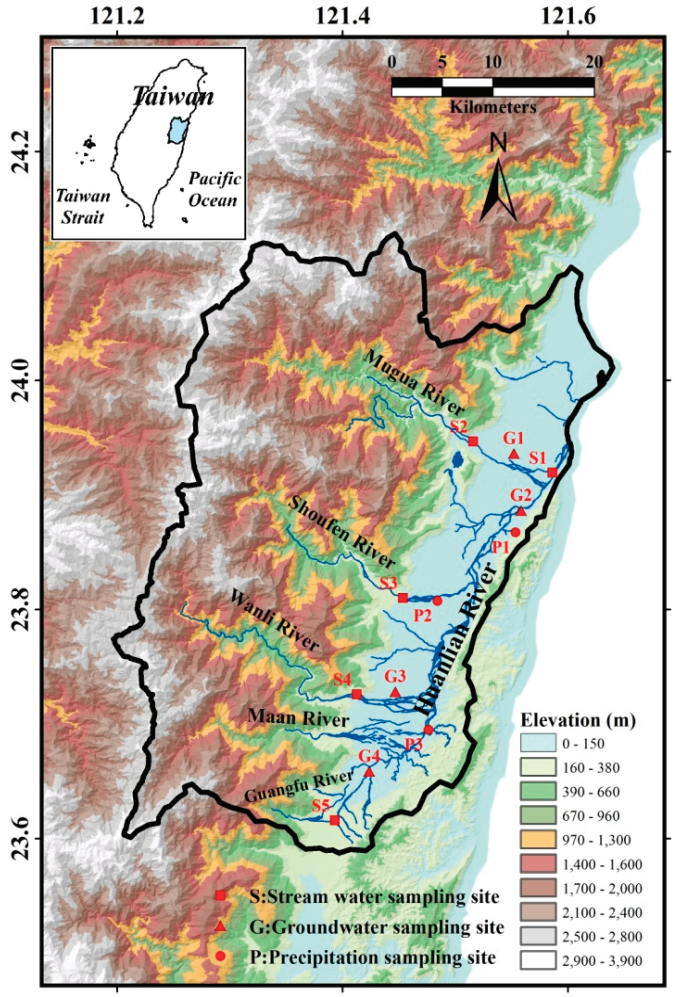

3. Sampling and Analytical Method

Precipitation, river water, and groundwater samples were collected for oxygen and hydrogen isotopic analyses from 2003 to 2012. Sampling was carried out during both wet and dry periods. Sampling procedures for precipitation were in accordance with IAEA guidelines [22]; in short, the procedures are designed to avoid evaporation of precipitation samples. Sampling locations are shown in Table 1 and Figure 1. Stable oxygen isotopic compositions were analyzed using the CO_2-H_2O equilibration method [23]. The equilibrated CO_2 gas was measured using a VG SIRA 10 isotope ratio mass spectrometer. The hydrogen isotopic compositions were determined on a VG MM602D isotope ratio mass spectrometer after water was reduced to H_2 using zinc shots made by the Biogeochemical Laboratory of Indiana University [24]. All isotopic ratio results were reported as the δ-notation (‰) relative to the international VSMOW (Vienna Standard Mean Ocean Water) standard. The precisions (2σ) for $\delta^{18}O$ and δD were 0.1‰ and 1.5‰, respectively.

Table 1. Sampling locations of the study region.

Site	Longitude	Latitude	Elevation (m)
S1	121.59	23.92	7
S2	121.52	23.95	96
S3	121.45	23.81	140
S4	121.41	23.73	143
S5	121.39	23.62	160
P1	121.55	23.87	76
P2	121.48	23.81	91
P3	121.48	23.70	106
G1	121.55	23.94	52
G2	121.56	23.89	18
G3	121.45	23.73	110
G4	121.42	23.66	116

4. Results and Discussion

4.1. Isotopic Compositions of Precipitation

For the purposes of this study, a total of 385 samples of precipitation in the Hualian River basin were analyzed to discuss the characteristic isotopic signatures of precipitation. The δD of the precipitation was between −149.5‰ and 22.7‰, with a mean of −22.9‰ ± 31.9‰. The $\delta^{18}O$ ranged between −20.2‰ and 1.5‰, with a mean −4.4‰ ± 3.7‰. The mean *d* was 12.1‰. Linear regression analysis showed the Local Meteoric Water Line (LMWL) of the Hualian River basin to be $\delta D = 8.40\ \delta^{18}O + 13.89$.

In this study, two local meteoric water regression lines (LMWL) were plotted to describe the isotopic data for different seasons: $\delta D = 8.03\delta^{18}O + 9.73$ for the wet season precipitation (May to October) and $\delta D = 8.04\delta^{18}O + 15.03$ for the dry season precipitation (November–April). The slope and intercept of the regression line for the wet season precipitation are virtually identical to those of the global meteoric water line (GMWL) of Craig (1961) [15]. The dry season precipitation was found to have an intercept of 15.03, which is much higher than that of the GMWL of 10 due to the different air masses affecting the study (see Figure 2).

In this study, the isotopic composition of precipitation during the wet and dry seasons in Hualian was also examined. The δD in wet seasons ranged between −149.5‰ and 17.5‰, with a mean of −40.6‰ ± 32.8‰. The $\delta^{18}O$ was between −20.2‰ and 0.8‰, with a mean of −6.3‰ ± 4.1‰. The mean of *d* was 9.5‰. The δD in dry seasons ranged between −69.8‰ and 22.7‰, with a mean of −3.7‰ ± 16.1‰. The $\delta^{18}O$ was between −9.6‰ and 1.5‰, with a mean of −2.3‰ ± 1.9‰. The mean of *d* was 14.7‰. More depleted composition of hydrogen and oxygen isotopes was found in the summer wet seasons than the dry seasons. This feature has been commonly observed in other regions of Taiwan [18,25–27]. In Taiwan, the composition of hydrogen isotopes, compared to the rainfall of the Northeast monsoon in winters, is depleted in the rainfall of the Southwest monsoon in summers. As for the effects of temperature, higher temperature may have enriched the signatures of hydrogen and oxygen isotopes in precipitation. In seasons with great rainfall, the rainfall amount effect [12] caused by the rain out of heavy precipitation amounts over a relatively short time duration,

the hydrogen and oxygen isotopes in precipitation are significantly depleted. Thus, rainfall also has an effect on isotopes. Temperature and rainfall amount exert opposite effects on the fractionation of hydrogen and oxygen isotopes. Moreover, the isotopes in the Hualian River basin are depleted more in wet seasons than is the case in dry seasons. The signatures of hydrogen and oxygen isotopes can be explained by the mutual influence of rainfall amount and temperature, with the former have a stronger effect than the latter. During rainy seasons in the summer, rainfall is often heavier with a greater amount of rainfall during a specific period of time and so a higher precipitation rate, despite higher temperatures. Consequently, the composition of the hydrogen and oxygen isotopes at this time is depleted relative to $\delta^{18}O$ and δD. Yurtsever and Gat (1981) [28] have pointed out generally that the temperature effect is normally pronounced in high-latitude continental regions, whereas the amount effect is pronounced in tropical regions. It is well known that the hydrogen and oxygen heavy isotope contents of precipitation decrease with increasing altitude. In this study, precipitation sites are located in the lowest area of the basin. Therefore, in this study it is difficult to discuss the range of altitude effect in the basin. Precipitation sites may not adequately represent the average precipitation in the basin. If the altitude effect is large, groundwater can also derive from precipitation in the mountainous area with depleted isotopic compositions similar to streams.

Figure 2. Plot of δD *vs.* $\delta^{18}O$ for precipitation samples. LMWL represents the local meteoric water line.

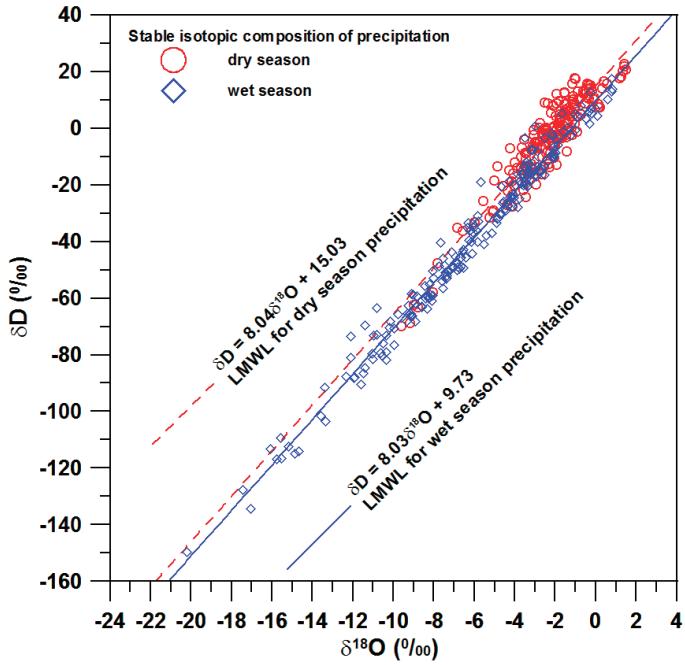

4.2. Isotopic Compositions of River Water

The δD of the river water in the Hualian River basin was between −70.0‰ and −46.2‰, with a mean of −61.3‰ ± 5.9‰. The $\delta^{18}O$ ranged between −10.3‰ and −7.8‰, with a mean of −9.1‰ ± 0.6‰ (Figure 3). The comparison of hydrogen and oxygen isotope compositions between rainwater and river water demonstrated that the composition of the hydrogen and oxygen isotopes from river water matched that of the local meteoric water across the Hualian River basin. This indicated that rainfall is

the primary source of the river water. Furthermore, the composition of the hydrogen and oxygen isotopes from the river water was more depleted as compared to that of the precipitation in the valley, indicating that the river water is composed of rainfall in the upstream catchment. Therefore, the precipitation in the valley had smaller effects on the river water. In wet seasons, the hydrogen and oxygen isotopes exhibited a depleted composition compared to that of dry seasons, a similar phenomenon to the rainwater. Thus, the composition of the rainwater was influenced by the season. In short, it can be concluded that the water recharge of the Hualian River basin is significantly affected by seasonal rainfall. Also, as mentioned, the hydrogen and oxygen isotope composition of the rainfall brought by the Southwest monsoon in the summer is more depleted than that brought by the Northeast monsoon in the winter.

Figure 3. Plot of δD *vs.* $\delta^{18}O$ for river water samples. The LMWL is established as $\delta D = 8.40\ \delta^{18}O + 13.89$ for local precipitation.

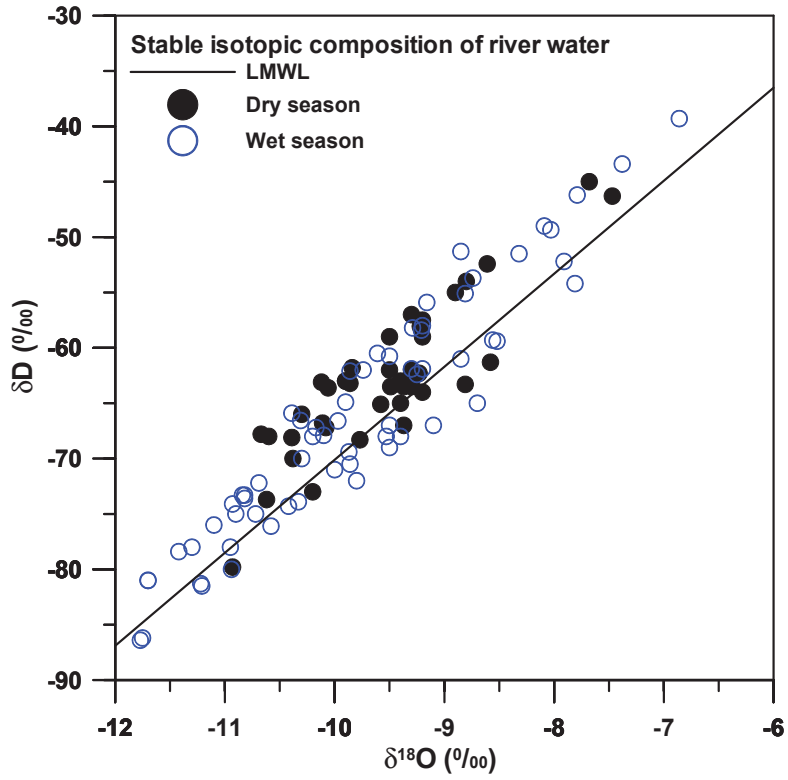

In this study, the signatures of hydrogen and oxygen isotopes for river water in the main stream and tributaries of the Hualian River (the Mugua River, the Shoufeng River, the Maan River, and the Wanli River) were also compared during dry and wet seasons. The results are illustrated in Figure 4. As shown in the figure, significant differences were observed in the hydrogen and oxygen isotope signatures in the mainstream and tributaries of the Hualian River. In wet seasons, streams leak water into the groundwater system. Alternatively, water can be discharge from the groundwater to surface waters in dry seasons. Thus, the groundwater compositions were similar to those of the river water, indicating that the source of the groundwater in this area may be related to river water. In both dry and wet seasons, the isotope signatures in the tributaries of the Hualian River were more depleted than those in the mainstream because the tributaries in mountainous catchment areas consisted of

primarily interflow before they entered the mainstream. Interflow is the lateral movement of water in the vadose zone, that first returns to the surface or enters a stream prior to becoming groundwater. The interflow blended with groundwater and then joined the Hualian River. Consequently, the compositions in the two were significantly different. These results may need to be verified by collecting related data.

Figure 4. Relationship between δD and $\delta^{18}O$ for river water in comparison to the main stream and tributaries of the Hualian River during dry and wet seasons. (**A**) Dry seasons; (**B**) Wet seasons.

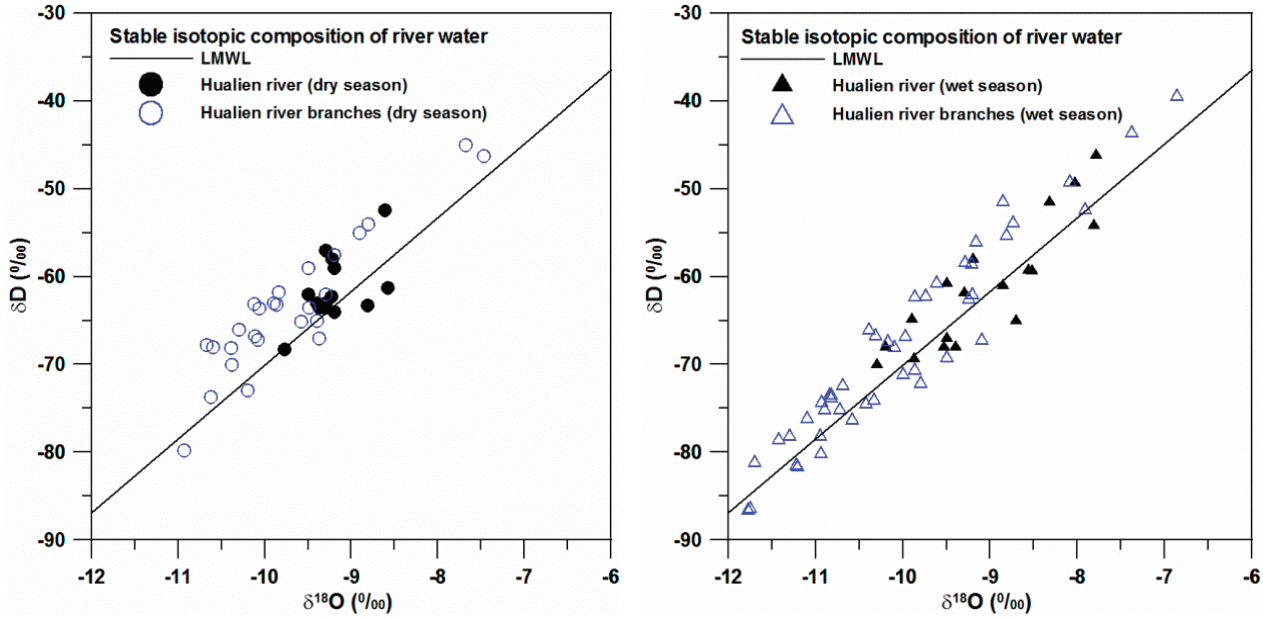

4.3. Isotopic Compositions of Groundwater

This research consisted of an analysis of the groundwater in the Hualian River basin. As illustrated in Figure 5, the hydrogen and oxygen isotope compositions in the groundwater samples obtained from observation wells corresponded to those of the rainfall along the Hualian River basin. The δD of the groundwater in the Hualian River basin was between −73.7‰ and −42.0‰, with a mean of −56.2‰ ± 9.1‰. The $\delta^{18}O$ ranged between −10.4‰ and −7.2‰, with a mean of −8.8‰ ± 1.0‰ (Figure 5). The isotopic composition of river water is controlled by the mixing rates of three major components: surface runoff, interflow, and groundwater (base flow). The difference between arrival times for interflow and surface runoff is of the order of hours, so they are both from recent storms and have similar isotopic compositions. Therefore, from the point of view of isotopic composition, river water can be considered as being composed of groundwater and runoff [29]. The basin groundwater is recharged from rainfall and river water. In this study, the groundwater compositions were similar to those of the river water, indicating that the source of the groundwater in this area may be related to river water. The primary groundwater source may be river water rather than simply rainfall recharge. In addition, the hydrogen and oxygen isotopes in the groundwater near the Hualian River slightly deviated from the hydrogen and oxygen isotopic local meteoric water line in Hualian.

Therefore, the groundwater might be a mixture of river water and rainwater, which explains why the effect of the river water recharge was greater than the rainfall infiltration.

Figure 5. Plot of δD *vs.* $\delta^{18}O$ of groundwater samples.

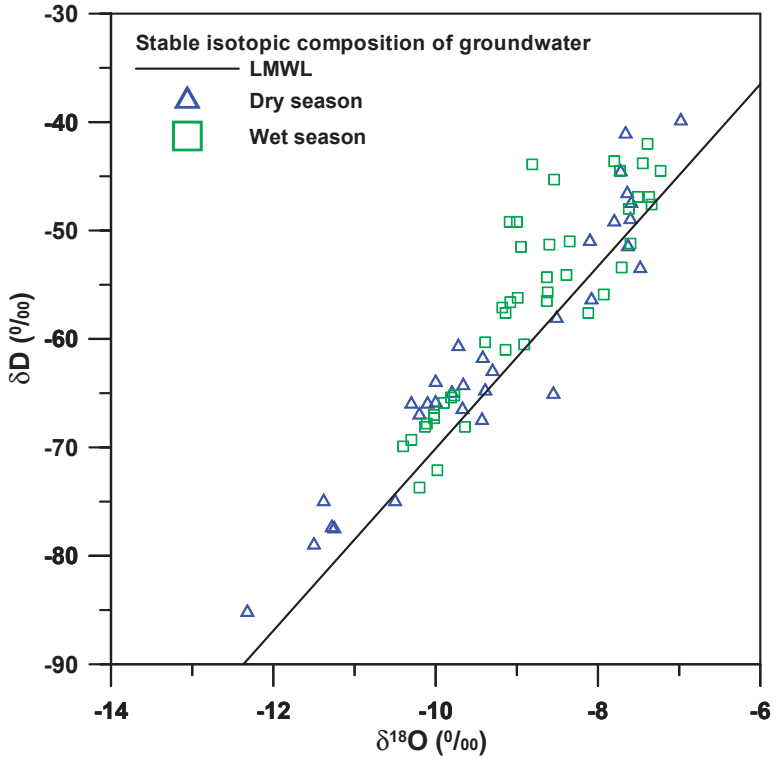

4.4. Mass Balance Analysis

The basin groundwater is recharged from rain that falls on the basin and from the tributaries of the Hualian River (the Mugua River, the Shoufeng River, the Maan River, and the Wanli River) drained from mountain watersheds (Figure 1). According to the depth of the well screens (80–90 m below ground) and hydro-geological profiles, groundwater from the four wells (G1, G2, G3, and G4) can be classified as shallow groundwater. The meteoric $\delta^{18}O$-δD signature is important for understanding the groundwater recharge. The isotopic composition of groundwater equals the average weighted values of recharge sources, such as the annual composition of precipitation and river water. Therefore, deviations of the groundwater isotopic ratio from that of precipitation are expected. The transfer function from precipitation to groundwater must be understood for groundwater provenance studies. The transfer function also provides basic information about the mechanisms of recharge [2]. In this study, the mean value of oxygen isotopic compositions of groundwater for the Huanlian River basin was −9.65‰ (ranging from −9.32‰ to −10.65‰). The mean values of oxygen isotopic compositions of dry and wet seasons for the Huanlian River basin were −4.18‰ and −6.46‰, respectively. The ratio of precipitation for dry and wet seasons was 0.19:0.81 from 2000 to 2012 (according to the Central Weather Bureau). The weighted average $\delta^{18}O$ of precipitation was −6.02‰ in the Huanlian River basin. The values of oxygen isotopic compositions of river water for the dry and wet seasons were −10.20‰ and −10.42‰, respectively. The ratio of stream flow for the dry and

wet seasons was 0.14:0.86 from 1980 to 2011 (according to the Water Resources Agency). The river water weighted average value for $\delta^{18}O$ was −10.39‰ in the Huanlian River (see Table 2).

Table 2. Precipitation and river water weighted average δD, $\delta^{18}O$ and *d*-excess and their standard error.

Weighted Average:	Precipitation		River Water	
	Dry Season	Wet Season	Dry Season	Wet Season
Ratio	0.19	0.81	0.14	0.86
n (used for average)	185	200	41	64
δD (‰)	−3.7 ± 16.1	−40.6 ± 32.8	−62.9 ± 6.5	−66.2 ± 10.6
$\delta^{18}O$ (‰)	−2.3 ± 1.9	−6.3 ± 4.1	−9.6 ± 0.7	−9.8 ± 1.2
d-excess (‰)	14.7 ± 5.6	−9.5 ± 4.6	13.5 ± 3.2	12.1 ± 3.5

In basin water budget studies, it is important to assess the proportion of the precipitation and river water from the mountain that actually recharges the groundwater. The stable isotopic composition of groundwater is determined by oxygen and hydrogen isotopic compositions and recharge percentages of concerned sources. Using mass balance analysis for the oxygen and hydrogen isotopic compositions, the groundwater recharge percentages of every recharge source can be evaluated. In this study, mixing between two distinct recharge sources can be quantified by a simple linear algebraic equation:

$$\begin{aligned} C(V_A + V_B) &= AV_A + BV_B \\ C &= A\frac{V_A}{V_A + V_B} + B\frac{V_B}{V_A + V_B} = A(1-X) + BX \end{aligned} \quad (3)$$

where A is the precipitation stable isotope value of the basin; B is the river water stable isotope value of the mountain watershed; C is the groundwater stable isotope value of the basin; V_A is the amount of precipitation; V_B is the amount of river water; X is the recharge proportion of river water; and (1–X) is the recharge proportion of precipitation.

Based on stable isotopic characteristics, the results show that 83% of the groundwater in the Huanlian River basin is derived from river water from the mountain watershed, and 17% is from the rain that falls on the basin. This indicates that the basin groundwater is mainly recharged from the river water from the mountain watershed, primarily due to the abundant precipitation in the mountain area. Using the mean *d*-value, the relative contributions of the wet and dry seasonal sources to the groundwater recharge can be calculated using a mass-balance equation:

$$d_{\text{groundwater}} = X\, d_{\text{wet season}} + (1 - X)\, d_{\text{dry season}} \quad (4)$$

where X and $(1 - X)$ are the fractions of wet and dry seasonal sources, respectively. Based on their *d*-values, the groundwater sources are composed of an average of approximately 75.8% wet seasonal sources and 24.2% dry seasonal sources.

5. Conclusions

The present study examined the stable isotopic composition of precipitation, river water, and groundwater in the Hualian River basin. Mountain river water accounted for 83%, and plain rainfall accounted for 17% of the groundwater recharge in the Huanlian River basin. Comparisons between hydrogen and oxygen isotopes in precipitation showed that differences in the amount of rainfall resulted in depleted oxygen and hydrogen isotopes for precipitation in wet seasons as compared to dry seasons. River water contained more depleted hydrogen and oxygen isotopes than precipitation did, implying that the river water mainly came from the upstream catchment. Using a mass balance equation, a comparison of *d*-values of precipitation and groundwater indicated the groundwater consists of 75.5% wet seasonal sources and 24.5% dry seasonal sources, representing a distinct seasonal variation of groundwater recharge in the study area.

Acknowledgments

This study was financially supported by funds from the National Science Council (NSC), Taiwan, under grant NSC 101-2221-E-006-196-MY2 and the Central Geological Survey of Taiwan under grant 102-5226904000-01-02. We would also like to thank Chung-Ho Wang of the Institute of Earth Sciences at the Academia Sinica for help with analyzing the water samples. Special thanks go to the two anonymous reviewers and the editors for their critical reviews and helpful comments.

Author Contributions

Hsin-Fu Yeh conceived the subject of the article, literature review and contributed to the writing of the paper; Hung-I Lin participated in the composition of the manuscript in the method, results and conclusion sections; Cheng-Haw Lee and Kuo-Chin Hsu provided expertise on groundwater-surface water interactions and hydrogeology in study area; Chi-Shin Wu participated in data processing, elaborated the statistical analysis, and figures.

Conflicts of Interest

The authors declare no conflict of interest.

References

1. Gat, J.R. Oxygen and hydrogen isotopes in the hydrologic cycle. *Ann. Rev. Earth Planet Sci.* **1996**, *24*, 225–262.
2. Clark, I.D.; Fritz, P. *Environmental Isotopes in Hydrology*; Lewis Publishers: New York, NY, USA, 1997.
3. Vandenschrick, G.; van Wesemael, B.; Frot, E.; Pulido-Bosch, A.; Molina, L.; Stiévenard, M.; Souchez, R. Using stable isotope analysis (δD and $\delta^{18}O$) to characterise the regional hydrology of the Sierra de Gador, south east Spain. *J. Hydrol.* **2002**, *265*, 43–55.

4. Deshpande, R.D.; Bhattacharya, S.K.; Jani, R.A.; Gupta, S.K. Distribution of oxygen and hydrogen isotopes in shallow groundwaters from Southern India: Influence of a dual monsoon system. *J. Hydrol.* **2003**, *271*, 226–239.
5. Gibson, J.J.; Edwards, T.W.D.; Birks, S.J.; St Amour, N.A.; Buhay, W.M.; McEachern, P.; Wolfe, B.B.; Peters, D.L. Progress in isotope tracer hydrology in Canada. *Hydrol. Process.* **2005**, *19*, 303–327.
6. Gammons, C.H.; Poulson, S.R.; Pellicori, D.A.; Reed, P.J.; Roesler, A.J.; Petrescu, E.M. The hydrogen and oxygen isotopic composition of precipitation, evaporated mine water, and river water in Montana, USA. *J. Hydrol.* **2006**, *328*, 319–330.
7. Blasch, K.W.; Bryson, J.R. Distinguishing sources of ground water recharge by using δ^2H and $\delta^{18}O$. *Ground Water* **2007**, *45*, 294–308.
8. Li, F.; Pan, G.; Tang, C.; Zhang, Q.; Yu, J. Recharge source and hydrogeochemical evolution of shallow groundwater in a complex alluvial fan system, southwest of North China Plain. *Environ. Geol.* **2008**, 55, 1109–1122.
9. Heilweil, V.M.; Solomon, D.K.; Gingerich, S.B.; Verstraeten, I.M. Oxygen, hydrogen, and helium isotopes for investigating groundwater systems of the Cape Verde Islands, West Africa. *Hydrogeol. J.* **2009**, *17*, 1157–1174.
10. Yin, L.; Hou, G.; Su, X.; Wang, D.; Dong, J.; Hao, Y.; Wang, X. Isotopes (δD and $\delta^{18}O$) in precipitation, groundwater and surface water in the Ordos Plateau, China: Implications with respect to groundwater recharge and circulation. *Hydrogeol. J.* **2011**, *19*, 429–443.
11. Singh, M.; Kumar, S.; Kumar, B.; Singh, S.; Singh, I.B. Investigation on the hydrodynamics of Ganga Alluvial Plain using environmental isotopes: A case study of the Gomati River Basin, northern India. *Hydrogeol. J.* **2013**, *21*, 687–700.
12. Dansgaard, W. Stable isotopes in precipitation. *Tellus* **1964**, *16*, 436–468.
13. Craig, H. Isotopic variations in meteoric waters. *Science* **1961**, *133*, 1702–1703.
14. Gat, J.R. The isotopes of hydrogen and oxygen in precipitation. In *Handbook of Environmental Isotope Geochemistry*; Fritz, P., Fontes, J.C., Eds.; Springer: Berlin, Germany, 1980; pp. 21–47.
15. Darling, W.G.; Armannsson, H. Stable isotopic aspects of fluid flow in the Krafla, Namafijall and Theistareykir geothermal systems of northeast Iceland. *Chem. Geol.* **1989**, *76*, 197–213.
16. Sakai, H.; Matsubaya, O. Stable isotopic studies of Japanese geothermal system. *Geothermics* **1977**, *5*, 97–124.
17. Lee, K.S.; Wenner, D.B.; Lee, I. Using H- and O-isotopic data for estimating the relative contributions of rainy and dry season precipitation to groundwater: Example from Cheju Island, Korea. *J. Hydrol.* **1999**, *222*, 65–74.
18. Peng, T.R.; Wang, C.H.; Huang, C.C.; Fei, L.Y.; Chen, C.T.A.; Hwong, J.L. Stable isotopic characteristic of Taiwan's precipitation: A case study of western Pacific monsoon region. *Earth Planet Sci. Lett.* **2010**, *289*, 357–366.
19. Water Resource Agency (WRA). *Investigation of Water Resource in Hualien*; Ministry of Economic Affairs: Taipei, Taiwan, 1997; p. 265.
20. Water Resource Agency (WRA). *Investigation of Groundwater Resource in Hualien Alluvial Valley*; Ministry of Economic Affairs: Taipei, Taiwan, 2005; p. 395.

21. Water Resource Agency (WRA). *Conjunctive Utilization of Surface Water with Groundwater for Hualien Area*; Ministry of Economic Affairs: Taipei, Taiwan, 2010; p. 525.
22. International Atomic Energy Agency (IAEA). *Guidebook on Nuclear Techniques in Hydrology*; IAEA Technical Reports Series No. 91; IAEA: Vienna, Austria, 1983; p. 439.
23. Epstein, S.; Mayeda, T. Variation of ^{18}O content of waters from natural sources. *Geochim. Cosmochim. Acta* **1953**, *4*, 213–224.
24. Coleman, M.L.; Shepherd, T.J.; Durham, J.J.; Rouse, J.E.; Moore, G.R. Reduction of water with zinc for hydrogen isotope analysis. *Anal. Chem.* **1982**, *54*, 993–995.
25. Wang, C.H.; Peng, T.R. Hydrogen and oxygen isotopic compositions of Taipei precipitation: 1990–1998. *West. Pac. Earth Sci.* **2001**, *1*, 429–442.
26. Peng, T.R.; Wang, C.H.; Lai, T.C.; Ho, S.K. Using hydrogen, oxygen, and tritium isotopes to identify hydrological factors contributing to landslides in a mountainous area, central Taiwan. *Environ. Geol.* **2007**, *52*, 1617–1629.
27. Yeh, H.F.; Lee, C.H.; Hsu, K.C. Oxygen and hydrogen isotopes for the characteristics of groundwater recharge: A case study from the Chih-Pen Creek basin, Taiwan. *Environ. Earth Sci.* **2011**, *62*, 393–402.
28. Yurtesever, Y.; Gat, J.R. Atmospheric waters. In *Stable Isotope Hydrology: Deuterium and Oxygen-18 in the Water Cycle*; IAEA Technical Report Series No. 210; Gat, J.R., Gonfiantini, R., Eds.; International Atomic Energy Agency: Vienna, Austria, 1981; pp. 103–142.
29. Lu, H.Y.; Peng, T.R.; Liu, T.K.; Wang, C.H.; Huang, C.C. Study of stable isotopes for highly deformed aquifers in the Hsinchu-Miaoli area, Taiwan. *Environ. Geol.* **2006**, *50*, 885–898.

Diagnosing Atmospheric Influences on the Interannual $^{18}O/^{16}O$ Variations in Western U.S. Precipitation

Nikolaus H. Buenning, Lowell Stott, Lisa Kanner and Kei Yoshimura

Abstract: Many climate proxies in geological archives are dependent on the isotopic content of precipitation ($\delta^{18}O_p$), which over sub-annual timescales has been linked to temperature, condensation height, atmospheric circulation, and post-condensation exchanges in the western U.S. However, many proxies do not resolve temporal changes finer than interannual-scales. This study explores causes of the interannual variations in $\delta^{18}O_p$ within the western U.S. Simulations with the Isotope-incorporated Global Spectral Model (IsoGSM) revealed an amplifying influence of post-condensation exchanges (*i.e.*, raindrop evaporation and vapor equilibration) on interannual $\delta^{18}O_p$ variations throughout the western U.S. Mid-latitude and subtropical vapor tagging simulations showed that the influence of moisture advection on $\delta^{18}O_p$ was relatively strong in the Pacific Northwest, but weak over the rest of the western U.S. The vapor tags correlated well with interannual variations in the $^{18}O/^{16}O$ composition of vapor, an indication that isotopes in vapor trace atmospheric circulation. However, vertical-tagging simulations revealed a strong influence of condensation height on $\delta^{18}O_p$ in California. In the interior of the western U.S., a strong temperature effect was found only after annual mean temperatures were weighted by monthly precipitation totals. These multiple influences on $\delta^{18}O_p$ complicate interpretations of western U.S. climate proxies that are derived from isotopes in precipitation.

Reprinted from *Water*. Cite as: Buenning, N.H.; Stott, L.; Kanner, L.; Yoshimura, K. Diagnosing Atmospheric Influences on the Interannual $^{18}O/^{16}O$ Variations in Western U.S. Precipitation. *Water* **2013**, *5*, 1116-1140.

1. Introduction

Stable oxygen and hydrogen isotopes (primarily ^{18}O and deuterium) preserved in geological archives are commonly used as proxies of past climatic changes (e.g., see reviews: [1–4]). Many of these proxies are derived from meteoric waters and thus record temporal variations in the isotopic composition of precipitation (hereafter $\delta^{18}O_p$, where the isotopic composition is defined as: $\delta = R/R_{STANDARD} - 1$, where R is the heavy to light isotope ratio). It is important for the interpretation of climate proxies to better understand the causes of temporal variations in $\delta^{18}O_p$ within a given region. Within the tropics and subtropics, $\delta^{18}O_p$ is typically linked to changes in precipitation rates (the amount effect) [5–12], whereas measurements from outside of the tropics and subtropics usually show correlations between $\delta^{18}O_p$ and air temperature (the temperature effect) [5,13–16]. However, within many middle latitude regions the relationship between $\delta^{18}O_p$ and climatic variables is not always as clear, which creates difficulties when interpreting climate proxies within these latitudes. It is likely that the isotopic composition of precipitation that falls in the middle latitudes is subject to a combination of influences. This study focuses on the western U.S., with the intent to understand the primary influences on the year-to-year changes in $\delta^{18}O_p$.

Previous studies of the western U.S. have examined δ values from ice cores [17,18], tree cellulose [16,19,20], speleothems [21–23], leaf wax *n*-alkanes [24], and lacustrine sediment archives [25–28]. These records provide estimates of $\delta^{18}O_p$ variations on several timescales, including seasonal, interannual and interdecadal. The variations within each record have been attributed to changes in near surface air-temperature, precipitation amount, surface latent heat release, and/or storm trajectories.

On sub-hourly timescales, precipitation δ variations have been linked to changes in condensation height [29] and raindrop re-evaporation [30]. At weekly to seasonal timescales, studies have suggested that seasonal temperature variations strongly impact $\delta^{18}O_p$ in the western U.S. [31,32], while several other studies [33–36] have suggested that storm trajectories were the primary influence on precipitation δ values. Recently, Buenning *et al*. [37] found through model sensitivity experiments and tagging simulations that the seasonal cycle of $\delta^{18}O_p$ was primarily a result of seasonal changes in vapor condensation height along the west coast of the U.S. However, one of the remaining issues of Buenning *et al.* [37] was whether or not the same mechanism drives interannual variations in precipitation δ values within the region, which would likely be more valuable for the interpretation of paleoclimate archives.

This study aims to answer the question of which mechanism(s) primarily drive interannual $\delta^{18}O_p$ variations in the western U.S. by using model simulations. The following sections discuss the model, the model experiments (Section 2), and validation (Section 3). Sensitivity experiments are assessed to find which fractionation process has the largest influence on interannual $\delta^{18}O_p$ variations within the model, and the influences of post-condensation exchanges, condensation height, moisture advection, and temperature on interannual $\delta^{18}O_p$ variations are discussed and quantified (Section 4). Finally, the paper concludes with a summary of the results and a discussion of the implications of the findings (Section 5).

2. Methods

A methodology similar to Buenning *et al.* [37] is used here to diagnose the cause of the interannual variations in $\delta^{18}O_p$. The model used for this study is the Experimental Climate Prediction Center's (ECPC) Isotope-incorporated Global Spectral Model (IsoGSM) [38]. The atmosphere in IsoGSM has 28 vertical layers, and the chosen horizontal resolution of the model is given by triangular truncation of the spherical harmonic spectrum at wave number 62 (approximately 1.85° longitude by 1.85° latitude). The model is forced with prescribed sea surface temperatures and sea-ice conditions from the optimal interpolation weekly data set, downloaded from the ECPC database [39]. Each IsoGSM simulation runs from 1953 through 2010 with a 10-minute time-step, and each simulation is spectrally nudged to the same wind and temperature fields (The National Centers for Environmental Predictions and National Center for Atmospheric Research Reanalysis version 1 [40]) every six hours. Yoshimura and Kanamitsu [41] describe the specific details of the spectral nudging technique.

IsoGSM accounts for water isotopologues (H_2O, $H_2{}^{18}O$, and HDO) in all three phases within the simulated atmosphere, and fractionation factors (defined as $\alpha = R_{cd} = R_g$, where subscripts cd and g refer to condensed phase and gas, respectively) are computed and applied when phase changes occur.

Using the temperature-dependent formulations of Majoube *et al.* [42,43], equilibrium oxygen isotopic fractionation is applied during vapor condensation in the atmosphere (α_{eq-con}) and during both ocean (α_{eq-ev}) and raindrop (α_{eq-rev}) evaporation. Kinetic fractionation is also accounted for in IsoGSM during ocean evaporation (α_{k-ev}) [44] and vapor deposition onto ice crystals (α_{k-con}) [45]. Isotopic exchange and both equilibrium and kinetic fractionation during raindrop evaporation is estimated following Stewart [46]. It is assumed that 45% of falling raindrops equilibrate with surrounding vapor for convective precipitation and 95% equilibrates for stratiform precipitation.

Interannual $\delta^{18}O_p$ variability is first evaluated in an unperturbed control simulation (CTRL). The model is then used to determine which fractionation processes contribute to the interannual $\delta^{18}O_p$ variations. Sensitivity experiments were conducted with IsoGSM by "turning off" isotope fractionation. Note, these model experiments were conducted previously by Buenning *et al.* [37]. Each sensitivity experiment (name in all capitals) turned off individual fractionation processes by setting the isotopic fractionation factors (α variables defined above) equal to one (a list and description of each experiment is given in Table 1). Two of the model experiments assess the influence of equilibrium oxygen isotope fractionation processes [42,43] on interannual $\delta^{18}O_p$ variance. These processes are equilibrium oxygen isotope fractionation during ocean evaporation (α_{eq-ev}, NOFEQ1) and condensation in the atmosphere (α_{eq-con}, NOFEQ2). These two experiments removed both the temperature dependence of α_{eq} and the isotope effect (*i.e.*, preferential evaporation or rainout). As such, two additional simulations were conducted where only the temperature dependence is removed by setting the equilibration temperature to a constant value, globally (CONFEQ1 and CONFEQ2, with α_{eq-ev} = 1.00980653 and α_{eq-con} = 1.01162795, respectively). Simulations that removed kinetic oxygen isotope fractionation were performed, which included isotope fractionation during ocean evaporation (α_{k-ev}, NOFKI1) [44] and vapor deposition onto ice crystals (α_{k-con}, NOFKI2) [45]. The final fractionation experiment was performed where raindrop equilibration rates were set equal to zero. This experiment removes all isotope effects associated with post-condensation exchanges, including vapor-rain equilibration and both equilibrium and kinetic fractionation during raindrop evaporation (NORNEV) [11,30,46–48] (see Yoshimura *et al.* [30] for equations used in IsoGSM's rain exchange model).

Vertical tagging simulations were performed with IsoGSM, such that tagged vapor mixing ratios were set equal to "normal" vapor mixing ratios at specific levels (TAGZ). Unlike the TAGLEV simulation of Buenning *et al.* [37] (which only tagged two layers), 14 individual tags were assigned to the 28 individual layers in IsoGSM to account for condensation height (one tag per 2 atmospheric levels). Tags were removed from the atmosphere if the tagged vapor advects vertical tagging level. Thus, resulting precipitation of each vertical water tag will quantify the amount of total precipitation from 14 different vertical levels of the atmosphere.

Table 1. Name and description of Isotope-incorporated Global Spectral Model (IsoGSM) simulations.

Simulation name	Description
CTRL	Unperturbed control simulation
NOFEQ1	Equilibrium oxygen isotopic fractionation during ocean water evaporation is turned off ($\alpha_{eq-ev} = 1$)
NOFEQ2	Equilibrium oxygen isotopic fractionation during condensation is turned off ($\alpha_{eq-con} = 1$)
NORNEV	All oxygen isotopic fractionation associated with raindrop evaporation is turned off
CONFEQ1	Equilibrium oxygen isotopic fractionation during ocean water evaporation is set to constant, removing the temperature dependence ($\alpha_{eq-ev} = 1.00980653$, T = 293 K)
CONFEQ2	Equilibrium oxygen isotopic fractionation during condensation is set to a constant, removing the temperature dependence ($\alpha_{eq-con} = 1.01162795$, T = 274 K)
NOFKI1	Kinetic oxygen isotopic fractionation during ocean water evaporation is turned off ($\alpha_{k-ev} = 1$)
NOFKI2	Kinetic oxygen isotopic fractionation during vapor deposition onto ice is turned off ($\alpha_{k-con} = 1$)
TAGY	Tagging simulation where tag1 is applied within 20°–40° N and 140°–170° W; Tag 2 is applied within 40°–60° N and 140°–170° W.
TAGZ	Tagging simulation where 14 separate tags are applied to the 28 vertical σ layers (2 layers per tag). Tag 1 is applied to the surface layer and layer 2; tag 2 is applied to layers 3 and 4; tag 3 is applied to layers 5 and 6; and so on to up to layers 27 and 28. This simulation is actually a combination of 7 simulations, with each model run simulating two of the tags.

To account for interannual variations in moisture advection, a horizontal tagging simulation was performed with IsoGSM (similar to the TAGLAT simulation of Buenning *et al.* [37]), where subtropical moisture was tagged within 20°–40° N and 140°–170° W and middle latitude vapor was tagged within 40°–60° N and 140°–170° W (TAGY). For the TAGY simulation, tagged vapor mixing ratios were set to "normal" vapor mixing ratios within each of the two tagging regions at every model time-step. When vapor from one tagging region is transported by the winds into the other region, it is immediately removed to avoid vapor having both tags. Outside of the tagging regions, the tagged vapor is treated the same as normal vapor, except they are not used in the energy calculations (*i.e.*, the vapor tags are allowed to advect, mix, condense, and rainout). It is important to note that the tracer method used here differs with the typical method of tagging vapor that evaporates off the ocean surface. The method used here allows a direct quantification of the amount of precipitation and vapor that was advected from each tagging region. Because both the TAGY and the CTRL simulations are nudged to the same reanalysis wind fields, $\delta^{18}O$ values can be compared to the fraction of vapor and precipitation with each tag. Correlation coefficients were calculated at each grid cell in the western U.S., to quantify the co-variability between $\delta^{18}O$ values and tagged fraction (for both TAGY and TAGZ).

3. Simulated $\delta^{18}O_p$ Variability

Previous studies have validated IsoGSM's ability to capture temporal variations on several timescales. Yoshimura *et al.* [38] first compared IsoGSM results with measurements from the Global Network for Isotopes in Precipitation (GNIP). By comparing IsoGSM and other models against long

records (>45 years) from GNIP stations, they concluded that an accurate simulation of atmospheric winds is necessary to reliably model interannual $\delta^{18}O_p$ variations. These results showed how spectral nudging constrains the simulated wind and temperature fields, which in turn allows for good model-data agreement. Within central/coastal California, Yoshimura *et al.* [30] demonstrated the ability of the regional version of IsoGSM (IsoRSM) to capture sub-hourly isotopic variations. Berkelhammer *et al.* [36] further validated IsoGSM on weekly timescales at 6 sites in California over the span of 2000–2005. Buenning *et al.* [37] showed how IsoGSM was able to capture the seasonal wintertime drop in $\delta^{18}O_p$ at 16 different sites in British Columbia, Washington, Oregon, and California. However, the lack of long continuous records of $\delta^{18}O_p$ in regions outside of Europe [12] makes it difficult to validate the model on interannual to multi-decadal timescales, especially in the western U.S.

To address this issue, studies have used tree cellulose $\delta^{18}O$ values ($\delta^{18}O_c$) as a measure of $\delta^{18}O_p$ variability [16,19,49–51]. This type of comparison typically involves the use of an offline biogeochemical model calculation that uses atmospheric model outputs to estimate $\delta^{18}O_c$. Berkelhammer and Stott [16] used IsoGSM output as input for a geochemical model put forth by Roden *et al.* [52] and found good model agreement with 2 bristlecone pine trees in the Rocky Mountains of Colorado. They note that the model's ability to capture the interannual variations declines going back in time (especially prior to 1950), which was attributed to a decline in the quality of the reanalysis forcing data due to less observational constraints. The same type of decline in IsoGSM model/observation agreement was found in southern California by Kanner *et al.* [53], who found that the model performed exceptionally well for the 1979–2004 period, but found a decline in model agreement from 1953 to 1979. They noted that the discrepancy between the two time periods could be a result of the increased constraints on the reanalysis data after 1979 (*i.e.*, the satellite era).

4. Attributing Interannual Isotopic Variations

Interannual variance is calculated at each grid cell by computing annual means (centered on the winter wet season: July through June) for the simulated period; a total of 56 annual means per grid cell (the first model year is not used). Figure 1a shows a map of the interannual variance of $\delta^{18}O_p$ for the control simulation (CTRL) over the Pacific and western North America. The largest variance occurs over the Baja Peninsula of Mexico, and the variance decreases northward along the coast and inland towards the Southwest U.S. This is consistent with the results of Buenning *et al.* [37], who showed that observed seasonal variations along the western U.S. coastline were largest for southern stations and decreased northward. Figure 1b–g shows the spatial distribution of interannual $\delta^{18}O_p$ variance for the seven model fractionation experiments. All but two of the experiments showed the same general pattern of variance as the control simulation; removing equilibrium oxygen isotopic fractionation during condensation (NOFEQ2) and removing post-condensation exchanges (NORNEV) being the two exceptions. These results show the importance of isotopic rainout and post-condensation exchanges in the western U.S., and suggest that other isotope processes (e.g., ocean evaporation, kinetic fractionation, and the temperature-dependence of α_{eq}) have less influence on interannual $\delta^{18}O_p$ variability. The variance was almost completely removed when equilibrium fractionation during condensation was removed (NOFEQ2), as was the case for the seasonal $\delta^{18}O_p$

cycle [37]. The variance difference between the control simulation (CTRL) and the simulation that removed post-condensation exchanges (NORNEV) is discussed in more detail in the subsection below.

4.1. Post-Condensation Exchanges

Post-condensation exchanges were removed by setting raindrop equilibration rates equal to zero, which not only prevented rain from isotopically equilibrating with the surrounding vapor, but it also prevented raindrops from fractionating during evaporation [30]. The absolute change in the variance due to post-condensation exchanges can be quantified by taking the difference in $\delta^{18}O_p$ variance between the CTRL and NORNEV simulations (Figure 2a). In general, the NORNEV experiment caused $\delta^{18}O_p$ variance to decrease over land, but increase over the ocean southwest of the Baja Peninsula (Figure 2a). The fractional change to the variance due to post-condensation exchanges can be quantified by dividing the variance difference (values in Figure 2a) by the variance from the control simulation (values in Figure 1a), which is shown in Figure 2b. The fraction of the variance that is removed by the model experiment (NORNEV) is more uniform over land than the absolute change, with the highest fractional change occurring over Oregon (Figure 2b). In general post-condensation exchanges contribute about 60% to the total interannual $\delta^{18}O_p$ variance in the western U.S., reaching as high as 74% over central Oregon.

What is not apparent in Figure 2a,b is that the removal of post-condensation exchanges (NORNEV) dampened interannual variations that existed in the control simulation. Figure 3 shows regional average time series for the CTRL and NORNEV simulations for the Pacific Northwest, the western US interior, and southern/central California. The curves in Figure 3 show that the variations produced by both simulation are similar and the inclusion of post-condensation exchanges (in CTRL) amplify the maxima and minima that would have existed without the processes. To demonstrate that this is not unique to these three regions, the contribution of post-condensation exchanges to interannual $\delta^{18}O_p$ variations (defined as the control minus experiment) is correlated to each original time series from each grid cell from the control simulation (Figure 2c). These calculations produce high positive correlations over most of the western U.S., ranging from 0.6 to 0.9 (Figure 2c). The highest correlations were found where the influence of post-condensation exchanges was also high (e.g., over Oregon). These results reveal that post-condensation exchanges contribute about 60%–75% of the $\delta^{18}O_p$ variance (Figure 2b), mostly by amplifying year-to-year maxima and minima caused by other processes (Figures 2c and 3).

Figure 1. (**a**) Spatial distribution of variance of $\delta^{18}O_p$ for the control simulation; and (**b**)–(**h**) 7 model experiments. Variance is calculated from interannual time series at each grid cell. Contour intervals are 0.25‰.

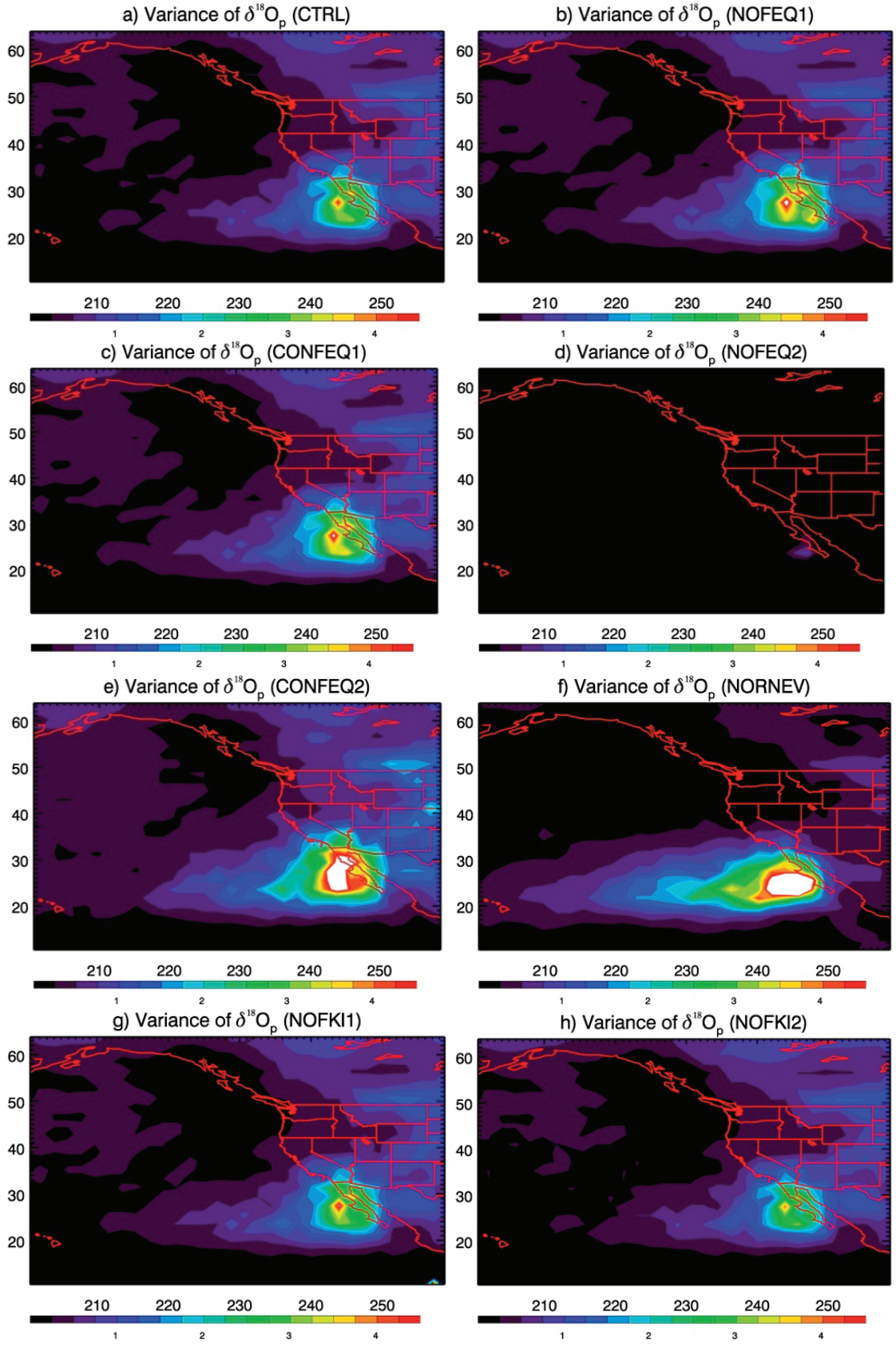

Figure 2. (**a**) Variance difference between the control simulation (CTRL) simulation and the simulation that removed isotope effects from post-condensation exchanges (NORNEV); (**b**) The same variance difference divided by the variance of the CTRL simulation; (**c**) Correlation between interannual $\delta^{18}O_p$ variations from the CTRL simulation and the difference in $\delta^{18}O_p$ between the CTRL simulation and NORNEV simulation. Open purple rectangles in panel (c) show the boxed regions for Figure 3.

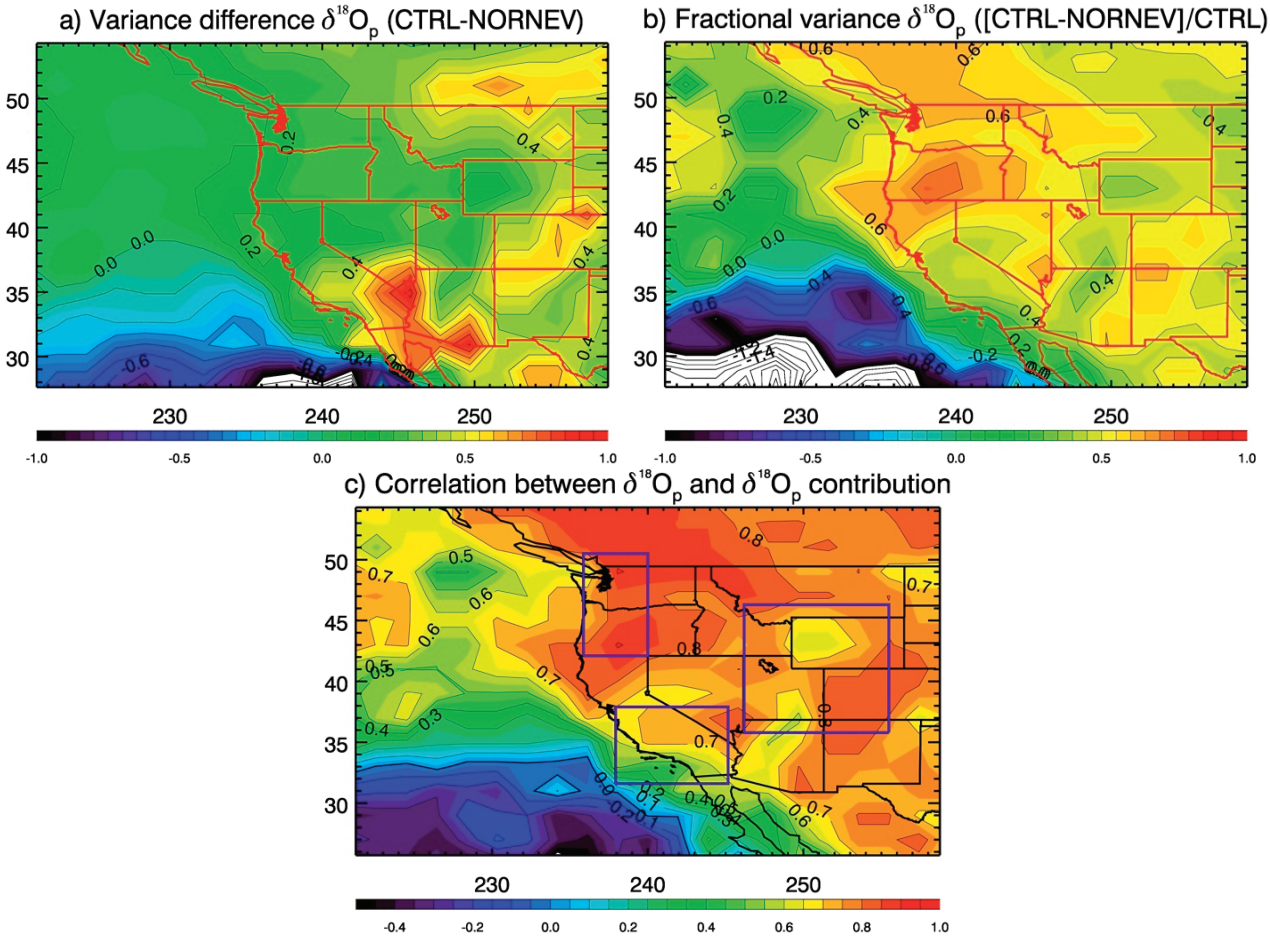

Figure 3. Regional average interannual time series of $\delta^{18}O_p$ for the CTRL and NORNEV simulations. The panels display the (**a**) Pacific Northwest; (**b**) the interior of the western U.S.; (**c**) and central/southern California.

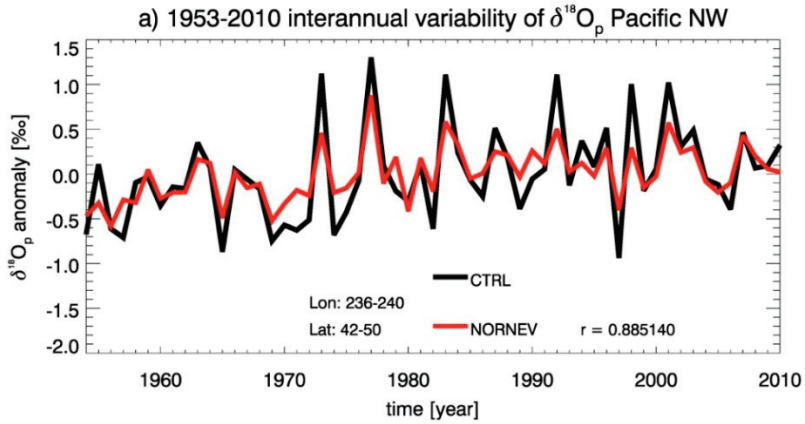

Figure 3. *Cont.*

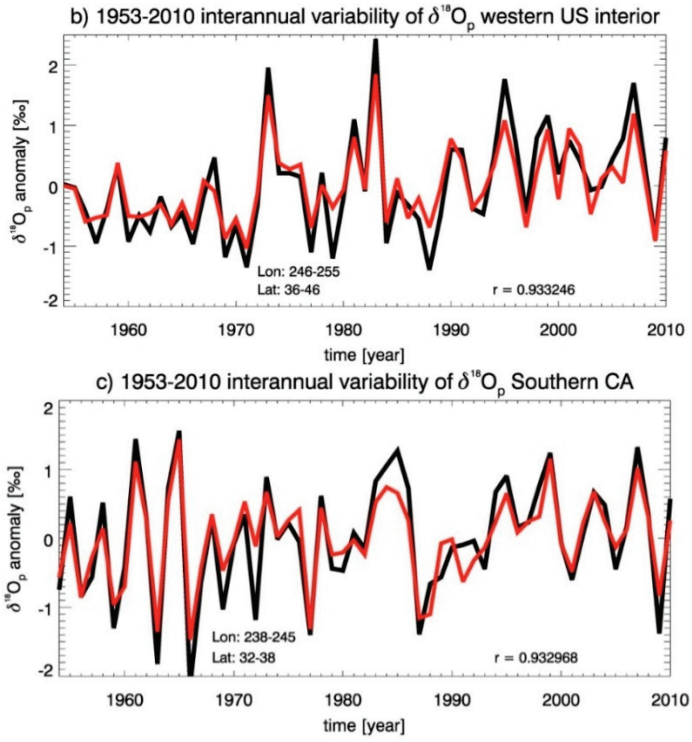

4.2. Condensation Height

Buenning *et al.* [37] found that $\delta^{18}O_p$ seasonality along the western U.S. coast was primarily driven by seasonal changes to condensation height. To examine if condensation height is also influencing interannual $\delta^{18}O_p$ variations, vertical tagging simulations were performed with IsoGSM, such that the 28 atmosphere levels in IsoGSM were divided into 14 tagged-levels, and 14 separate tags were added to each of the 14 levels. The tagging was done such that tagged vapor was set equal to normal vapor within each level at every time step. Tagged vapor is allowed to advect and condense in the predefined tagged level; however, if the vapor is transported vertically across tagged level boundaries, it is immediately removed. This approach is similar to the TAGLEV simulation conducted by Buenning *et al.* [37], with the exception that the atmosphere is divided into 14 tagged-levels and not 2.

For most areas, the bottom 14 levels of IsoGSM (the bottom 7 tagged-levels) contributed over 95% of the total precipitation during the course of a typical year. As such, results from the bottom seven tags are presented here. Figure 4 shows the interannual correlation between the fraction of precipitation with a vertical tag (*i.e.*, p_{tag}/p_{total}) and $\delta^{18}O_p$ for each of the 7 tags at each grid cell in the western U.S. Though the correlation coefficients do not imply causation, they do quantify the co-variability between $\delta^{18}O_p$ and condensation height. They will also reveal locations where there are connections between $\delta^{18}O_p$ and condensation height. For the bottom 3 tags (tags 1–3, hereafter) correlations are high and positive throughout most of California, with the largest correlation occurring along the coast of southern and central California (Figure 4a–c). Correlations for tags 1–3 are also high and positive in northern Oregon and southern Washington. The correlations become weaker for the inland western states and northeastern California.

Figure 4. (**a**)–(**g**) Correlation between interannual $\delta^{18}O_p$ variations and the fraction of precipitation from each of the vertical tags. Correlations with the bottommost tag is shown in panel (**a**) (tag 1); and correlations with higher level tags are shown in panels (**b**)–(**g**). Contour intervals are 0.1. Absolute values of *r* above 0.263 are significant above the 95% confidence level.

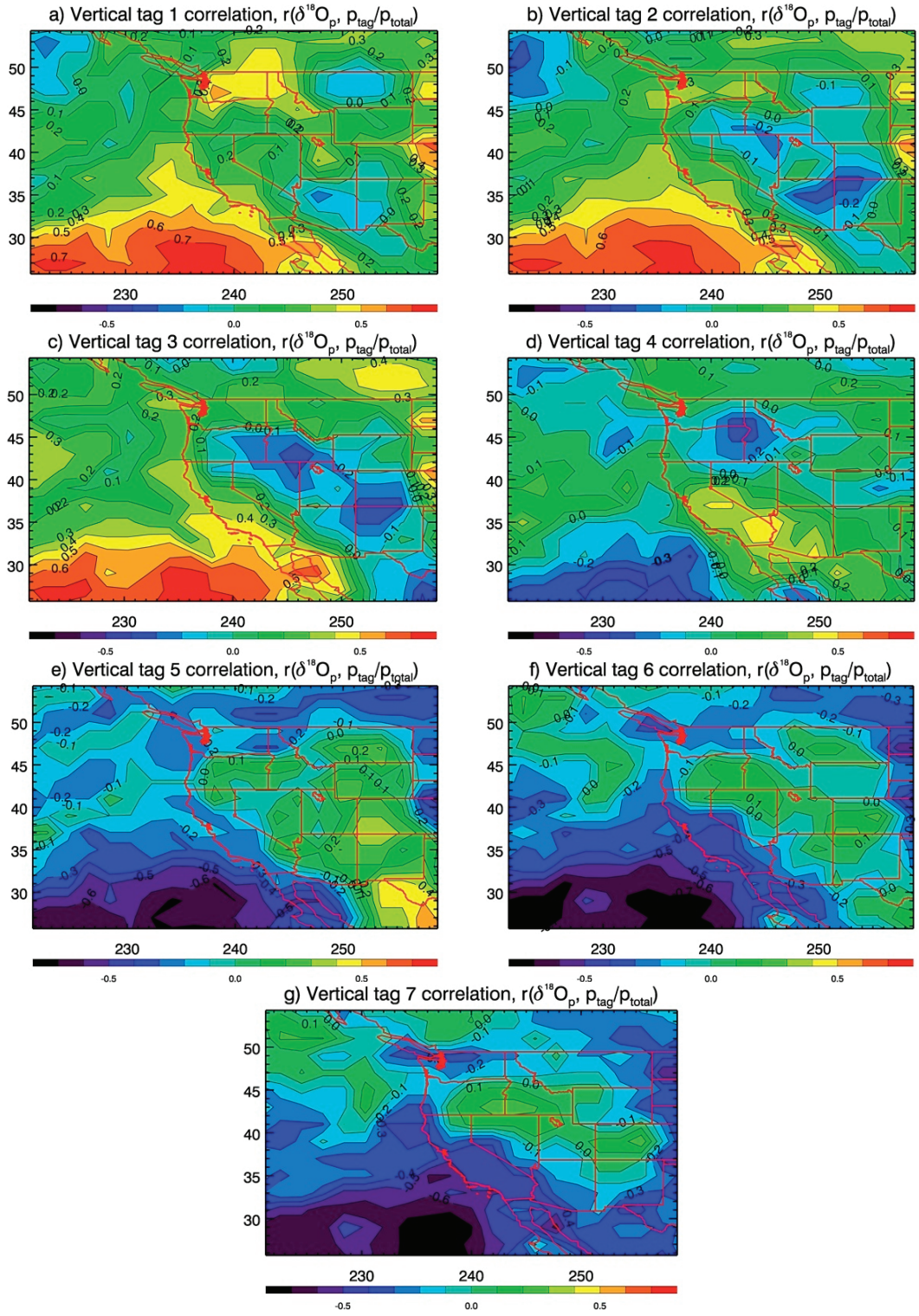

The correlation changes significantly for tag 4 (Figure 4d) with many regions seeing reduced correlation, except for parts of southern California, where *r*-values are at their highest. High negative correlations exist between $\delta^{18}O_p$ and the fraction of precipitation with higher-level tags (hereafter, tags 5–7) for many regions in the western U.S. (Figure 4e–g). These shifts from positive to negative correlations suggests that annual mean $\delta^{18}O_p$ tends to be lower (higher) during years when a larger fraction of the precipitation was derived from higher (lower) in the atmosphere, where vapor $\delta^{18}O$ values are typically more (less) negative. The spatial distributions of the correlation coefficients for the higher-level tags (5–7) are almost mirror images of the lower level tags (1–3), but of opposite sign (Figure 4). Like tags 1–3, correlations are high (though negative) for almost all of California, southern Washington, and northern Oregon. Also, correlations between $\delta^{18}O_p$ and the fraction of precipitation with tags 5–7 are significantly reduced for the inland western states. The correlations in Figure 4 reveal evidence of an influence of condensation height on interannual $\delta^{18}O_p$ variations in some, but not all, regions of the western U.S., similar to the isotope seasonality results of *Buenning et al.* [37].

To quantify the contribution of condensation height on interannual $\delta^{18}O_p$ variations, multiple correlation coefficients were calculated for each location, using the fraction of precipitation from each tag (p_{tag}/p_{total}) as the predictor and $\delta^{18}O_p$ as the dependent variable. Based on the fractional contribution from each tag (discussed below), only tags 2–6 are used for each calculation. Though this approach is not a direct measurement of the contribution from condensation height, the r^2 value does give a measure of shared variance, which can be used as a first order estimate of the fraction of the variance attributable to condensation height. Figure 5a shows the multiple correlation coefficients, suggesting that condensation height contributes roughly 25%–40% to interannual $\delta^{18}O_p$ variance in central and southern California (*r* ranging from 0.5 to 0.63). In coastal northern California, Oregon, and Washington, the contribution is slightly less at about 10%–15% (*r* ranging from 0.3 to 0.4). The *r*-values in the interior states of the western U.S. are not viewed as a contribution to the interannual variance because of the sign of the single variable correlations in Figure 4 (which indicates another effect/process is overriding interannual variations in condensation height in these regions). Performing the same calculations with $\delta^{18}O_p$ values from the NORNEV simulation resulted in higher *r*-values (Figure 5b), which is not surprising since the simulation removed processes that have already been shown to highly influence interannual $\delta^{18}O_p$ variations. These results show that condensation height is most influential on interannual $\delta^{18}O_p$ variations in southern and central California with decreasing influence northward into coastal Washington.

To demonstrate why condensation height drives interannual $\delta^{18}O_p$ variations in some regions more than others, Figure 6 shows the mean fractional contribution of precipitated tag to the total precipitation (the mean value used in the correlation calculation) for tags 1 through 7. The contribution of the bottom tag was only 3%–4% of the total precipitation, but the contribution of tag 2 was higher and above 10% in most grid cells. Tags 3–5 contributed the highest fraction to the total precipitation throughout the western U.S., ranging from about 20%–40% for each tag. Further up in the modeled atmosphere, the fractional contribution decreases sharply for tags 6 and 7, which are similar to tags 2 and 1, respectively.

Figure 5. (**a**) Multiple correlation between tags 2–6 (p_{tag}/p_{total}) and $\delta^{18}O_p$ from the CTRL simulation; and (**b**) the NORNEV simulation.

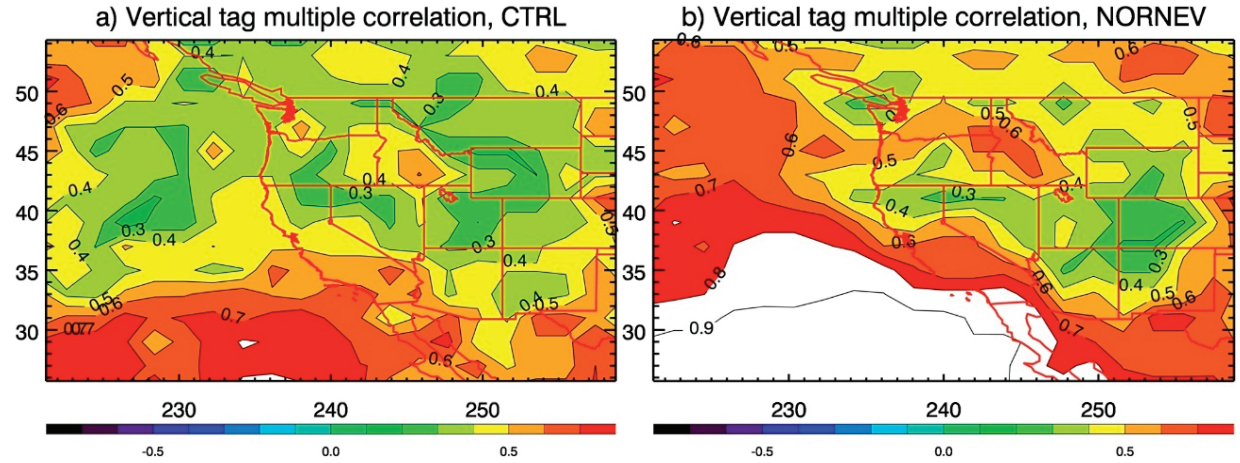

Figure 6. (**a**–**g**) The contribution of each vertical tag to the total precipitation. Closed contour intervals are 0.01.

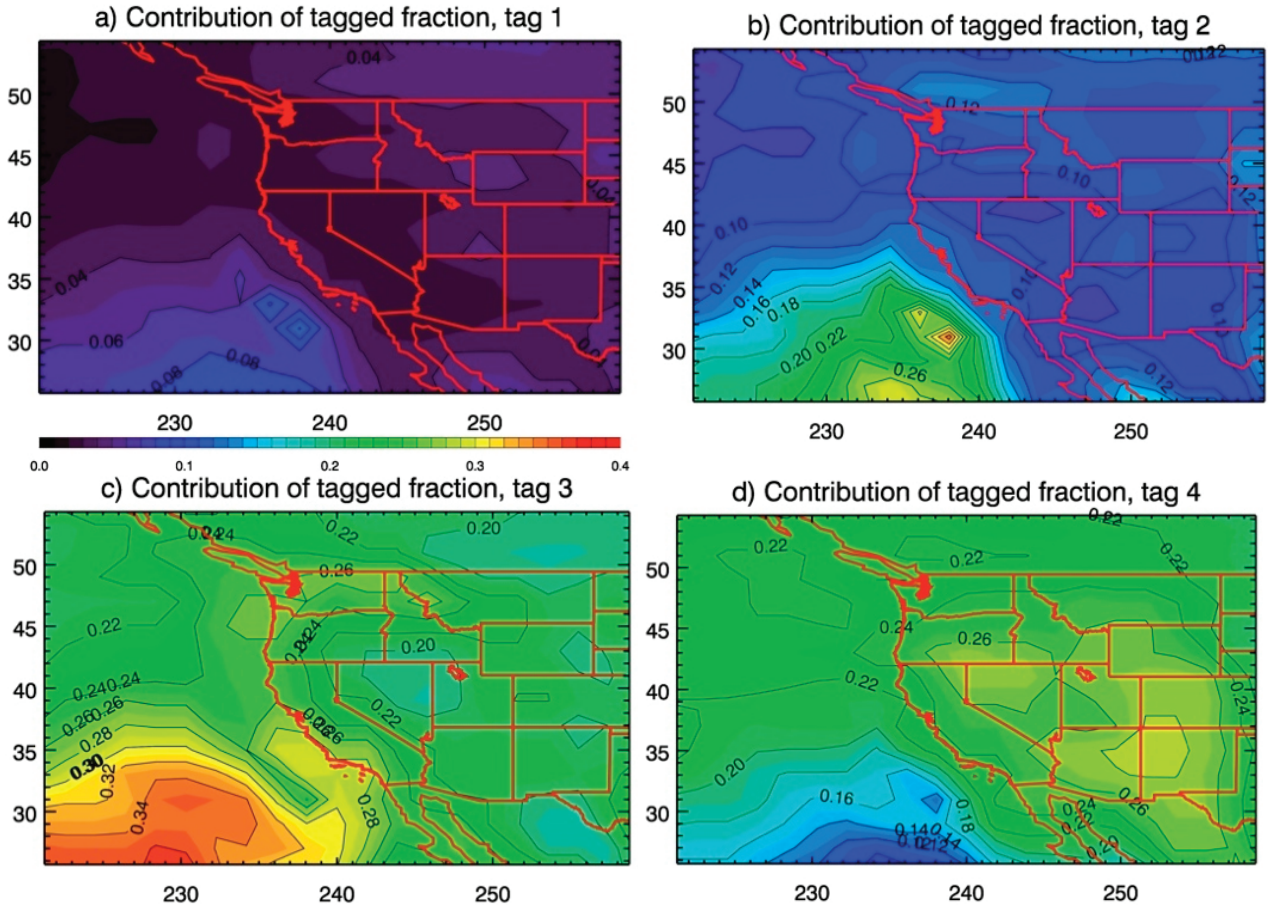

Figure 6. *Cont.*

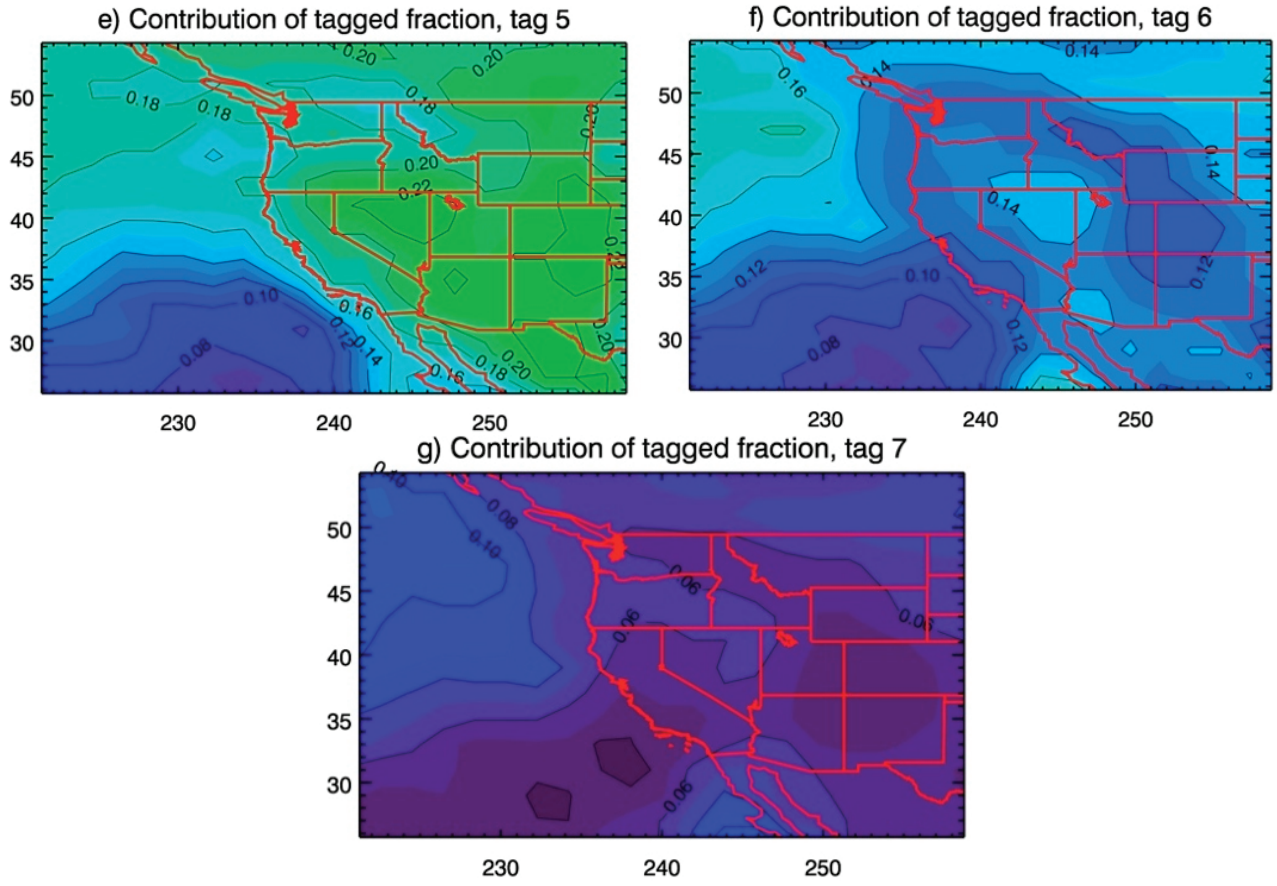

Figure 7 shows the mean isotopic composition associated with each vertical tag by amount weighting (based on tagged vapor) the $\delta^{18}O$ value of vapor ($\delta^{18}O_v$) from the control (CTRL) simulation. Though the mean $\delta^{18}O_v$ values of tags 1 and 2 are roughly the same, $\delta^{18}O_v$ decreases upward, as would be expected due to vertical isotope gradients in $\delta^{18}O_v$ [54–56]. Figure 8 shows the difference in $\delta^{18}O$ values between tags 3 and 5 (*i.e.*, Figure 7e minus Figure 7c), which are two of three tags that contributed the most to the total precipitation. The difference in the isotopic composition of vapor between the two tags clearly shows the vertical gradient (at levels that contribute the most to total precipitation) is strongest along the coastline and decreases inland. This feature is partially responsible for the strength of the condensation height effect over most of Washington, Oregon, and California.

Figure 8 does not reconcile why the influence of condensation height is strongest in southern and central California and decreases northward along the coast. Figure 9 displays the interannual variance of the fraction of precipitation with tags 3 and 5. The spatial distribution of the variance is remarkably similar to Figure 1f (the variance of $\delta^{18}O_p$ from the NORNEV simulation), showing that the largest variability was near the Baja Peninsula with decreased variance northward along the coast and inland. Not surprisingly, Figure 9 reveals that the influence of condensation height on $\delta^{18}O_p$ was strongest in regions where variations in condensation height were also large.

Figure 7. (**a**–**g**) The isotopic composition of vapor ($\delta^{18}O_v$) corresponding with each of the vertical tags. Mean values are calculated by weighting vertical $\delta^{18}O_v$ from the CTRL simulation by the vertical distribution of the given tag. The bottommost tag is shown in panel a (tag 1), and higher level tags are shown in panels (**b**)–(**g**). Contour intervals are 1‰.

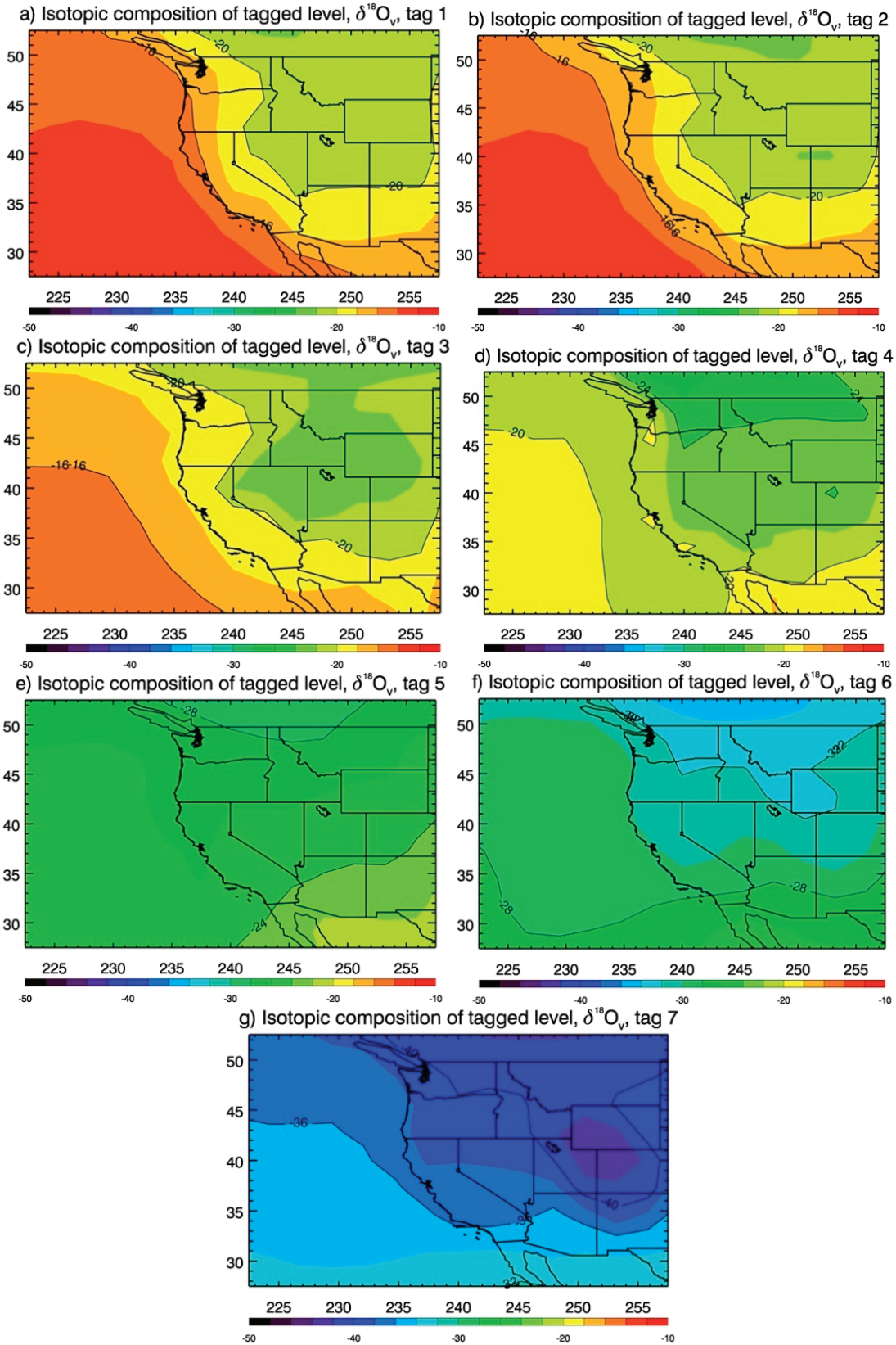

Figure 8. Difference between the isotopic composition of vapor between vertical tags 3 and 5 (Figure 7e and Figure 7c). More negative values indicate a steeper veritcal gradient in $\delta^{18}O$ values of vapor ($\delta^{18}O_v$). Closed contour intervals are 0.5‰.

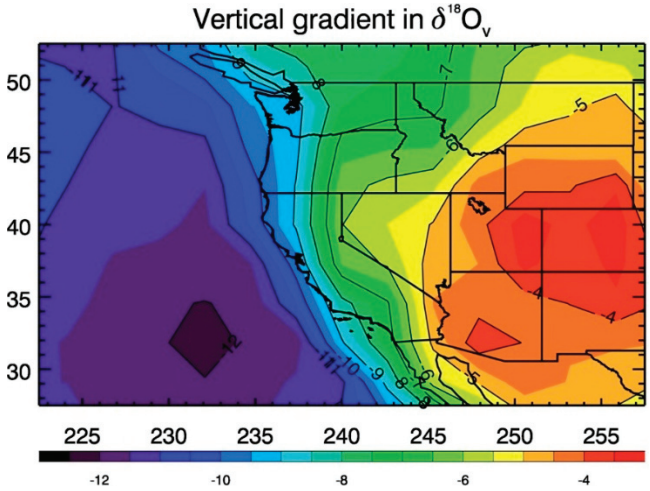

Figure 9. Interannual variance of fraction of precipitation from (**a**) vertical tag 3; and (**b**) vertical tag 5.

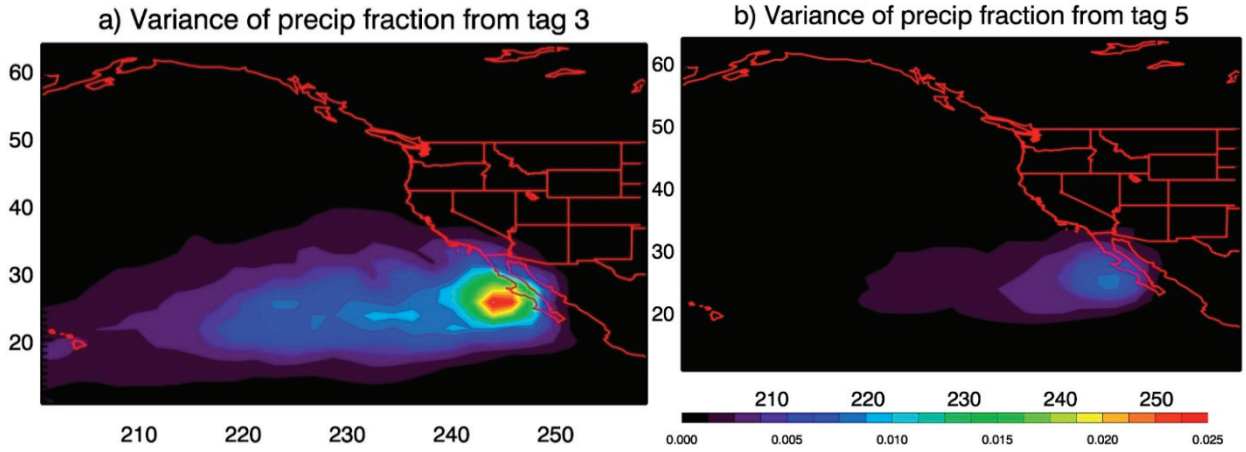

4.3. Circulation Effects

4.3.1. Circulation Effects and $\delta^{18}O_p$

The TAGY simulation was designed to determine how interannual $\delta^{18}O_p$ variations are influenced by shifts in moisture advection from either the subtropics or middle latitudes. In TAGY, vapor was continually tagged at all 28 levels of the IsoGSM atmosphere within two boxed regions over the North Pacific: one in the subtropics and one in the middle latitudes. Outside of these two regions, the vapor tags are subject to the same atmospheric processes as normal water (*i.e.*, advection, mixing, condensation, and rainout). As with all atmospheric General Circulation Models, IsoGSM simulates and accounts for these processes. Furthermore, since both the tagging simulation (TAGY) and the control simulation (CTRL) are nudged to the same wind and temperature fields, the water isotopologues and water tags are subject to the same atmospheric and oceanic conditions (e.g.,

temperature and rainout histories along air mass trajectories and ocean evaporation conditions). A fraction of the resulting simulated precipitation that falls in the western U.S. will contain the middle latitude tag and another fraction will contain the subtropical tag, which is compared to the simulated $\delta^{18}O$ values below.

As in Subsection 4.2, interannual correlations coefficients were calculated to quantify covariance between precipitated tags and $\delta^{18}O_p$. Figure 10a,b show the interannual correlations between $\delta^{18}O_p$ and the fraction of precipitation with the middle latitude and subtropical tags. For both tags, correlations are weak across almost all of the western U.S. This result suggests there is little covariance between interannual $\delta^{18}O_p$ variations and the fraction of precipitation advected from either the subtropics or the middle latitudes. Thus, any influence of moisture advection would be difficult to detect from $\delta^{18}O_p$ at interannual timescales. The exceptions to this include Washington and Oregon, where correlations with subtropical and middle latitude tagged precipitation fractions exceed 0.4 and −0.4, respectively. These correlations suggest that the Pacific Northwest might be a region where precipitation δ values adequately trace atmospheric circulation at interannual timescales.

To see if the correlations improve without the influence of post-condensation exchanges and condensation height, individual interannual time series of $\delta^{18}O_p$ from the NORNEV simulation were regressed against the fraction of precipitation from the bottom 7 vertical layers from the TAGZ simulations (values in Figure 6):

$$\delta_{regress} = \sum_{i=1}^{7} A_i \frac{p_i}{p} + B \tag{1}$$

In Equation (1), p values are simulated precipitation rates, indices i refer to each of the 7 vertical tags, and the values of A_i and B (‰) are the regression slopes and intercepts (respectively) used to fit interannually varying $\delta^{18}O_p$ from the NORNEV simulation (δ_{NORNEV}). The residual of the regression ($\delta_{residual}$) will have removed both the influence of post-condensation exchanges and condensation height:

$$\delta_{residual} = \delta_{NORNEV} - \delta_{regress} \tag{2}$$

The interannual variations of $\delta_{residual}$ were correlated with the fraction of precipitation from the middle latitude and subtropical regions of the TAGY simulation. The correlations between $\delta_{residual}$ and the fraction of precipitation advected from the middle latitude-tagged region become slightly more negative (Figure 10c), which was originally the anticipated relationship. Similarly, the correlations with the fraction of precipitation with the subtropical tag significantly increased and were positive at almost all western U.S. locations (Figure 10d). For both tags, the correlations with $\delta_{residual}$ are highest in Washington and Oregon (where the correlations already existed). These results indicate that the influence of circulation changes on $\delta^{18}O_p$ is secondary and only detectable after the removal of the primary influences of post-condensation exchanges and condensation height in California and the western U.S. interior.

Figure 10. (**a**) Correlation between interannual $\delta^{18}O_p$ variations and the fraction of precipitation from middle latitude tags; and (**b**) subtropical tags; Panels (**c**) and (**d**) show the same correlations, as (**a**) and (**b**) (respectively), but with the influence of post-condensation exchanges and condensation height removed. Contour intervals are 0.1. Absolute values of *r* above 0.263 are significant above the 95% confidence level.

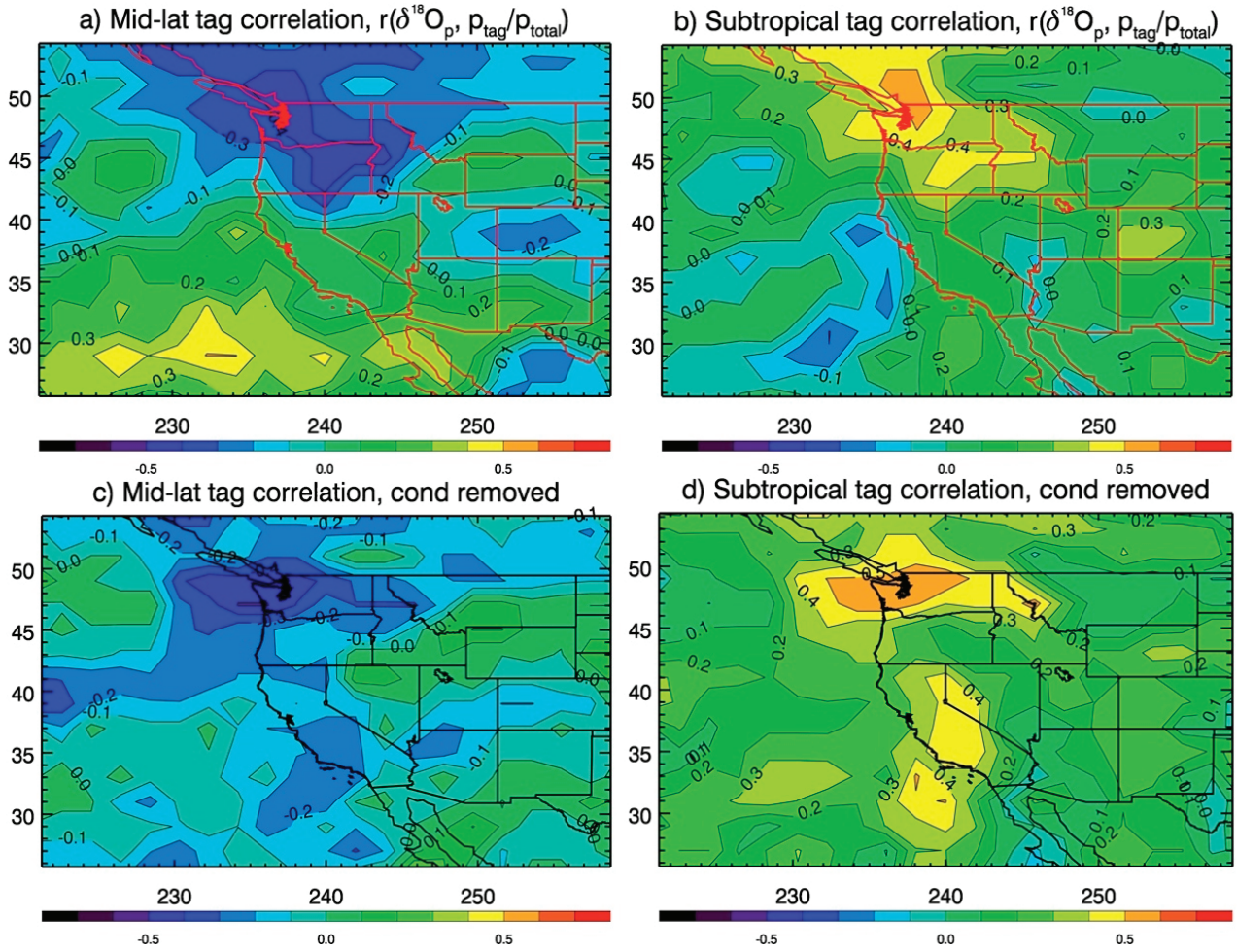

4.3.2. Circulation Effects and $\delta^{18}O_{PW}$

Results from the TAGY simulation revealed that in most regions of the western U.S. the influence of circulation changes on interannual $\delta^{18}O_p$ variations is small. However, atmospheric circulation does affect the isotopic composition of vapor. Correlations between the isotopic composition of precipitable water (column integrated tropospheric vapor), $\delta^{18}O_{PW}$, and the fraction of precipitable water with the middle latitude and subtropical tags are shown in Figure 11. Figure 11a reveals a strong negative correlation between $\delta^{18}O_{PW}$ and the mid-latitude tags throughout much of the western U.S. The strongest negative correlation in Figure 11a is located at the California/Nevada border near Lake Tahoe. However, the same figure was generated with additional tagging simulations, and it was found that the location of the strongest negative correlations was dependent on the location of boxed regions where the vapor tags were being added (figure not shown). Nonetheless, the additional simulations also revealed that the negative correlation that exists in the western U.S. is robust.

Figure 11. (**a**) Correlation between interannual $\delta^{18}O_{PW}$ variations and the fraction of precipitable water from middle latitude tags; and (**b**) subtropical tags. Contour intervals are 0.1. Absolute values of *r* above 0.263 are significant above the 95% confidence level.

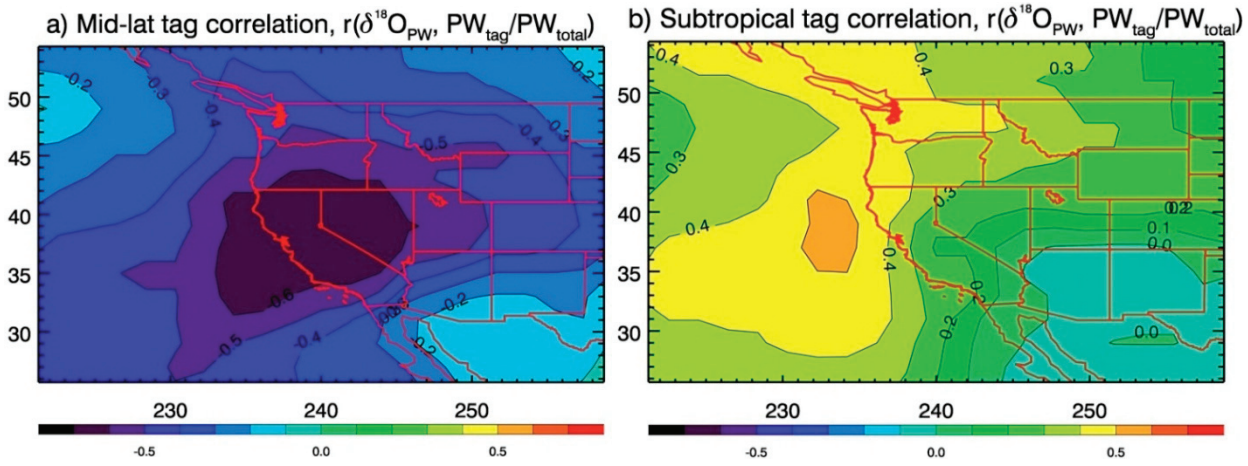

Correlations with the subtropical tags are positive throughout most of the western U.S. The largest correlation exists in coastal locations within Oregon and Washington, which are the same regions that had positive correlations with $\delta^{18}O_p$. The correlations are not as high for the southwest U.S. and southern California. The additional tagging simulations revealed that the locations of the good and poor correlations in Figure 11b are robust and not dependent on the location of the boxed regions where vapor is being tagged. The robustness of both the negative correlation in Figure 11a and the positive correlation in Figure 11b indicates a strong relationship between the oxygen isotopic composition of tropospheric vapor and atmospheric circulation in the western U.S. However, this relationship was not seen in precipitation δ values in most regions because of the strong influence of post-condensation exchanges and condensation height. Indeed, the atmospheric circulation effect was only transferred to precipitation δ values in regions where variations in condensation height are relatively small like the Pacific Northwest (Figure 9).

4.4. Temperature Effect

Though the NORNEV simulation demonstrated that roughly 60% of the interannual $\delta^{18}O_p$ variations were due to post-condensation exchanges throughout the western U.S., the tagging simulations discussed in Sections 4.2 and 4.3 failed to describe the remaining variance in the interior states of the western U.S. Past studies [16,57] have found or suggested that regions of the interior of the U.S. show a temperature effect (positive correlations between $\delta^{18}O_p$ and local temperatures). This relationship is due to increases (decreases) in Rayleigh distillation with lower (higher) temperatures and subsequently lower (higher) δ values of vapor upon arrival at a given location. In this subsection, IsoGSM's temperature effect relationship will be quantified within the western U.S.

The correlations between $\delta^{18}O_p$ and surface air temperature were calculated at each grid cell within the western U.S. for the CTRL simulation. Because the precipitation seasonal cycle peaks in the summer within the interior states, annual means in this subsection are calculated as the normal January to December average (though this did not change the general results). Correlations are low

in the coastal areas and all of California (Figure 12a), as expected since the modeling results presented above indicated other processes drive interannual $\delta^{18}O_p$ variations. Relatively high correlations ($r > 0.3$) were found in an area of New Mexico spanning northward into Montana and eastern Washington (Figure 12a). The lack of high correlations between local annual mean temperatures and $\delta^{18}O_p$ reveals a problem for using climate proxies based on $\delta^{18}O_p$ values to reconstruct annual mean temperatures in the western U.S. However, when the mean temperatures are weighted by monthly precipitation the correlations significantly increase over all of the interior states of the western U.S. (Figure 12b); a result that has been found elsewhere using a different model [15]. Indeed, using precipitation-weighted temperatures increased the correlations from about 0.3 to 0.7 for many regions of the interior western U.S. These results reveal that reconstructed annual mean temperatures in the western U.S. interior could be biased towards wet season temperatures when using proxies derived from $\delta^{18}O_p$.

Figure 12. (**a**,**b**) Correlation between $\delta^{18}O_p$ and annual mean temperature; and (**c**,**d**) surface level specific humidity (bottom panels). Right panel annual means of temperature and specific humidity were weighted by monthly precipitation. Absolute values of r above 0.263 are significant above the 95% confidence level.

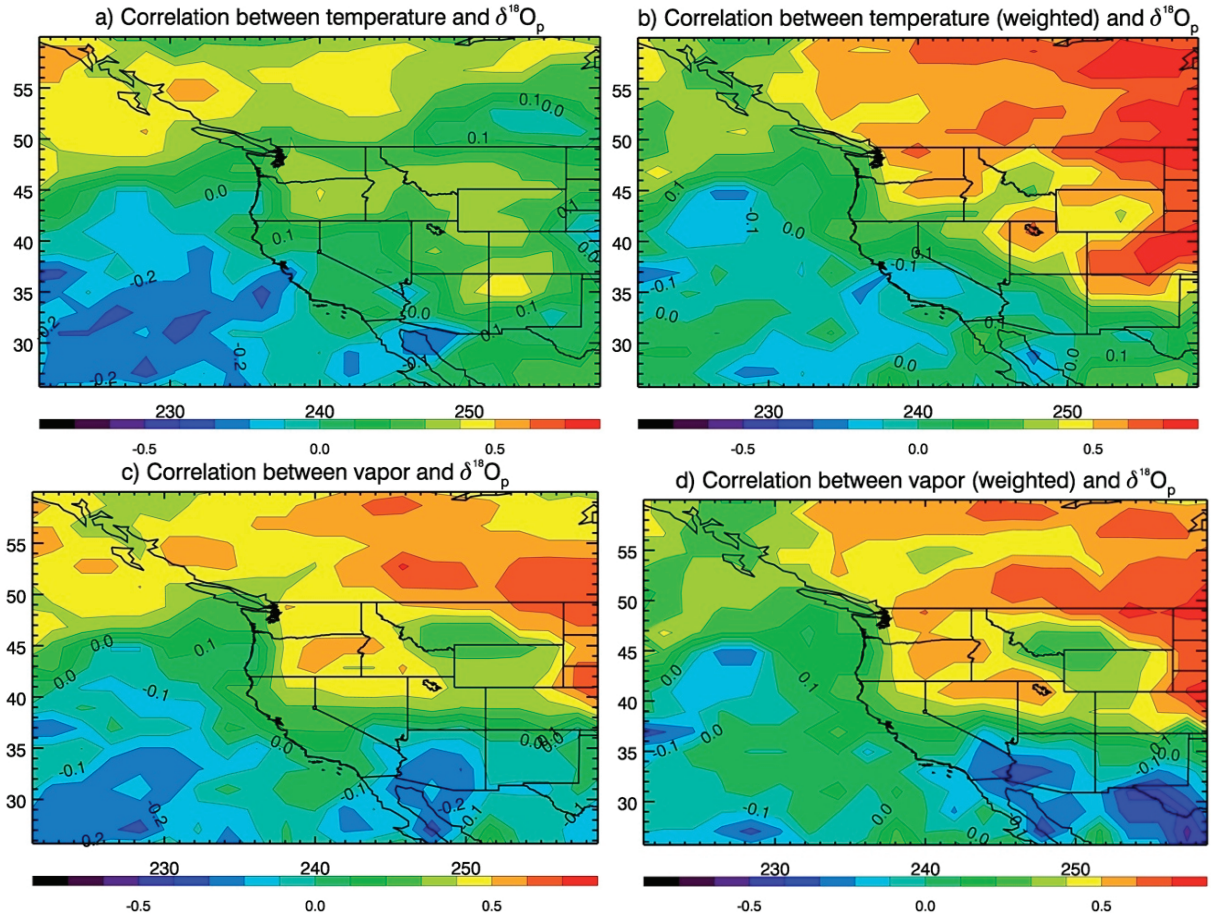

To demonstrate that this temperature effect in the western U.S. was a result of rainout as air masses moved through the interior of the continent, similar correlation maps were made for specific humidity (q) and precipitation-weighted specific humidity (Figure 12c,d). Though the correlation maps are not

identical to the corresponding temperature plots, they both highlight the interior of the western U.S. as a region where strong correlations exist, and suggest that the simulated interannual $\delta^{18}O_p$ variations were driven by the extent of Rayleigh distillation from the coastline to the location where precipitation occurs. Thus, this rainout process gives rise to the "precipitation-weighted temperature effect", as simulated by IsoGSM.

5. Conclusions

The modeling results suggest that interannual variations in precipitation δ values in the western U.S. are primarily caused by a combination of mechanisms, though some atmospheric processes are detectable at interannual timescales in certain regions. In the western coastal areas and almost all of California, the variations are largely controlled by changes in condensation height. These induced variations in $\delta^{18}O_p$ that account for about 20%–40% of the interannual variance, but the year-to-year changes are amplified by post-condensation exchanges, accounting for about 60% of the variance. Most of the remaining variance in California and coastal Oregon and Washington is attributable to subtropical *versus* middle latitude moisture advection changes (*i.e.*, an atmospheric circulation effect), which is most prominent and detectable in the Pacific Northwest of the United States. Further north, Field *et al.* [58] found a similar relationship between precipitation δ values and atmospheric circulation in western Canada. In California, the atmospheric circulation effect can only be detected after the influences of post-condensation exchanges and condensation height are removed from individual time series. However, the model results suggest that atmospheric circulation is a primary influence on vapor δ values throughout almost all of the western U.S.

A temperature effect was found for the inland regions of the western U.S., such that years with anomalously cooler (warmer) temperatures will lead to more (less) isotopic rainout and lower (higher) δ values of vapor and subsequently precipitation. Like the coastal regions, these isotopic variations in $\delta^{18}O_p$ are amplified by post-condensation exchanges, contributing about 60% to the interannual variance. The $\delta^{18}O_p$-temperature correlations found here were only large after annual mean temperatures were weighted by precipitation amounts, indicating a problem for reconstructing annual mean temperatures in the western U.S. interior.

The results presented here will help guide the interpretation of climate proxies in the western U.S. that are influenced by precipitation δ values, such as ice-cores [17,18], speleothems [21,22], tree cellulose [16,19], leaf wax *n*-alkanes [24,59], and lacustrine archives [25–28]. The model results suggest that climate proxy δ values from California and parts of Washington and Oregon might reflect variations in condensation height on interannual timescales. However, Washington and Oregon were also areas where $\delta^{18}O_p$ correlated with subtropical and mid-latitude tags, indicating covariance between the vertical and north-south tags in the Pacific Northwest (*i.e.*, moisture transported from the subtropics typically rains out lower in the atmosphere). In the interior of the western U.S., proxy δ values likely trace precipitation-weighted temperatures changes, which may differ from annual mean temperatures. The TAGY tagging simulation demonstrated that vapor δ values ($\delta^{18}O_v$) trace atmospheric circulation over most regions of the western U.S. This particular finding may be useful in the context of the results of Helliker *et al.* [60] who showed through controlled experiments and model calculations that epiphyte Tillandsia usneoides from CAM plants

record δ values of vapor. Thus, these plants may be useful in detecting shifts in middle latitude storm tracks [61,62]. Furthermore, the model results suggest that the Pacific Northwest is a region where $\delta^{18}O_p$ values trace atmospheric circulation, highlighting an area where shifts in storm tracks may be detectable through measurements of either precipitation or vapor δ values. Additionally, past shifts may be reconstructed through water isotope based proxy records in the Pacific Northwest. However, it is important to note that the mean circulation variations that are typical at interannual timescales (e.g., ENSO variability and the position of the North Pacific High), may differ from the type of circulation changes on longer timescales, such as multi-decadal and inter-glacial variations.

Detecting shifted storm tracks through isotope measurements should be the focus of future work, either through direct measurements of isotopes in precipitation or vapor or from climate proxy reconstructions. This is particularly important because poleward shifted middle latitude storm tracks are features of a warmer climate that almost all global climate models agree upon [61,62]. Detecting such shifts is vital for regions, like the southwest U.S., where water resources are already stressed due to an inadequate supply and growing demand. The results presented here suggest that storm track shifts can be detected through ongoing monitoring of $\delta^{18}O_p$ in the Pacific Northwest. This stresses the need to continue station observations of the isotopic composition of precipitation at sites in Oregon and Washington (e.g., the Olympic site from *Buenning et al.* [37]). Furthermore, ongoing measurements of isotopes in vapor may serve useful at detecting storm track shifts in the western US, either from satellite retrievals [63–65] or ground-based remote sensing [66]. The modeling results presented here demonstrate how moisture advection can influence the isotopes in atmospheric moisture in the western U.S.; thus, future work should focus on developing isotope-based methodologies to monitor and detect storm track variability over the western U.S.

Acknowledgments

Funding for this work was provided by the NOAA/CPO Climate Change & Detection Program: Paleoclimate Studies (grant NA10OAR4310129). This work was also supported by a grant from the National Science Foundation (award AGS-1049238). We also thank the helpful comments and suggestions from two anonymous reviewers.

Conflict of Interest

The authors declare no conflict of interest.

References

1. Lorius, C.; Jouzel, J.; Raynaud, D.; Hansen, J.; Letreut, H. The ice-core record: Climate sensitivity and future greenhouse warming. *Nature* **1990**, *347*, 139–145.
2. Vimeux, F.; Ginot, P.; Schwikowski, M.; Vuille, M.; Hoffmann, G.; Thompson, L.G.; Schotterer, U. Climate variability during the last 1000 years inferred from Andean ice cores: A review of methodology and recent results. *Palaeogeogr. Palaeocl.* **2009**, *281*, 229–241.
3. McDermott, F. Palaeo-climate reconstruction from stable isotope variations in speleothems: A review. *Quat.Sci. Rev.* **2004**, *23*, 901–918.

4. Sternberg, L.D.L.O. Oxygen stable isotope ratios of tree-ring cellulose: The next phase of understanding. *New Phytol.* **2009**, *181*, 553–562.
5. Dansgaard, W. Stable isotopes in precipitation. *Tellus* **1964**, *16*, 436–468.
6. Araguas-Araguas, L.; Froehlich, K.; Rozanski, K. Stable isotope composition of precipitation over southeast Asia. *J. Geophys. Res. Atmos.* **1998**, *103*, 28721–28742.
7. Yamanaka, T.; Shimada, J.; Hamada, Y.; Tanaka, T.; Yang, Y.H.; Zhang, W.J.; Hu, C.S. Hydrogen and oxygen isotopes in precipitation in the northern part of the North China Plain: Climatology and inter-storm variability. *Hydrol. Process.* **2004**, *18*, 2211–2222.
8. Risi, C.; Bony, S.; Vimeux, F. Influence of convective processes on the isotopic composition ($\delta^{18}O$ and δD) of precipitation and water vapor in the tropics: 2. Physical interpretation of the amount effect. *J. Geophys. Res. Atmos.* **2008**, *113*, D19306.
9. Lee, J.E.; Fung, I. "Amount effect" of water isotopes and quantitative analysis of post-condensation processes. *Hydrol. Process.* **2008**, *22*, 1–8.
10. Lee, J.E.; Risi, C.; Fung, I.; Worden, J.; Scheepmaker, R.A.; Lintner, B.; Frankenberg, C. Asian monsoon hydrometeorology from TES and SCIAMACHY water vapor isotope measurements and LMDZ simulations: Implications for speleothem climate record interpretation. *J. Geophys. Res. Atmos.* **2012**, *117*, D15112.
11. Field, R.D.; Jones, D.B.A.; Brown, D.P. Effects of postcondensation exchange on the isotopic composition of water in the atmosphere. *J. Geophys. Res. Atmos.* **2010**, *115*, D24305.
12. Buenning, N.H.; Noone, D.C.; Riley, W.J.; Still, C.J.; White, J.W.C. Influences of the hydrological cycle on observed interannual variations in atmospheric $CO^{18}O$. *J Geophys. Res. Biogeo.* **2011**, *116*, G04001.
13. Rozanski, K.; Sonntag, C.; Munnich, K.O. Factors controlling stable isotope composition of european precipitation. *Tellus* **1982**, *34*, 142–150.
14. Bowen, G.J. Spatial analysis of the intra-annual variation of precipitation isotope ratios and its climatological corollaries. *J. Geophys. Res. Atmos.* **2008**, *113*, D05113.
15. Sturm, C.; Zhang, Q.; Noone, D. An introduction to stable water isotopes in climate models: Benefits of forward proxy modelling for paleoclimatology. *Clim. Past* **2010**, *6*, 115–129.
16. Berkelhammer, M.; Stott, L.D. Secular temperature trends for the southern Rocky Mountains over the last five centuries. *Geophys. Res. Lett.* **2012**, *39*, L17701.
17. Naftz, D.L.; Susong, D.D.; Schuster, P.F.; Cecil, L.D.; Dettinger, M.D.; Michel, R.L.; Kendall, C. Ice core evidence of rapid air temperature increases since 1960 in alpine areas of the Wind River Range, Wyoming, United States. *J. Geophys. Res. Atmos.* **2002**, *107*, ACL 3.
18. Schuster, P.F.; White, D.E.; Naftz, D.L.; Cecil, L.D. Chronological refinement of an ice core record at Upper Fremont Glacier in south central North America. *J. Geophys. Res. Atmos.* **2000**, *105*, 4657–4666.
19. Berkelhammer, M.; Stott, L.D. Modeled and observed intra-ring $\delta^{18}O$ cycles within late Holocene Bristlecone Pine tree samples. *Chem. Geol.* **2009**, *264*, 13–23.
20. Berkelhammer, M.B.; Stott, L.D. Recent and dramatic changes in Pacific storm trajectories recorded in $\delta^{18}O$ from Bristlecone Pine tree ring cellulose. *Geochem. Geophys. Geosy.* **2008**, *9*, Q04008.

21. Vacco, D.A.; Clark, P.U.; Mix, A.C.; Cheng, H.; Edward, R.L. A speleothem record of Younger Dryas cooling, Klamath Mountains, Oregon, USA. *Quat. Res.* **2005**, *64*, 249–256.
22. Oster, J.L.; Montanez, I.P.; Sharp, W.D.; Cooper, K.M. Late Pleistocene California droughts during deglaciation and Arctic warming. *Earth Planet Sci. Lett.* **2009**, *288*, 434–443.
23. Ersek, V.; Clark, P.U.; Mix, A.C.; Cheng, H.; Edwards, R.L. Holocene winter climate variability in mid-latitude western North America. *Nat. Commun.* **2012**, *3*, doi: 10.1038/ncomms2222.
24. Feakins, S.J.; Sessions, A.L. Controls on the D/H ratios of plant leaf waxes in an arid ecosystem. *Geochim. Cosmochim. Acta* **2010**, *74*, 2128–2141.
25. Benson, L.V.; Burdett, J.W.; Kashgarian, M.; Lund, S.P.; Phillips, F.M.; Rye, R.O. Climatic and hydrologic oscillations in the Owens Lake basin and adjacent Sierra Nevada, California. *Science* **1996**, *274*, 746–749.
26. Benson, L.V.; Lund, S.P.; Burdett, J.W.; Kashgarian, M.; Rose, T.P.; Smoot, J.P.; Schwartz, M. Correlation of late-Pleistocene lake-level oscillations in Mono Lake, California, with North Atlantic climate events. *Quat. Res.* **1998**, *49*, 1–10.
27. Li, H.C.; Ku, T.L. Delta C-13-delta O-18 covariance as a paleohydrological indicator for closed-basin lakes. *Palaeogeogr. Palaeoclimatol.* **1997**, *133*, 69–80.
28. Li, H.C.; Ku, T.L.; Stott, L.D.; Anderson, R.F. Stable isotope studies on Mono Lake (California). 1. Delta O-18 in lake sediments as proxy for climatic change during the last 150 years. *Limnol. Oceanogr.* **1997**, *42*, 230–238.
29. Coplen, T.B.; Neiman, P.J.; White, A.B.; Landwehr, J.M.; Ralph, F.M.; Dettinger, M.D. Extreme changes in stable hydrogen isotopes and precipitation characteristics in a landfalling Pacific storm. *Geophys. Res. Lett.* **2008**, *35*, L21808.
30. Yoshimura, K.; Kanamitsu, M.; Dettinger, M. Regional downscaling for stable water isotopes: A case study of an atmospheric river event. *J. Geophys. Res. Atmos.* **2010**, *115*, D18114.
31. Vachon, R.W.; Welker, J.M.; White, J.W.C.; Vaughn, B.H. Monthly precipitation isoscapes $\delta^{18}O$ of the United States: Connections with surface temperatures, moisture source conditions, and air mass trajectories. *J. Geophys. Res. Atmos.* **2010**, *115*, D21126.
32. Ersek, V.; Mix, A.C.; Clark, P.U. Variations of delta O-18 in rainwater from southwestern Oregon. *J. Geophys. Res. Atmos.* **2010**, *115*, D09109.
33. Friedman, I.; Harris, J.M.; Smith, G.I.; Johnson, C.A. Stable isotope composition of waters in the Great Basin, United States—1. Air-mass trajectories. *J. Geophys. Res. Atmos.* **2002**, *107*, doi: 10.1029/2001JD000565.
34. Friedman, I.; Smith, G.I.; Gleason, J.D.; Warden, A.; Harris, J.M. Stable Isotope Composition of Waters in Southeastern California. 1. Modern Precipitation. *J. Geophys. Res. Atmos.* **1992**, *97*, 5795–5812.
35. Friedman, I.; Smith, G.I.; Johnson, C.A.; Moscati, R.J. Stable isotope compositions of waters in the Great Basin, United States—2. Modern precipitation. *J. Geophys. Res. Atmos.* **2002**, *107*, doi: 10.1029/2001JD000566.
36. Berkelhammer, M.; Stott, L.; Yoshimura, K.; Johnson, K.; Sinha, A. Synoptic and mesoscale controls on the isotopic composition of precipitation in the western United States. *Clim. Dynam.* **2012**, *38*, 433–454.

37. Buenning, N.H.; Stott, L.; Yoshimura, K.; Berkelhammer, M. The cause of the seasonal variation in the oxygen isotopic composition of precipitation along the western U.S. coast. *J. Geophys. Res. Atmos.* **2012**, *117*, D18114.
38. Yoshimura, K.; Kanamitsu, M.; Noone, D.; Oki, T. Historical isotope simulation using Reanalysis atmospheric data. *J. Geophys. Res. Atmos.* **2008**, *113*, D19108.
39. Reynolds, R.W.; Smith, T.M. Improved global sea-surface temperature analyses using optimum interpolation. *J. Climate* **1994**, *7*, 929–948.
40. Kalnay, E.; Kanamitsu, M.; Kistler, R.; Collins, W.; Deaven, D.; Gandin, L.; Iredell, M.; Saha, S.; White, G.; Woollen, J.; *et al.* The NCEP/NCAR 40-year reanalysis project. *Bull. Amer. Meteorol. Soc.* **1996**, *77*, 437–471.
41. Yoshimura, K.; Kanamitsu, M. Dynamical global downscaling of global reanalysis. *Mon. Weather Rev.* **2008**, *136*, 2983–2998.
42. Majoube, M. Fractionation in O-18 between ice and water vapor. *J. Chim. Phys. Phys. Chim. Biol.* **1971**, *68*, 625–636.
43. Majoube, M. Oxygen-18 and deuterium fractionation between water and steam. *J. Chim. Phys. Phys. Chim. Biol.* **1971**, *68*, 1423–1436.
44. Merlivat, L.; Jouzel, J. Global climatic interpretation of the deuterium-oxygen-18 relationship for precipitation. *J. Geophys. Res.* **1979**, *84*, 5029–5033.
45. Jouzel, J.; Merlivat, L. Deuterium and oxygen 18 in precipitation: Modeling of the isotopic effects during snow formation. *J. Geophys. Res.* **1984**, *89*, 11749–11757.
46. Stewart, M.K. Stable isotope fractionation due to evaporation and isotopic-exchange of falling waterdrops—Applications to atmospheric processes and evaporation of lakes. *J. Geophys. Res.* **1975**, *80*, 1133–1146.
47. Bony, S.; Risi, C.; Vimeux, F. Influence of convective processes on the isotopic composition ($\delta^{18}O$ and δD) of precipitation and water vapor in the tropics: 1. Radiative-convective equilibrium and Tropical Ocean-Global Atmosphere-Coupled Ocean-Atmosphere Response Experiment (TOGA-COARE) simulations. *J. Geophys. Res. Atmos.* **2008**, *113*, D19305.
48. Wright, J.S.; Sobel, A.H.; Schmidt, G.A. Influence of condensate evaporation on water vapor and its stable isotopes in a GCM. *Geophys. Res. Lett.* **2009**, *36*, L12804.
49. Feng, X.H.; Reddington, A.L.; Faiia, A.M.; Posmentier, E.S.; Shu, Y.; Xu, X.M. The Changes in North American atmospheric circulation patterns indicated by wood cellulose. *Geology* **2007**, *35*, 163–166.
50. Zhu, M.F.; Stott, L.; Buckley, B.; Yoshimura, K. 20th century seasonal moisture balance in Southeast Asian montane forests from tree cellulose $\delta^{18}O$. *Climatic Change* **2012**, *115*, 505–517.
51. Zhu, M.F.; Stott, L.; Buckley, B.; Yoshimura, K.; Ra, K. Indo-Pacific Warm Pool convection and ENSO since 1867 derived from Cambodian pine tree cellulose oxygen isotopes. *J. Geophys. Res. Atmos.* **2012**, *117*, D11307
52. Roden, J.S.; Lin, G.G.; Ehleringer, J.R. A mechanistic model for interpretation of hydrogen and oxygen isotope ratios in tree-ring cellulose. *Geochim. Cosmochim. Acta* **2000**, *64*, 21–35.

53. Kanner, L.; Buenning, N.H.; Stott, L.; Stahle, D. Climatologic and hydrologic influences on the oxygen isotope ratio of tree cellulose in coastal southern California during the late 20th century. *Geochem. Geophys. Geosy.* **2013**, Submitted for publiation.
54. Risi, C.; Noone, D.; Worden, J.; Frankenberg, C.; Stiller, G.; Kiefer, M.; Funke, B.; Walker, K.; Bernath, P.; Schneider, M.; *et al.* Process-evaluation of tropospheric humidity simulated by general circulation models using water vapor isotopologues: 1. Comparison between models and observations. *J. Geophys. Res. Atmos.* **2012**, *117*, D05303.
55. Ehhalt, D.H.; Rohrer, F.; Fried, A. Vertical profiles of HDO/H_2O in the troposphere. *J. Geophys. Res. Atmos.* **2005**, *110*, D13301.
56. Sayres, D.S.; Pfister, L.; Hanisco, T.F.; Moyer, E.J.; Smith, J.B.; St Clair, J.M.; O'Brien, A.S.; Witinski, M.F.; Legg, M.; Anderson, J.G. Influence of convection on the water isotopic composition of the tropical tropopause layer and tropical stratosphere. *J. Geophys. Res. Atmos.* **2010**, *115*, D00J20.
57. Vachon, R.W.; White, J.W.C.; Gutmann, E.; Welker, J.M. Amount-weighted annual isotopic $\delta^{18}O$ values are affected by the seasonality of precipitation: A sensitivity study. *Geophys. Res. Lett.* **2007**, *34*, L21707.
58. Field, R.D.; Moore, G.W.K.; Holdsworth, G.; Schmidt, G.A. A GCM-based analysis of circulation controls on $\delta^{18}O$ in the southwest Yukon, Canada: Implications for climate reconstructions in the region. *Geophys. Res. Lett.* **2010**, *37*, L05706.
59. Romero, I.C.; Feakins, S.J. Spatial gradients in plant leaf wax D/H across a coastal salt marsh in southern California. *Org. Geochem.* **2011**, *42*, 618–629.
60. Helliker, B.R. On the controls of leaf-water oxygen isotope ratios in the atmospheric crassulacean acid metabolism epiphyte tillandsia usneoides. *Plant Physiol.* **2011**, *155*, 2096–2107.
61. Yin, J.H. A consistent poleward shift of the storm tracks in simulations of 21st century climate. *Geophys. Res. Lett.* **2005**, *32*, L18701.
62. Salathe, E.P. Influences of a shift in North Pacific storm tracks on western North American precipitation under global warming. *Geophys. Res. Lett.* **2006**, *33*, L19820.
63. Worden, J.; Bowman, K.; Noone, D.; Beer, R.; Clough, S.; Eldering, A.; Fisher, B.; Goldman, A.; Gunson, M.; Herman, R.; *et al.* Tropospheric emission spectrometer observations of the tropospheric HDO/H2O ratio: Estimation approach and characterization. *J. Geophys. Res. Atmos.* **2006**, *111*, D16309.
64. Worden, J.; Noone, D.; Bowman, K.; Spect, T.E. Importance of rain evaporation and continental convection in the tropical water cycle. *Nature* **2007**, *445*, 528–532.
65. Frankenberg, C.; Yoshimura, K.; Warneke, T.; Aben, I.; Butz, A.; Deutscher, N.; Griffith, D.; Hase, F.; Notholt, J.; Schneider, M.; *et al.* Dynamic processes governing lower-tropospheric HDO/H2O ratios as observed from space and ground. *Science* **2009**, *325*, 1374–1377.
66. Wunch, D.; Toon, G.C.; Wennberg, P.O.; Wofsy, S.C.; Stephens, B.B.; Fischer, M.L.; Uchino, O.; Abshire, J.B.; Bernath, P.; Biraud, S.C.; *et al.* Calibration of the total carbon column observing network using aircraft profile data. *Atmos. Meas. Tech.* **2010**, *3*, 1351–1362.

Effect of Hydrograph Separation on Suspended Sediment Concentration Predictions in a Forested Headwater with Thick Soil and Weathered Gneiss Layers

Naoki Kabeya, Akira Shimizu, Jian-Jun Zhang and Tatsuhiko Nobuhiro

Abstract: Two-component hydrograph separation using oxygen-18 concentrations was conducted at a sediment runoff observation weir installed in a small subcatchment of a forested gneiss catchment in Japan. The mean soil thickness of this catchment is 7.27 m, which comprises 3.29 m of brown forest soil (A and B layers) and a 3.98-m layer of heavily weathered gneiss. Data were collected for a storm on 20–21 May 2003, and the percentage of event water separated by the stable isotope ratio in comparison with the total rainfall amount was about 1%. This value is within the ratio of a riparian zone in a drainage area. Temporal variation of suspended sediment concentration exhibited higher correlation with the event water component than with the total runoff or pre-event water component. This shows that the riparian zone causes rainwater to flow out quickly during a rain event, and that this is an important area of sediment production and transportation in a forested headwater with thick soil and weathered gneiss layers.

Reprinted from *Water*. Cite as: Kabeya, N.; Shimizu, A.; Zhang, J.-J.; Nobuhiro, T. Effect of Hydrograph Separation on Suspended Sediment Concentration Predictions in a Forested Headwater with Thick Soil and Weathered Gneiss Layers. *Water* **2014**, *6*, 1671-1684.

1. Introduction

Soil sediment discharge from a forested catchment has been studied for over 60 years [1–3]. These studies have shown that soil sediment discharge is related to drainage area, rainfall intensity, and vegetation type and density. Recently, the relationship between suspended sediment (SS) concentration and runoff amount has been observed in small, forested catchments in various parts of the world [4–7].

In Japan, attention to research on runoff and SS concentration from forested catchments has increased remarkably following the Great East Japan Earthquake on 11 March 2011. Radioactive material, such as Cs, was released because of the accident at the Fukushima Daiichi nuclear power plant. Although forest ecosystems are thought to exhibit a tendency to retain radioactive Cs, there is concern that radioactive Cs might flow out from forest ecosystems in steep areas when subject to considerable rainfall—environments and weather conditions that are common in Japan [8]. Shinomiya *et al.* [8] observed that radioactive Cs in a small, forested catchment in Fukushima Prefecture mainly flowed out as suspended matter.

Over the past several decades, research into the rainfall-runoff process for small catchments has been progressed via the use of tracer information [9–12]. A small, forested headwater is the beginning of a river and serves as the minimum unit of the water budget and nutrient cycles in a forest ecosystem [13]. Moreover, as the objective area is relatively small, detailed observations of geographical features and of the situation generating storm runoff, both in and around a stream

channel, are also possible. However, few reports of work exist in which the variations of component separation by stable isotope ratio and SS concentration have been observed simultaneously by such research.

Measurement of water and sediment discharge from a headwater catchment is the most elementary study for soil and water conservation. Williams [14] suggested that there is hysteresis between SS concentration and runoff from a catchment. This hysteresis has been an obstacle when the temporal variations of SS concentration and discharge have been modeled simultaneously, and much research relevant to this topic has been performed [15,16]. To improve the predictive accuracy of models forecasting SS runoff from a catchment, it is thought necessary to promote the understanding of both the streamflow mechanism and the SS transport process within a catchment.

Research clarifying the streamflow mechanism from a catchment using a stable isotope tracer is progressing steadily. For example, by measuring the stable isotope ratio, runoff water and event rainwater can be separated into two components: pre-event water and event water [17–19]. Many reports describe the simultaneous observations of dissolved ion concentration and stable isotope ratio in runoff water [20,21]; however, only a few studies report simultaneous observations of SS concentration and stable isotope ratio in runoff water.

This research simultaneously observed the temporal change of the stable isotope ratio of stream water and SS concentration during storm runoff in a small, forested catchment. By performing hydrograph separation using a stable isotope tracer, the relation between each component of runoff and SS concentration was investigated. The runoff mechanism and the SS transport process were considered by comparing these results with information relating to geographical features, especially the riparian zone. The riparian zone refers to the area relating to the stream bank, and the function of this zone has been studied recently with respect to both ecological and hydrological aspects [22]. In this research, a riparian zone is defined as the area that is constantly in a state of wet condition around a spring point and a stream channel between stream banks. Strictly, the spring point and stream channel are not classified as the riparian zone, but such areas are relatively small and thus, they are also included within the definition in this paper. On the other hand, the field of hillslope hydrology provides a related technical term, “source area”. This is defined by the “variable source area concept” of Kirkby [23], and it means an area within a catchment that contributes to storm runoff. This paper also follows this definition.

Research is progressing with regard to the function of the riparian zone as a site for the generation of soil and water movement. The results of this research could be expected to be useful in clarifying the function of water and soil movement in a riparian zone of a small, headwater catchment with thick soil and weathered gneiss layers.

2. Experimental

2.1. Study Area

The research was conducted in the Tsukuba Experimental Watershed (TEW), located in southern Ibaraki Prefecture, Japan (36°20' N, 140°18' E; Figure 1). In 1978, this watershed was established as an experimental study site for investigations of hydrological processes in a forested mountainous

area [24]. The watershed drains 3.79 ha. The main slope direction is to the north and the mean slope is 25°. In the 10-year period from 1972 to 1981, the average annual air temperature was 14.1 °C at Kakioka, which is the nearest weather station (36°14' N, 140°12' E; altitude 27.7 m). The annual rainfall and discharge from 1979 to 1990 (excluding 1988 when data were lacking) were 1429.1 and 641.6 mm, respectively. Although the TEW experiences several snowfalls per year, snow depths greater than 20 cm are rare and most precipitation is rainfall. Geologically, the watershed is composed mainly of biotite gneiss overlain by weathered volcanic ash; the soil in this area is brown forest soil, or Cambisol in the FAO classification [25]. Plantations of *Cryptomeria japonica* (common name "sugi" or Japanese cedar) and *Chamaecyparis obtusa* ("hinoki" or Japanese cypress) are the main types of vegetation. *Pleioblastus chino*, a type of bamboo grass, and *Aucuba japonica*, an evergreen shrub, both grow on the forest floor. The mean soil thickness is 7.27 m, which comprises 3.29 m of brown forest soil (A and B layers) and a 3.98 m layer of heavily weathered gneiss [26,27].

The stream channel in the TEW originates from three springs (Figure 1) and is one of the headwaters of the Koise River that flows into Lake Kasumigaura as part of the Tone River system. To observe the discharge from the three spring subcatchments, 60° V-notch flow-gauging weirs are operated at the three springs (referred to as A, B, and C). The drainage areas of subcatchments A, B, and C are 0.60, 0.93, and 0.36 ha, respectively. The discharge amount from the entire TEW is observed by a 45° V-notch flow-gauging weir at point O (Figure 1). Based on the results of a drilling investigation, an impermeable wall structure was constructed through the subsurface at point O and attached to the base rock (6.0 m depth); the weir was then built to measure the amount of watershed outflow [24]. In contrast, the impermeable walls of weirs A, B, and C are only 1.2 m deep and are not attached to the rock. In addition to these weirs, a temporary flow-gauging weir was placed at point S in the TEW to observe flow and to investigate sediment production in the forested catchment; observations were conducted at this weir for about two years from May 2003, to May 2005. The S subcatchment drains an area of 2.97 ha. Zhang *et al.* [28] reported that for the S subcatchment, the discharge amount of SS was determined mainly by the maximum 10-minute precipitation. Each rainfall event also greatly contributed to SS discharge. The SS discharge from one storm accounted for about 5% of the total annual sediment discharge and that from a few storms contributed about 30% of the yearly SS discharge. In addition, the observation of annual sediment discharge and the application of a 5-m meshed distributed type sediment discharge model have been conducted within this catchment [29]. Shimizu *et al.* [29] showed that the annual sediment discharge of the S subcatchment was 0.372 t/year. They applied the distributed type sediment yield model to this catchment and concluded that the area of high sediment production was restricted to the riparian zone near the stream channel in the catchment.

Figure 1. Topography and observation points in the Tsukuba Experimental Watershed.

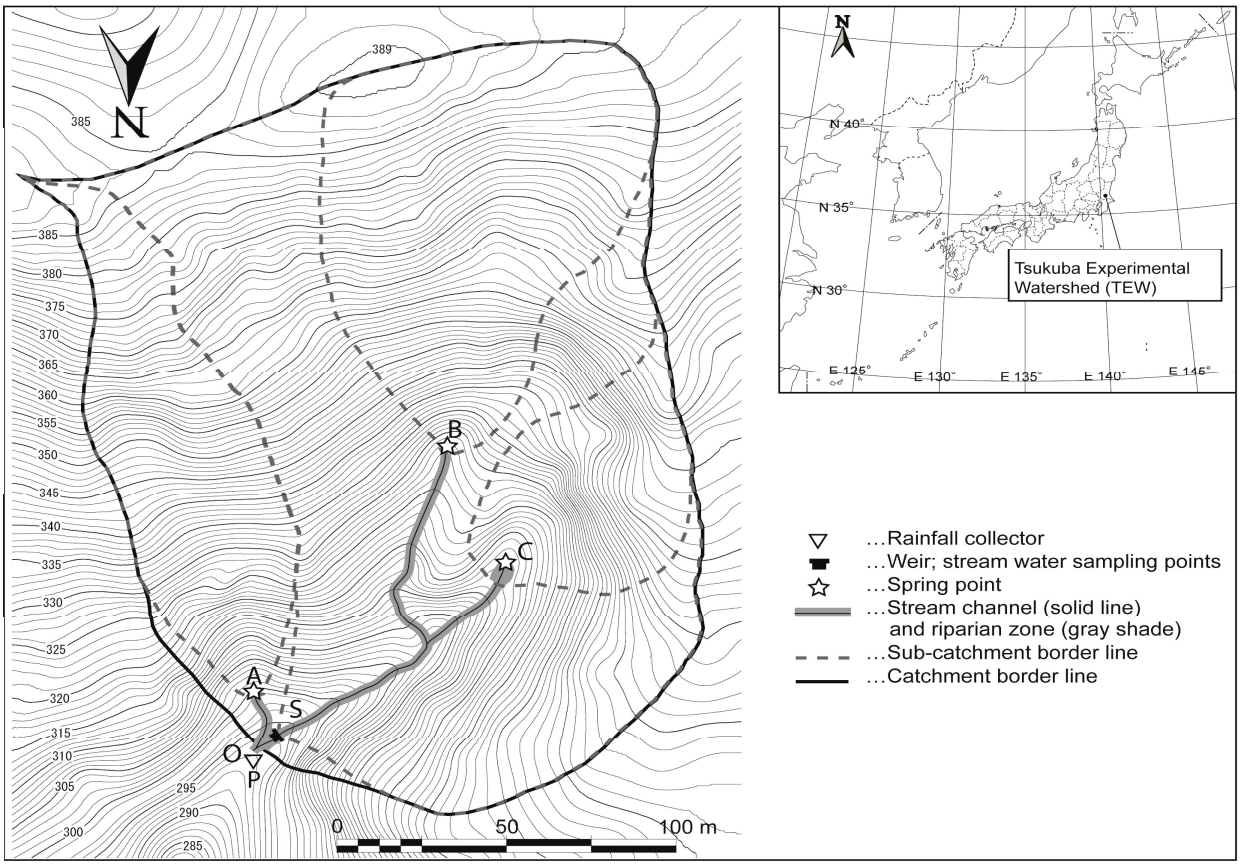

At spring points A and B, the flat valley bottoms are very narrow (only 0.5 m^2), whereas the valley bottom at spring C is 31.2 m^2. The S and O watersheds contain parts of the stream channel (Figure 1), and the area of the riparian zone of the S subcatchment was calculated by detailed survey as 492.0 m^2. This included the riparian area along the stream channel (stream length (153.4 m) × riparian width (3.0 m) = 460.3 m^2) and the total flat valley bottom area (flat valley bottom of B catchment (0.5 m^2) + flat valley bottom of C catchment (31.2 m^2) = 31.7 m^2) of the wet zones of the B and C catchments. Therefore, the percentage of the drainage area occupied by the riparian zone in the S subcatchment is 1.7%. This riparian zone is including stream channel. In this study, the SS and stable isotope of the runoff were assessed at the V-notch in the S subcatchment of the Tsukuba Experimental Watershed (Figure 1). Precipitation was observed by a tipping bucket rain gauge (1 tip = 0.1 mm; Ikeda Keiki Co., Tokyo, Japan) installed on the roof of the catchment gauging station at O (Figure 1). In addition, because event water sampling was performed every hour from 17:15 on 17 May 2003, the precipitation and runoff data were also arranged as hourly values at corresponding times, *i.e.*, commencing at 15 min past the hour.

2.2. Storm Runoff Observation and SS Concentration Analysis

The collection of stream water was performed using automatic water sampling equipment (model 6700; Teledyne Isco, Lincoln, NE, USA), and the SS concentration and stable isotope ratios of the sampling water were analyzed in the laboratory. Water sampling was set up to obtain samples every

hour when the rainfall intensity was 1.5 mm/h or more. Thus, the rain event from 20 to 21 May 2003, was applicable to this research. This 19 h rainfall event produced 52.1 mm of total rainfall with a peak hourly intensity of 24.6 mm/h (Table 1).

Table 1. Characteristics of the observed rainfall event.

Rainfall characteristic	Amount or Time
Total rainfall amount (Σ P) (mm)	52.1
Start time of the rainfall event	16:15 on 20 May 2003
End time of the rainfall event	11:15 on 21 May 2003
Duration of rainfall (hours)	19
A maximum 1-hour rainfall intensity (mm)	24.6
The time of a maximum 1hour rainfall intensity	18:15 on 20 May 2003

After passing a water sample through a 106-μm-mesh sieve at the laboratory, 20 cc were isolated in an airtight, screw-top vial for the stable isotope analysis. Next, it was filtered using the suction filtration machine equipped with glass filter paper, which was weighed after drying at 105 °C for 3 h. The GF/F filter (d = 0.47 μm; Whatman, UK) was used for suction filtration. After filtration, the glass filter paper was placed in the drier and dried at 80 °C for 48 h, and then weighed with an electronic balance. The difference in weight before and after drying at 80 °C serves as a measurement of the amount of SS contained in the sample.

Rainwater was gathered in a 20 L plastic bottle, which was attached to a 21 cm-diameter funnel installed on the roof of the water level gauging house at O (Figure 1). To prevent the evaporation of rainwater saved in the bottle and causing a change in the stable isotope ratio, silicone oil was added to the bottle at the time of commencement of sampling, which made a film on the water's surface. Subsequently, the bottle was returned to the laboratory and the oil was removed using a separation funnel. The rainwater obtained in this way was saved in airtight 20 cc screw-top glass vials.

2.3. Stable Isotope Analysis

A mass spectrometer (MAT252; Thermo Scientific, Waltham, MA, USA) was used for the oxygen stable isotope analysis of the water samples. The CO_2–H_2O equilibrium method was used to measure the hydrogen and oxygen stable isotope ratios. The isotope ratio was expressed as the δ value with respect to that of the Vienna Standard Mean Ocean Water (V-SMOW), which is given as:

$$\delta^{18}O_{sa} = \left(\frac{(^{18}O/^{16}O)_{sa}}{(^{18}O/^{16}O)_{re}} - 1 \right) \times 1000\,‰\ \text{V - SMOW} \quad (1)$$

where *sa* and *re* refer to the sample and standard reference, respectively. V-SMOW is a standard reference material for measuring stable isotope ratios in water. The standard uncertainties of the $\delta^{18}O$ measurements were ±0.02%.

2.4. Storm Runoff Hydrograph Separation Using Tracer Information

The runoff component of the stream water is divided into the "event water" (event rainwater) newly added to the catchment in connection with the rain, and the "pre-event water" (precedent moisture) already stored in the catchment before the onset of the rain. The contribution of each runoff component to the rate of total runoff can be calculated using the hydrograph separation method with a tracer. If it is assumed that a chemical reaction does not arise between the event and pre-event waters during the observation time, then the following two equations can be formed for an observed section of a catchment [9]:

$$Q_t = Q_{evt} + Q_{pre} \quad (2)$$

$$C_t\, Q_t = C_{evt}\, Q_{evt} + C_{pre}\, Q_{pre} \quad (3)$$

Here, Q is the discharge; C is the tracer concentration; and subscripts t, evt, and pre express the total runoff, event water, and pre-event water, respectively. The contribution of the pre-event water to the total runoff, derived from Equations (2) and (3), is given by the following Equation:

$$Q_{pre} = [(C_t - C_{evt})/(C_{pre} - C_{evt})]\, Q_t \quad (4)$$

In Equation (4), Q_{evt} and Q_{pre} are unknowns, whereas Q_t could be surveyed as a streamflow rate and used as the observed runoff from the S subcatchment.

3. Results and Discussion

3.1. Hydrograph Separation by Stable Isotope Ratio

The timing of peak runoff was coincident with the peak of precipitation. Moreover, the peak of SS concentration was also coincident with the peaks of precipitation and runoff (Figure 2). These findings were similar to previous researches conducted within this catchment [28,29].

The $\delta^{18}O$ value of the stream water immediately after the start of the event (17:15 on 20 May 2003) was −7.94%. Two weeks after the end of the rain event, the streamflow had returned to the baseflow state. The $\delta^{18}O$ value of the stream water sampled in the baseflow state was the same as that of the stream water at the onset of the rainfall event. Therefore, the $\delta^{18}O$ value of the pre-event water was assumed fixed at −7.94% during the rainfall event.

Thus, the $\delta^{18}O$ value of the pre-event water (C_{pre}) during the event period was set as −7.94%. The measured value of the isotopic ratio of the rain during the event period was −10.45%. This value was set as the $\delta^{18}O$ value of the event water (C_{evt}). By setting the $\delta^{18}O$ value of the hourly sampled stream water to C_t, Equation (3) was used and the runoff at each interval was separated into two components: event water and pre-event water. Thus, when precipitation and runoff simultaneously reached their peaks, the contribution rate of the event water was the highest, which was determined as 60% (Figure 2). The temporal variation of the event water component exhibited a similar pattern to that of SS concentration. The peak of the pre-event water component was 1 h after the peak of the event water component and SS concentration.

Figure 2. Temporal variations in rainfall, runoff, suspended sediment (SS) concentration, and oxygen-18 concentration, and the result of hydrograph separation using oxygen-18 concentration.

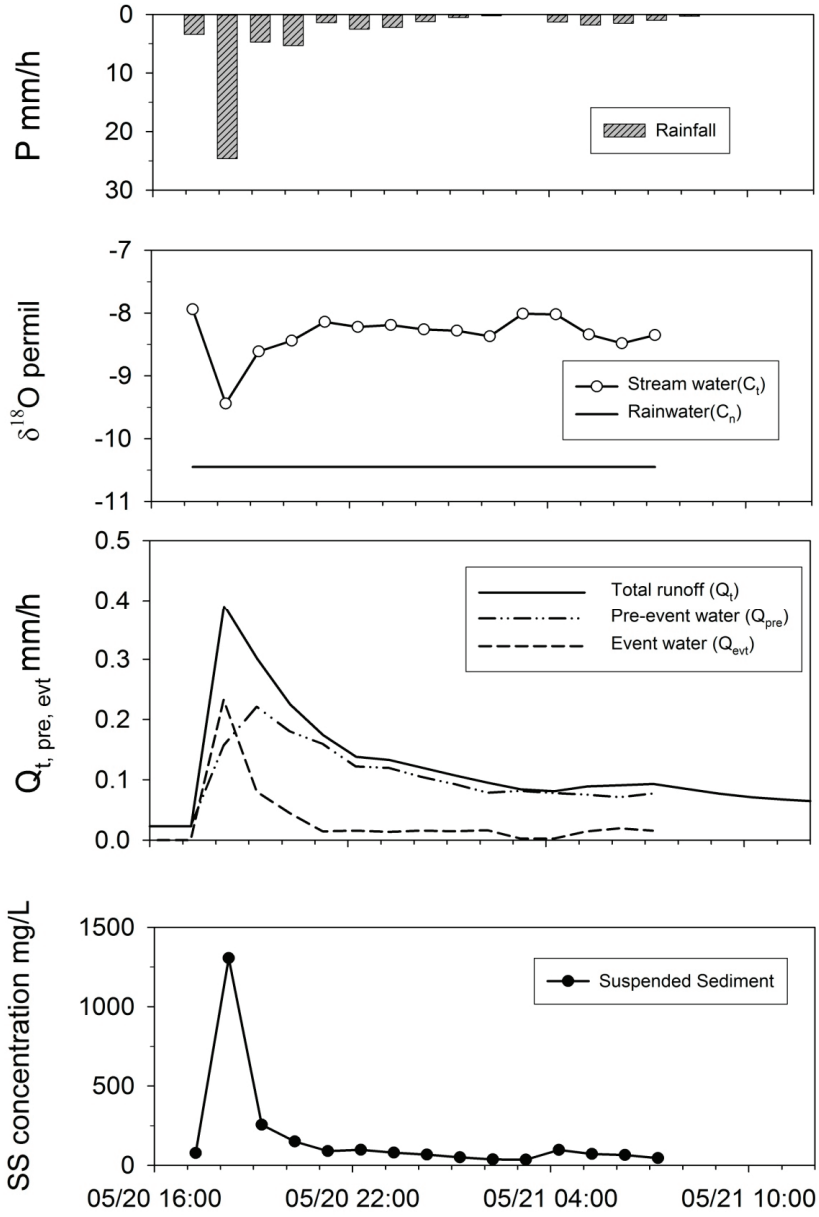

The result of hydrograph separation using the stable isotope tracer is shown in Table 2. The ratio of the runoff component of event water to the total rainfall is 1.0%. This is within the value of 1.7% for the ratio of the riparian zone to the drainage area, based on a survey result of the S subcatchment when the riparian zone width was 3.0 m.

Table 2. Storm runoff amounts separated by stable isotope tracer information.

Runoff component	Symbol	Runoff Amount (mm)	Percentage (%)
Total runoff amount	ΣQ_t	2.17	
The pre-event component water	ΣQ_{pre}	1.66	
The event component water	ΣQ_{evt}	0.50	
The ratio of pre-event component water to total runoff amount	$\Sigma Q_{pre}/\Sigma Q_t$		77
The ratio of event component water to total runoff amount	$\Sigma Q_{evt}/\Sigma Q_t$		23
The ratio of total runoff amount to total rainfall amount	$\Sigma Q_t/\Sigma P$		4.2
The ratio of pre-event component water to total rainfall amount	$\Sigma Q_{pre}/\Sigma P$		3.2
The ratio of event component water to total rainfall amount	$\Sigma Q_{evt}/\Sigma P$		1.0

The stream and hillslope conditions were checked several times during rainfall events, and no overland runoff on the hillslope was observed; *i.e.*, the streamflow was flowing only within the stream channel.

The ratio of event water to total runoff was 23%, and that of pre-event water to total runoff was 77%. The generation of most of the event component of the water was restricted to a few hours with strong intensity rainfall. Most of the recession period of the hydrograph comprised the pre-event component of the water.

3.2. Runoff Generation Mechanism

In the TEW, as in other forested catchments, the infiltration capacity of the soil surface was high and Horton overland flow was not observed during the rainfall events. However, the topographical features and soil structure of this catchment are quite different from other catchments. In this catchment, the watershed has a thick covering of a highly permeable soil layer and a weathered gneiss layer. However, the valleys around the spring points are steep and narrow, and groundwater exists in the weathered gneiss layer rather than the soil. For these reasons, changes of the groundwater level in the source area are small, and a riparian zone can be considered almost the same as the source area. This differs from other forested catchments where the source area expands more significantly than the usual riparian zone, for example, where the saturated throughflow dominates runoff generation in weathered granite catchments [30,31] or in normal vegetated catchments [32]. The spring water is provided by groundwater flow through the weathered gneiss layer [33]. In subcatchments A and B that almost do not have a riparian zone, the runoff hardly increased for small-scale rainfall events of 20 mm or less, and the runoff showed a slow response for large-scale rain events of 100 mm or more [27]. The hydrographs of subcatchments A and B are similar to the upper weir at CB1 of Figure 4, in Anderson *et al.* [34], which represents a steep unchanneled catchment with thick weathered layers. On the other hand, subcatchments C and S and the entire catchment at O, which have riparian zone, respond quickly to small-scale rainfall events in the catchment [27]. When a large-scale rainfall event occurred, the quantity of the baseflow of all subcatchments and the entire catchment rose significantly and the baseflow took seven months to come back to pre-storm conditions after a large event [27].

This implies that the quick runoff component is related to the size of the riparian zone within a catchment and the slow runoff component is related to the groundwater flow through the weathered gneiss layer.

The total rainfall during this study was 52.1 mm, which is a mid-scale rain event for this catchment. However, almost half of the total rain fell during a 1 h period of peak rainfall. In the hydrograph separation of the S subcatchment, the runoff peak comprised 60% event water. The runoff of event water occurred only at the time when rainfall was strong. In this catchment with soils that are deeply weathered and have generally high infiltration capacities, surface runoff is restricted mainly to the stream channels, so the storm runoff production must be controlled by subsurface response. Based on this, it is considered that the runoff component of event water comprised subsurface stormflow from the riparian zone. Although the source area in a riparian zone is changed for every rainfall event, it is probably decided by intensity of rainfall and antecedent moisture conditions.

On the other hand, the peak runoff component of pre-event water was 1 h later than the peak of the event water. Moreover, pre-event water comprised a greater proportion of runoff water at the time of recession, when the rainfall intensity had weakened. Thus, the runoff component of pre-event water is mainly formed by groundwater flow.

3.3. Runoff Component and SS Concentration

The SS concentration at each interval was compared with the relation between the total runoff (Q_t), runoff (Q_{pre}) of a pre-event water component, and runoff (Q_{evt}) of an event water component, and the regression line between each runoff component and the SS concentration was calculated (Figure 3). The coefficient of determination of the regression line to the SS concentration of Q_t was $R^2 = 0.6508$, the coefficient of determination of the regression line to the SS concentration of Q_{evt} was $R^2 = 0.9574$, and the coefficient of determination of the regression line to the SS concentration of Q_{pre} was $R^2 = 0.1496$. Thus, the highest correlation is seen between SS concentration and the runoff of an event water component. From this, the subsurface stormflow component generated with event rainwater can be said to play an important role in SS concentration formation during the peak hour. The width in a stream channel in this catchment was an average of 0.30 m, and this was not expanded too much even at the time of a heavy rain. Stream bed material was covered with many stones and soil sediment was stored between the stones. In a heavy rainfall intensity, subsurface stormflow is generated in the riparian zone, and it flows into the stream channel. As a result, soil sediment in the stream channel is transported by tractive forces of streamflow.

The event water component is constituted by the subsurface stormflow that occurs in a riparian zone. At this catchment, the temporal variation of SS concentration depended on the intensity of rainfall over a short unit of time (10 min) [28], and soil sediment production is only active in the riparian zone [29].

Thus, the source areas of water runoff and sediment production overlapped in the riparian zone of this catchment, which is why it is thought that the correlation of temporal variation of subsurface stormflow and SS concentration increased.

Figure 3. Relationship between suspended sediment (SS) concentration and total runoff (Q_t), runoff of pre-event water component (Q_{pre}), and runoff of event water component (Q_{evt}).

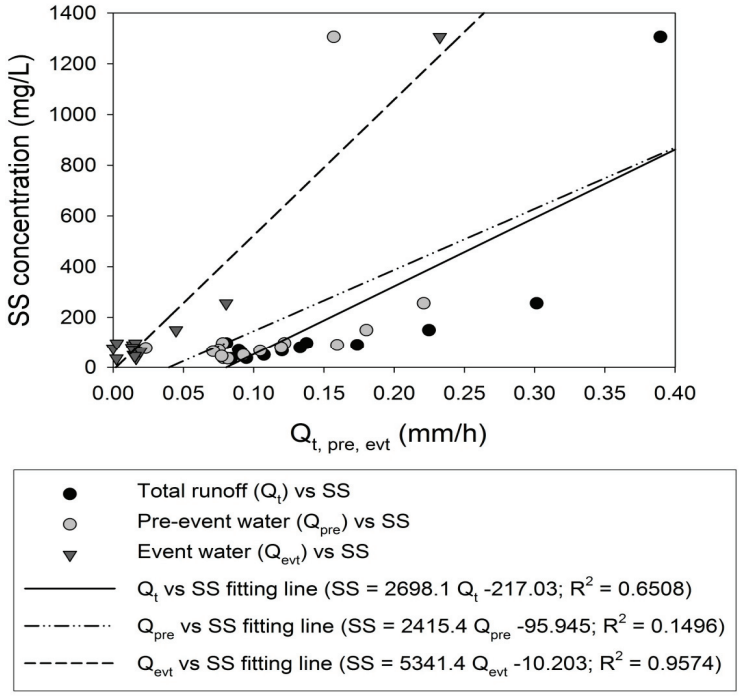

Lenzi and Marchi [35] investigated the relation between runoff and SS concentration in extremely steep mountainous catchments (mean slope: 52°) of the Dolomites in the Italian Alps. Vegetation cover consisted mainly of herbaceous associations and 14% of the catchment comprised bare land. They reported that the relation varied, but found a case where the SS concentration peak appeared after a runoff peak. Following a particle size analysis, they also reported that the origin of SS was not the stream channel, but the erosion of a slope. Based on their findings and the results of this research, it can be suggested that the difference in the spatial origin of SS within the catchment determines the relation between runoff and SS.

4. Conclusions

This research simultaneously observed the temporal change of the stable isotope ratio of stream water and SS concentration during storm runoff in a small, forested catchment with thick soil and weathered gneiss layers. By performing hydrograph separation using a stable isotope tracer, the relation between each component of runoff and SS concentration was investigated. The runoff and SS concentration during a storm event were shown to peak simultaneously with the maximum intensity of rainfall, which is similar to the findings of previous researches conducted within this catchment [28,29]. The percentage of event water to the total rainfall amount, separated by the stable isotope ratio, was about 1%. This value is within the ratio of a riparian zone within a drainage area. It is considered that the runoff component of event water comprised subsurface stormflow from the riparian zone. Although the source area in a riparian zone is changed for every rainfall event, it is probably decided by intensity of rainfall and antecedent moisture conditions. In a heavy rainfall intensity, subsurface stormflow is generated in the riparian zone, and it flows into the stream channel.

And soil sediment in the stream channel is transported by tractive forces of streamflow. These results suggest that the riparian zone causes rainwater to flow out quickly during a rain event in a forested headwater and that it is an important area for sediment production and transportation.

Temporal variation of SS concentration exhibited higher correlation with the event water component than with total runoff or the pre-event water component. SS discharge correlates well with event-based runoff, and the runoff mechanisms responsible for bringing event-based water to the stream channel during storm events are also likely responsible for increasing the sediment load of the stream channel, thus the runoff mechanism and sources are a critical component to sediment budgets in headwaters.The SS discharge process, based on the runoff mechanism determined by tracer information, was examined and it was established as effective to have used the event water extracted by the stable isotope tracer as a factor of direct SS concentration formation. To reduce the hysteresis between SS concentration and runoff, it was effective to extract the event water component, as a direct driving force for transporting SS, using stable isotope tracer information.

The source areas of water runoff and sediment production overlapped in the riparian zone of this catchment. Such a feature originates in the geographical features and soil structure of this catchment. Thus, in such a case, it is especially important for sediment management to preserve the riparian zone.

Acknowledgments

We thank Tatsurou Kanazashi, Takashi Yoshitake, Masayuki Sugiyama, and the staff of the Forest Site Section in the Forestry and Forest Products Research Institute for their help in the field. We also thank Koji Tamai, the chief of the Forest Hydrology Laboratory in the Forestry and Forest Research Institute for introducing a suitable cited reference. Part of this work was financially supported by the Ministry of Agriculture, Forestry and Fisheries, Japan, through a research project entitled “Development of technologies for mitigation and adaptation to climate change in Agriculture, Forestry and Fisheries (A-8)”. A part of this work was done at the Lancaster University under the OECD Co-operative Research Program fellowship 2012. We wish to thank Nick A Chappell and Wlodek Tych at the Lancaster Environmental Centre of Lancaster University provided us valuable suggestions.

Author Contributions

The study was design and conceived by Naoki Kabeya and Akira Shimizu. Fieldwork was carried out in the Tsukuba Experimental Watershed by Naoki Kabeya, Jian-Jun Zhang and Tastuhiko Nobuhiro under the supervision of Akira Shimizu. Stable isotope analysis was carried out by Naoki Kabeya with the mass spectrometer of Forestry and Forest Products Research Institute. Hydrological analysis was carried out by Tatsuhiko Nobuhiro and Naoki Kabeya under the supervision of Akira Shimizu. Sediment analysis was carried out by Jian-Jun Zhang and Tatsuhiko Nobuhiro under the supervision of Akira Shimizu. The manuscript was largely written by Naoki Kabeya and Akira Shimizu but all authors contributed to the writing and review of the manuscript.

Conflicts of Interest

The authors declare no conflict of interest.

References

1. Anderson, H.W.; Trobitz, H.K. Influence of some watershed variables on a major flood. *J. For.* **1949**, *47*, 347–356.
2. Kawaguchi, T. Suggestion to the elucidation method of influence exerted on the sediment discharge of a forest. *For. Technol.* **1952**, *124*, 9–13. (In Japanese)
3. Namba, S.; Kawaguchi, T. Influences of some factors upon soil losses from large mountainous watersheds. *Bull. For. For. Prod. Res. Inst.* **1965**, *173*, 93–166 (In Japanese).
4. Kim, H.; Marutani, T.; Miyazaki, T. Volumetric changes in suspended sediment load and bed load from mountainous catchments. *J. Jpn. Soc. Eros. Control. Eng.* **2003**, *55*, 21–23. (In Japanese)
5. Chappell, N.A.; Douglas, I.; Hanapi, J.M.; Tych, W. Sources of suspended sediment within a tropical catchment recovering from selective logging. *Hydrol. Process.* **2004**, *18*, 685–701.
6. Fukuyama, T.; Onda, Y.; Gomi, T.; Yamamoto, K.; Kondo, N.; Miyata, S; Kosugi, K.; Mizugaki, S.; Tsubonuma, N. Quantifying the impact of forest management practice on the runoff of the surface-derived suspended sediment using fallout radionuclides. *Hydrol. Process.* **2010**, *24*, 596–607.
7. Wanga, J.; Edwards, P.J.; Wood, F. Turbidity and suspended-sediment changes from stream-crossing construction on a forest haul road in West Virginia, USA. *Int. J. For. Eng.* **2013**, *24*, 76–90.
8. Shinomiya, Y.; Tamai, K.; Kobayashi, M.; Ohnuki, Y.; Shimizu, T.; Iida, S.; Nobuhiro, T.; Sawano, S.; Tsuboyama, Y.; Hiruta, Y. The behavior of radioactive materials in stream water from a forested watershed. *Kanto J. For. Res.* **2013**, *64*, 53–55. (In Japanese)
9. Pearce, A.J.; Stewart, M.K.; Sklash, M.G. Storm runoff generation in humid headwater catchments; 1. Where does the water come from? *Water Resour. Res.* **1986**, *22*, 1263–1272.
10. Kendall, C.; McDonnell, J.J. *Isotope Tracers in Catchment Hydrology*; Elsevier Science: Amsterdam, The Netherlands, 1998; p. 839.
11. Soulsby, C.; Malcolm, R.; Helliwell, R.; Ferrier, R.C.; Jenlins, A. Isotope hydrology of the Allt a' Mharcaidh catchment, Cairngorms, Scotland: Implications for hydrological pathways and residence times. *Hydrol. Process.* **2000**, *14*, 747–762.
12. Soulsby, C.; Perty, J.; Brewer, M.J.; Dunn, S.M.; Ott, B.; Malcom, I.A. Identifying and assessing uncertainty in hydrological pathway: A novel approach to end member mixing in a Scottish agricultural catchment. *J. Hydrol.* **2003**, *274*, 109–128.
13. Likens, G.E. *Biogeochemistry of a Forested Ecosystem*, 3rd ed.; Springer-Verlag: New York, NY, USA, 2013; p. 208.
14. Williams, G.P. Sediment concentration *versus* water discharge during single hydrologic events in rivers. *J. Hydrol.* **1989**, *111*, 89–106.

15. Kurashige, Y. Mechanism of suspended sediment supply to headwater rivers and its seasonal variation in West Central Hokkaido, Japan. *Jpn. J. Limnol.* **1993**, *54*, 305–315.
16. Eder, A.; Strauss, P.; Krueger, T.; Quinton, J.N. Comparative calculation of suspended sediment loads with respect to hysteresis effects (in the Petzenknirchen catchment, Austria). *J. Hydrol.* **2010**, *389*, 168–176.
17. Kubota, T.; Tsuboyama, Y. Intra-inter-storm oxygen-18 and deuterium variations of rain, throughfall, and stemflow, and two-component hydrograph separation in a small forested catchment in Japan. *J. For. Res.* **2003**, *8*, 179–190.
18. Gomi, T.; Asano, Y.; Uchida, T.; Onda, Y.; Sidle, R.C.; Miyata, S.; Kosugi, K.; Mizugaki, S.; Fukuyama, T.; Fukushima, T. Evaluation of storm runoff pathways in steep nested catchments draining a Japanese cypress forest in central Japan: a geochemical approach. *Hydrol. Process.* **2010**, *24*, 550–566.
19. Chaplot, V.; Ribolzi, O. Hydrograph separation to improve understanding of dissolved organic carbon dynamics in headwater catchments. *Hydrol. Process.* **2013**, doi:10.1002/hyp.10010.
20. Hooper, R.P.; Shoemaker, C.A. A comparison of chemical and isotopic hydrograph separation. *Water Resour. Res.* **1986**, *22*, 1444–1454.
21. Buttle, J.M. Isotope hydrograph separations and rapid delivery of pre-event water from drainage basins. *Prog. Phys. Geogr.* **1994**, *18*, 16–41.
22. Burt, T.; Pinay, G.; Sabater, S. What do we still need to know about the ecohydrology of riparian zones? *Ecohydology* **2010**, *3*, 373–377.
23. Kirkby, M.J. *Hillslope Hydrology*; Wiley: Chichester, UK, 1978; p. 389.
24. Water Resources Laboratory and Flood Control Laboratory. Statistical reports of hydrological observation at the Tsukuba Experimental Watershed (May, 1978–December, 1987). *Bull. For. For. Prod. Res. Inst.* **1993**, *364*, 125–168. (In Japanese)
25. Ohnuki, Y.; Yoshinaga, S.; Noguchi, S. Distribution and physical properties of colluvium and saprolite in unchannelized valleys in Tsukuba Experimental Basin, Japan. *J. For. Res.* **1999**, *4*, 207–215.
26. Shimizu, A.; Kabeya, N.; Nobuhiro, T.; Zhang, J.; Kubota, T.; Abe, T. Estimation of subsurface structure in Tsukuba Forest Experimental Watershed. *Kanto J. For. Res.* **2007**, *58*, 153–156. (In Japanese)
27. Kabeya, N.; Shimizu, A.; Tsuboyama, Y.; Nobuhiro, T.; Zhang, J. Mean residence times of stream and spring water in a small forested watershed with a thick weathered layer. In *Lake Pollution Research Progress*; Miranda, F.R., Bernard, L.M., Eds.; NOVA Science: New York, NY, USA, 2009; pp. 289–309.
28. Zhang, J.; Shimizu, A.; Kabeya, N.; Nobuhiro, T. Research on suspended sediment of upland small forest watershed in Japan. *J. Beijing For. Univ.* **2005**, *27*, 12–19.
29. Shimizu, A.; Kabeya, N.; Nobuhiro, T.; Tsuboyama, Y.; Abe, T.; Kubota, T. Application of erosion and sediment yield model with GIS to a small experimental forest watershed. *Kanto J. For. Res.* **2006**, *57*, 299–302. (In Japanese)

30. Kabeya, N.; Katsuyama, M.; Kawasaki, M.; Ohte, N.; Sugimoto, A. Estimation of mean residence times of subsurface waters using seasonal variation in deuterium excess in a small headwater catchment in Japan. *Hydrol. Process.* **2007**, *21*, 308–322.
31. Fujimoto, M.; Ohte, N.; Tani, M. Effects of hillslope topography on hydrological responses in a weathered granite mountain, Japan: Comparison of the runoff response between the valley-head and the side slope. *Hydrol. Process.* **2008**, *22*, 2581–2594.
32. Steenhuis, T.S.; Hrnčíř, M.; Poteau, D.; Luna, E.J.R.; Tilahun, S.A.; Caballero, L.A.; Guzman, C.D.; Stoof, C.R.; Šanda, M.; Yitaferu, B.; *et al*. A saturated excess runoff pedotransfer function for vegetated watersheds. *Vadose. Zone J.* **2013**, *12*, doi:10.2136/vzj2013.03.0060.
33. Kabeya, N.; Shimizu, A.; Tamai, K.; Iida, S.; Shimizu, T. Transit times of soil water in thick soil and weathered gneiss layers using deuterium excess modelling. In *Conceptual and Modelling Studies of Integrated Groundwater, Surface Water, and Ecological Systems (IAHS Publ. 345)*; Abesser, C., Naütman, G., Hill, M.C., Blöshl, G., Laksmanan, E., Eds.; IAHS Press: Wallingford, UK, 2011; pp. 163–168.
34. Anderson, S.P.; Dietrich, W.E.; Montgomery, D.R.; Torres, R.; Conrad, M.E.; Loague, K. Subsurface flow paths in a steep, unchanneled catchment. *Water Resour. Res.* **1997**, *33*, 2637–2653.
35. Lenzi, M.A.; Marchi, L. Suspended sediment load during floods in a small stream of the Dolomites (Northeastern Italy). *Catena* **2000**, *39*, 267–282.

Water Isotopes as Environmental Tracers for Conceptual Understanding of Groundwater Flow: An Application for Fractured Aquifer Systems in the "Scansano-Magliano in Toscana" Area (Southern Tuscany, Italy)

Marco Doveri and Mario Mussi

Abstract: The "Scansano-Magliano in Toscana" area is characterized by a morpho-structure chiefly made-up by sandstone and shelly-calcareous lithologies. Generally, these complexes host minor aquifers in Tuscany, since they have medium to medium-low permeability. In the area under examination, a sandstone outcrop develops with continuity along the ridge of the structure for several kilometers and above a shelly substratum. Consequently, this hydrostructural context suggested the possibility that a significant groundwater body was hosted in the sandstones. In order to verify this assumption, an isotopic study was carried out taking into account several wells and springs sited on the sandstone outcrop and its surrounding area; the samples collected over a period of two years were analyzed to obtain $\delta^{18}O‰$, $\delta^{2}H‰$ and ^{3}H. A study of the hydrostructural and morphological condition was also performed, and minor springs were selected. The analyses of this spring-water resulted in the characterization of the isotopic features of the infiltration water in the studied area, which represents a fundamental base of work for the interpretation of the data of groundwater points which drain long flow paths. By means of this approach, the groundwater framework was defined and the presence of a significant and continuous groundwater body within the sandstone complex was verified. A preliminary conceptual hydrogeological model was also proposed.

Reprinted from *Water*. Cite as: Doveri, M.; Mussi, M. Water Isotopes as Environmental Tracers for Conceptual Understanding of Groundwater Flow: An Application for Fractured Aquifer Systems in the "Scansano-Magliano in Toscana" Area (Southern Tuscany, Italy). *Water* **2014**, *6*, 2255-2277.

1. Introduction

Water isotopes in hydrogeology act as real natural tracers because their signatures are not affected by water-rock interaction processes up to temperatures of about 200 °C [1]. Their main properties, such as the variation of values in rainfall both over the different periods of the year and with the altitude of precipitation [2–4], can consequently be used to define several aspects of the groundwater flow. By analyzing the ratios $^{18}O/^{16}O$, $^{2}H/^{1}H$ and ^{3}H in springs and/or in water collected from wells, it is possible to: (i) highlight the existence of different groundwater systems, even when these have same chemical features; (ii) evaluate the recharge average altitude of groundwater systems; (iii) achieve information about the hydrodynamic conditions in the aquifer and so on the groundwater vulnerability; (iv) achieve information about the groundwater residence time.

In fractured and/or karst aquifers, the water isotopes usefulness may be enhanced by the considerable range of altitude in which these systems normally develop and by the strong heterogeneity of hydraulic properties that affects isotopic ratios in groundwater, both in space and in time. As shown by several works of literature (e.g., [5–8]), isotopic applications are a fundamental tool for groundwater flow understanding in such hydrogeological systems.

In this paper, a study mainly based on water isotopes is discussed in order to make observations, as this kind of survey is able to point out if groundwater framework is characterized by propitious conditions for water supplying, such as the presence of extensive groundwater bodies. In particular, the research was carried out on a sandstone aquifer that runs for more than 10 km along the Scansano-Magliano in Toscana ridge, in southern Tuscany (Figure 1). Few hydrogeological data are available for this area, because of the lack of previous studies. Nevertheless, the hydrostructural framework suggests that such fractured aquifer might be a strategic and alternative resource for water supply, also taking into account the overexploitation and contamination of the nearby alluvial aquifers. Despite the sandstone is characterized by medium to medium-low permeability and the wells therein generally have flow rates of a few liters per second, given its extension it can hold a large volume of water, which might be tapped by a multiple well solution once verified the presence of a continuity of groundwater circulation. In this context, several springs and wells were sampled in the Scansano-Magliano in Toscana zone and its surrounding areas, and analyses of $\delta^{18}O‰$, $\delta^{2}H‰$ and ^{3}H were performed, with the aim to define the groundwater framework and to identify the main groundwater flow systems, thus verifying whether propitious conditions exist to improve the water supply of the area.

Figure 1. Geological sketch map and distribution of sampled water points (geological data from [9], modified).

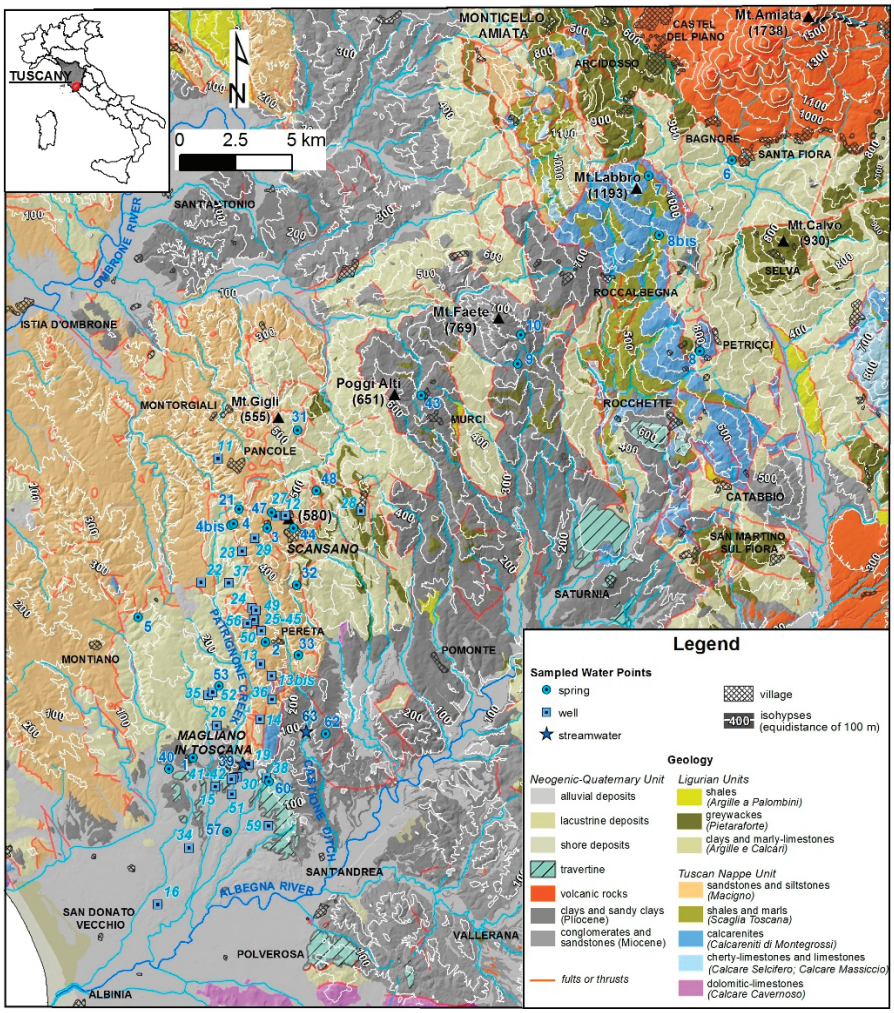

2. Study Area and Methods

2.1. Climate, Geology and Hydrogeology

The Scansano-Magliano in Toscana ridge is located in southern Tuscany between the Albegna and Ombrone rivers (Figure 1). It develops S-N between 50 and 580 m (a.s.l.) of altitude, starting from the Albegna plain. The main streamwaters in the studied area are the Patrignone creek and the Castione ditch, which develop from Scansano toward Magliano in Toscana area, where they flow into the Albegna River.

Using the data collected by Tuscan Region Administration at the "Scansano raingauge" and "Manciano thermometric" stations [10], the average annual values of rainfall and temperature of the area can be assessed as about 880 mm and 14.5 °C, respectively. Based on sixty years of hydrology data, the maximum value of rainfall is in November (about 125 mm), whereas the minimum is in July (about 25 mm); the thirteen years of temperature data that are available highlight that the minimum and maximum values of average temperature occur in January (about 6 °C) and August (about 23 °C). According to Vittorini (1972) [11] the area belongs to subhumid and subarid climate classes.

From a geological point of view, the study area fits into an inner portion of the northern Apennine chain, which is characterized by eastward nappe stacking. In particular, the tectonic evolution is characterized by early compressional stages, started in the Early-Cretaceous, with the progressive suture of the Jurassic Ligurian ocean by convergence of Adria and European plates, leading to continental collision in the Middle Eocene ([12–15] and references therein). The convergence continued during the post-Oligocene with the eastward overthrusting of the Ligurian Units (derived from the oceanic domain and its transition to the continental margin) on the detached sedimentary cover of the continental margin (Tuscan Nappe) [16–18]. From the Middle Miocene, the structural stacking was affected by extensional processes, related to the development of the Tyrrhenian Sea [19–21]. Such processes generated Plio-Pleistocene basins, interpreted by many authors as controlled by longitudinal systems of high angle normal faults, assuming a continuous extensional regime from the Middle Miocene to the Present [21–23]. The tectonic depressions of the Neogene Basins have been so affected by a deposition of continental and marine sediments (Neogene-Quaternary age). Moreover, the extensional regime also controlled the emplacement of magmatic bodies at limited depths and in some case the eruption of volcanic products (e.g., the Mt. Amiata volcanic rocks; Figure 1).

In this geological framework, the Scansano-Magliano in Toscana zone and its surrounding areas are characterized by three main units (Figure 1): (1) the youngest one (Neogene-Quaternary age) mainly consists of alluvial deposits, travertines, volcanic rocks, Pliocenic clays and sandy clays, and Miocenic conglomerates and sandstones; (2) the Tuscan Nappe Unit, here represented by sandstones and siltstones (Macigno formation, upper Oligocene–lower Miocene), shales and marls (Scaglia Toscana formation), calcarenites (Calcareniti di Montegrossi formation), cherty-limestones and limestones (formations of Calcare Selcifero, Calcare Massiccio), and dolomitic-limestones (Calcare Cavernoso); (3) the Ligurian Units, consisting of greywackes (Pietraforte Formation,

Medium–Upper Cretaceous), shales (Argille a Palombini formation) and of a sequence of clays and marly-limestones (mainly Argille e Calcari formation).

Based on this geological context, some major hydrogeological units can be defined:

- The first unit consists of alluvial deposits, travertine and Miocenic sand, and it is characterized by medium to high permeability;
- The second unit is composed by volcanic rocks, whose permeability is medium-high to high;
- The third unit, composed of Pliocene clays, is considered impermeable;
- The fourth unit consists of siltstones, shales and of a sequence of clays and marly-limestones (mainly Ligurian Units and Scaglia Toscana formation), and has medium-low to very low permeability;
- The fifth unit is represented by sandstones (mainly Macigno formation and to a lesser extent Pietraforte formation). This unit is considered to have medium to medium-low permeability.
- The sixth unit, made up by calcarenites, cherty-limestones, limestones and dolomitic-limestones of the Tuscan Nappe. Its permeability is medium to very high.

In the specific zone of the Scansano-Magliano in Toscana ridge, the most important hydrogeological complex is represented by the sandstones of the Macigno formation, because it covers with continuity a surface of about 35 km^2 and it is limited, both downward and laterally (eastward and westward), by medium-low to very low permeability complexes mainly made up by shales and marly-limestones ("Scaglia Toscana" and "Argille e Calcari" of the Tuscan Nappe and Ligurian Unit, respectively). Because the sandstone outcrops and is unconfined in this area, a significant groundwater body can be presumed to reside within this complex, also taking into account the brittle deformation that may have locally improved the general medium degree of permeability. Indeed, Francese *et al*. (2009) [24] highlighted a complex geometry of the fracture network in the Scansano area, which presents fractures and faults with major NNW-SSE, N-S and E-W trends. Several farm wells already exploit this resource, which is also drained by some springs with average flowrate of the order of 0.5 L/s. Only a few springs and wells are present on the marly-limestones outcropping westward and eastward, showing only minor groundwater flow there.

2.2. Methodology

During the 2004–2005 period, six sampling fields were carried out in order to collect water sample from 25 springs, 31 wells and 2 stream waters (120 samples in total). Analyses were performed to achieve the abundance ratios of the water stable isotopes ($^{18}O/^{16}O$, $^{2}H/^{1}H$), which are expressed as δ‰ compared to the V-SMOW standard [25], and the ^{3}H content (expressed as tritium units, TU; 1 TU = 1 ^{3}H atom every 10^{18} total hydrogen atoms). The $\delta^{18}O‰$ was analyzed for each collected sample, whereas $\delta^{2}H‰$ values and tritium contents were achieved for 90 and 40 samples, respectively.

The $\delta^{18}O$ value was determined through analysis of gaseous CO_2, previously equilibrated with water at 25 °C [26]. The mass-spectrometric measurement of the $^{18}O/^{16}O$ ratio requires correction, because a fractionation between CO_2 and H_2O occurs. Analytical precision on $\delta^{18}O‰$ values is better than 0.10‰. The $\delta^{2}H$ value was measured by reducing the water to elemental hydrogen [27] using magnesium instead of zinc. Because the totality of water is reduced and all hydrogen is converted to

hydrogen gas, the isotopic fractionation does not occur and a correction of the mass-spectrometric measurement is not necessary. The analytical error for δ^2H is 1.5‰. The isotopic ratios of CO_2 and H_2 were measured by dual inlet mass spectrometer.

Tritium is a short-lived isotope of hydrogen with a half-life of 12.3 years. It is analyzed through measurement of β^- decay events in a liquid scintillation counter. Direct liquid-scintillation counting has a precision of 7 TU. For tritium contents lower than 20 TU, increased precision is gained through concentration by electrolytic enrichment of ^3H in the water before counting, thus reaching a precision better than 0.8 TU.

As shown in Figure 1, the sampled water points are distributed not only along the Scansano-Magliano in Toscana ridge but also in its surrounding areas. Such points were selected with the aim to define, in terms of groundwater flow, the relationships between the sandstone aquifer and the other hydrogeological complexes, and moreover to obtain a good isotopic characterization of the rainfall/infiltration water. Indeed, the application of isotopic methods is closely dependent on the knowledge of some local parameters, such as the distribution of the isotopic composition of rainwater/infiltration water and vertical isotopic gradient in the area. This basic information is obtained by examining the $\delta^{18}O$‰, δ^2H‰ and ^3H in the rainwater collected every month and at various altitudes for a period of at least two-three years (e.g., [28]). In the absence of a well distributed raingauge-network, but also to avoid the long time required by this methodology and to get information directly on the infiltrated water, it is possible to collect some samples (3–4 each year) in small springs (low flowrate) that are fed by limited extension basins (e.g., [8,29]). In this way the stable isotopes of the water are representative of an infiltration average altitudes that is not very different from the springs' altitudes and assessable by morphological and hydrogeological considerations. In order to minimize the error in the assessing of the infiltration average altitudes, it is preferable to identify springs at the base of small reliefs and in hydrostructural contexts that suggest a local circulation of groundwater (see the example in Figure 2).

Figure 2. Cross section (A–B) in the zone of the spring "8".

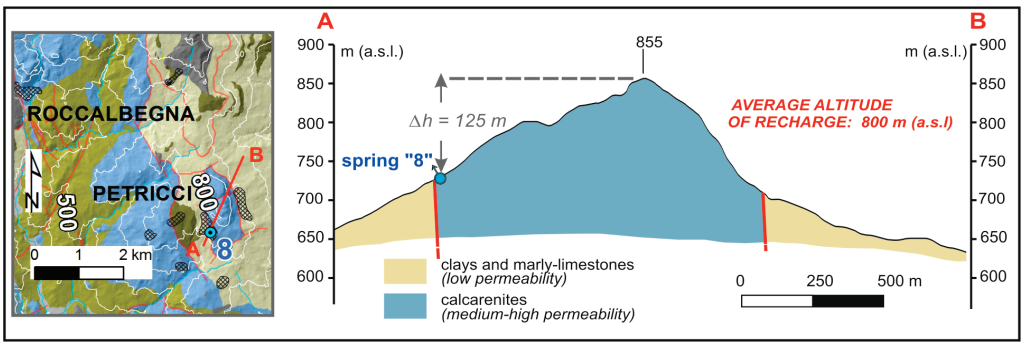

Based on the latter approach, several springs with low flowrate were identified over the altitude interval of 40–995 m a.s.l. These springs are representative of a groundwater circulation in aquitard complexes, or in aquifers complexes that have a limited extension. Despite its high flowrate and wide recharge area, the main spring draining the Mt. Amiata volcanic aquifer [30] was also included, in order to achieve isotopic information that are representative of the highest altitudes encountered in the area surrounding the site under examination. The data derived from all these selected springs

allowed fundamental background information to be obtained, e.g., the relationship altitude/$\delta^{18}O‰$ (or alternatively altitude/$\delta^{2}H‰$), which was then used to assess the average altitude of the feeding area for the groundwater tapped by wells into the hydrogeological complexes of the Scansano-Magliano in Toscana area.

The tritium values achieved for the water points were also compared with the tritium annual data of rainfall, which were recorded at the Genova and Pisa stations [29,31,32]. This data can be considered homogeneous in the whole Mediterranean area and not affected by the precipitation altitudes [29]. In order to conduct a preliminary assessment of the average residence time of groundwater flow, the exponential law of radioactive decay was applied to the ^{3}H average annual values of rainfall occurred in the past years, and the achieved results were compared with the contents of water points under examination.

3. Results and Discussion

3.1. Isotopic Features of the Infiltration Water

In order to define isotopic features of infiltration water, samples collected at 25 springs, which are located in the area between Magliano in Toscana and the Mt. Amiata (Figure 1), were analyzed. Seventeen of such springs were sampled at least two time in different periods, whereas the remaining springs were collected only once.

The selection of the springs was performed on the base of morphological and hydrostructural conditions, with the aim to individuate water points which represent local groundwater, whose average altitudes of feeding are similar to the springs' altitudes and assessable with a good approximation (see Figure 2, such as example among the several elaborated hydrogeological sections). In this way, the relationship between infiltration average altitudes and isotopic values (in particular that of stable isotopes) can be achieved. The only exception is spring 6, which has an extended recharge area, whose average altitude was estimated on the base of previous studies [30,33].

Results of isotopic analyses are reported in Table 1. For the springs that were analyzed more than once, the isotopic composition was observed to be stable over time. Given this general behavior, in the data processing and interpretation the average isotopic values were considered for such springs; moreover, also for the springs that were sampled only once, the isotopic values were involved as representative of the annual average values.

The $\delta^{2}H‰$ and $\delta^{18}O‰$ values of the springs are compared in Figure 3 with the global meteoric (GMWL) [34] and the Mediterranean meteoric (MMWL) [35] water lines. The spring water fall between these two lines and give a regression line equation of $\delta^{2}H‰ = 5.7 \times \delta^{18}O‰ - 2.4$ ($R^2 = 0.97$), which can be considered as representative of the local meteoric water line (LMWL). As previously observed in the southern Tuscany (e.g., [36]), groundwater points dispose between the GMWL and the MMWL with a slope lesser than 8. Taking also into account that the low and high altitude springs fall close to GMWL and MMWL, respectively, such behavior likely reflects an evaporative influence on the isotopic values of rainfall of Mediterranean origin. The wide range of values observed for $\delta^{18}O$ and $\delta^{2}H$ (about 2.5‰ and 15‰, respectively) is nevertheless mainly linked to the altitude effect.

Table 1. Springs isotopic data.

Sampled Springs	Spring Altitudes (m a.s.l.)	Infiltration Average Altitudes * (m a.s.l.)	$\delta^{18}O$‰ (VSMOW) (Precision 0.10‰) Mean Value or Single Datum	$\delta^{18}O$‰ Values (March 04/June–July 04/ September 04/May–June 05/ September 05/October 05)	$\delta^{2}H$‰ (VSMOW) (Precision 1.5‰) Mean Value or Single Datum	$\delta^{2}H$‰ Values (March 04/June–July 04/ September 04/May–June 05/ September 05/October 05)	^{3}H(TU) ± Err Mean Value or Single Datum	^{3}H(TU) Values (March 04/June–July 04/ September 04/May–June 05/ September 05/October 05)
1	75	150	−5.58	(−5.53/−5.54/−5.63/ns/−5.62/ns)	−34.2	(−33.6/−33.2/−35.8/ns/na/ns)	2.9 ± 0.7	(na/3.0/2.8/ns/na/ns)
2	260	310	−6.24	(−6.28/−6.18/ns/−6.25/ns/ns)	−38.5	(−38.1/−38.9/ns/na/ns/ns)	4.7 ± 0.7	(na/4.7/ns/na/ns/ns)
3	490	530	−6.68	(−6.59/−6.71/−6.73/−6.67/ns/ns)	−39.4	(−38.3/−40.4/−39.4/na/ns/ns)	na	(na/na/ns/na/ns/ns)
4	380	500	−6.64	(−6.62/−6.65/ns/ns/ns/ns)	−40.3	(−39.4/−41.2/ns/ns/ns/ns)	na	(na/na/ns/ns/ns/ns)
4bis	395	500	−6.74	(−6.79/−6.68/ns/ns/ns/ns)	−40.2	(−38.6/−41.7/ns/ns/ns/ns)	na	(na/na/ns/ns/ns/ns)
5	175	200	−5.57	(−5.54/−5.56/−5.55/−5.61/ns/ns)	−34.1	(−34.4/−34.6/−32.3/na/ns/ns)	4.2 ± 0.6	(na/na/4.2/na/ns/ns)
6	650	1300	−7.89	(−8.00/−7.83/−7.86/−7.86/ns/ns)	−48.3	(−47.9/−47.4/−49.5/na/ns/ns)	6.3 ± 0.7	(na/na/6.3/na/ns/ns)
7	995	1080	−7.42	(−7.52/−7.30/−7.33/−7.51/ns/ns)	−44.8	(−44.8/−43.6/−45.9/na/ns/ns)	5.5 ± 0.7	(na/na/5.5/na/ns/ns)
8	730	800	−6.97	(−7.03/−6.94/−6.96/−6.93/−6.99/ns)	−41.9	(−40.4/−43.0/−42.3/na/na/ns)	5.5 ± 0.8	(na/na/5.5/na/na/ns)
8bis	845	950	−7.17	(−7.29/−7.17/−7.06/ns/ns/ns)	−44.2	(−44.1/−44.5/−43.9/ns/ns/ns)	na	(na/na/na/ns/ns/ns)
9	630	660	−6.66	(−6.67/−6.64/ns/ns/ns/ns)	−40.7	(−39.6/−41.7/ns/ns/ns/ns)	4.7 ± 0.7	(na/4.7/ns/ns/ns/ns)
10	690	730	−6.81	(−6.86/−6.79/−6.73/−6.85/ns/ns)	−41.4	(−40.7/−41.5/−41.9/na/ns/ns)	4.1 ± 0.6	(na/4.2/4.0/na/ns/ns)
21	460	510	−6.69	(ns/−6.69/ns/ns/ns/ns)	−39.7	(ns/−39.7/ns/ns/ns/ns)	na	(ns/na/ns/ns/ns/ns)
31	450	540	−6.53	(ns/ns/−6.50/−6.56/ns/ns)	−41.0	(ns/ns/−41.0/na/ns/ns)	4.8 ± 0.8	(ns/ns/4.8/na/ns/ns)
32	400	430	−6.28	(ns/ns/−6.27/−6.24/−6.32/ns)	−38.6	(ns/ns/−38.6/na/na/ns)	na	(ns/ns/na/na/na/ns)
33	180	250	−6.03	(ns/ns/−5.98/−6.08/ns/ns)	−36.6	(ns/ns/−36.6/na/ns/ns)	na	(ns/ns/na/na/ns/ns)
40	45	150	−5.65	(ns/ns/ns/−5.65/ns/ns)	−33.2	(ns/ns/ns/−33.2/ns/ns)	na	(ns/ns/ns/na/ns/ns)
43	545	630	−6.74	(ns/ns/ns/−6.74/ns/ns)	−40.5	(ns/ns/ns/−40.5/ns/ns)	na	(ns/ns/ns/na/ns/ns)
44	490	520	−6.62	(ns/ns/ns/−6.73/ns/−6.40)	−39.6	(ns/ns/ns/−39.6/ns/na)	3.4 ± 0.6	(ns/ns/ns/3.4/ns/na)
47	515	530	−6.60	(ns/ns/ns/ns/−6.60/−6.60)	−39.6	(ns/ns/ns/ns/−39.6/na)	5.9 ± 0.6	(ns/ns/ns/ns/5.9/na)
48	490	530	−6.43	(ns/ns/ns/ns/−6.46/−6.40)	−39.4	(ns/ns/ns/ns/−39.4/na)	5.8 ± 0.6	(ns/ns/ns/ns/5.8/na)
53	190	240	−5.95	(ns/ns/ns/ns/−5.95/ns)	−37.5	(ns/ns/ns/ns/−37.5/ns)	na	(ns/ns/ns/ns/na/ns)
57	40	50	−5.55	(ns/ns/ns/ns/ns/−5.55)	−34.3	(ns/ns/ns/ns/ns/−34.3)	na	(ns/ns/ns/ns/ns/na)
60	95	130	−5.62	(ns/ns/ns/ns/ns/−5.62)	−34.8	(ns/ns/ns/ns/ns/−34.8)	4.3 ± 0.5	(ns/ns/ns/ns/ns/4.3)
62	140	170	−5.85	(ns/ns/ns/ns/ns/−5.85)	−36.8	(ns/ns/ns/ns/ns/−36.8)	na	(ns/ns/ns/ns/ns/na)

Notes: *: assessed by morphological and hydrogeological considerations. The only exception is for the spring 6 (see text); ns: not sampled; na: not analyzed.

Figure 3. δ^2H‰ *vs*. δ^{18}O‰ for the spring samples.

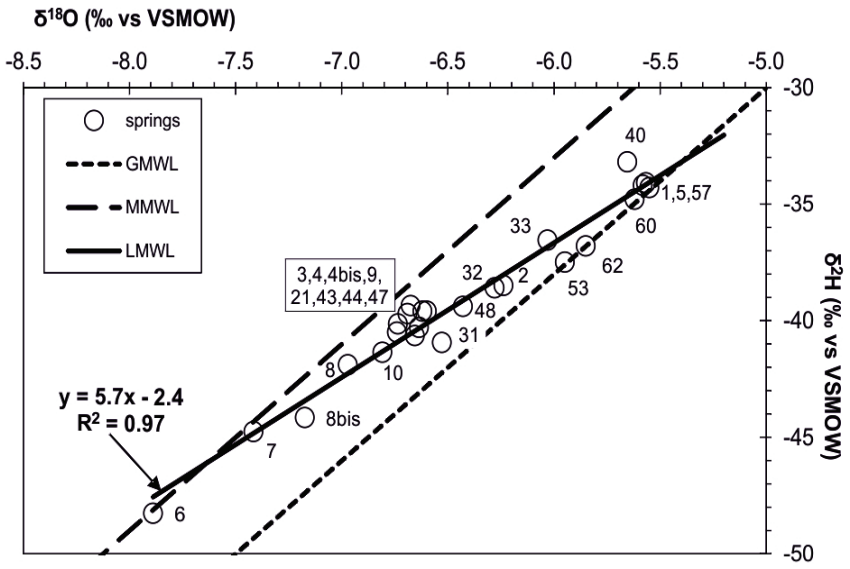

The regression line showing the δ^{18}O‰ values variation with the altitude is achieved in Figure 4 by means of a comparison among the isotopic contents of the springs and the respective estimated basin average altitudes. The springs 3, 4, 4bis, 21, 44, 47 (located nearby Scansano; Figure 1) and 2 (sited nearby Pereta; Figure 1) are not involved in the computed regression line, because, if compared to the behavior of the other springs, they show an incompatibility between the estimated feeding average altitudes and the respective δ^{18}O‰ values. In other words, the isotopic contents of these springs require higher recharge altitudes in respect to the estimated ones. On the other hand such required altitudes are not detectable on the hilly reliefs neighboring the springs, so the latter seem to drain not only local groundwater but also more extended flow paths, which will be discussed in the next paragraph.

Figure 4. Recharge average altitudes *vs*. δ^{18}O‰ for the spring waters (see text for the methodology through which the recharge altitudes were estimated).

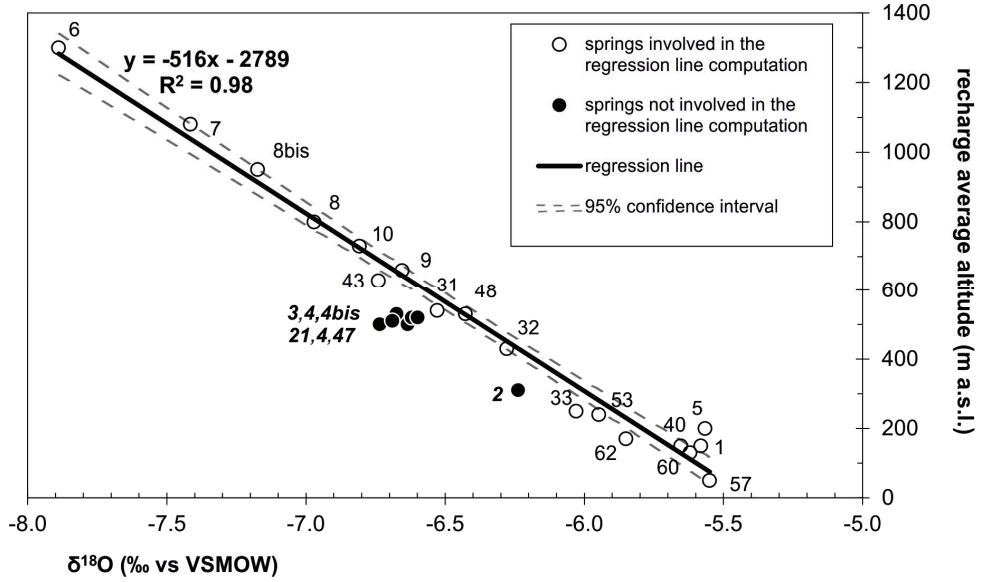

The regression line equation is "Altitude (m) = −516 × δ^{18}O‰ − 2789" (R^2 = 0.98) and will be used to assess the feeding average altitude of the major groundwater flow systems. The δ^{18}O vertical gradient is about −0.2‰ every 100 meters of altitude increasing, with a δ^{18}O‰ of about −5.4 at sea level. Such values are in agreement with those generally observed along the Tyrrhenian coast of Italy [28,29,37–39].

Fourteen of the 25 sampled springs were analyzed for tritium contents, achieving values between 2.9 and 6.3 TU (Table 1). In order to achieve preliminary indications on the average age of the spring water, such contents were compared to the rainfall tritium values, the latter opportunely depleted according to the decay low (Figure 5). Most of the analyzed springs showed tritium values between 3.4 and 5.5 TU, which are likely linked to the rainfall annual values of the recent years, taking also into account that such springs drain local flow path from unconfined systems. The 6.3 TU of the spring 6 indicate an average residence time of about 20 years or longer, in agreement with the extension and hydrodynamic behavior of the volcanic aquifer which is drained by the same spring [30,33]. In addition, the values of 5.9 and 5.8 TU, which were detected for the springs 47 and 48, can be representative of an average age of 20 or more years, anyway such springs were analyzed only once and the relative values may be affected by annual fluctuations that occur in rainfall tritium contents. Finally, groundwater drained by the spring 1, which showed 2.9 TU practically constant in two samplings performed at different periods of the same year, seems to have an average residence time longer than 20 years, which is congruent with the marly lithology in which the relative aquifer is developed.

Figure 5. Tritium values of the springs in comparison to tritium values of precipitations.

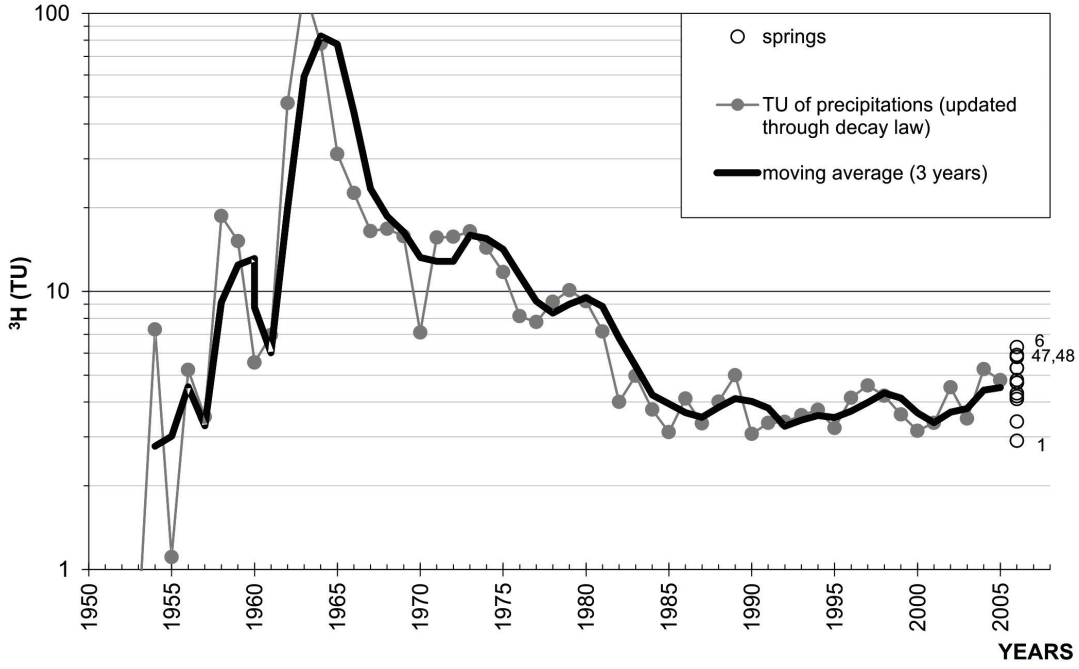

3.2. Groundwater Flow Framework

The isotopic data of the water collected at the wells and streamwaters located in the Scansano-Magliano in Toscana area are inserted in Table 2. Water from wells generally showed an

isotopic stability over time, which indicates groundwater flow in the region is not significantly affected by the seasonal isotopic variability of the rainfall. Thus, the average isotopic values can be used for the discussion of the source of groundwater flow. As showed by Figure 6, the wells waters cluster along the local meteoric line (LMWL). Consequently, isotopic exchange phenomena does not appear to be an issue for the groundwater at this study site and the observed features are completely linkable at that of the infiltration water, or, in other words, water stable isotopes work as environmental tracers.

The range of $\delta^{18}O$ in the well water was from −6.75‰ to −5.35‰, with the lighter signatures referred at the Scansano-Pancole zone and the heavier ones registered in the Albegna Plain. A general increasing of the values is observed moving from Scansano to Magliano in Toscana, with a substantial agreement with a decrease in altitude. However, this trend and the distribution of the absolute values across the territory seem to be also affected by the hydro-structural features. Generally, the lighter signatures were detected for most of the wells that tap into the sandstones aquifer (Figures 6 and 7), whereas the heavier $\delta^{18}O$ signatures were found in the groundwater flowing into the marly/shaly complexes. These features for groundwater flow hosted in the sandstones is confirmed by the isotopic values of the springs that drain this aquifer in the Scansano zone. Two groundwater flow systems can be so identified in the Scansano-Magliano in Toscana ridge: (i) the first concerns the marly/shaly complexes and have heavier isotopic signatures; (ii) the second develops in the sandstones aquifer and shows lighter isotopic signatures.

Figure 6. $\delta^{2}H$‰ *vs*. $\delta^{18}O$‰ for the wells waters. (**1**) wells into the sandstones; (**2**) wells into the other hydrogeological complexes; **LMWL** is as defined in Figure 3.

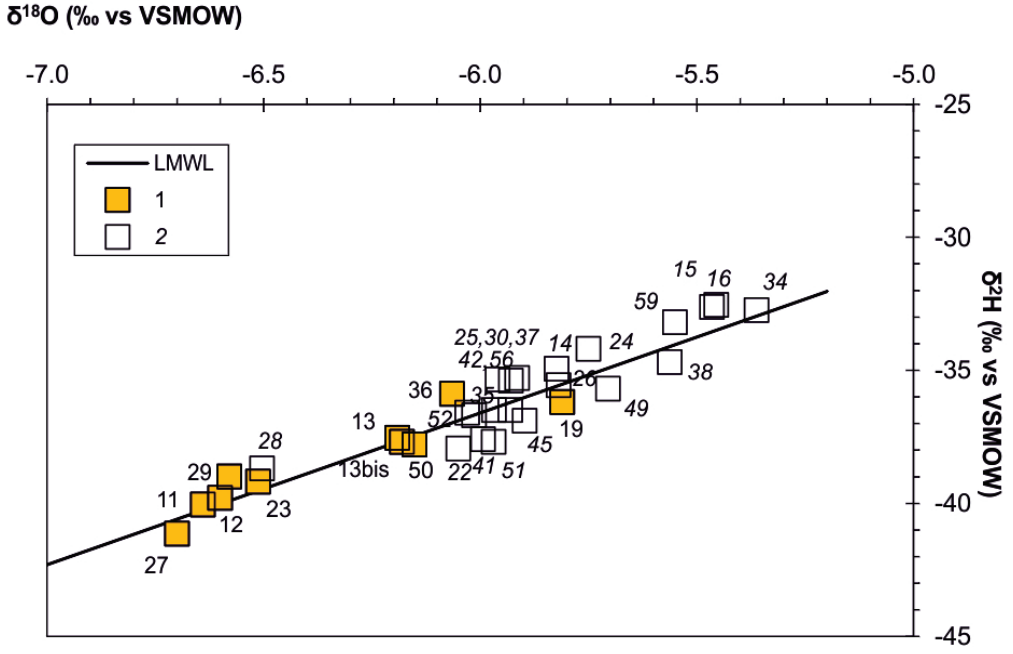

Table 2. Isotopic data of wells and streamwaters.

Sampled Wells or Streamwaters	Altitudes of Ground Level (m a.s.l.)	Depth of Well (m) or Name of Streamwater	$\delta^{18}O$‰(VSMOW) (Precision 0.10‰) Mean Value or Single Datum	$\delta^{18}O$‰ Values (March 04/June–July 04/ September 04/May–June 05/ September 05/October 05)	$\delta^{2}H$‰(VSMOW) (Precision 1.5‰) Mean Value or Single Datum	$\delta^{2}H$‰ Values (March 04/June–July 04/ September 04/May–June 05/ September 05/October 05)	^{3}H(TU) ± Err Mean Value or Single Datum	^{3}H(TU) Values (March 04/June–July 04/ September 04/May–June 05/ September 05/October 05)
11	415	50	−6.64	(−6.67/−6.61/ns/ns/ns)	−40.1	(−40.4/−39.7/ns/ns/ns)	3.7 ± 0.6	(na/3.7/ns/ns/ns)
12	545	80	−6.60	(−6.62/−6.58/ns/ns/ns)	−39.8	(−39.2/−40.4/ns/ns/ns)	4.2 ± 0.7	(na/4.2/ns/ns/ns)
13	255	30	−6.19	(−6.23/−6.13/−6.21/ns/ns)	−37.6	(−38.2/−36.9/na/ns/ns)	3.7 ± 0.6	(na/3.6/3.7/ns/ns)
13bis	190	5	−6.18	(−6.18/ns/ns/ns/ns)	−37.7	(−37.7/ns/ns/ns/ns)	na	(na/ns/ns/ns/ns)
14	185	11	−5.82	(−5.79/ns/ns/−5.86/ns)	−35.0	(−35.0/ns/ns/na/ns)	5.9 ± 0.7	(5.9/ns/ns/na/ns)
15	60	40	−5.46	(−5.51/−5.40/ns/ns/ns)	−32.6	(−33.1/−32.0/ns/ns/ns)	6.6 ± 0.7	(na/6.6/ns/ns/ns)
16	26	48	−5.47	(−5.42/−5.51/ns/ns/ns)	−32.6	(−33.8/−31.5/ns/ns/ns)	3.7 ± 0.7	(na/3.7/ns/ns/ns)
19	58	85	−5.81	(−5.81/ns/ns/ns/ns)	−36.2	(−36.2/ns/ns/ns/ns)	na	(na/ns/ns/ns/ns)
22	250	55	−6.05	(−6.00/−6.10/ns/ns/ns)	−38.0	(−37.1/−38.8/ns/ns/ns)	2.6 ± 0.6	(2.5/2.7/ns/ns/ns)
23	400	66	−6.51	(−6.52/−6.46/−6.56/ns/ns)	−39.2	(−38.5/−39.9/na/ns/ns)	na	(na/na/na/ns/ns)
24	365	54	−5.75	(−5.78/−5.72/ns/ns/ns)	−34.2	(−35.2/−33.2/ns/ns/ns)	4.3 ± 0.7	(na/4.3/ns/ns/ns)
25	345	3	−5.96	(−5.93/ns/−5.99/ns/ns)	−35.4	(−35.4/ns/na/ns/ns)	na	(na/ns/na/ns/ns)
26	120	60	−5.82	(−5.79/−5.78/−5.89/ns/ns)	−35.6	(−35.3/−35.9/na/ns/ns)	5.4 ± 0.8	(na/5.4/na/ns/ns)
27	550	83	−6.70	(−6.67/−6.68/−6.75/ns/ns)	−41.2	(−42.7/−39.6/na/ns/ns)	3.7 ± 0.7	(na/3.9/3.5/ns/ns)
28	495	8	−6.50	(ns/−6.42/−6.59/ns/ns)	−38.7	(ns/−37.7/−39.7/ns/ns)	5.0 ± 0.7	(ns/5.0/na/ns/ns)
29	500	50	−6.58	(ns/−6.55/−6.61/ns/ns)	−39.0	(ns/−39.0/na/ns/ns)	2.4 ± 0.5	(ns/2.5/2.3/ns/ns)
30	50	30	−5.93	(ns/−5.92/−5.94/ns/ns)	−35.4	(ns/−35.4/na/ns/ns)	4.6 ± 0.7	(ns/4.1/5.0/ns/ns)
34	42	80	−5.36	(ns/−5.28/−5.44/ns/ns)	−32.8	(ns/−31.7/−33.8/ns/ns)	3.2 ± 0.6	(ns/3.2/na/ns/ns)
35	223	70	−6.01	(ns/−6.09/ns/−5.94/ns)	−36.7	(ns/−36.7/ns/na/ns)	5.6 ± 0.7	(ns/5.6/ns/na/ns)
36	185	32	−6.06	(ns/−6.08/−6.05/ns/ns)	−33.8	(ns/−33.8/na/ns/ns)	0.8 ± 0.4	(ns/0.8/0.9/ns/ns)
37	285	80	−5.91	(ns/−5.81/−6.02/ns/ns)	−35.3	(ns/−35.3/na/ns/ns)	3.8 ± 0.7	(ns/3.8/na/ns/ns)

Table 2. *Cont.*

Sampled Wells or Streamwaters	Altitudes of Ground Level (m a.s.l.)	Depth of Well (m) or Name of Streamwater	$\delta^{18}O$‰(VSMOW) (Precision 0.10‰) Mean Value or Single Datum	$\delta^{18}O$‰ Values (March 04/June–July 04/ September 04/May–June 05/ September 05/October 05)	$\delta^{2}H$‰(VSMOW) (Precision 1.5‰) Mean Value or Single Datum	$\delta^{2}H$‰ Values (March 04/June–July 04/ September 04/May–June 05/ September 05/October 05)	^{3}H(TU) ± Err Mean Value or Single Datum	^{3}H(TU) Values (March 04/June–July 04/ September 04/May–June 05/ September 05/October 05)
38	80	5	−5.56	(ns/ns/−5.56/ns/ns)	−34.7	(ns/ns/−34.7/ns/ns)	na	(ns/ns/na/ns/ns)
41	49	40	−5.99	(ns/ns/−6.02/−6.07/−5.89)	−37.6	(ns/ns/−37.6/na/na)	na	(ns/ns/na/na/na)
42	49	35	−5.97	(ns/ns/−5.97/ns/ns)	−36.5	(ns/ns/−36.5/ns/ns)	na	(ns/ns/na/ns/ns)
45	346	40	−5.90	(ns/ns/−5.90/ns/ns)	−36.9	(ns/ns/−36.9/ns/ns)	5.3 ± 0.7	(ns/ns/5.3/ns/ns)
49	360	4	−5.70	(ns/ns/ns/−5.70/ns)	−35.7	(ns/ns/ns/−35.7/ns)	4.1 ± 0.6	(ns/ns/ns/4.1/ns)
50	328	38	−6.15	(ns/ns/ns/−6.15/ns)	−37.8	(ns/ns/ns/−37.8/ns)	na	(ns/ns/ns/na/ns)
51	38	50	−5.97	(ns/ns/ns/−5.97/ns)	−37.7	(ns/ns/ns/−37.7/ns)	na	(ns/ns/ns/na/ns)
52	218	60	−6.03	(ns/ns/ns/−6.03/ns)	−36.6	(ns/ns/ns/−36.6/ns)	na	(ns/ns/ns/na/ns)
56	355	50	−5.93	(ns/ns/ns/−5.93/ns)	−36.5	(ns/ns/ns/−36.5/ns)	na	(ns/ns/ns/na/ns)
59	52	40	−5.55	(ns/ns/ns/ns/−5.55)	−33.2	(ns/ns/ns/ns/−33.2)	na	(ns/ns/ns/ns/na)
39	53	Patrignone	−5.53	(ns/ns/−5.80/ns/−5.27)	−34.1	(ns/ns/−34.1/ns/na)	4.5 ± 0.6	(ns/ns/4.5/ns/na)
63	72	Castione	−5.84	(ns/ns/ns/ns/−5.84)	−34.9	(ns/ns/ns/ns/−34.9)	na	(ns/ns/ns/ns/na)

Notes: ns: not sampled; na: not analyzed.

Figure 7. Thematic map of the $\delta^{18}O‰$ values.

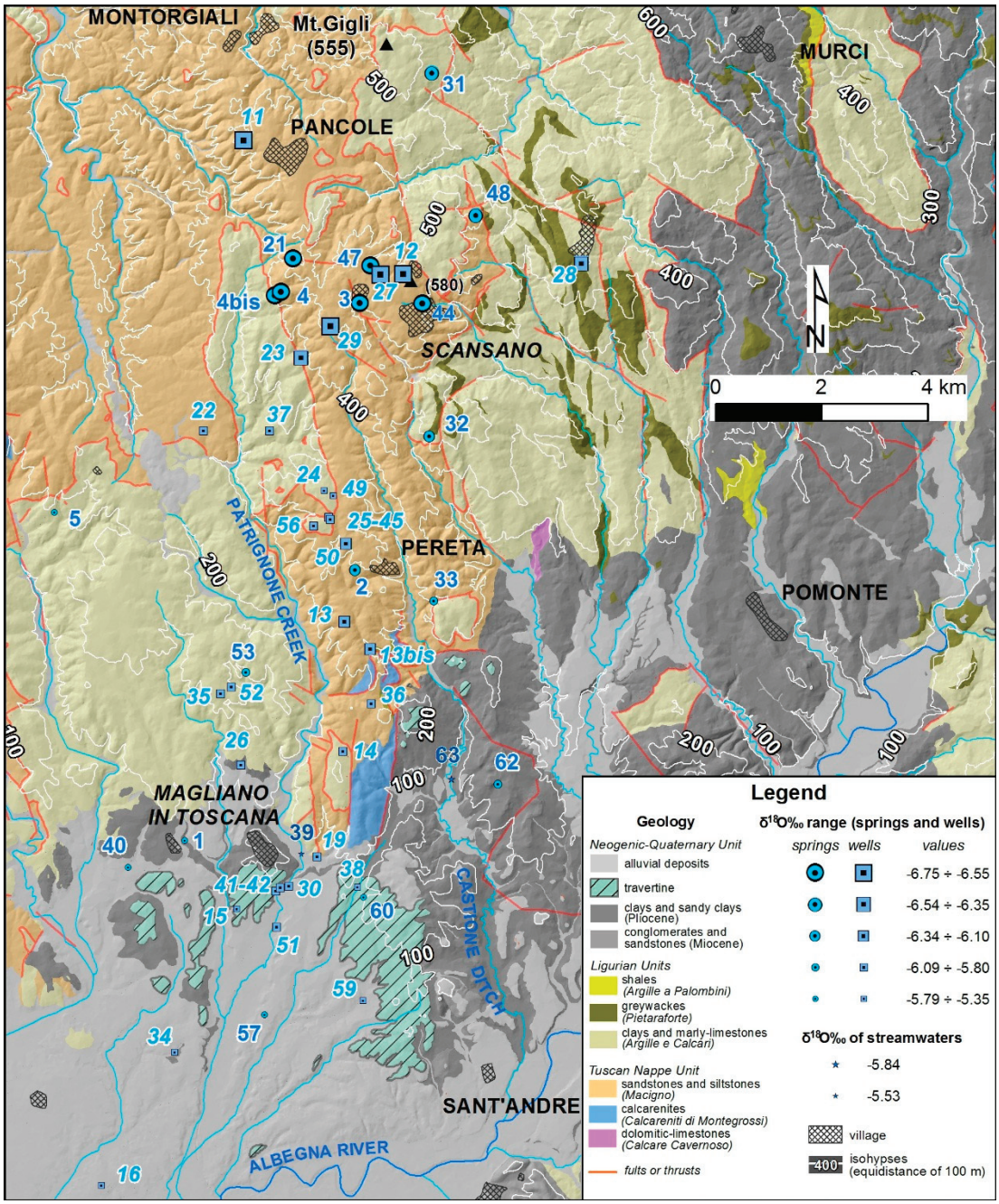

Downstream of Magliano in Toscana, where the alluvial system dominates, very different values of $\delta^{18}O$ were detected in wells that are close to each other and have a similar depth. The most evident case regards the well 15, whose average value is −5.4‰, and the wells 30, 41, 42, 51, which are characterized by values from −5.9‰ to −6.0‰ (Figures 6 and 7). The latter values are congruent with those detected in the sandstones groundwater flow, thus suggesting a likely groundwater transfer from the sandy aquifer toward the alluvial aquifer system. This is in agreement with the distribution of the wells, since the 30, 41, 42, 52 are in front of the zone in which the alluvial sediments overlap the sandstones, contrarily to the 15 which is westward. The possibility that the Patrignone creek, given the proximity, affects the isotopic features of the wells 30, 41, 42, 51, seems instead to be

unlikely, because in contrast with the homogeneity and stability observed in the wells water values the streamwater showed a consistent $\delta^{18}O$ variability, between −5.3‰ and −5.8‰.

An evaluation of the recharge average altitudes for the groundwater flowing in the study area can be performed by means of the diagram in Figure 8. The latter takes into account the "infiltration average altitudes/$\delta^{18}O$ values" relationship, previously achieved (Figure 4), and moreover the average $\delta^{18}O$ values of all wells and of the springs which denoted a draining of groundwater not exclusively fed by local infiltration water (to insert the wells and springs points into the diagram the altitudes of ground level were considered).

Figure 8. Comparison between the "infiltration average altitudes/$\delta^{18}O$ values" relationship (**1**) and the $\delta^{18}O$‰ values achieved in the Scansano-Magliano in Toscana zone from wells and springs draining sandstones aquifer (**3** and **4**, respectively), and from wells draining the other hydrogeological complexes (**2**).

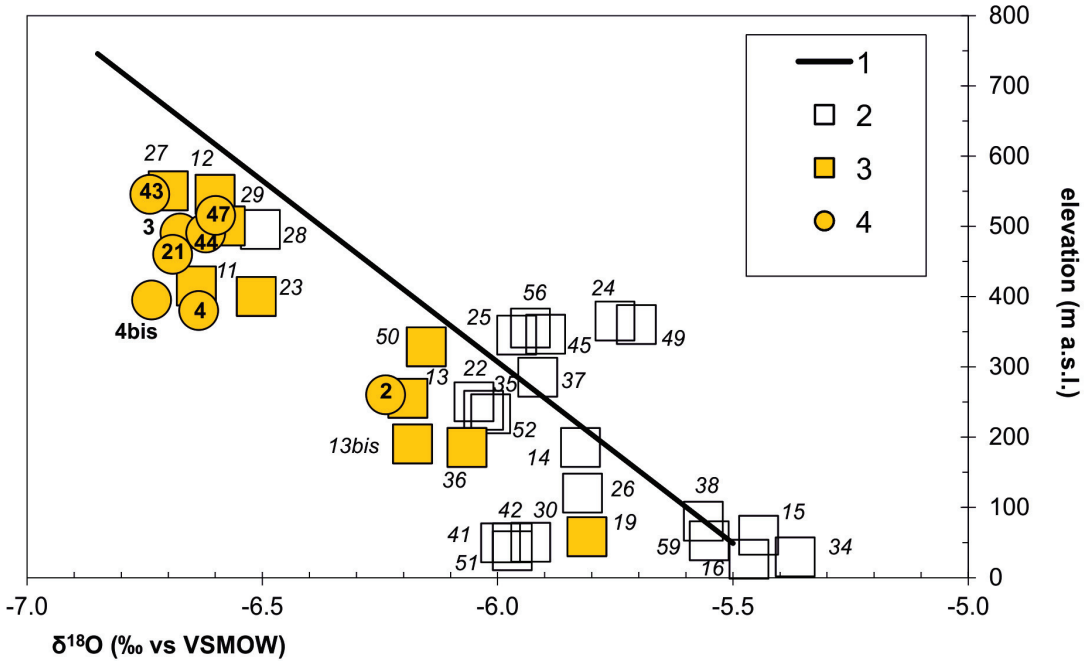

For the springs (3, 4, 4bis, 21, 44, 47) and wells (11, 12, 23, 27, 29) that drain groundwater from sandstones in the Scansano-Pancole zone, a recharge average altitude in the range 600–700 m (a.s.l.) is assessable. Considering that this zone mainly develops between 450 and 550 m (a.s.l.), and that its highest altitude is about 580 m (a.s.l.) (Figures 1 and 7), the presence of a significant regional groundwater component is required to justify the above mentioned range of feeding average altitudes. Indeed, in the surrounding area the nearest zones with altitudes of 600–700 m a.s.l. (and higher ones, necessarily involved to obtain such range of average values) are present toward NE and at more than 13 km from Scansano.

The water sampled in the Pereta zone (2, 13, 13bis, 36, 50), and again representative of the sandstones aquifer, have isotopic features that indicate the range 350–450 m a.s.l. as average altitudes of feeding. These elevations are detectable between Pereta and Scansano at about 4–6 km from the sampling sites; at any rate, the groundwater flow paths may also be considered more extended,

because, being average elevations, a feeding from altitudes higher than 450 m a.s.l., such as that of the Scansano zone, is likely. A probable hypothesis is that the groundwater of the Scansano zone represents the starting point of a flow path that develops with continuity southward, and whose $\delta^{18}O$ values are influenced by the $\delta^{18}O$ values of the water that infiltrates into the sandstones aquifer at the minor altitudes encountered moving in this direction. At least up to Magliano in Toscana, such sandstones groundwater flow system and its transfer in the alluvial deposits are verified by isotopic features of the wells 19, 30, 41, 42, 51. In fact, as highlighted in Figure 8, recharge average altitudes of about 200–300 m a.s.l. are assessable for these water points, and they are consistent with an involvement of the zones that develop northward from Pereta. All other points plotted into the diagram, and representative of groundwater hosted in marly, shelly or alluvial complexes, denote a recharge from average altitudes that are similar to the elevation of the zones in which they are located, thus suggesting that these groundwater flow systems have generally a local importance. Five wells (24, 25, 45, 49, 56) even showed $\delta^{18}O$ values apparently incompatible with the regression line in the Figure 8, because based on the same line a recharge average altitude below the ground level is achieved (also taking into account the bottom of the well the incongruence persists). These wells are all located in a restricted area near Pereta (Figure 7), so the verified behavior seems to be connected to local causes. Although with the available data it is not possible to reach a conclusion, a probable influence of hydro-structural conditions on the local groundwater isotopic features can be supposed. The marly complex, in which the wells tap groundwater, is here interested by a wide fractured zone between two main sub-vertical faults, for the presence of the nearby tectonic contact with the sandstones [24]. High rainfall infiltration rates can so occur and locally lead to an isotopic variability in groundwater during the hydrologic year. Since the mentioned wells were sampled only once or twice, their isotopic values in such hypothesis would not be representative of the average annual values in local groundwater and therefore not even of the average altitudes of the recharge area.

In the framework above delineated, Figure 6 might be also viewed as representative of a mixing in which regional groundwaters and shallower, locally recharged groundwaters are involved. This would suggest that regional water mixes upwards into the shallower systems. However, further hydrogeological investigation is required to resolve the appropriate conceptual model.

Tritium was analyzed on 19 of the 31 wells (Table 2), and where the analyses were twice performed the contents have been stable over time. In order to achieve preliminary indications on the average age of the well water, the results of analysis are compared in Figure 9 to the annual average content of rainfall, previously depleted by means of the decay law. Most of the well water is characterized by values that are congruent with those of the rain of the last 4–5 years, anyway such values may be also affected by water infiltrated in the period 1980–2000.

The wells 15, 22, 29, 36 are distinguished from other ones. The water of the well 15 (6.6 TU) seems to be characterized by an average age of 25 or more years, which may be due to low-permeability conditions for a local prevalence of clayey sediments in the alluvial system. The tritium contents of 2.6, 2.4 and 0.8 TU, detected for the other three wells, are compatible with average residence times of 50 or more years. Since on the base of $\delta^{18}O$ values these water wells belong to sandstones groundwater flow system and most of water points of this system showed shorter residence time, local conditions of low-permeability in this aquifer can be supposed.

Figure 9. Tritium values of the well water in comparison to tritium values of precipitations.

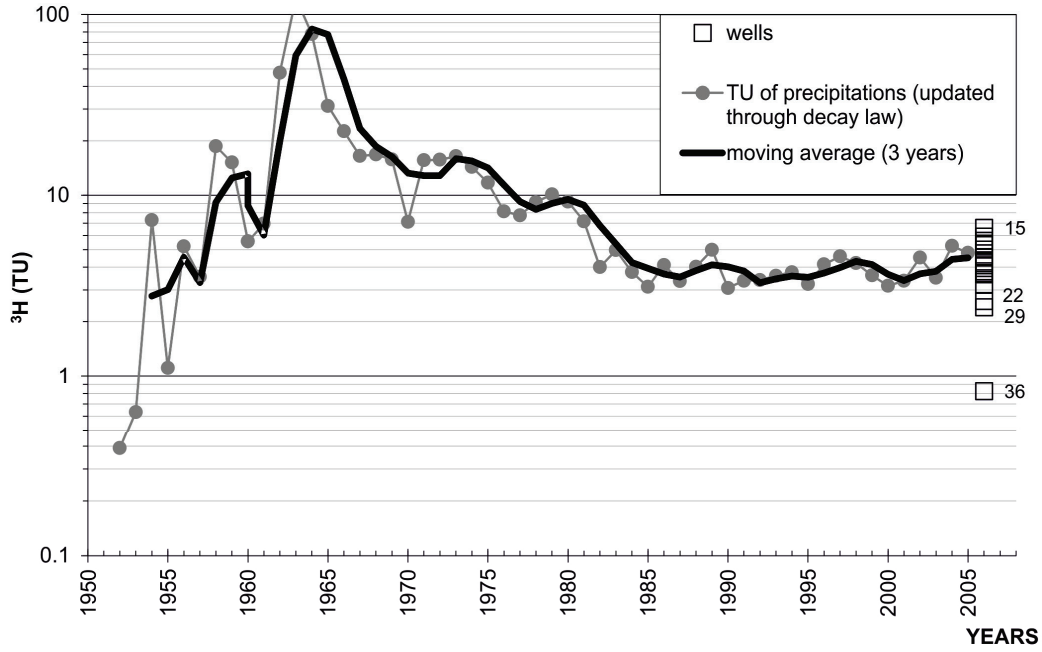

3.3. Preliminary Elaboration of the Conceptual Hydrogeological Model

Previous discussion has highlighted as in the Scansano zone the sandstones aquifer receives, in addition to local infiltration water, an input from regional groundwater. Presuming mixing of these two components as end-members, their mixing can be translated into the following equations, which refer to $\delta^{18}O$ and ^{3}H parameters:

$$-6.4\times(1-R)+X\times R=-6.6 \quad (1)$$

$$5\times(1-R)+Y\times R=4 \quad (2)$$

Where,

- −6.4 (‰) is the value of $\delta^{18}O$ for the local water. It corresponds to the approximation to first decimal place of the value (−6.37‰) achieved from the "infiltration average altitudes/$\delta^{18}O$ values" relationship, considering the average altitude of the Scansano zone (500 m a.s.l.). At this value of altitude, the upper and lower limit of the 95% confidence interval of regression line in Figure 4 are −6.32‰ and −6.42‰, respectively;
- −6.6 (‰) is the value of $\delta^{18}O$ for the result of the mixing. It is the approximation to first decimal place of the value (−6.64‰) achieved by the average of the data of the twelve water points (wells and springs) which are representative of such mixing. The standard deviation "σ" of the data set is 0.07;
- 5 (TU) is the value of ^{3}H for the local water. It corresponds to the approximation of the average value (5.1 TU; σ = 0.4) of the tritium annual data of rainfall for the years 2004 and 2005 (just before the study period);

- 4 (TU) is the value of ^{3}H for the result of the mixing. It is the approximation of the value (3.8 TU) achieved by the average of the available data for the water points which are representative of the mixing (number of points = 4; σ = 0.3);
- $(1 - R)$ and R are, respectively, the percentages of local and regional groundwater involved in the mixing;
- X and Y are, respectively, the $\delta^{18}O$ and ^{3}H values of the regional groundwater.

It should be noted that the differences between the isotopic values inserted in the equations for the local water and for the mixing result are of the order of the analytical error (for both $\delta^{18}O$ and ^{3}H). Even so, taking into account the performed approximations, the σ values and the 95% confidence interval above mentioned, it is possible to state that such differences are significant.

Solving the Equations (1) and (2) for R, and after simplifications, the following equation is achieved:

$$X = -7.4 + 0.2Y \quad (3)$$

Taking into account the ^{3}H values of the local input and of the mixing result, the ^{3}H value in regional groundwater is necessarily less than 4.0 TU. A value in the range 0–3 TU can be considered realistic, given that:

- based on the morphology, the average altitude achieved from the $\delta^{18}O$ value of the mixing indicates as the regional groundwater flow is activated more than 13 km from Scansano. Especially in such hydrostructural context, a resident time of several tens of years is consequently probable, and in this case the range 0-3 TU is consistent with the tritium curve showed in Figure 9;
- as showed by the evolution of the $\delta^{18}O$ values occurring in groundwater along the Scansano-Magliano in Toscana ridge, a significant rate of local infiltration in sandstone occurs, consequently to modify the value from 5 TU (local groundwater) up to 4 TU (mixing result) a tritium content abundantly lower than 4 TU is likely for regional groundwater.

Assuming that Y in Equation (3) is 0 or 3 TU, alternatively, we obtain $\delta^{18}O$ values of −6.8‰ and −7.4‰, which indicate recharge average altitudes for the regional groundwater within the range 700–1000 m (a.s.l.); at these two extreme conditions of mixing, percentages of regional groundwater (R) of 50% and 20% are respectively achieved. Such average altitudes, if crossed with the morphologic and hydrostructural features of the region, suggest that the main recharge area for regional groundwater could develop among Mt. Labbro, Rocchette, Catabbio and Petricci, in which calcarenites and limestone outcrop (Figure 1). Indeed, the volcanites of Mt. Amiata (altitudes up to 1700 m a.s.l.) are not involved in regional flow because for this aquifer the infiltration is completely balanced by perennial yield [33]. Thus, in agreement with the general low permeability of the lithologies, important contributes from the zone between Scansano and Roccalbegna (Figure 1) may also be excluded, because in the absence of input from Mt. Amiata they would lead to lower recharge average altitudes than 700–1000 m (a.s.l.).

A preliminary conceptual model for the groundwater flow in the sandstone aquifer can be at this point proposed (Figure 10):

- regional groundwater, mainly fed from the Mt. Labbro-Rocchette-Catabbio-Petricci zone, reaches the sandstones aquifer in the Scansano zone by means of an upflow in the fault systems, and mixes with the local infiltration water. An uprising of regional groundwater along such fault systems was also suggested by Francese *et al*. (2009) [24];
- groundwater resources resulting from such mixing are partially drained by springs and withdrawn by wells, and partially take part in a groundwater flow system that with continuity develops within sandstones at least up to Magliano in Toscana, where a groundwater transfer toward the alluvial system also occurs.

Figure 10. Groundwater flow conceptual model: (**a**) simplified map of the hydrogeological complexes and location of the main recharge area supposed for regional groundwater; (**b**) hydrogeological cross section showing hypothesized flow lines of the components involved in the groundwater flow.

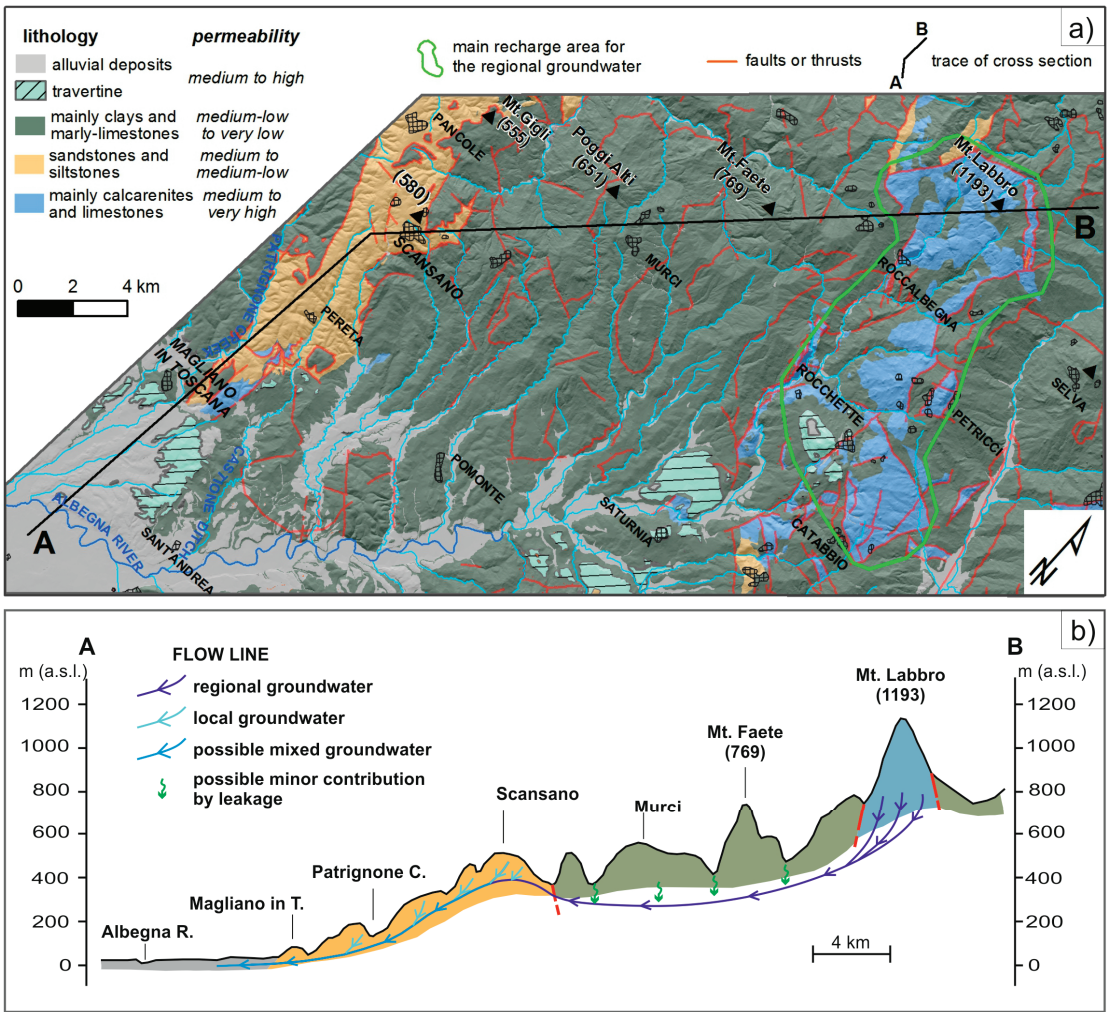

4. Conclusions

The water isotopes, which were analyzed in groundwater, allowed us to define the groundwater framework in the area of Scansano-Magliano in Toscana ridge and to propose a conceptual hydrogeological model. Thanks to a detailed isotopic characterization of infiltration water, which

was achieved by analyzing minor springs opportunely selected, the data of groundwater from wells and major springs highlighted the presence of a main groundwater flow system. The latter develops with continuity within the sandstones complex for more than 12 km, moving from Scansano up to Magliano in Toscana, where at least partially it transfers groundwater to the alluvial aquifer system. In the highest part of such groundwater system, nearby Scansano, the isotopes suggest a mixing process that involves local infiltration water and regional groundwater, whose recharge area, on the base of $\delta^{18}O$ and ^{3}H mass balances, seems mainly develops on the calcarenite and limestones outcropping in the Mt. Labbro-Rocchette-Catabbio-Petricci zone, more than 15 km away from Scansano.

The results discussed in this work underpin that water isotopes help groundwater flow understanding, especially in fractured aquifer for which the application of conventional methodology is not always effortless. In the specific case, the isotopic tools pointed out as the sandstone aquifer of the Scansano-Magliano in Toscana ridge may be a strategic and alternative resource for water supplying, given the overexploitation and contamination of the nearby alluvial aquifers. In this context, the sandstone aquifer, in addition to representing an important water source for the isolated villages that exist on the ridge, might also be tapped to improve, both in quality and quantity, the water supplying for the villages in the nearby coastal plain. Indeed, in the latter, especially during the summer period, the high water demand linked to the touristic vocation of the region leads to an excessive drawdown in the local groundwater body with consequent seawater intrusion occurrence and worsening of water quality.

Finally, the achieved results encourage and promote more detailed surveys of the chemical, geophysical, and hydrodynamic type, which should be aimed at defining what zones of the sandy aquifer are more suitable for groundwater exploitation.

Acknowledgments

The authors wish to thank Sandra Trifiro', Enrico Calvi, Elisa Ferrari, Maurizio Catania, Caterina Giorgi of the IGG-CNR for their precious work in field sampling and laboratory analyzing. The authors thank the editor and two anonymous reviewers for their useful comments, which helped us to improve the manuscript. This research was financially supported by a grant of AATO6-Ombrone.

Author Contributions

Both Authors planned and carried out this research, and cooperated in the elaboration and interpretation of the achieved data. The paper was prepared under the direction of Marco Doveri.

Conflicts of Interest

The authors declare no conflict of interest.

References

1. Panichi, C.; Gonfiantini, R. Environmental isotopes in geothermal studies. *Geothermics* **1978**, *6*, 143–161.
2. Fontes, J.C. Environmental Isotopes in Groundwater Hydrology. In *Handbook of Environmental Isotope Geochemistry*, 1st ed.; Fritz, P., Fontes, J.C., Eds.; Elsevier Scientific Publishing: Amsterdam, The Netherlands, 1980; Volume 1, pp. 75–134.
3. Yurtsever, Y.; Gat, J.R. Atmospheric waters. In *Stable Isotope Hydrology (Deuterium and Oxygen-18 in the Water Cycle)*, 1st ed.; Technical Reports 210; Gat, J.R., Gonfiantini, R., Eds.; International Atomic Energy Agency (IAEA): Vienna, Austria, 1981; pp. 103–142.
4. Clark, I.; Fritz, P.; Precipitation. In *Environmental Isotopes in Hydrogeology*, 1st ed.; Stein, J., Starkweather, A.W., Eds.; Lewis Publishers CRC Press: Boca Raton, FL, USA, 1997; pp. 63–78.
5. Wood, W.W.; Sanford, W.E. Chemical and isotopic methods for quantifying groundwater recharge in a regional, semiarid environment. *Ground Water* **1995**, *33*, 458–468.
6. Mohammad, Z.I. Application of environmental isotopes in storm-discharge analysis of two contrasting stream channel in a watershed. *Water Res.* **1998**, *32*, 2959–2968.
7. Marfia, A.M.; Krishnamurthy, R.V.; Atekwana, E.A.; Panton, W.F. Isotopic and geochemical evolution of ground and surface waters in a karst dominated geological setting: A case study from Belize, Central America. *Appl. Geochem.* **2004**, *19*, 937–946.
8. Doveri, M.; Menichini, M.; Cerrina Feroni, A. Stable water isotopes as fundamental tool in karst aquifer studies: Some results from isotopic applications in the Apuan Alps carbonatic complexes (NW Tuscany). *Italian J. Eng. Geol. Environ.* **2013**, *1*, 33–50.
9. Consorzio Lamma. Territorio: Geologia, Carta Geologica Regionale 1:10,000. Available online: http://www.lamma.rete.toscana.it/territorio/geologia (accessed on 15 January 2013).
10. Servizio Idrologico Regionale: Archivio dati. Available online: http://www.sir.toscana.it (accessed on 21 March 2013).
11. Vittorini, S. Ricerche sul clima della Toscana in base all'evapotraspirazione potenziale e al bilancio idrico. *Rivista Geografica Italiana* **1972**, *1*, 1–30.
12. Boccaletti, M.; Elter, P.; Guazzone, G. Plate tectonics models for the development of Western Alps and Northern Apennines. *Nature* **1971**, *234*, 108–111.
13. Boccaletti, M.; Coli, M.; Decandia, F.A.; Giannini, E.; Lazzarotto, A. Evoluzione dell'Appennino settentrionale secondo un nuovo modello strutturale. *Memorie della Società Geologica Italiana* **1981**, *21*, 359–373.
14. Molli, G. Northern Apennine-Corsica orogenic system: An updated review. *Geol. Soc. Lond. Spec. Publ.* **2008**, *298*, 413–442.
15. Mongelli, F.; Zito, G. Flusso di calore nella regione Toscana. *Studi Geologici Camerti* **1991**, *1*, 91–98.
16. Elter, P. L'ensemble ligure. *Bulletin de la Société Géologique de France* **1975**, *17*, 984–997.
17. Marroni, M.; Treves, B. Hidden terranes in the northern Apennines, Italy: A record of Late Cretaceous-Oligocene transpressional tectonics. *J. Geol.* **1998**, *106*, 149–162.

18. Nirta, G.; Pandeli, E.; Principi, G.; Bertini, G.; Cipriani, N. The Ligurian Units of Southern Tuscany. *Bollettino della Società Geologica Italiana* **2005**, *3*, 29–54.
19. Jolivet, L.; Daniel, J.M.; Truffert, C.; Goffé, B. Exhumation of deep crustal metamorphic rocks and crustal extension in back-arc regions. *Lithos* **1994**, *33*, 3–30.
20. Carmignani, L.; Decandia, F.A.; Disperati, L.; Fantozzi, P.L.; Lazzarotto, A.; Liotta, D.; Oggiano, G. Relationships between the Sardinia-Corsica-Provencal Domain and the Northern Apennines. *Terra Nova* **1995**, *7*, 128–137.
21. Brunet, C.; Monié, P.; Jolivet, L.; Cadet, J.P. Migration of compression and extension in the Tyrrhenian Sea: Insights from 40Ar/39Ar ages on micas along a transect from Corsica to Tuscany. *Tectonophysics* **2000**, *321*, 127–155.
22. Carmignani, L.; Kligfield, R. Crustal extension in the Northern Apennines: Transition from compression to extension in the Alpi Apuane core complex. *Tectonics* **1990**, *9*, 1275–1303.
23. Brogi, A.; Lazzarotto, A.; Liotta, D.; Ranalli, G. Extensional shear zones as imaged by reflection seismic lines: The Larderello geothermal field (Central Italy). *Tectonophysics* **2003**, *363*, 127–139.
24. Francese, R.; Mazzarini, F.; Bistacchi, A.; Morelli, G.; Pasquarè, G.; Praticelli, N.; Robain, H.; Wardell, N.; Zaja, A. A structural and geophysical approach to the study of fractured aquifers in the Scansano-Magliano in Toscana Ridge, southern Tuscany, Italy. *Hydrogeol. J.* **2009**, *17*, 1233–1246.
25. Fritz, P.; Fontes, J.C. Introduction. In *Handbook of Environmental Isotope Geochemistry*, 1st ed.; Fritz, P., Fontes, J.C., Eds.; Elsevier Scientific Publishing: Amsterdam, The Netherlands, 1980; Volume 1, pp. 1–19.
26. Epstein, S.; Mayeda, T. Variation of O^{18} content of waters from natural sources. *Geochim. Cosmochim. Acta* **1953**, *4*, 213–224.
27. Coleman, M.L.; Shepherd, T.J.; Durham, J.J.; Rouse, J.E.; Moore, G.R. Reduction of water with zinc for hydrogen isotope analysis. *Anal. Chem.* **1982**, *54*, 993–995.
28. Longinelli, A.; Selmo, E. Isotopic composition of precipitation in Italy: A first overall map. *J. Hydrogeol.* **2003**, *270*, 75–88.
29. Mussi, M.; Leone, G.; Nardi, I. Isotopic geochemistry of natural water from the Alpi Apuane-Garfagnana area, Northern Tuscany, Italy. *Mineral. Petrogr. Acta* **1998**, *41*, 163–178.
30. Doveri, M.; Nisi, B.; Cerrina Feroni, A.; Ellero, A.; Menichini, M.; Lelli, M.; Masetti, G.; Da Prato, S.; Principe, C.; Raco, B. Geological, hydrodynamic and geochemical features of the volcanic aquifer of Mt. Amiata (Tuscany, central Italy): An overview. *Acta Vulcanol.* **2011–2012**, *23–24*, 51–72.
31. International Atomic Energy Agency and World Meteorological Organization. *Global Network of Isotopes in Precipitation: The GNIP Database*. Available online: http://isohis.iaea.org (accessed on 24 November 2005).
32. Doveri, M.; Leone, G.; Mussi, M.; Zanchetta, G. Composizione isotopica di acque ipogee nell'Antro del Corchia (Alpi Apuane, Toscana nord-occidentale). *Memorie dell'Istituto Italiano di Speleologia Serie 2* **2005**, *18*, 119–132.

33. Barazzuoli, P.; Bosco, G.; Nante, N.; Rappuoli, D.; Salleolini, M. The aquifer of Mount Amiata: Evaluation of the perennial yield and its quality. *Memorie della Società Geologica Italiana* **1994**, *48*, 825–832.
34. Craig, H. Isotopic Variation in meteoric waters. *Science* **1961**, *133*, 1702.
35. Gat, J.R.; Carmi, I. Evolution of the isotopic composition of atmosferic waters in the Mediterranean area. *J. Geophys. Res.* **1970**, *75*, 3039–3048.
36. Minissale, A.; Magro, G.; Vaselli, O.; Verrucchi, C.; Perticone, I. Geochemistry of water and gas discharges from the Mt. Amiata silic complex and surrounding areas (central Italy). *J. Volcanol. Geotherm. Res.* **1997**, *79*, 223–251.
37. Hauser, S.; Dongarrà, G.; Favara, R.; Longinelli, A. Composizione isotopica delle piogge in Sicilia. Riferimenti di base per studi idrogeologici e relazioni con altre aree mediterranee. *Rendiconti della Società Italiana di Mineralogia e Petrologia* **1980**, *36*, 671–680.
38. Leone, G.; Mussi, M. Gli isotopi ambientali nelle acque di sorgenti e pozzi e nelle emergenze sulfuree sottomarine di Capo Palinuro, Salerno. *Geologia tecnica e ambientale* **2004**, *3*, 35–55.
39. Celati, R.; Grassi, S.; D'Amore, F.; Marcolini, L. The low temperature hydrothermal system of Campiglia, Tuscany (Italy): A geochemical approach. *Geothermics* **1991**, *20*, 67–81.

Section 2: *Multi-Isotope Studies*

Isotopes as Tracers of Water Origin in and Near a Regional Carbonate Aquifer: The Southern Sacramento Mountains, New Mexico

Christopher J. Eastoe and Ryan Rodney

Abstract: High-elevation groundwater sampled in 2003 in the Sacramento Mountains defines a line resembling an evaporation trend in δD-$\delta^{18}O$ space. The trend results from recharge of winter precipitation into fractured limestone, with evaporation prior to recharge in broad mountain valleys. The same trend occurs in basin groundwater east and west of the range, indicating the high Sacramento Mountains as the principal regional water source, either direct from the limestone aquifers or from mountain-derived surface water. Tritium and carbon-14 indicate bulk residence times of a few decades in the high Sacramento Mountains and at Alamogordo, and of thousands of years south of Alamogordo and in the artesian aquifer near Artesia. Stable O, H isotope data fail to demonstrate the presence of Sacramento Mountains water in a saline aquifer of the Hueco Bolson (Texas).

Reprinted from *Water*. Cite as: Eastoe, C.J.; Rodney, R. Isotopes as Tracers of Water Origin in and Near a Regional Carbonate Aquifer: The Southern Sacramento Mountains, New Mexico. *Water* **2014**, *6*, 301-323.

1. Introduction

In the Basin and Range province of the southwest USA, stable isotope studies have proved useful in distinguishing sources of recharge where altitude effects are large, e.g., Tucson Basin [1], or where isotope effects due to latitude/altitude and evaporation generate river water that is distinctive beside native basin groundwater [2,3].

The Sacramento Mountains of south-central New Mexico (Figure 1) include a broad area of forested, well-watered terrain, the source of perennial streams flowing east toward the Roswell Basin and the Pecos River and of intermittent streams flowing west into the Tularosa Valley. Pre-development and recent water level data indicate groundwater movement from Tularosa Valley to the Hueco Bolson [4–6]. Mayer and Sharp [7] suggested regional flow of groundwater from the Sacramento Mountains to the Texas-New Mexico border, through karst aquifers.

Figure 1. Map showing the study areas. Abbreviations are: NM = New Mexico; TX = Texas; A = Alamogordo; C = Cloudcroft; E = Elk; EP = El Paso; FM = Franklin Mountains; HB = Hueco Bolson; M = Mayhill; OM = Organ Mountains; P = Piñon; R = Red Bluff; T = Tularosa; TV = Tularosa Valley; W = Weed. X-X' is the line of the geological section in Figure 2.

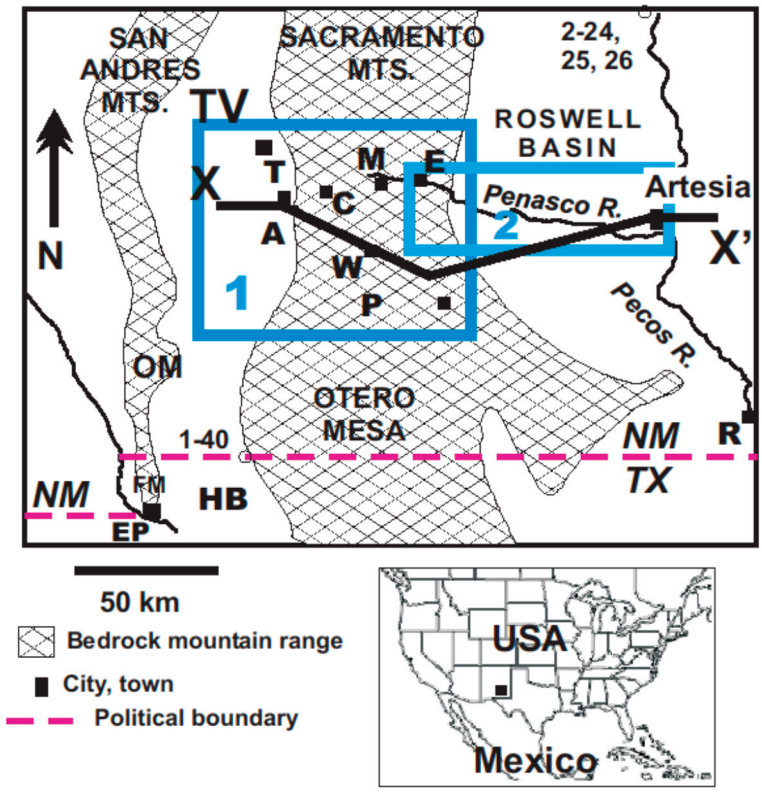

Groundwater samples for this study were collected in the Sacramento Mountains and the flanking basins from 2003 to 2008. The aim of the study was to use environmental isotopes to determine the relationship between water from the Sacramento Mountains and the adjacent basin aquifers. The relationship between groundwater in the high mountains and that in the Tularosa Valley, the deep alluvial basin to the west, is the first topic to be addressed. The relationship between groundwater in the high mountains and that in the hard-rock Roswell artesian basin to the east is the second topic to be addressed. In both cases, we also attempt to constrain groundwater residence times, and to determine the seasonality of recharge. Finally, we discuss whether the isotope signature of Sacramento Mountains groundwater can be recognized as far south as the Hueco Bolson in Texas (Figure 1).

2. Background

Figure 1 shows the location of the study areas. Area 1, encompassing the Sacramento Mountains near Cloudcroft and Weed, and the freshwater lens on the western flank of the mountains, encompasses sites sampled for the first topic described above. Area 2 stretches from the eastern flank of the mountains to the Pecos River at Artesia, and encompasses sites samples for the second topic.

2.1. Topography, Climate and Vegetation

The Sacramento Mountains rise to 2500–2800 m above sea level (m.a.s.l.) in the study area. A steep western escarpment with deep canyons abuts the Tularosa Valley, a typical fault-bounded basin of the Basin-and-Range province. Tularosa Valley continues southward into Texas where the valley is named the Hueco Bolson; Neogene alluvium fills the entire extent of the combined basin to depths of 600 to 3000 m in the basin center [6]. The eastern flank of the Sacramento Mountains approximates a dip-slope, and descends gradually toward the Pecos River. No deep alluvial basin is present on the east side of the range. The climate in the basins is semi-arid; average annual precipitation is 335 mm at Alamogordo and 340 mm at Artesia. In the high mountains, precipitation is higher, e.g., 715 mm at Cloudcroft near the range crest [8]. There are two wet seasons, a weak summer monsoon (June to October) providing 65%–70% of the precipitation, and a winter season of rain and snow from frontal weather systems [8]. The amounts of both winter and summer precipitation vary greatly from year to year (Figure 15 of [9]). Vegetation consists of coniferous forest interspersed with grassy valleys above 2300 m.a.s.l.. At lower elevation, scrubby oak forest and desert scrub predominate, except along perennial streams where riparian forest is present. Much of the study area is dry ranch land on which groundwater pumping is essential to the survival of cattle herds. Large-scale irrigated agriculture, using quarter-section and larger center-pivot and side-roll equipment, is practiced on the Pecos River flood plain near Artesia. Scattered irrigated plots are present near Tularosa.

2.2. Geology

The Sacramento Mountains constitute a tilted horst with range-bounding faults on the western side (Figure 2), and consist of Paleozoic marine sedimentary rocks, mostly Permian-Mississippian limestone and evaporite, overlying concealed Precambrian basement [9,10]. The surface east of the range crest approximates a dip slope, with a discontinuous veneer of lower members of the San Andres formation overlying dolomite and anhydrite of the Yeso formation, both overlain to the east by the Queen-Grayburg anhydrite and limestone and dolomite of the San Andres formation. Thin (40 m) Quaternary alluvium overlies Paleozoic strata on the Pecos River flood plain. West of the range crest, the entire Paleozoic section of the region, mainly carbonate strata, is exposed. Neogene alluvium fills the Tularosa Valley to depths of 230 to 300 m at Alamogordo.

2.3. Geohydrology

The carbonate strata constitute a regional aquifer system conveying water from the mountains to the basins, eastward from the range crest through the Yeso formation, and westward through the highly fractured Paleozoic carbonate section. A map of the potentiometric surface east of the range crest is available in ([9], Figure 18), and indicates general eastward groundwater flow. West of the range crest, groundwater levels are less precisely known within area 1, but they decline steeply towards the west and southwest elsewhere on the escarpment [9]. In the high mountains, the geohydrology is complex and governed by the detailed lithology of the Yeso formation. The following geohydrologic features are present ([9], Figure 25): a regional aquifer, locally confined

beneath impermeable interbeds of the Yeso formation, and probably continuous with regional aquifers east of the range; multiple perched aquifers overlying the regional aquifer, some discharging in small springs controlled by impermeable strata; and vadose zones above and between the perched aquifers. Large summer rain events in 2006 and 2008 caused rapid water-level response in the perched aquifers, but slower response in the regional aquifer. In the Roswell artesian basin, a shallow unconfined aquifer is present in carbonate strata overlying the Queen-Grayburg anhydrite, at depths less than 100 m below the surface at Artesia. The regional aquifer in this area, at 200–300 m below the surface, is confined beneath the Queen-Grayburg anhydrite and was artesian at the time of first development; subsequent pumping has lowered static water levels by tens of meters (Table 1) [11]. Groundwater is present in an unconfined basin-fill aquifer in the alluvium of the Tularosa Valley, where supply wells pump water from the upper 50 m.

Figure 2. Cross section X-X' (see Figure 1 for location), after Roswell Geological Society (1956). SL = sea level. The east slope of the Sacramento Mountains is a dip-slope with widespread veneer, too thin to depict here, of the Glorieta Sandstone and overlying members of the San Andres formation.

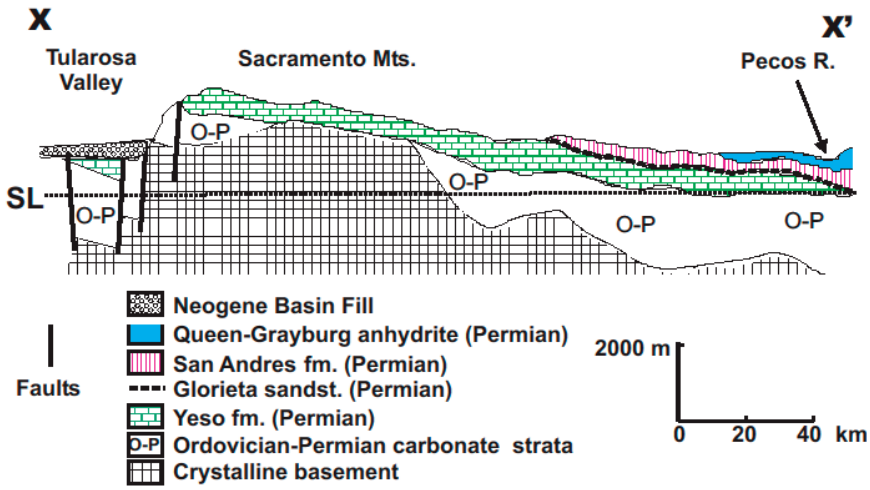

2.4. Previous Isotope Studies

Stable oxygen and hydrogen isotope and tritium data were collected for rainwater, surface water and groundwater from Roswell Basin in the late 1970s [12,13], in order to identify sources of recharge and groundwater residence times. The authors concluded that more detailed sampling was required, but were able to identify loci of local, rapid recharge using tritium data in the mountain areas and near Roswell [13]. Stable oxygen and hydrogen isotope data for surface water in the Pecos River [14,15], have been used to determine the relative contributions of winter snow and monsoon precipitation to the river in Texas, the authors concluding that the latter predominates [14]. Sulfur isotopes in Sacramento Mountains groundwater have been utilized to determine the relative inputs of evaporite gypsum, oxidized sulfides and rain sulfate to the dissolved sulfate inventory [16]. Reference [17] provided stable O and H isotope and ^{14}C data for the well-field supplying water to the air-force base in Tularosa Valley, and interpreted the data to indicate water residence times greater than 1000 years. The most detailed recent work is in reference [9], which presented detailed

stable isotope data for precipitation and groundwater collected in 2006–2009 between the range crest and Hope, New Mexico. The authors identified predominant summer recharge in years of heavy summer rainfall, and used tritium, ^{14}C and CFCs to estimate groundwater residence times of decades in the high mountains, to thousands of years in the aquifer extending east of the range. The pattern of stable O and H isotope data in groundwater presented in reference [9] differs markedly from that in our dataset, allowing for an improved understanding of the hydrology of the mountain range when both datasets are taken into account. Our study also complements reference [9] in extending spatial coverage into flanking basins east and west of the Sacramento Mountains.

3. Methods

3.1. Analytical Methods

Samples were taken from domestic, agricultural and municipal production wells, springs, and surface water in the Peñasco and Pecos Rivers, and from rain gauges near Weed. Isotope measurements (except accelerator mass spectrometry carbon-14) were performed at the Environmental Isotope Laboratory, University of Arizona. Stable O, H and C isotopes were measured on a Finnigan Delta S® dual-inlet mass spectrometer equipped with an automated CO_2 equilibrator (for O) and an automated Cr-reduction furnace (for H). Stable S isotopes were measured on a Thermo Electron Delta Plus XL® continuous flow mass spectrometer equipped with a Costech® elemental analyzer for preparation of SO_2. Carbon-14 was measured by accelerator mass spectrometry at the NSF-Arizona Accelerator Facility, University of Arizona. Data generated for this study are listed in Table 1. Analytical precisions (1σ) are 0.08‰ (O), 0.9‰ (H), 0.15‰ (C) and 0.15‰ (S). Detection limits are 0.6 TU (^3H) and 0.2 pMC (^{14}C).

3.2. Correction of Raw Carbon-14 Data

The data lack sufficient detail for chemical balance modeling; therefore a simpler method based on $\delta^{13}C$ values is used, following ([18], p. 210). Values of $\delta^{13}C$ for soil gas are assumed to be −23‰ (corresponding to 100% C3 plant matter input) for the forested mountains, and −19.9‰ (corresponding to 75% C_3 input) for desert areas. “Dead” rock carbonate of Guadalupian age has $\delta^{13}C$ values from +1 to +5‰ [19,20]; for these strata corrections were calculated for +1‰ and +4‰. Corrected ages are given in Table 1. In the basin-fill aquifer near Alamogordo, corrections were calculated for rock $\delta^{13}C$ from 0‰ to +3‰, representing the entire Paleozoic section.

Table 1. Site information and isotope data.

Well	Site name (Group)	Lat	Long	Site altitude m.a.s.l.	Date	Well depth m	SWL m.a.s.l.	$\delta^{18}O$ ‰	δD ‰	$\delta^{34}S$ ‰	$\delta^{13}C$ DIC ‰	Tritium TU	C-14 pMC	Corrected age yrs BP
Study area 1: high Sacramento Mountains														
1-1	Fields (H2)	32.959	−105.525	2270	10 December 2003	121	na	−7.9	−53	12.1	−8.2	0.5	82.0	post-bomb
1-2	Cloudcroft well 4 (H1)	32.9505	−105.7019	2550	8 August 2003	164	2474.5	−9.3	−63	10.3	−9.8	5.1	82.7	post-bomb
1-3	Ehret (W)	32.945	−105.8405	2007	9 August 2003	206	1861.5	−9.9	−71					
1-4	Bearden (W)	32.9601	−105.8844	1627	10 August 2003	9	na	−8.5	−61			2.3		
1-5	Macon (W)	32.9951	−105.8437	1900	9 August 2003	19	1886.0	−9.7	−66	12.3		2.4	78.5	post-bomb
1-6	Macon spring (W)	32.9951	−105.8437	1900	9 August 2003	na	na	−9.5	−66			2.5		
1-7	Williams (W)	32.9905	−105.894	1624	9 August 2003	16	na	−9.6	−66	12.3		1.3	72.6	post-bomb
1-8	Warnock (W)	32.9892	−105.8474	1820	8 August 2003	90	1793.6	−9.9	−66	12.2		1.7	72.5	post-bomb
1-9	Sect. 22 Water Assoc.Spr. (W)	32.991	−105.871	1760	9 August 2003			−9.6	−66			A 0.5		
1-10	Posey spring (H1)	32.793	−105.5779	2450	7 December 2003			−9.3	−64	9.0	−10.2	5.7	95.0	post-bomb
1-11	Sky Ridge (H1)	32.792	−105.5672	2350	7 December 2003	na	na	−9.6	−65					
1-12	Sky Ridge spring (H1)	32.794	−105.5783	2355	7 December 2003			−9.4	−64		−9.7			
1-13	Scott (H2)	32.798	−105.5521	2230	7 December 2003	48	na	−8.1	−57		−9.4			
1-14	Sac. Methodist Academy (H2)	32.794	−105.558	2240	7 December 2003	na	na	−8.6	−60		−9.9	0.7		
1-15	Essek (H1)	32.716	−105.5305	2225	7 December 2003	273	na	−10.2	−69	13.0	−4.3	2.0	22.1	2,000–4,500
1-16	Wright (H2)	32.7414	−105.4793	2075	9 December 2003	na	na	−8.1				2.9		
1-17	Bell (H2)	32.7414	−105.4793	2075	8 December 2003	na	na	−8.2	−57					
1-18	Stewart (H2)	32.6953	−105.4219	2035	8 December 2003	252	na	−8.1	−57	12.2	−7.4	0.6	44.3	1,800–2,800
1-19	Sand spring (H1)	32.713	−105.684	2600	7 December 2003			−10.0	−68		−9.5			
1-20	Apple Tree Canyon spring (H1)	32.713	−105.747	2380	7 December 2003			−9.9	−66	12.1	−10.1	6.2	92.8	post-bomb
Study area 1: Alamogordo and Tularosa														
1-21	Abercrombie	33.091	−106.015	1380	25 January 2005	91	1330.0	−8.5	−59			2.1		
1-22	Cates	33.075	−106.045	1347	25 January 2005	na	na	−10.5	−67		−8.1		84.4	post-bomb
1-23	Hornback	33.062	−106.063	1326	25 January 2005	42	1305.4	−8.2	−59		−8.1	2.0	79.7	post-bomb
1-24	Cinert	33.040	−106.011	1357	25 January 2005	na	na	−8.4	−59		−4.6	1.2	36.5	post-bomb
1-25	McGinn	32.99	−105.99	1360	25 January 2005	56	na	−9.1	−63					

Table 1. *Cont.*

Well	Site name (Group)	Lat	Long	Site altitude	Date	Well depth	SWL	$\delta^{18}O$	δD	$\delta^{34}S$	$\delta^{13}C$ DIC	Tritium	C-14	Corrected age
1-26	Dyer	32.9157	−105.9864	1319	8 August 2003	58	1291.7	−8.9	−62	12.6		3.3		
1-27	McDonald	32.9009	−106.0069	1299	8 August 2003	91	1279.3	−8.9	−62	12.1	−6.0	1.2		
1-28	Dellacorino	32.90	−105.96	1326	25 January 2005	96	na	−9.1	−63					
1-29	Noriega	32.8954	−105.9885	1303	9 August 2003	30	na	−8.9	−62		−6.3	3.9	53.6	post-bomb
1-30	City of Alamogordo well 2	32.9681	−105.9369	1440	September 2003	na	na	−8.9	−63		−6.0	1.3	50.6	post-bomb
1-31	City of Alamogordo well 8	32.9681	−105.9369	1440	September 2003	na	na	−9.0	−63					
1-32	Harrington	32.9462	−105.9469	1402	8 August 2003	121	na	−9.1	−63	12.6		1.6		
1-33	Moore	32.83	−105.96	1294	8 August 2003	61	1259.0	−9.3	−64	11.2	−6.0	<0.5	39.8	500–2,200
1-34	Boyle	32.81	−105.99	1253	25 January 2005	46	1234.8	−9.5	−66			A 0.5		
1-35	Harrell	32.81	−105.99	1253	25 January 2005	61	1233.3	−9.4	−65					
1-36	Baca	32.81	−105.99	1253	25 January 2005	76	1239.4	−9.2	−64					
1-37	Mount	32.74	−105.97	1234	25 January 2005	52		−9.0	−63					
1-38	Wisdom	32.744	−105.966	1237	25 January 2005	49	1203.1	−9.2	−64					
	Southeastern Tularosa Valley													
1-39	Otero County landfill	32.562	−106.025	1230	22 March 2004	na	na	−8.9	−69		−3.8	<0.6	2.9	17,850–21,000
1-40	El Paso WU Brine injection site	31.973	−106.106	1269	early 2007	na	na	−9.5	−71		−1.8	<0.4	2.8	12,100–18,500
1-40	El Paso WU Brine injection site	31.973	−106.106	1269	early 2008	na	na	−9.5	−70					
	Study area 2													
2-1	Unnamed spring	32.931	−105.282	1750	July 2006			−7.9	−55					
2-2	J. Powell windmill	32.955	−105.277	1758	July 2006	73	1694.0	−7.9	−55		−8.9	1.8	75.2	post-bomb
2-3	J. Powell well	32.979	−105.248	1748	July 2006	24	1732.8	−8.3	−58	12.3		1.5		
2-4	H. Powell	32.921	−105.252	1740	July 2006	33	1709.5	−8.4	−58					
2-5	Orton	32.892	−105.08	1602	July 2006	259	1419.1	−8.1	−56	13.8	−8.8	1.0	57.5	900–1600
2-6	Duncan	32.845	−104.892	1380	July 2006	na	na	−8.3	−56	12.4				
2-7	Young	32.840	−104.773	1277	July 2006	na	1086.5	−7.9	−55			<0.7		
2-8	Hope Water Co.	32.810	−104.734	1250	July 2006	na	na	−8.3	−58					
2-9	Bannon	32.783	−104.713	1042	July 2006	195	875.3	−8.3	−57		−6.7	<0.7	29.2	4,400–5,600
2-10	Jones	32.847	−104.613	1060	July 2006	na	999.0	−8.1	−54	14.3				

Table 1. *Cont.*

Well	Site name (Group)	Lat	Long	Site altitude	Date	Well depth	SWL	$\delta^{18}O$	δD	$\delta^{34}S$	$\delta^{13}C$ DIC	Tritium	C-14	Corrected age
2-11	Lamb	32.843	−104.568	1035	July 2006	na	na	−8.3	−57		−5.9	<0.6	29.9	2,600–4,000
2-12	Brown 1 D	32.741	−104.496	1085	July 2006	130	1021.0	−8.3	−58					
2-13	Brown 2 D	32.764	−104.534	1085	July 2006	130	na	−7.1	−51					
2-14	Brown 3 D	32.712	−104.552	1085	July 2006	na	na	−8.1	−57					
2-15	Joy 1 S	32.833	−104.378	1020	July 2006	81	1000.2	−7.9	−54	13.0				
2-16	Joy 2 D	32.834	−104.368	1020	July 2006	290	na	−8.3	−57	13.2		<0.5		
2-17	Pardue S	32.820	−104.362	1015	July 2006	61	954.0	−8.1	−55					
2-18	Rodney S	32.882	−104.424	1045	July 2006	64	990.1	−7.8	−55					
2-19	Mayberry 3 S	32.925	−104.412	1032	July 2006	61	1000.0	−7.2	−51	12.8		1.3		
2-20	Mayberry 4 D	32.925	−104.412	1032	July 2006	304	na	−8.4	−58	13.4				
2-21	Mayberry 2 D	32.937	−104.412	1030	July 2006	304	975.1	−8.2	−56	13.8	−6.1	0.5	33.7	1,350–3,000
2-22	Mayberry 1 D	32.963	−104.509	1070	July 2006	274	na	−8.3	−58	13.4	−5.4		35.6	
2-23	Menefee D	32.970	−104.508	1072	July 2006	274	1044.6	−8.2	−57	13.1				
	Roswell													
2-24	Hatfield N well	33.574	−104.482	1105	May 2007	na	na	−6.6	−49					
2-25	Hatfield E well	33.572	−104.479	1104	May 2007	na	na	−7.6	−53					
2-26	Hatfield artesian	33.574	−104.483	1104	May 2007	na	na	−8.4	−56					
	Surface Water	32.887	−105.186	1730	July 2006			−8.4	−57	12.7				
	Rio Penasco	32.886	−104.344	1010	July 2006			−3.3	−34	12.2				
	Pecos river	32.886	−104.344	1010	December 2006			−6.5	−49					
	Pecos R.	33.209	−104.395	1041	December 2006			−6.7	−51					
	Pecos R.	33.382	−104.404	1056	May 2007			−2.7	−35					
	Pecos R.													
	Precipitation													
1-8		32.9892	−105.8474		August 2003			−6.4	−47			4.6		
1-16		32.7414	−105.4793	2075	August–October 2003			−10.4	−70			4.7		
1-16		32.7414	−105.4793	2075	March 2004			−8.2	−54			7.4		
1-13		32.798	−105.5521	2230	August–September 2003			−6.8	−57			3.9		

Notes: S = shallow aquifer, D = Deep (Principal) aquifer in Artesia area; na = not available; A = Apparent tritium; * meters below surface.

4. Area 1: High Sacramento Mountains

Samples were collected from wells near La Luz and Fresnal canyons and areas near New Mexico Route 24 east of the range crest (Figure 3). All samples are from fractured limestone except for 1–4, which is from shallow alluvium in Fresnal Canyon.

Figure 3. Sample location map for areas 1and 2 (see Figure 1). Stream/canyon names are abbreviated thus: AC = Agua Chiquita; Bw = Bluewater; Fr = Fresnal; LL = La Luz; SR = Sacramento River. Town/village names are A = Alamogordo; C = Cloudcroft; M = Mayhill; T = Tularosa; W =Weed. Site numbers (e.g., 1) correspond to entries in Table 1, where the corresponding number is 1-1 for area 1, or 2-1 for area 2. Black circles: sample sites for this study; white circles: sample sites from reference [17].

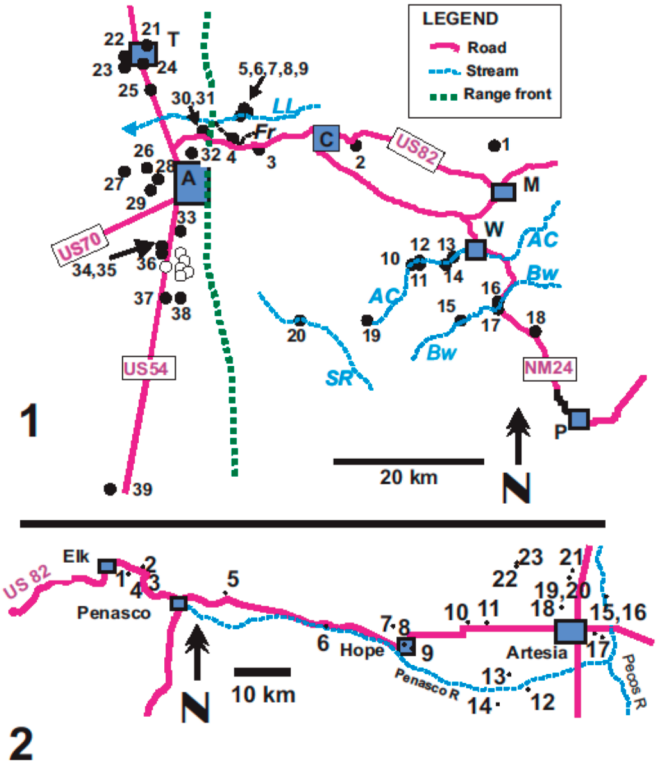

4.1. O and H Isotopes

On a plot of δD vs. $\delta^{18}O$, most of the data fall on a straight line with a slope near 5.6 (Figure 4A), henceforth called the Sacramento Mountains Trend (SMT). The straight line intersects an estimate of average winter precipitation at a station at 2790 m.a.s.l. (calculated as arithmetic means (because amount data are not available) of $\delta^{18}O$ and δD for three bulk collections in March 2007, 2008 and 2009, and representing the prior 3 months; data from [9]), but does not intersect mean summer precipitation [9] for that station. In Figure 4B, three groups of $\delta^{18}O$ values emerge in relation to site altitude. For the wells, collar altitude is used because static water levels are not available in all cases. Values of $\delta^{18}O$ of group W (western slopes) overlap those of group H1 (high elevations), despite the large altitude difference between the two groups. The difference between groups H2 (high elevations, but generally lower than H1) and H1 is too great to attribute to altitude. Group H2 sites (1-13, 1-14,

1-16, 1-17) are adjacent to broad, flat, canyon bottoms, a typical geomorphic feature of the Sacramento Mountains. In such places, deep soil (more than 1 m near site 1-16) overlies carbonate strata, while elsewhere carbonate outcrop is widespread. The data for groundwater in 2003 differ from data for groundwater in 2006–2009 [9]. The latter occupy a field between the SMT and summer rain for 2006 and 2008 (Figure 4A), and reflect rapid recharge from heavy monsoon rains in 2006 and 2008. Prior to 2003, there had been no large monsoon rain totals since 1997.

Figure 4. (**A**) Plot of $\delta^{18}O$ *vs.* δD for groundwater samples from the high Sacramento Mountains. The green line encloses groundwater isotope data from [9]. Seasonal means for precipitation and the local meteoric water line (LMWL) are for years 2006–2009 [9]. Data plotted as individual points were collected for this study in 2003; (**B**) Plot of elevation of well collars *vs.* $\delta^{18}O$ for sample sites in the high Sacramento Mountains. The diagonal lines show the long-term $\delta^{18}O$ lapse-rates of −1.2‰/1000 m (Tucson Basin [21], and 1.8‰/1000 m [13]. Site numbers (e.g., 3) correspond to entries in Table 1, where the corresponding number is 1-3.

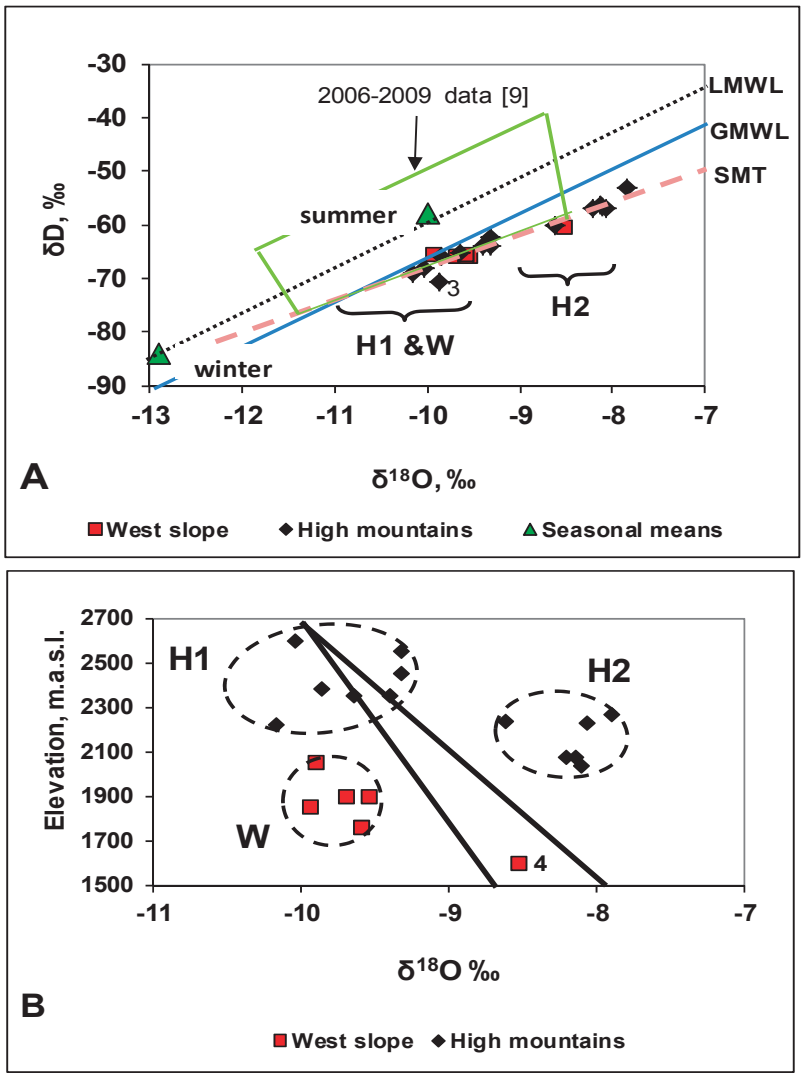

4.2. Other Parameters

Groundwater in this area generally has $\delta^{34}S$ values of 10‰ to 13‰, tritium concentrations of 1 to 3 TU, and ^{14}C in the range 72 to 93 pMC (cf. 0 to 7 TU, and 83 to 93 pMC, for samples from 2006 to 2008 [9]). Corrected ^{14}C data indicate post-bomb water in the west-slope canyons and in two high-elevation springs, with older groundwater (300–4500 years) at sites 1–15 and 1–18 (Table 1).

4.3. Interpretation

The SMT can be explained as an evaporation trend originating in winter precipitation. Evaporation prior to infiltration varies in degree, and is greatest in groundwater near the broad canyon bottoms, (sites 1–13, 1–14, 1–16 and 1–17), where standing water and wet soil are likely to undergo partial evaporation. Well-mixed high altitude groundwater will plot between groups H1 and H2, and this isotope signature will be found in groundwater of the limestone aquifer at lower elevations unless water of different isotope composition is added downgradient. Evaporated runoff from high elevations may plot on the SMT to the right of group H2. Addition of water from local low-elevation precipitation would shift groundwater isotopes towards the GMWL.

The difference between the 2003 and 2006–2009 data sets indicates two modes of recharge. In years with unusually wet summers, (e.g., 2006 and 2008), summer recharge with little evaporation is the dominant source of recharge. The local meteoric water line (LMWL) in Figure 4A is governed by rainfall from those years, and may not apply under drier conditions. Following a succession of dry to average summers, however, winter recharge predominates, even though there is more precipitation in summer than in winter rain on average. Such was the case from summer 1998 to 2003 when sampling for this study occurred. Under these conditions, evaporation of the infiltrating water occurs in the broad canyon bottoms east of the range crest, but is not observed between the range crest and the canyons on the steep west escarpment.

Tritium and corrected ^{14}C contents of high-elevation groundwater indicate the presence of post-bomb recharge, but tritium levels in 2003 were predominantly lower than average tritium in post-1992 precipitation (4–7 TU, see Table 1 and [9]; compare a better-constrained average of 5.3 TU for Tucson [22]), indicating mixing with pre-bomb meteoric water. By 2006–2008, more post-bomb recharge was present, tritium-helium dates were mainly 1–15 years, and CFC ages were largely 20–30 years [9]. Values of $\delta^{34}S$ indicate Permian marine gypsum (+12‰ to +13‰) as the main source of sulfate; lower values most likely reflect oxidation of sulfide present in these strata [16].

5. Area 1—Alamogordo and Tularosa

Sampling from supply wells in basin-fill alluvium represents lower-TDS water suitable for human consumption; brackish water is also present >5 km west of the range front. Groundwater in this area flows west at Alamogordo and Tularosa [4,5], but parallel to the range front south of Alamogordo, where no major canyons contribute water to the basin.

5.1. O and H Isotopes

Most data plot on the SMT (Figure 5), to the right of group W. Samples from Tularosa include the most and least evaporated of the set. Data for wells south of site 1-33 ($\delta^{18}O$ between −9.9‰ and −9.5‰ in reference [17]) differ from data collected for the present study in the same area ($\delta^{18}O$ between –9.5‰ and –9.0‰). Actual variation in $\delta^{18}O$ (as opposed to measurement error) is unlikely in such old groundwater (see below); the earlier data are not used here. In southeastern Tularosa Valley, sites 1-39 and 1-40 (Figure 1) have groundwater that plots below the SMT

Figure 5. Plot of $\delta^{18}O$ *vs.* δD for groundwater samples from basin sediments near Alamogordo and Tularosa, in relation to samples from La Luz and nearby canyons and the high Sacramento Mountains. Samples 1-39 and 1-40 are from basin fill more than 40 km south of Alamogordo (see Figures 1 and 3).

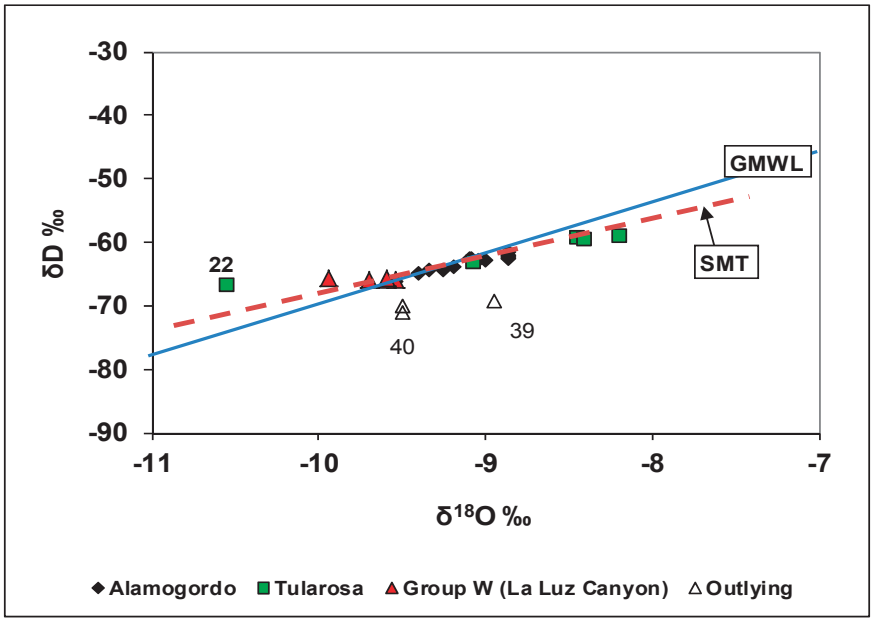

5.2. Other Parameters

Tritium is present (1-3 TU) north of site 1-33, and is generally absent (below detection to 0.5 TU) south of 1-33. ^{14}C generally decreases from near 80 pMC near Tularosa to 20 pMC south of Alamogordo (Figure 6). Corrected ^{14}C data indicate young groundwater (post-bomb to a few hundred years) north of Alamogordo and in La Luz canyon, and much older water (500–7500 years, considering also corrected data from [17]) south of Alamogordo. Values of $\delta^{34}S$ are near +12‰. At sites 1–39 and 1–40, tritium is below detection, ^{14}C levels are 3 pMC, and corrected ages are 12,000 to 21,000 years (Table 1).

Figure 6. Detail of Figure 3, showing distribution of carbon-14 (pMC) in groundwater samples. Black circles: this study; white circles: data from [17].

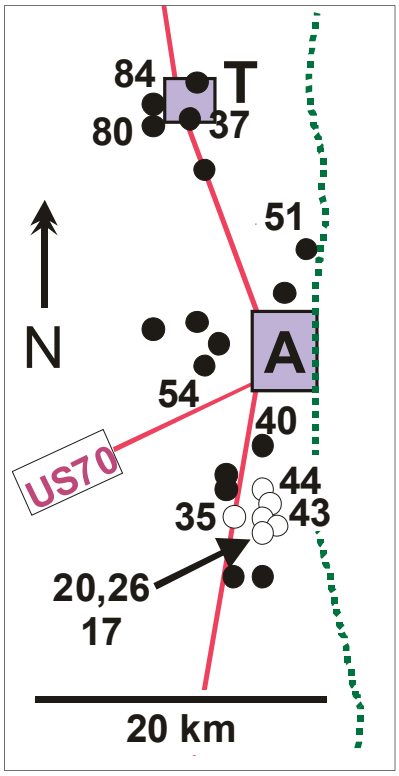

5.3. Interpretation

O and H isotope data plotting on the SMT indicate high-elevation precipitation as the source of groundwater in basin alluvium near Alamogordo and Tularosa. Groundwater from the high Sacramento Mts. flows to La Luz Canyon sample sites without isotopic shift. The higher degree of evaporation in samples from the alluvial aquifer could be explained: (1) as mountain-block recharge combining more-evaporated and less-evaporated recharge from high elevations; or (2) as mountain-front recharge of surface water supplied from high elevations by way of the mountain canyons. The absence of an evaporation signature in groundwater from carbonate strata in La Luz Canyon, between the range crest and the basin) argues against the first possibility, while the presence of evaporated water in the alluvium argues for the second. The higher degree of evaporation of groundwater farther from the range front (Tularosa, 12–15 km from the range front), in contrast to groundwater nearer to the range front (Alamogordo, within 6 km), suggests that the sites of infiltration of surface water extend into the basin, rather than being confined to a narrow zone at the range front. This is particularly evident in the case of site 1-22 at Tularosa, (Figure 5), where the coincidence of low δD and $\delta^{18}O$ with high ^{14}C indicates recharge of very recent runoff at a distance of up to 15 km from the range front. Both mountain-front and mountain-block recharge seem likely, but the data do not indicate the relative amounts. In the basin fill south of Alamogordo, tritium and ^{14}C data are consistent with slow southward flow of groundwater, with little recharge from nearby mountain canyons.

6. Area 2: Peñasco to Artesia

Samples were collected between Peñasco and Artesia (Figure 3). Near Peñasco, groundwater samples were taken from a spring and a windmill in limestone, and from wells in the Rio Peñasco flood plain. East of the range front, as far as site 2-10, an unconfined aquifer (the principal aquifer of [11]) is present near the boundary of the Yeso and San Andres formations. Recharge to these strata may occur near the range front. Samples are from domestic and agricultural wells up to 260 m deep, with static water levels (SWLs) near 190 m below the surface. East of site 2-10, beneath a broad plain west of the Pecos River, two major aquifers were sampled. An unconfined aquifer with SWLs from 30 to 60 m below the surface exists in flood-plain sediments near Artesia. The eastward continuation of the principal aquifer, 275 to 300 m below the surface, is confined beneath the Queen-Grayburg anhydrite (Figure 2). It was artesian at the time of first exploitation; SWLs at present range from 20 to 60m below the surface. Surface water samples were collected from the Peñasco and Pecos Rivers.

From Peñasco to Hope, groundwater flow is east-southeast (Figure 18 of [9]). Allowing for variation due to pumping, SWLs in the principal aquifer east of Hope are close to 1000 m.a.s.l. (Table 1). Southward flow is likely in this area.

6.1. O and H Isotopes

All groundwater and surface water samples plot close to the SMT (Figure 7A). Most data cluster at the intersection of the SMT with the GMWL, where the separation of the lines is less than 2‰ in δD, and therefore impossible to resolve within measurement error. Data for the principal aquifer from Mayhill to Hope [9] match the present data set in δD but include lower values of $\delta^{18}O$. Two groundwater samples from near Artesia (2-13, 2-19) plot to the right of the main data cluster. Surface water from the Pecos River in the reaches between Artesia and Red Bluff ([15] for 1984–1987, [14] for 2005, and data from this study) largely plot as a linear trend, close to an extrapolated SMT (Figure 7A,B).

At the range front, groundwater from limestone (sites 2-1, 2-2) is distinct in $\delta^{18}O$ from groundwater and surface water in the Rio Peñasco flood plain (sites 2-3, 2-4) (Figure 7, inset). These two groups of data bracket the $\delta^{18}O$ range of the principal aquifer to the east. The unconfined aquifer at Artesia has $\delta^{18}O$ values >–8.1‰, higher than for the principal aquifer; two of the samples (2-15, 2-17) may plot on the GMWL, while one other (2-19) plots on the SMT. One principal aquifer sample (2-10) plots above the GMWL. Three outlying samples (2-24, 25 and 26, locations in Figure 1) from the principal (artesian) and shallow aquifers near Roswell plot on a trend similar to, but slightly above, the SMT.

Previous data for the principal aquifer [13] pre-date automated isotope methods, and partially overlap the main data cluster from the present study. The two data sets correspond in $\delta^{18}O$, but the older δD data have a spread >20‰, apparently spurious, and appear not to be useful. Weighted precipitation averages from [12] are for $\delta^{18}O$ alone, and have been plotted on the GMWL in Figure 7.

6.2. Tritium

In 1977-1978, when bomb tritium averaged about 35 TU in local precipitation, surface water and alluvial groundwater from the Peñasco River flood plain contained about 10 TU, and tritium in the principal aquifer near Artesia was below detection [13]. In samples collected for this study, tritium is present at low levels (<2 TU) in groundwater from near the range front (sites 2-2, 2-3, 2-5), at site 2-19 in the shallow aquifer, and in one deep aquifer sample (site 2-21, 0.5 TU); at other sites it is below detection (Figure 8). Groundwater from the alluvial aquifer beneath the Peñasco River (site 2-3) contains 1.5 TU, distinctly lower than the average for precipitation, and consistent (*cf.* [13]), with a large pre-bomb groundwater contribution to the surface water of the river. Reference [9] listed tritium contents <2 TU in groundwater between Elk and Hope.

Figure 7. (**A**) Plot of $\delta^{18}O$ *vs.* δD for groundwater and surface water samples from study area 2. (**A**) All data from this study. The field of data from [13] is for the principal aquifer from Artesia to Roswell, and encompasses all but three outlying data points. The inset shows a magnified view of clustered data. Site numbers (e.g., 1) correspond to entries in Table 1, where the corresponding number is 2-1; (**B**) Plot of $\delta^{18}O$ *vs.* δD for the Pecos River between Artesia and Red Bluff, from other studies [14,15], relative to the SMT.

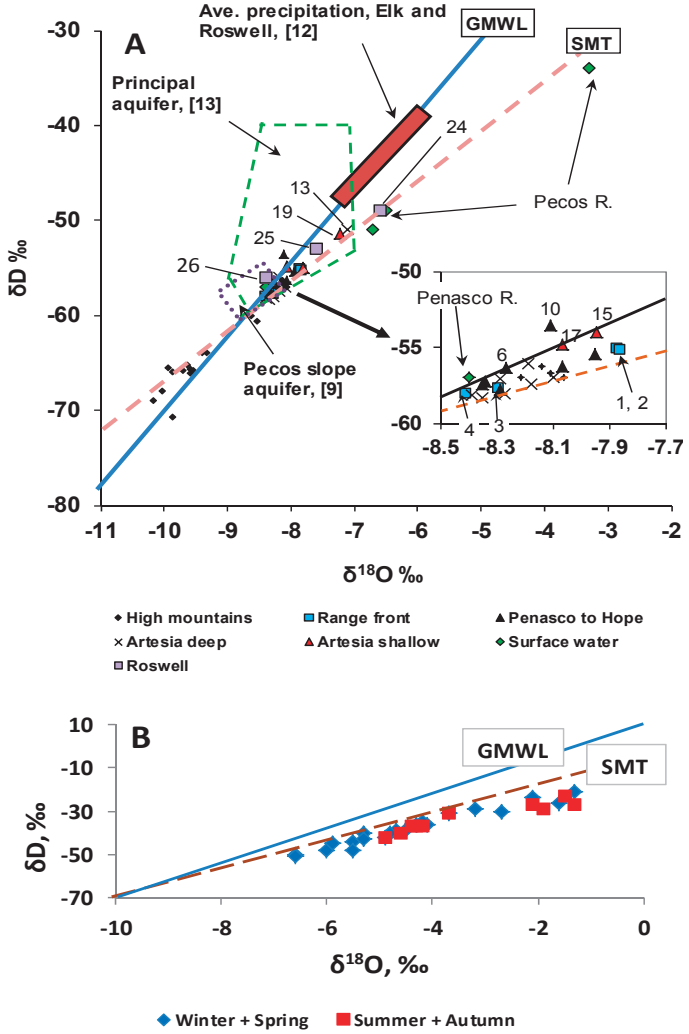

Figure 8. A. East-west profile of Area 2 (refer to Figure 2 for location) showing well depths and static water levels (SWL) in relation to the surface. "Shallow" refers to the shallow aquifer at Artesia, and "deep" to the deeper artesian aquifer. Also shown are measurements of carbon-14 (pMC) and tritium (TU). Tritium below detection is indicated as "bd".

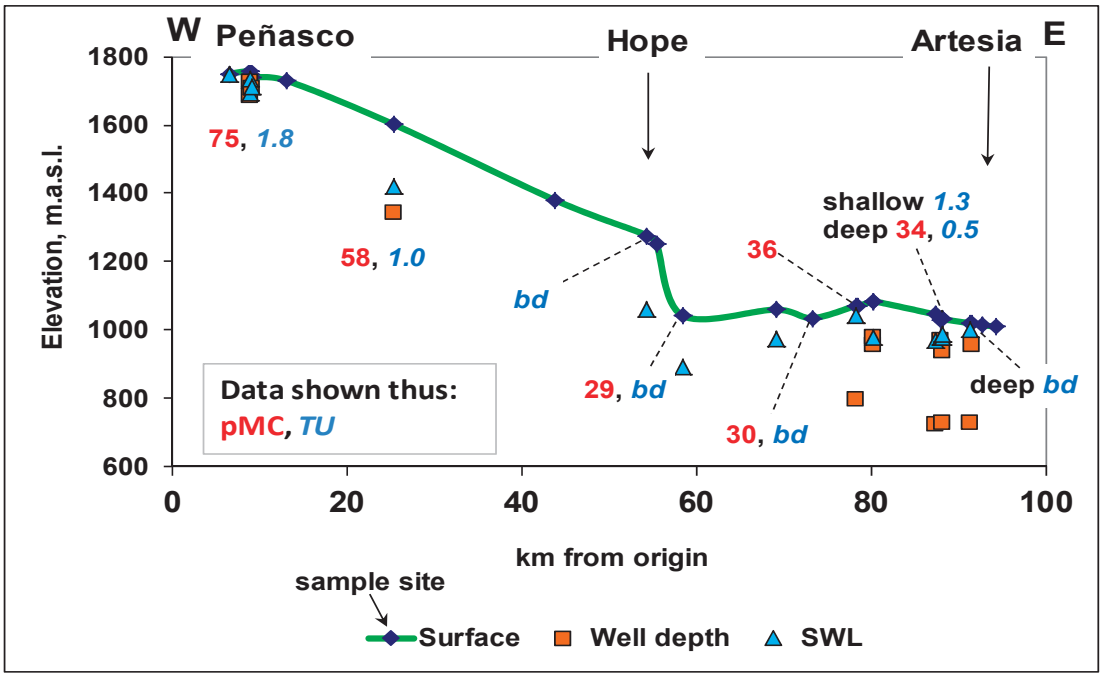

6.3. Other Parameters

^{14}C is higher (78 and 55 pMC, corrected to 115 and 82 pMC) in two samples (2-2, 2-5) from near the range front, than in four samples between Hope and Artesia, (29–36 pMC, corrected to 50–70 pMC (Figure 8). Reference [9] gave 40–50 pMC in most groundwater between Elk and Hope. Values of $\delta^{34}S$ are 12‰ to 14‰.

6.4. Interpretation

Groundwater in the Pecos Slope and artesian aquifers is largely uniform in isotope content over an east-west extent of about 100 km, and lies on or close to the SMT. A dominant water source in the high Sacramento Mountains is therefore likely. East of Peñasco, a few samples (2-13, 2-19, 2-24 and 2-25) have isotope data plotting on the SMT, but to the right of the main data cluster; these may reflect local recharge of evaporated surface water. Site 2-13 is close to the ephemeral lower reach of the Rio Peñasco, where recharge of evaporated surface water may occur. The other three samples are from the shallow aquifer beneath irrigated fields, where reflux of evaporated irrigation water is probable. Addition of local rainwater is likely for site 2-10 (Figure 7).

Bulk groundwater residence times (the corrected versions of the data shown in Figure 8) in the principal aquifer are 1300 to 5600 years east of Hope, greater than those suggested in [13].

Most of the $\delta^{18}O$ and δD data for the Pecos River between Artesia and Red Bluff plot on a linear trend close to an extrapolated SMT, regardless of season (Figure 7B), and can be therefore be

generated as a result of evaporation of water like that in the principal aquifer at Artesia. The principal source of river water in this area is therefore most likely the Sacramento Mountains, either by natural recharge from the aquifer, or by way of irrigation on the Pecos flood plain. If this is true, mountain-derived water is discharged with an isotope signature of evaporation into the river near Roswell and Artesia. This suggests a modification to the modeling, based on deuterium excess, of river water sources in reference [14].

7. Discussion

7.1. Water Sources in Study Area

Most water sampled for this study plots on the Sacramento Mountains trend (SMT) in δD–$\delta^{18}O$ space. The SMT originates in high-altitude winter precipitation. Such precipitation is therefore the principal and ultimate source of groundwater in the area between Alamogordo and the Pecos River. Most water in the Pecos River near Artesia also appears to be of that origin. There is scant evidence for recharge of local meteoric water at low altitudes. The few exceptions include groundwater from the southeastern part of Tularosa Valley (where ancient water from high elevations appears to be present), and some unconfined-aquifer samples from Artesia (where local recharge probably occurs).

7.2. Seasonality of Recharge

The heavy monsoon rains of 2006 and 2008 generated recharge of distinctive δD–$\delta^{18}O$ signature in groundwater of the high Sacramento Mountains, but in drier years, 2007 and 2009, groundwater isotopes shifted towards the SMT [9]. Monsoon rainfall comparable to that in 2006 had not occurred since 1997, and in the 2003 sampling for this study, winter recharge, plotting on the SMT as a result of local evaporation prior to infiltration, was predominant. Where old groundwater is present (south of Alamogordo and in the principal aquifer of Roswell Basin), δD and $\delta^{18}O$ conform largely to the SMT. In the long term, therefore, recharge in dry to average years contributes the larger volume to low-elevation aquifers around the Sacramento Mountains. Years with unusually wet summers lead to a transient (a few years) response in the high-altitude aquifers, but make little contribution to the old groundwater in basins at the foot of the mountains.

The Sacramento Mountains are therefore an unusual example of a mountain block in which the dominant season of recharge can change in response to seasonal precipitation amounts, although winter precipitation, only 35% of total precipitation on average, predominates in the long-term. Winter recharge is considered predominant in a number of other mountain ranges in the arid western USA. In the Spring Mountains, Nevada, another carbonate-rock range, winter precipitation is dominant; summer rain contributes about 30% of annual precipitation, but only about 10% of recharge [23]. Winter recharge also predominates in the Huachuca Mountains, Arizona, where summer precipitation contributes 54% of the annual total on average, but winter precipitation accounts for 65% ± 25% of recharge [24]. In the Santa Catalina Mountains, Arizona [25], and the ranges delimiting the Verde River watershed, Arizona [26], winter recharge is considered predominant, contributing 98% of recharge in the latter case.

7.3. Sacramento Mountain Carbonate Strata as a Karst Aquifer

A continuum of aquifers exists in carbonate rock [27]. At one extreme, carbonate dissolution leads to wide solution cavities that self-organize into dendritic drainage networks discharging through large springs; water flow rates are commonly 10^2 to 10^4 m/day over distances of 10^3 to 10^4 m. At the other extreme, solution cavities are narrow and of limited interconnection, generating an aquifer with lower flow rates and discharge through many small springs. Although small-scale collapse structures are recognized [9], cavern networks are not developed in the thinly bedded strata, some impermeable, of the study area. A flow rate of 10 m/day over 30 km between the range crest and the eastern range front would result in water travel times of about 8 years. The tritium and ^{14}C data imply residence times >60 years in the mountain aquifers several cases, while surface water in the Rio Peñasco and associated flood-plain groundwater also contain some pre-bomb precipitation. The isotope evidence indicates widespread persistence of pre-bomb precipitation in groundwater, and flow rates typically much lower than 10 m/day. The Sacramento Mountains therefore fall at the latter end of the continuum of karst aquifers as described above.

Nonetheless, the carbonate strata in and east of the Sacramento Mountains compose a regional aquifer system over a distance of 130 km. Regional carbonate aquifers of similar extent have been demonstrated elsewhere in the region on the basis of geochemical modeling, east of the Salt Basin in West Texas [28], and in the region southwest of the Cuatrocienegas Basin of Coahuila, Mexico [29].

7.4. Mode of Mountain-Front Recharge to Basin Alluvium

The location of mountain-front recharge relative to the interface between hard-rock mountain blocks and basin alluvium in the southwest USA has been addressed in several studies. In the middle Rio Grande Basin (New Mexico), infiltration is thought to occur in a narrow zone along the range front of the Sandia and Manzano Mountains [30]. In Chino Valley (Arizona) [26] and Tucson Basin (Arizona) [1], evidence indicates infiltration from stream beds downstream of the mountain fronts, at distances of 6 to 10 km in the case of Tucson Basin. Groundwater isotope data also indicate recharge of ponded surface water in the center of the Hueco Bolson (Texas) [31]. The present study concurs with the possibility of infiltration as far as 15 km downstream of the range front.

7.5. Source of Hueco Bolson Groundwater

The question addressed here is the source of saline water in the center of the Hueco Bolson, an alluvial basin near El Paso, Texas, 100–130 km southwest of Alamogordo (Figure 1). Subsurface movement of groundwater from the Tularosa Valley to the Hueco Bolson is physically possible according to piezometric data [4,6]. An alternative source is recharge from the Organ and Franklin Mountains (Figure 1), which supply a freshwater aquifer, the Franklin Mountains freshwater lens (FMFWL) in ancient fluvial deposits at the western edge of the Hueco Bolson [6]. The catchment for the FMFWL is largely at altitudes between 1300 and 2400 m.a.s.l. in the Organ Mountains, in contrast to a catchment at 2400–2800 m.a.s.l. for the four large canyons that focus fresh water from

the Sacramento Mountains into basin sediment near Alamogordo. H and O isotopes might therefore discriminate between the two sources, as discussed inconclusively in [31].

Groundwater from the FMFWL plots along the global meteoric water line with $\delta^{18}O$ values between –9‰ and –11‰ (Figure 9). The upper end of the data array corresponds to groundwater of short residence time, while the lower end corresponds largely to groundwater resident for thousands of years [2]. The SMT and the suggested paleo-SMT (based on samples 1-39 and 1-40) intersect the FMFWL trend near –9‰ and –11‰, respectively. On the one hand, the $\delta^{18}O$ and. δD values of the saline, evaporated water in the center of the Hueco Bolson plot between the SMT and the paleo-SMT, and could therefore represent mixtures of older and younger water from the Sacramento Mountains. On the other hand, $\delta^{18}O$ and. δD values define an evaporation trend that could originate in older FMFWL water, so that the water could have originated in the Frankin and Organ Mountains, perhaps as surface water ponded and evaporated in the basin center at a time of cooler, wetter climate. The stable isotopes fail to distinguish the two possibilities because of the likely presence of ancient groundwater.

Figure 9. Plot of $\delta^{18}O$ *vs*. δD showing: (**a**) The Sacramento Mountains Trend (SMT, as in Figure 4) and data for groundwater at Alamogordo; (**b**) Data for groundwater in the Hueco Bolson in Texas, from [2] and [24], distinguished according to salinity (HB-saline at the basin center, and HB-fresh from the Franklin Mountains fresh water lens on the western side of the basin); (**c**) A suggested paleo-SMT based on two samples of ancient water in the southeastern part of Tularosa Valley.

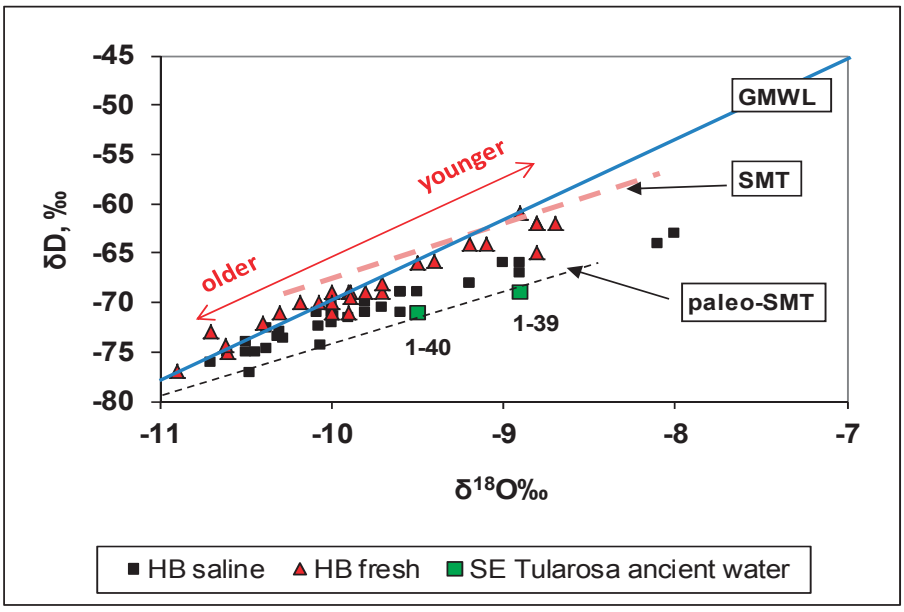

7.6. Implications for Groundwater Management

High-elevation winter recharge is the principal source of groundwater over the long term in the aquifers of the Sacramento Mountains and the flanking basins. If winter precipitation declines, for instance in response to global climate change, groundwater supply will decrease. The effect would be felt initially in the high mountain communities such as Weed and Cloudcroft (but might be

mitigated if occasional wet summers persist) and in areas from La Luz Canyon to Alamogordo and Tularosa where groundwater is of post-bomb age (Table 1). In the Roswell basin, where artesian water has been resident for thousands of years, there would be no short-term effect of diminished winter recharge; over-pumping for irrigation would be of more immediate concern.

8. Conclusions

Stable O and H isotopes have proved useful as environmental tracers in determining the relationships among various occurrences of groundwater in the study area, and the seasonality of recharge. Tritium and ^{14}C have provided valuable constraints on groundwater residence times.

A. Relationship between groundwater in the Sacramento Mountains and in flanking basins. Groundwater sampled from the high Sacramento Mountains in 2003 has a characteristic isotope signature. On a $\delta^{18}O$ *vs*. δD diagram, it plots on an evaporation trend (the Sacramento Mountains trend, SMT) of slope near 5.6. Recharge in subsequent years of high summer precipitation plots above the SMT, and has the isotope signature of summer rain [9]. The SMT signature is found in carbonate and basin-fill aquifers west and east of the Sacramento Mountains, indicating winter precipitation in the high mountains as the principal long-term source of groundwater in those basins. Water derived from high elevations is supplied to aquifers at lower elevations by a combination of flow through the carbonate aquifers, and mountain-front recharge of surface water showing the isotope effect of evaporation.

Recharge of local low-altitude meteoric water and irrigation reflux occurs in the shallow aquifer at Artesia. The principal (artesian) aquifer of the Roswell Basin receives little or no recharge east of the range front (near Peñasco).

B. Groundwater residence times. Short residence times, a few decades, are characteristic of the high Sacramento Mountains (cf. [9]). Bulk residence times for groundwater near Hope and Artesia range from 1000 to 5000 years. In Tularosa Valley, bulk residence times are a few decades near Alamogordo and Tularosa, hundreds to thousands of years immediately south of Alamogordo, and up to 20,000 years at distances of 50 or more km south of Alamogordo. The oldest water has $\delta^{18}O$ and δD values lower than those on the SMT.

C. Recharge seasonality. Groundwater plotting on the SMT is the result of winter recharge. However, both winter recharge and summer recharge can occur in the carbonate rock of the high Sacramento Mountains. Summer recharge is contributes greatly to mountain groundwater during years of unusually high monsoon rainfall [9], but winter recharge is predominant at other times.

D. Origin of waters more distant from the mountains. Surface water in the Pecos River between Artesia and Red Bluff has isotope compositions consistent with a predominant origin in the principal artesian aquifer of Roswell Basin. Groundwater of the central area of the Hueco Bolson near El Paso, Texas, may have originated from the Sacramento Mountains or from the Organ and Franklin Mountains. Stable H and O isotopes cannot distinguish the two sources.

Acknowledgements

Richard Warnock, Russell Wright and Elaine Wright of the Sacramento Mountains Watershed Restoration Corporation, and Monroe Curtis of Otero County introduced us to numerous well-owners who kindly permitted us to take samples. Bob Mayberry, A.J. Posey, Elaine Wright, Bobbie Melton and Richard Warnock accompanied us in the field. Lynwood Hume kindly provided river and groundwater samples from Roswell. The authors gratefully acknowledge the contributions of three reviewers, whose comments greatly improved the article. The study was funded though SAHRA (Sustainability of semi-Arid Hydrology and Riparian Areas) under the STC Program of the National Science Foundation, Agreement No. EAR-9876800, except for Study Area 2, where work was funded by the Environmental Isotope Laboratory at the University of Arizona.

Conflicts of Interest

The authors declare no conflict of interest.

References

1. Eastoe, C.J.; Gu, A.; Long, A. The Origins, Ages and Flow Paths of Groundwater in Tucson Basin: Results of a Study of Multiple Isotope Systems. In *Groundwater Recharge in a Desert Environment: The Southwestern United States*, Water Science and Applications Series; Hogan, J.F., Phillips, F.M., Scanlon, B.R., Eds.; American Geophysical Union: Washington, DC, USA, 2004; Volume 9, pp. 217–234.
2. Eastoe, C.J.; Hibbs, B.J.; Olivas, A.G.; Hogan, J.; Hawley, J.; Hutchison, W.R. Isotopes in the Hueco Bolson Aquifer, Texas (USA) and Chihuahua (Mexico): Local and general implications for recharge sources in alluvial basins. *Hydrogeol. J.* **2008**, *16*, 737–747.
3. Eastoe, C.J.; Hutchison, W.R.; Hibbs, B.J.; Hawley, J.; Hogan, J.F. Interaction of a river with an alluvial basin aquifer: Stable isotopes, salinity and water budgets. *J. Hydrol*. **2010**, *395*, 67–78.
4. Meinzer, O.E.; Hare, F.R. *Geology and Water Resources of Tularosa Basin, New Mexico*; U.S. *Geological* Survey Water-Supply Paper 343; U.S. Government Printing Office: Washington, DC, USA, 1915; p. 317.
5. Huff, G.F. *Simulation of Ground-Water Flow in the Basin-Fill Aquifer of the Tularosa Basin, South-Central New Mexico, Predevelopment through 2040*; Scientific Investigations Report; U.S. Geological Survey: Reston, VA, USA, 2005; pp. 2004–5197.
6. Hibbs, B.J.; Boghici, R.N.; Hayes, M.E.; Ashworth, J.B.; Hanson, A.N.; Samani, Z.A.; Kennedy, J.F.; Creel, R.J. *Transboundary Aquifers of the El Paso/Ciudad Juarez/Las Cruces Region*; Contract Report; Texas Water Development Board, Austin & New Mexico Water Resources Research Institute: Las Cruces, NM, USA, 1997; p. 148.
7. Mayer, J.R.; Sharp, J.M., Jr. Fracture control of regional groundwater flow in a carbonate aquifer in a semi-arid region. *Geol. Soc. Am. Bull.* **1998**, *110*, 1657–1671.

8. National Oceanic and Atmospheric Administration. Climatography of the United States No. 81, Monthly Normals of Temperature, Precipitation and Heating and Cooling Degree Days, 1971–2000. Available online: http://cdo.ncdc.noaa.gov/climatenormals/clim81/NMnorm.pdf (accessed on 15 January 2013).
9. Newton, T.B.; Rawling, G.C.; Timmons, S.S.; Land, L.; Johnson, P.S.; Kludt, T.J.; Timmons, J.M. *Sacramento Mountains Hydrogeology Study*; New Mexico Bureau of Geology and Mineral Resources Open-File Report 543; New Mexico Bureau of Geology and Mineral Resources: Socorro, NM, USA, 2012; p. 78.
10. Roswell Geological Society; Stratigraphic Research Committee. *West-East Correlation Section, San Andres Mts. to N.Mex.-Texas Line, Southeastern New Mexico*; Roswell Geological Society: Roswell, NM, USA, 1956.
11. Havenor, K.C. The Hydrogeologic Framework of the Roswell Groundwater Basin, Chaves, Eddy, Lincoln, and Otero Counties, New Mexico. Ph.D. Thesis, University of Arizona, Tucson, AZ, USA, 1996.
12. Gross, G.W.; Hoy, R.N.; Duffy, C.J.; Rehfeldt, K.R. Isotope Studies of Recharge in Roswell Basin. In *Isotope Studies in Hydrologic Processes*; Perry, E.C., Jr., Montgomery, C.W., Eds.; Northern Illinois University Press: DeKalb, IL, USA, 1982; pp. 25–33.
13. Hoy, R.N.; Gross, G.W. *A Baseline Study of Oxygen 18 and Deuterium in the Roswell, New Mexico, Groundwater Basin*; New Mexico Water Resources Research Institute: Las Cruces, NM, USA, 1982; Volume 144, p. 98.
14. Yuan, F.; Miyamoto, S. Characteristics of oxygen-18 and deuterium composition in waters from the Pecos River in American Southwest. *Chem. Geol.* **2008**, *255*, 220–230.
15. Coplen, T.B.; Kendall, C. *Stable Oxygen and Hydrogen Isotope Ratios for Selected Sites of the U.S. Geological Survey's NASQAN and Benchmark Surface Water Networks*; U.S. Geological Survey Open-File Report 00-160; U.S. Geological Survey: Reston, VA, USA, 2000; p. 409.
16. Szynkiewicz, A.; Newton, B.T.; Timmons, S.S.; Borrok, D.M. The sources and budget for dissolved sulfate in a fractured carbonate aquifer, Southern Sacramento Mountains, New Mexico, USA. *Appl. Geochem.* **2012**, *27*, 1451–1462.
17. Huff, G.F. Apparent Age of Ground Water Near the Southeastern Margin of the Tularosa Basin, Otero County, New Mexico. In *Geology of White Sands: New Mexico Geological Society Guidebook*; Giles, K.A., Lueth, V.W., Lucas, S.G., Kues, B.S., Myers, R., Ulmer-Scholle, D.S., Eds.; New Mexico Geological Society: Alamogordo, NM, USA, 2002; Volume 53, pp. 303–307.
18. Clark, I.; Fritz, P. *Environmental Isotopes in Hydrogeology*; Lewis Publishers: Boca Raton, FL, USA, 1997; p. 328
19. Veizer, J.; Hoefs, J. The nature of $^{18}O/^{16}O$ and $^{13}C/^{12}C$ secular trends in sedimentary carbonate rocks. *Geochim. Cosmochim. Acta* **1976**, *40*, 1387–1395.
20. Colgan, R.E.; Scholle, P.A. Carbon isotopic stratigraphy of the San Andres Formation; A possible correlation tool? (Abstract). *Am. Assoc. Pet. Geologists Bull*. **1991**, *75*, 555.

21. Wright, W.E. δD and $\delta^{18}O$ in Mixed Conifer Systems in the U.S. Southwest: The Potential of $\delta^{18}O$ in Pinus Ponderosa Tree Rings as a Natural Environmental Recorder. Ph.D. Thesis, Department of Geosciences, The University of Arizona, Tucson, AZ, USA, 2001.
22. Eastoe, C.J.; Watts, C.J.; Ploughe, M.; Wright, W.E. Future use of tritium in mapping pre-bomb groundwater volumes. *Ground Water* **2011**, *50*, 87–93.
23. Winograd, I.J.; Riggs, A.C.; Coplen, T.B. The relative contributions of summer and cool-season precipitation to groundwater recharge, Spring Mountains, Nevada, USA. *Hydrogeol. J.* **1998**, *6*, 77–93.
24. Wahi, A.K.; Hogan, J.F.; Ekwurzel, B.; Baillie, M.N.; Eastoe, C.J. Geochemical quantification of semiarid mountain recharge. *Ground Water* **2008**, *46*, 414–425.
25. Cunningham, E.E.B.; Long, A.; Eastoe, C.J.; Bassett, R.L. Migration of recharge waters downgradient from the Santa Catalina Mountains into the Tucson Basin aquifer. *Hydrogeol. J.* **1998**, *6*, 94–103.
26. Blasch, K.W.; Bryson, J.R. Distinguishing sources of ground water recharge by using $\delta^{2}H$ and $\delta^{18}O$. *Ground Water* **2007**, *45*, 294–308.
27. Worthington, S.R.H.; Ford, D.C. Self-organized permeability in carbonate aquifers. *Ground Water* **2009**, *47*, 326–336.
28. Uliana, M.M.; Sharp, J.M. Tracing regional flow paths to major springs in Trans-Pecos Texas using geochemical data and geochemical models. *Chem. Geol*. **2001**, *179*, 53–72.
29. Wolaver, B.D.; Sharp, J.M.; Rodriguez, J.M.; Ibarra, F. Delineation of regional karstic aquifers: An integrative data approach. *Ground Water* **2008**, *46*, 396–413.
30. Plummer, L.N.; Bexfield, L.M.; Anderholm, S.K.; Sanford, W.E.; Busenberg, E. *Geochemical Characterization of Ground-Water Flow in the Santa Fe Group Aquifer System, Middle Rio Grande Basin, New Mexico*; U.S.G.S. Water-Resources Investigation Report 03-4131; U.S. Geological Survey: Reston, VA, USA, 2004; 1–395.
31. Druhan, J.L.; Hogan, J.F.; Eastoe, C.J.; Hibbs, B.; Hutchison, W.R. Hydrogeologic controls on groundwater recharge and salinization: A geochemical analysis of the Northern Hueco Bolson Aquifer, El Paso, Texas. *Hydrogeol. J.* **2008**, *16*, 281–296.

A Combined Radio- and Stable-Isotopic Study of a California Coastal Aquifer System

Peter W. Swarzenski, Mark Baskaran, Robert J. Rosenbauer, Brian D. Edwards and Michael Land

Abstract: Stable and radioactive tracers were utilized in concert to characterize geochemical processes in a complex coastal groundwater system and to provide constraints on the kinetics of rock/water interactions. Groundwater samples from wells within the Dominguez Gap region of Los Angeles County, California were analyzed for a suite of major cations (Na^+, K^+, Mg^{2+}, Ca^{2+}) and anions (Cl^-, SO_4^{2-}), silica, alkalinity, select trace elements (Ba, B, Sr), dissolved oxygen, stable isotopes of hydrogen (δD), oxygen ($\delta^{18}O$), dissolved inorganic carbon ($\delta^{13}C_{DIC}$), and radioactive isotopes (^3H, ^{222}Rn and $^{223,224,226,228}Ra$). In the study area, groundwater may consist of a complex mixture of native groundwater, intruded seawater, non-native injected water, and oil-field brine water. In some wells, Cl^- concentrations attained seawater-like values and in conjunction with isotopically heavier $\delta^{18}O$ values, these tracers provide information on the extent of seawater intrusion and/or mixing with oil-field brines. Groundwater ^3H above 1 tritium unit (TU) was observed only in a few select wells close to the Dominguez Gap area and most other well groundwater was aged pre-1952. Based on an initial ^{14}C value for the study site of 90 percent modern carbon (pmc), groundwater age estimates likely extend beyond 20 kyr before present and confirm deep circulation of some native groundwater through multiple aquifers. Enriched values of groundwater $\delta^{13}C_{DIC}$ in the absence of SO_4^{2-} imply enhanced anaerobic microbial methanogenesis. While secular equilibrium was observed for $^{234}U/^{238}U$ (activity ratios ~1) in host matrices, strong isotopic fractionation in these groundwater samples can be used to obtain information of adsorption/desorption kinetics. Calculated Ra residence times are short, and the associated desorption rate constant is about three orders of magnitude slower than that of the adsorption rate constant. Combined stable- and radio-isotopic results provide unique insights into aquifer characteristics, such as geochemical cycling, rock/water interactions, and subsurface transport and mixing.

Reprinted from *Water*. Cite as: Swarzenski, P.W.; Baskaran, M.; Rosenbauer, R.J.; Edwards, B.D.; Land, M. A Combined Radio- and Stable-Isotopic Study of a California Coastal Aquifer System. *Water* **2013**, *5*, 480-504.

1. Introduction

Widespread demands on the groundwater resources of Los Angeles County, California during the early 20th century have resulted in substantial groundwater-level declines, as well as associated coastal seawater intrusion and deteriorating water quality [1,2]. In an effort to stave off saltwater intrusion in the 1950s to the early 1970s, three series of injection wells were installed along the coast where injected water could create artificial hydraulic barriers, named West Coast Basin, Dominguez Gap, and Alamitos Gap barrier projects [3,4]. Over the past decade, ~26 to 37 million m^3 of water are annually injected into these three barriers and while seawater intrusion has been generally

reduced, at Dominguez Gap saltwater intrusion is still occurring [4]. This inefficiency in halting the seawater intrusion is due in part to an incomplete characterization of the stratigraphic architecture that partially controls the groundwater flow in this region. In an effort to better understand the geochemical character of this regional groundwater and to better predict future groundwater quality change, a study incorporating stable isotopes was initiated [4–6] and complemented with select U/Th radionuclide work.

Geochemical and isotopic tracers have been widely used to investigate rock/water interactions, recharge rates of meteoric water, evaporation effects, and groundwater transport phenomena [7,8]. For example, stoichiometric ratios of various cations and anions may provide insight into the chemical weathering rates of source minerals [9]. Oxygen isotopes in groundwater have been used to identify source water and to assess evaporation kinetics [10,11]. Furthermore, a fingerprint of historic fluctuations in water vapor and air mass trajectories can be preserved in the isotopic composition of meteoric groundwater [12,13]. The presence of ^{3}H, with a half-life of 12.3 years, in groundwater can provide information on recharge rates and vertical flow velocities [14]. Stable isotopic composition of carbon in the dissolved inorganic matter in groundwater may yield information on the carbonate equilibrium, infiltration of atmospheric CO_2, as well as the microbial degradation of organic matter. In principal, the ^{14}C concentration in groundwater can yield information on age data from a few thousand years to 45,000 years that can be used to help constrain groundwater flow velocities and direction, recharge rates, hydraulic conductivities, and effective porosity.

Select U/Th series radionuclides have been utilized to characterize an aquifer's physicochemical properties, such as adsorption-desorption rate constants and aquifer retardation factors [15–21]. Because the geochemical behavior of many contaminants of interest is quite similar to the geochemistry of select members of the U- and Th-series radionuclides, these nuclides can provide unique information on the rates of some of these subsurface processes [22]. The movement of a dissolved species in groundwater can be retarded by several processes, such as ion exchange, adsorption, diffusion into blind pores, chemical precipitation, and membrane filtration [15,23,24]. The retardation of these species depends on particular aquifer characteristics (e.g., lithology, water chemistry, residence time), but parameters that control the retardation factor and absorption-desorption rate constants are not fully understood [17–20,25]. In particular, the dependence of these parameters on aquifer characteristics that are complexly mixed with diverse source waters, warrants further study.

To apply our combined radio- and stable-isotope approach, a suite of groundwater samples from the Dominguez Gap region of the southwest Los Angeles Basin, California were collected and analyzed for major and minor ions, select trace elements (Ba, B, and Sr) and stable isotopes ($\delta^{18}O$, δD, $\delta^{13}C_{DIC}$), tritium (^{3}H) and a suite of U- and Th-series radionuclides (^{223}Ra, ^{224}Ra, ^{226}Ra, ^{228}Ra, and ^{222}Rn). The study area is tectonically active [26–29], and as a result, uplift and erosion have winnowed many of the fine-grained confining units that serve to protect the underlying aquifers from seawater intrusion. As a consequence, there exists the potential for enhanced vertical and horizontal migration of seawater into the producing aquifers and subsequent landward migration of intruded waters beneath the Dominguez Gap Barrier Project [4,30,31]. The interaction between seawater and the aquifer system makes the sorption characteristics study of this aquifer of interest due to its relevance to other tectonically-active or structurally complex coastal areas.

2. Geographic Setting

Natural and artificial recharge to the Los Angeles Basin occurs through local precipitation and infiltration, seawater intrusion along the coast, injection of non-native water into the barrier wells, and regional groundwater flow from adjacent basins. Each water-mass end member is geochemically distinct and has been identified with a suite of isotopes and geochemical parameters [6]. Groundwater samples for this study were collected from the Dominguez Gap region of the southwest Los Angeles Basin, located along the coastal plain of Los Angeles County adjacent to San Pedro Bay (Figure 1). The Dominguez Gap denotes a hydrologic “gap” that occurs just south of the Dominguez Hills, where the Los Angeles River transverses the Newport-Inglewood Uplift. In general, exposed Late Pleistocene alluvial deposits cover large parts of the coastal plain except close to the Los Angeles River, where as much as ~10 m of Holocene-aged fluvial and marine sediment has filled in parts of the paleo-river channel of the Los Angeles River during a lower sea level stand. The hydrogeology of the Dominguez Gap region has been well studied [26,27,32] and is summarized in a shore-perpendicular cross-section (Figure 2). Injection of fresh water in the West Coast Basin and Dominguez Gap Barrier Projects is a significant source of recharge to the West Coast Groundwater Basin [6]. Ponti *et al.* [30] developed a sequence stratigraphic model of the Dominguez Gap area that further refined these water-bearing depositional systems relative to sediment supply, sea level, and accommodation space. Their work also identified the Pacific Coast Highway (PCH) Fault, which may play an important role in the mixing of seawater into deep aquifers.

Figure 1. Base map of the well sites and the prominent geologic and hydrologic features of the study area, Los Angeles County, California. The Huntington Park monitoring well site is located in the adjacent Central Basin, 6.5 km south of downtown Los Angeles, and in an area known as the Los Angeles forebay. The forebay is an area of groundwater recharge for some of the water contained in the West Coast Basin. Note the following abbreviations: LWEB = Webster; LBCH = Cabrillo; LBPC = Pier C; LBPF = Pier F are used throughout the text, figures, and tables.

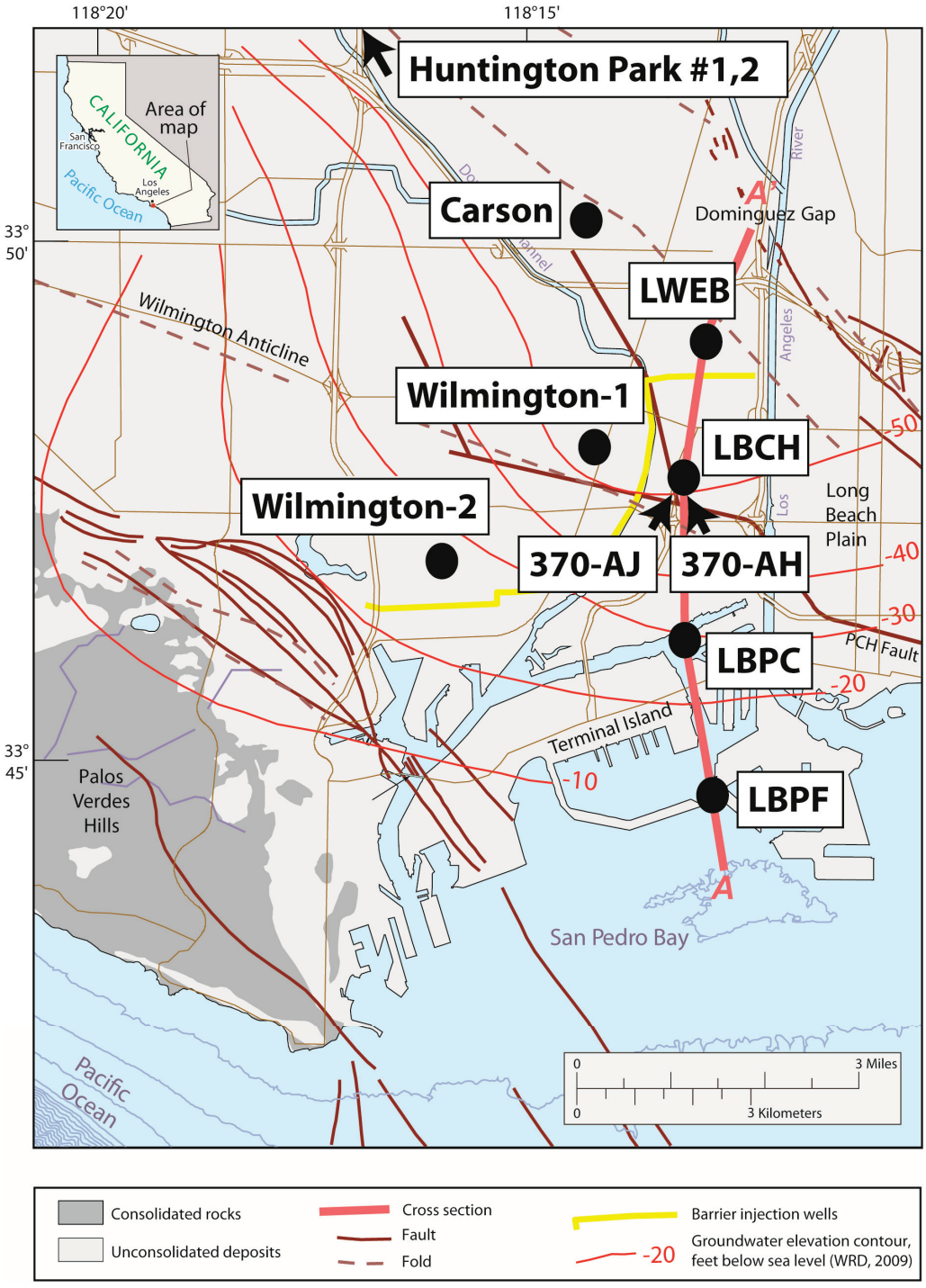

Figure 2. An idealized hydrogeologic cross-section of the Dominguez Gap area, also showing the sequence boundaries as defined by Ponti *et al.* [30]. Geographic location of the **A–A'** transect is shown in Figure 1.

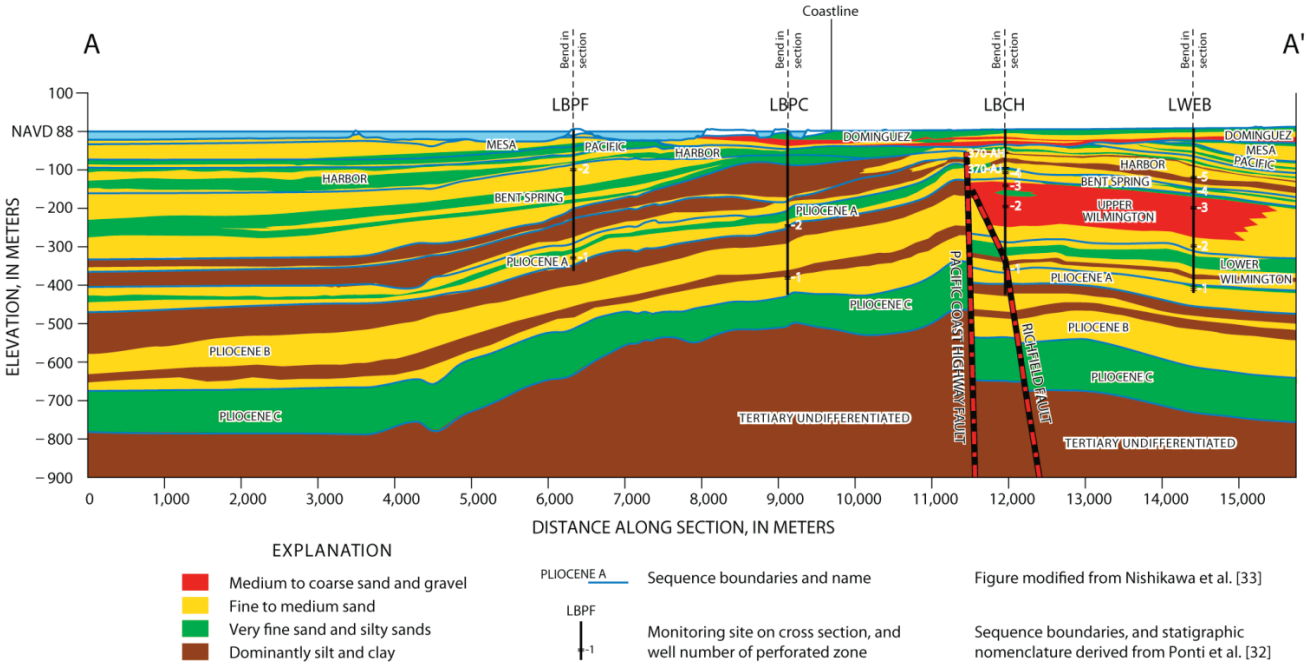

3. Groundwater Radionuclide Transport

The fate of U/Th series radionuclides in groundwater continues to be an active area of research primarily to better understand and predict subsurface contaminant actinide transport [21]. Many of the early advances in modeling naturally-occurring radionuclides in groundwater were pioneered by Rama and Moore [25] and Krishnaswami *et al.* [15] and later summarized by Ku *et al.* [20] and Porcelli and Swarzenski [21]. The following model stems largely from the original Krishnaswami *et al.* [15] formulations. The dominant processes that can control the fate of U/Th series radionuclides in groundwater include both *input* terms, such as, (1) recoil mechanisms, (2) congruent dissolution within an aquifer solid, (3) desorption reactions from solid surfaces, and (4) *in-situ* radioactive decay of a dissolved parent nuclide, as well as *removal* terms, such as (1) chemical precipitation, (2) radioactive decay, and (3) reversible sorption onto particle surfaces. If we assume the kinetics of adsorption and desorption to be first order [20,21], then the steady-state mass balance reactions for a radionuclide in an aquifer can be reduced to the following equations [15]:

$$\text{Dissolved phase:} \quad P + k_2 N_s = \lambda N_d + k_1 N_d \tag{1}$$

$$\text{Solid phase:} \quad k_1 N_d = \lambda N_s + k_2 N_s \tag{2}$$

Here P (atoms per second per volume of water) defines the production rate of a nuclide in solution by such processes as chemical dissolution (*i.e.*, weathering), *in-situ* production and recoil, λ is the decay constant ($0.693/t_{1/2}$) of a radionuclide, k_1 and k_2 are first-order adsorption and desorption rate constants, respectively, and N_d and N_s describe the respective concentration of a nuclide in water (atoms per volume of water) and adsorbed onto an aquifer matrix. The recoil term is the dominant

supply term for short-lived radionuclides (*i.e.*, ^{224}Ra, ^{223}Ra, ^{228}Ra, with a mean-life < 10 years), although there could be some contribution from congruent weathering for ^{226}Ra (mean-life = 2309 years). The ratio (Ω) of the activity of a nuclide ($= \lambda N_d$) to its production (P) in solution can be calculated from Equations (1) and (2), as follows:

$$\Omega = \lambda N_d / P = (k_2 + \lambda)/(k_1 + k_2 + \lambda) \quad (3)$$

Assuming negligible isotopic fractionation [21], the adsorption (k_1) and desorption (k_2) rate constants are expected to be the same for two isotopes of the same element. If we assume "*i*" and "*j*" to describe two isotopes of one element, then the mass balance equations of each of these nuclides can be combined and solved for k_1 and k_2 [15] as follows:

$$k_1 = [(\lambda_i - \lambda_j)\,(1 - \Omega_i)\,(1 - \Omega_j)]/(\Omega_i - \Omega_j) \quad (4)$$

and

$$k_2 = [\Omega_i\Omega_j\,(\lambda_j - \lambda_i) + \lambda_i\Omega_j - \lambda_j\Omega_i)]/(\Omega_i - \Omega_j) \quad (5)$$

From the measured groundwater ^{222}Rn, ^{224}Ra, and ^{228}Ra activities and their radiogenic parents, ^{230}Th, ^{228}Th, and ^{232}Th activities, in the solid phase, we can determine k_1 and k_2 using Equations (4) and (5).

4. Materials and Methods

Most samples for this effort were collected as part of a larger U.S. Geological Survey (USGS) project on the groundwater quality and geochemical character underlying Los Angeles County and thus more complete sampling protocols and analytical methods are described in detail therein [4–6]. Briefly, each well was sufficiently purged and then sampled using "clean" procedures to avoid contamination as per standard USGS water quality sampling protocols. Chemically unstable constituents, such as alkalinity and ^{222}Rn, were processed and/or preserved in the field. Water quality data including stable and radiogenic isotopes were determined at the USGS Water Quality Laboratory in Denver, CO [5,6]. Stable isotopes were determined using isotope mass spectrometry with a gas-source stable isotope mass spectrometer, as per methods described in Epstein and Mayeda [33] and Coplen *et al.* [34]. The 2-sigma uncertainty of oxygen and hydrogen isotopic results is 0.2‰ and 2‰, respectively.

Radon-222 activities were measured in the field using a commercially available Rn-in-air monitor (RAD7—DURRIDGE, Inc., Billerica, MA, USA) coupled to a RAD-H2O discrete water sampling kit [35–38]. Radium-223 and ^{224}Ra activities were quantified using delayed-coincidence alpha counting techniques [37–39]. Briefly, Ra was quantitatively removed from large groundwater samples (50–100 L) using MnO_2 fiber cartridges. The partially dried fiber was subsequently placed into a closed, recirculating loop and a RaDeCC detector. The ^{223}Ra and ^{224}Ra isotopes were recounted after ~20 days to correct for supported ^{224}Ra activities (from ^{228}Th), and subsequently decay-corrected to the mid-point sampling time. Propagated errors for the delayed coincidence counters are typically <10%. After the counting for short-lived Ra isotopes was completed, the fiber was leached with a 6M HCl-H_2O_2-hydroxylamine hydrochloride mixture to quantitatively remove Ra from the Mn fiber. The Ra was co-precipitated with $BaSO_4$ using $Ba(NO_3)_2$-H_2SO_4 [40] and the $BaSO_4$ precipitate

was counted after 20 days (allowing for the in-growth of ^{222}Rn daughters) in a high-purity Ge well detector coupled to an InSpector gamma spectrometry software package. The ^{226}Ra and ^{228}Ra activities were quantified using gamma energies of 352 and 609 keV for ^{226}Ra and 338 and 911 keV for ^{228}Ra.

Seven soil samples from well cuttings that represented a spectrum of geologic material from the well sites were also analyzed for ^{238}U, ^{234}U, and ^{230}Th using an inductively coupled plasma mass spectrometer (ICP-MS). Briefly, ~200 mg of dried, pulverized sample was brought into solution using HF and concentrated HNO_3. Blanks and reference standards for radionuclides in sediment, IAEA 385 (Irish Sea sediment) were prepared and analyzed as quality control measures. The concentrations of ^{238}U, ^{234}U and ^{230}Th were measured by ICP-MS in the single-collector mode.

5. Results and Discussion

5.1. Major Ion Composition

In addition to two well parameters (approximate horizontal flow path distance, x, and depth to the top of the screened interval, z), concentrations of the major cations (Na^+, K^+, Ca^{2+} and Mg^{2+}) and anions (Cl^-, alkalinity (as $CaCO_3$), and SO_4^{2-}), dissolved oxygen (DO), as well as Ba, B, and Sr are presented in Table 1. The DO concentration, which can be a useful proxy for oxidation effects during sampling of reduced groundwater, ranged between <0.1 to 2.6 mg L^{-1}. Of the 30 samples that were measured for DO, only one sample (LWEB-4) was slightly above a "hypoxic" condition. While most chloride concentrations of native groundwater did not exceed 35 mg L^{-1} in the Lower aquifer systems, some wells close to the coast had historic Cl^- values as high as 90 mg L^{-1}. Table 2 lists summary parameters and descriptions of well waters. Water levels of many of these near-shore wells increased in response to sustained freshwater injection, yet a concomitant decrease in Cl^- values is not always observed [41]. For example, elevated Cl^- concentrations have been measured in several Upper and Lower aquifer system wells east of the Dominguez Gap Barrier Project; Long Beach 3 and Long Beach 4. In water from the wells, the Na^+ concentration varied between 39 (Huntington Park #1) and 10,800 mg L^{-1}, while the Cl^- concentration ranged from 18.5 to 19,900 mg L^{-1} (seawater-like value observed at LBPF-2). Excluding LBPF-2 as groundwater here consist mostly of seawater, a plot of Cl^- as a function of Na^+ (Figure 3A) illustrates that many of the wells are variably influenced by elevated Cl^- concentrations. There is an expected [41] strong positive correlation ($R^2 = 0.88$) between SO_4^{2-} and Ca^{2+} concentrations (Figure 3B). Extensive SO_4^{2-} reduction and cation exchange reactions result in most native groundwater within the study area having a characteristic Ca/Na-bicarbonate to Na-bicarbonate composition with very low Cl^- concentrations, <65 mg L^{-1} [6,42]. Non-native water typically exhibits a dominant Ca/Na-sulfate composition, while wells intruded by seawater or mixed with oil-field brines have a Na-Cl composition [6]. As many Tertiary brine fluids are also defined by a high Na-Cl composition, it is not easy to separate these from seawater-intruded waters (e.g., Wilmington-2 #2). See Table 2 for a summary of characteristic geochemical parameters that define these well waters as well as recent trends in water quality.

Table 1. Select well characteristics and water quality data for wells sampled. Well location for all but Huntington Park sites shown in Figure 1. The Huntington Park site is located in a recharge area of the adjacent Central Basin, near downtown Los Angeles [6].

Well ID	x [1]	z [2]	DO [3]	Ca^{2+}	Mg^{2+}	K^{+}	Na^{+}	Alk. [4]	Cl^{-}	SO_4^{2-}	Ba	B	Sr
	km	m	mg L^{-1}	mg L^{-1}	mg L^{-1}	mg L^{-1}	mg L^{-1}	mg L^{-1}	mg L^{-1}	mg L^{-1}	µg L^{-1}	µg L^{-1}	µg L^{-1}
Huntington Park #1 (4/9/1997)	0.0	271	0.2	59	14	3	39	168	21	80	58	132	451
Huntington Park #2 (4/10/1997)	0.0	210	0.5	59	14	3	40	178	22	82	70	133	470
Carson-1 #1 (1/6/1998)	16.7	279	<0.1	19	4	3	51	141	20	<0.1	12	96	185
Carson-1 #2 (1/5/1998)	16.7	238	0.2	32	7	2	42	169	21	<0.1	39	102	369
Carson-1 #3 (1/6/1998)	16.7	168	0.2	44	12	3	47	164	23	62	58	105	398
Carson-1 #4 (1/6/1998)	16.7	69	0.2	86	21	4	74	204	112	112	199	117	835
Wilmington-1 #1 (4/24/1999)	20.8	279	0.1	50	16	7	106	134	213	<0.1	12	123	371
Wilmington-1 #2 (4/25/1999)	20.8	238	0.2	124	27	6	130	135	337	59	11	175	1,153
Wilmington-1 #3 (4/25/1999)	20.8	168	<0.2	214	47	9	346	173	907	50	27	240	2,129
Wilmington-1 #4 (4/25/1999)	20.8	69	0.1	282	96	13	457	142	1,209	288	121	221	3,688
Wilmington-1 #5 (4/24/1999)	20.8	37	<0.2	85	31	7	145	197	233	140	103	203	1,089
Wilmington-2 #1 (4/21/1999)	23.0	290	<0.1	3	2	5	195	377	56	<0.1	7	653	39
Wilmington-2 #2 (2/18/1999)	23.0	230	<0.1	35	24	13	499	450	513	<0.1	57	1,578	407
Wilmington-2 #3 (2/21/1999)	23.0	165	<0.1	20	7	4	102	180	72	<0.1	23	266	177
Wilmington-2 #4 (4/21/1999)	23.0	119	<0.1	143	67	16	492	308	1,012	29	117	557	1,266
Wilmington-2 #5 (2/18/1999)	23.0	37	<0.1	761	363	31	2,604	202	5,232	595	162	732	6,905
LWEB-1 (3/29/2001)	19.0	411	0.1	11	3.47	3.8	156	392	18.5	1	8.7	372	120
LWEB-2 (3/29/2001)	19.0	304	0.2	15.9	2.73	2.5	61.5	144	18.8	25.3	10	138	191
LWEB-3 (3/28/2001)	19.0	204	0.4	17.9	3.24	2.7	55.8	159	24.8	0.2	13	132	226
LWEB-4 (3/27/2001)	19.0	162	2.6	88.8	24	6.2	72.9	139	213	57.9	31	109	962
LWEB-5 (3/26/2001)	19.0	125	0.2	238	57.3	7.8	98.6	148	619	62.7	109	110	2,530
LBCH-1 (8/27/2003)	21.4	360	<0.1	6.2	3.03	4.8	206	503	22.9	3	6.3	785	77.2
LBCH-2 (8/26/2003)	21.4	198	0.1	13.5	4.08	3.5	107	181	74.4	1.2	4.6	238	171
LBCH-3 (8/26/2003)	21.4	143	<0.1	12.8	4.43	3.2	97.1	177	67.6	4	3.5	223	185
LBCH-4 (8/25/2003)	21.4	110	0.2	463	174	21	615	145	2,100	278	113	419	4,860
370-AJ (6/08/2005)	21.0	66	-	295	109	12	438	129	1,420	184	78	198	2,770
370-AH (6/08/2005)	21.0	20	-	454	335	34	1,440	200	3,810	391	167	361	4,650
LBPC-1 (4/03/2001)	24.2	366	<0.1	9.57	4.63	5.8	259	492	21.4	3.6	15	1,100	134
LBPC-2 (4/04/2001)	24.2	244	<0.1	6.55	7.18	11	422	614	337	1.4	17	1,150	97.5
LBPF-1 (4/24/2002)	27.0	332	0.1	17.8	30.5	26	1,500	1,230	1,650	-	127	8,400	734
LBPF-2 (4/24/2002)	27.0	102	0.1	519	1,220	272	10,800	289	19,900	2,640	82	4,130	8,500

Notes: [1] Approximate distance along flow path [6]; [2] Depth to top of perforation; [3] Dissolved oxygen, mg L^{-1}; [4] As $CaCO_3$; [5] LWEB = Webster; LBCH = Cabrillo; LBPC = Pier C; LBPF = Pier F.

Table 2. Summary parameters and description of well water for this study.

Well ID	Stratigraphic unit [1]	Chemical composition [2]	Change in chemical composition (1998–2011) [3]	Chloride range [4]	Stable isotope [5]	Relative age of water [6]	Comment
Huntington Park #1	Bent Spring	Ca-HCO_3	unchanged	low	N	old	Native water of good quality; end member for flow system
Huntington Park #2	Harbor	Ca-HCO_3	unchanged	low	N	old	Native water of good quality; end member for flow system
Carson-1 #1	Upper Wilmington	Na-HCO_3	unchanged	low	N	old	Native water of good quality; source of recharge similar to Huntington Park
Carson-1 #2	Upper Wilmington	Na/Ca-HCO_3	unchanged	low	N	old	Native water of good quality; source of recharge similar to Huntington Park
Carson-1 #3	Harbor	Ca/Na-HCO_3	unchanged	low	N	old	Native water of good quality; source of recharge similar to Huntington Park
Carson-1 #4	Pacific	Ca/Na-HCO_3	mixing	low	N	old	Gradual decrease in TDS since initial sampling; [Cl] from 210 to ~40 mg L^{-1}
Wilmington-1 #1	Upper Wilmington	Na-Cl	unchanged	low	N	old	Possible enhanced lateral movement due to intense nearby pumping
Wilmington-1 #2	Upper Wilmington	Ca/Na-Cl	mixing	medium	N	old	Possible enhanced lateral movement due to intense nearby pumping
Wilmington-1 #3	Upper Wilmington	Na/Ca-Cl	mixing	medium	I-S-N	recent	Inland from Dominguez Gap Seawater Barrier Project; contains mixture of native water, seawater, and imported water from overlying unit
Wilmington-1 #4	Harbor	Na-Cl	variable	medium	I	recent	Likely mixture of imported and seawater
Wilmington-1 #5	Pacific	Ca/Na-Cl	variable	low	I	recent	Likely mixture of imported and seawater
Wilmington-2 #1	Pliocene B	Na-HCO_3	variable	low	N	old	Isotopically light water recharged during Pleistocene
Wilmington-2 #2	Pliocene A	Na-Cl	mixing	medium	S	old	Principally isotopic light water (similar to Wilm2 #1); localized saline unit attributed to partial mixing with an oil-field brine
Wilmington-2 #3	Lower Wilmington	Na-Cl/HCO_3	variable	low	N	old	Native, fresh, sodium-bicarbonate water
Wilmington-2 #4	Upper Wilmington	Na-Cl	mixing	medium	I-S-N	recent	Significant improvement in TDS likely a result of more effective injection; [Cl] decreased from ~1000 to 290 mg L^{-1}

Table 2. *Cont.*

Well ID	Stratigraphic unit [1]	Chemical composition [2]	Change in chemical composition (1998–2011) [3]	Chloride range [4]	Stable isotope [5]	Relative age of water [6]	Comment
Wilmington-2 #5	Harbor	Na-Cl	mixing	high	S-I	recent	Some imported water is present, though masked by seawater intrusion. Significant improvement in TDS likely a result of more effective injection; [Cl] decreased from ~5200 to 2600 mg L^{-1}
LWEB-1	Pliocene A	Na-HCO_3	unchanged	low	N	old	Isotopically light water recharged during Pleistocene
LWEB-2	Upper Wilmington	Na-HCO_3	mixing	low	N	old	Geochemistry suggests subtle reactions or long-term pumping effects
LWEB-3	Upper Wilmington	Na-HCO_3	variable	low	N	old	Native, fresh, sodium-bicarbonate water
LWEB-4	Bent Spring	Ca-Cl	variable	low	N	old	Native, fresh, sodium-bicarbonate water
LWEB-5	Harbor	Ca-Cl	variable	low	N	old	Native, fresh, sodium-bicarbonate water
LBCH-1	Lower Wilmington	Na-HCO_3	unknown	low	N	old	Isotopically light water recharged during Pleistocene
LBCH-2	Upper Wilmington	Na-HCO_3	unknown	low	N	old	Isotopically light water recharged during Pleistocene
LBCH-3	Upper Wilmington	Na-HCO_3	unknown	low	N	old	Isotopically light water recharged during Pleistocene
LBCH-4	Bent Spring	Na/Ca-Cl	unknown	low	N-S	recent	
370-AJ	Harbor	Na/Ca-Cl	unknown	medium	N-S	recent	
370-AH	Dominguez	Na-Cl	unknown	high	N-S	recent	
LBPC-1	Pliocene B	Na-HCO_3	unknown	low	N	old	Isotopically light water recharged during Pleistocene
LBPC-2	Pliocene A	Na-HCO_3/Cl	unknown	medium	N	old	Isotopically light water recharged during Pleistocene
LBPF-1	Pliocene A	Na-Cl/HCO_3	unknown	medium	N	old	Old seawater, distinct major ion composition and trace element ratios
LBPF-2	Bent Spring	Na-Cl	unknown	high	S	old	Groundwater consisting mostly of seawater

Notes: [1] Nomenclature consistent with most recent model layer assignments [43]; as well as in Ponti *et al.* [30] and Figure 2; [2,3] Change in chemical composition: where period of record is available, a general description of water quality over time is given; [4] Chloride range: low = <250 mg L^{-1}, medium = 250–2500 mg L^{-1}, and high = >2500 mg L^{-1}; [5] N, native water; S, seawater; I, imported water; [6] Relative age: see Section on Tritium; about 1 tritium unit (TU) used for recent/old categorization.

5.2. Tritium

The tritium data provide insight as to the relative age or "old" *versus* "new" groundwater in our study. Tritium (^3H; $t_{1/2}$ = 12.4 years) is the only radioactive isotope of hydrogen and while it is naturally present only in minute (<<1%) quantities, it is also produced as a fission product in nuclear weapons tests and nuclear power reactors. The convention for reporting ^3H concentrations is the tritium unit (TU), which equals 3.2 pCi L^{-1} (7.104 dpm L^{-1}). As tritium is naturally incorporated into the water molecule and its abundance is only affected by radioactive decay, ^3H serves as a useful tracer for identifying recently recharged water. A pre-fallout (pre-1952) background ^3H abundance in southern California coastal precipitation was ~2 TU [44]. Beginning in 1952, ^3H was released into the atmosphere, reaching a maximum in 1963 [45]. A reconstructed Los Angeles County precipitation tritium concentration curve [6] identifies a narrow 1963 peak at ~700 TU that rapidly decreased to <100 TU by 1970. As a consequence, without consideration for complex mixing scenarios, groundwater with a ^3H value less than <1 TU may be considered "older" water that was recharged prior to 1952. Conversely, groundwater with a tritium content >1 TU can be interpreted as "recent" water being wholly or partially recharged post-1952. Along the coast, such interpretation may be more complicated as recent seawater may provide another source of tritium.

Figure 3. (**A**) Chloride *versus* Na^+ (except LBPF-2) and (**B**) SO_4^{2-} *versus* Ca^{2+}.

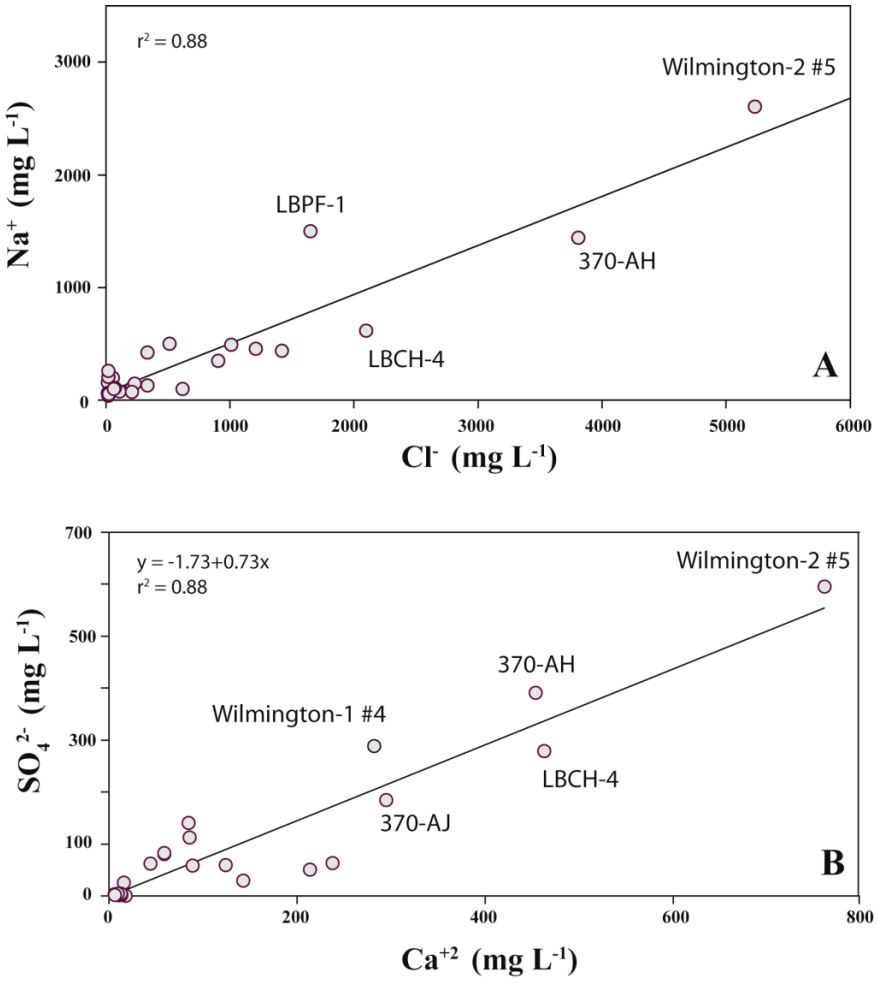

Of the 31 groundwater samples analyzed for tritium (average ^{3}H value = 4.3 TU), seven samples had a ^{3}H concentration >1 TU and of these, three had ^{3}H >10 TU (Table 3); each of these wells perforated the Pacific and Harbor sequences. The large number of low or less than measureable (0.1 TU) tritium values indicates that most sampled groundwater in the Dominguez Gap region appears to be older water (pre-1952). Notable exceptions include wells close to the coast (Wilmington-1 #4, Wilmington-1 #5, and Wilmington-2 #5) that are directly influenced by recent seawater intrusion and the seawater barrier injection wells that may introduce additional, substantial ^{3}H as a result of complex mixing scenarios (Table 2; Figure 2).

Table 3. Select stable and radiogenic isotope data for wells sampled in the study site. Note: pmc = percent modern carbon.

Well ID	$\delta^{18}O$	δD	^{3}H	$\delta^{13}C_{DIC}$	^{14}C
	(‰)	(‰)	(TU)	(‰)	(pmc)
Huntington Park #1	−7.32	−47.5	<0.1	−13.6	83.7
Huntington Park #2	−7.23	−47.3	<0.1	−13.5	83.5
Carson-1 #1	−7.33	−48.4	0.1	−12.4	27.6
Carson-1 #2	−7.27	−46.6	<0.1	−12.3	43.6
Carson-1 #3	−7.30	−47.3	<0.1	−14.2	56.1
Carson-1 #4	−7.12	−47.0	0.1	-	-
Wilmington-1 #1	−7.29	−46.8	<0.1	−15.8	29.6
Wilmington-1 #2	−7.13	−46.0	<0.1	−18.4	44.5
Wilmington-1 #3	−7.34	−49.4	1.6	-	-
Wilmington-1 #4	−9.77	−77.5	19	-	-
Wilmington-1 #5	−9.58	−73.3	11.9	-	-
Wilmington-2 #1	−8.73	−59.7	<0.1	−0.3	2.5
Wilmington-2 #2	−8.63	−55.8	<0.1	−0.3	5.2
Wilmington-2 #3	−7.84	−50.6	<0.1	−15.0	14.4
Wilmington-2 #4	−7.96	−51.3	1.5	-	-
Wilmington-2 #5	−7.57	−57.7	16.9	-	-
LWEB-1	−9.17	−62.7	<0.1	6.3	1.8
LWEB-2	−7.72	−51.1	0.1	−15.8	24.1
LWEB-3	−8.07	−53.2	<0.1	−18.9	14.1
LWEB-4	−7.32	−48.4	<0.1	−14.3	42.8
LWEB-5	−7.10	−47.4	<0.1	−13.9	55.1
LBCH-1	−9.39	−64.0	<0.1	4.7	3.5
LBCH-2	−8.37	−55.1	0.1	−10.6	8.8
LBCH-3	−8.15	−53.6	<0.1	−16.0	9.8
LBCH-4	−6.86	−45.9	1.8	−16.0	61.4
370-AJ	−7.12	−49.9	1.1	-	-
370-AH	−6.76	−47.3	0.9	-	-
LBPC-1	−9.23	−61.1	0.2	3.1	2.5
LBPC-2	−7.54	−49.2	<0.1	−12.7	4.3
LBPF-1	−7.47	−47.1	<0.1	−6.4	0.8
LBPF-2	−0.42	−3.65	<0.1	−12.3	48.5

5.3. Isotopic Composition of Oxygen ($\delta^{18}O$) and Hydrogen (δD)

The behavior of stable oxygen ($\delta^{18}O$) and hydrogen (δD) isotopes in groundwater can provide insight into the geochemical character, origin, and transport phenomena of groundwater [8]. Reporting convention for both isotopes is expressed in terms of relative difference, per mill (‰), from the Vienna Standard Mean Ocean Water (VSMOW) value. In general, the predominant source of precipitation is from evaporation of seawater, and as a result, the observed global composition of $\delta^{18}O$ and δD in rainwater is linearly expressed as the global meteoric water line (GMWL; $\delta D = 8\delta^{18}O + 10‰$; [46,47]).

In the 31 groundwater samples, the $\delta^{18}O$ composition ranged from −0.42‰ (LBPF-2) to −9.77‰ (Wilmington-1#4), while the δD composition varied between −3.65‰ (LBPF-2) to −77.5‰ (Wilmington-1#4) (Table 3). A plot of δD *versus* $\delta^{18}O$ (Figure 4) indicates a strong linear relationship ($R^2 = 0.93$), with a slope of 7.2—close to that of the global meteoric water line (GMWL; slope = 8). Notable exceptions of groundwater (*i.e.*, Wilmington-1#4; Wilmington-2 #5) that influence such a shift below the GMWL include isotopically heavier water that likely consists of a recent mixture of saline (e.g., seawater) and imported fresh water [4]. Lighter δD values (<−50‰), observed in some groundwater samples (e.g., LBPF-1,2, Wilmington-1#1-3, Huntington Park 1,2, Carson-1#1-4, 370-AJ, 370-AH, LWEB-4,5) may identify older groundwater with a isotopically unique signature.

Figure 4. δD *versus* $\delta^{18}O$ in selected groundwater samples from the study area. The global meteoric water line is per Craig (1961). Regression results include all groundwater data. Water recharged from Los Angeles and Montebello Forebays has a $\delta^{18}O$ signature of −7.5‰ to −6.7‰ and −9.5‰ to −8.0‰, respectively, and is isotopically distinct from non-native, seawater, and oil-field brine values.

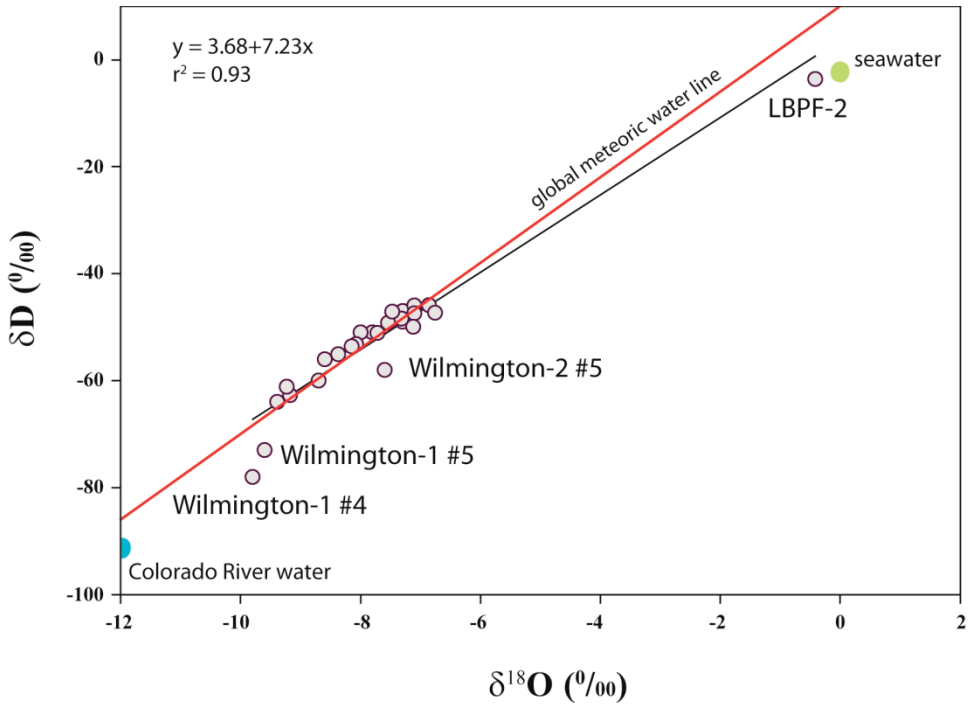

The composition of δD and $\delta^{18}O$ in precipitation may also be influenced by local air mass and vapor trajectories, changes in evaporation, and isotope exchange processes below the cloud base [10,47]. Thus, climatic variations may be recorded in the composition of $\delta^{18}O$ and δD in groundwater [12]. In LBPF-2, where the Cl^- concentration approaches a seawater-like value (Figure 4), both $\delta^{18}O$ and δD isotopic compositions are highly enriched (heavy) (−0.42‰ for $\delta^{18}O$ and δD for −3.65‰) compared to other well waters (−6.76 to −9.77‰ for $\delta^{18}O$ and −45.9 to −77.5‰ for δD). The isotopic composition of the well waters, coupled with the major ion chemistry, implies variable mixing with recent seawater. In addition, isotopically lighter water with low Cl^- content has also been attributed to Colorado River water [6] that is used as a source of injection water at the barrier wells [48]. Observed high Cl^- concentrations along with enriched $\delta^{18}O$ reveal non-native inputs from seawater and/or oil-field brines (Table 2).

5.4. Isotopic Composition of $\delta^{13}C$ in Dissolved Organic Carbon (DIC)

Dissolved inorganic carbon (DIC = $[CO_{2aq}] + [HCO_3^-] + [CO_3^{2-}]$) is generally produced in groundwater by the dissolution of CO_2 during plant (*i.e.*, C_3 and/or C_4) respiration, the microbial decomposition of organic matter, and the direct dissolution of carbonate minerals [49]. The composition of $\delta^{13}C$, expressed as per mill (‰) relative to the VPDB (Vienna PeeDee Belemnite) standard, provides a useful tracer to assess the relative contribution of C from these various sources. Under an open CO_2 system, the groundwater $\delta^{13}C_{DIC}$ should approach ~9‰ by simple hydrolysis reactions of soil CO_2 alone [7]. Conversely, if the groundwater is closed to soil CO_2, then the $\delta^{13}C_{DIC}$ should approach values of about −13‰. In groundwater that is strongly reducing and sulfate-poor [50], the composition of $\delta^{13}C_{DIC}$ can increase to values in excess of 30‰ as a result of methanogenesis [51]. Observed saturation calculations for portions of the study area, and elsewhere in the basin, indicate that calcite should precipitate.

In this study, the groundwater $\delta^{13}C$ in dissolved inorganic carbon ranged from −18.9 (LWEB-3) to 6.3‰ (LWEB-1) (Table 3), which reflects the contribution of different DIC sources and/or the evolution from an open to a closed system. Wells sampled for this study, with the exception of 370-AH and possibly Wilmington-1#5 appear to respond within a confined system. Three deep samples (LWEB-1, LBCH-1, LBPC-1) contain $\delta^{13}C_{DIC}$ values >0‰ and very little SO_4^{2-}, which would suggest a unique carbon source, such as from an incomplete bacterially-mediated methanogenic pathway [52]. There have been a number of studies indicating a linear relationship between $\delta^{13}C_{DIC}$ and 1/dissolved inorganic carbon (DIC) [49,52–55]. In lieu of direct dissolved inorganic carbon measurements alkalinity (expressed as $CaCO_3$) can serve as a proxy for DIC, under the condition that CO_2 remains constant [56]. If one excludes values from wells closest to the coast and down-gradient from the PCH Fault (e.g., LBPC-2, LBPF-1,2) there is a good correlation (R^2 = 0.88) between $\delta^{13}C_{DIC}$ and 1/alkalinity (Figure 5). Such a trend, which implies more than simple carbonate mineral dissolution, is expected in a complexly mixed coastal aquifer undergoing chemical evolution [11,13,57].

Figure 5. $\delta^{13}C_{DIC}$ *versus* 1/alkalinity (excluding wells closest to the coast; LBPC-2, LBPF1,2).

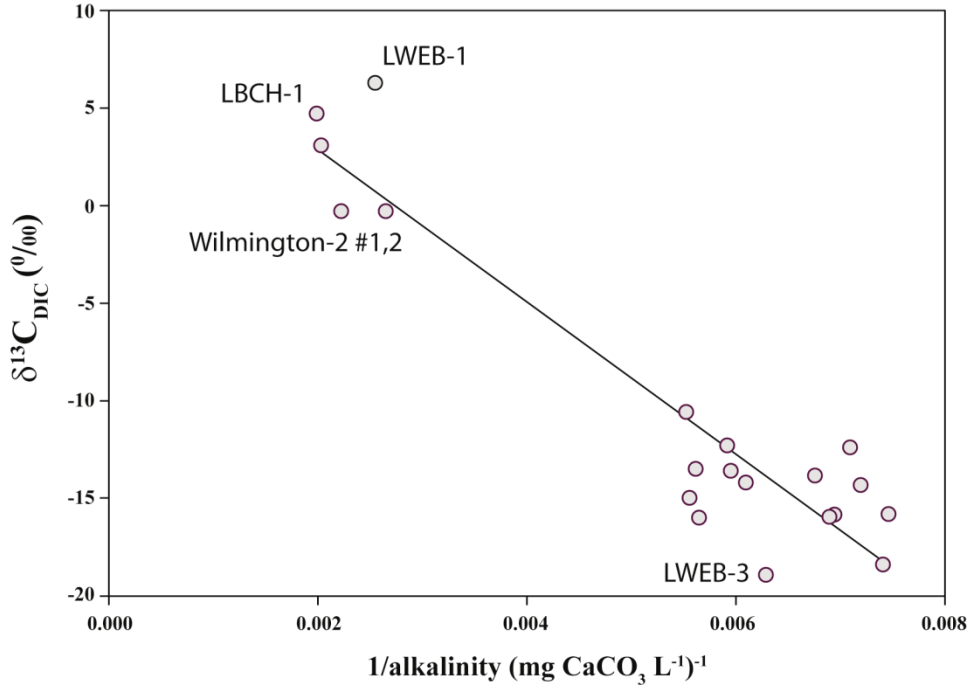

5.5. Carbon-14 (^{14}C)

To assess the relative age of select groundwater samples, ^{14}C ($t_{½}$ = 5730 years) was also determined. Natural ^{14}C is mainly produced in the atmosphere by interaction of cosmic ray derived secondary neutrons with ^{14}N. Carbon-14 derived age results are often expressed as percent modern carbon ^{14}C (pmc) by comparing the ^{14}C activity of a sample to the known activity of an oxalic acid standard. Carbon-14 age data are generally interpreted within the context of a geochemical reactions/evolution model that can account for the various sources and sinks of carbon [58].

In the Los Angeles County groundwater samples, the percent modern carbon (pmc) exhibited a wide range from 0.8 pmc (LBPF-1) to 83.7 pmc (Huntington Park #1) (Table 3) with an average value of ~30 pmc. Assuming an initial ^{14}C value of 90 pmc [4], the corresponding groundwater age estimates may extend from recent to beyond 20 kyr before present and suggest that some well water undergoes deep circulation of native water through multiple aquifer systems. Age estimates, however, are not corrected for potential exchange reactions of carbon within the aquifer, and thus may not reflect the true age of the groundwater. The observed variations in the percentage of modern ^{14}C indicate that the groundwater system is comprised of complex mixtures of diverse waters. A plot of $\delta^{13}C_{DIC}$ *versus* ^{14}C (Figure 6) indicates that in samples with <10 pmc, $\delta^{13}C_{DIC}$ values fluctuated from −16‰ to +6‰, while in samples with >10 pmc, the $\delta^{13}C_{DIC}$ values ranged from −12‰ to −18‰. Select groundwaters (e.g., Wilmington 2-1, LWEB1,2, LBCH1-3, and LBPC1,2) that likely were recharged during Pleistocene, are also isotopically light. Nonetheless, ^{14}C data confirm complex water mixing and transport scenarios involving multiple aquifer systems that reside within a tectonically active geologic framework.

Figure 6. $\delta^{13}C_{DIC}$ *versus* percentage of modern ^{14}C in groundwater samples from Los Angeles Basin.

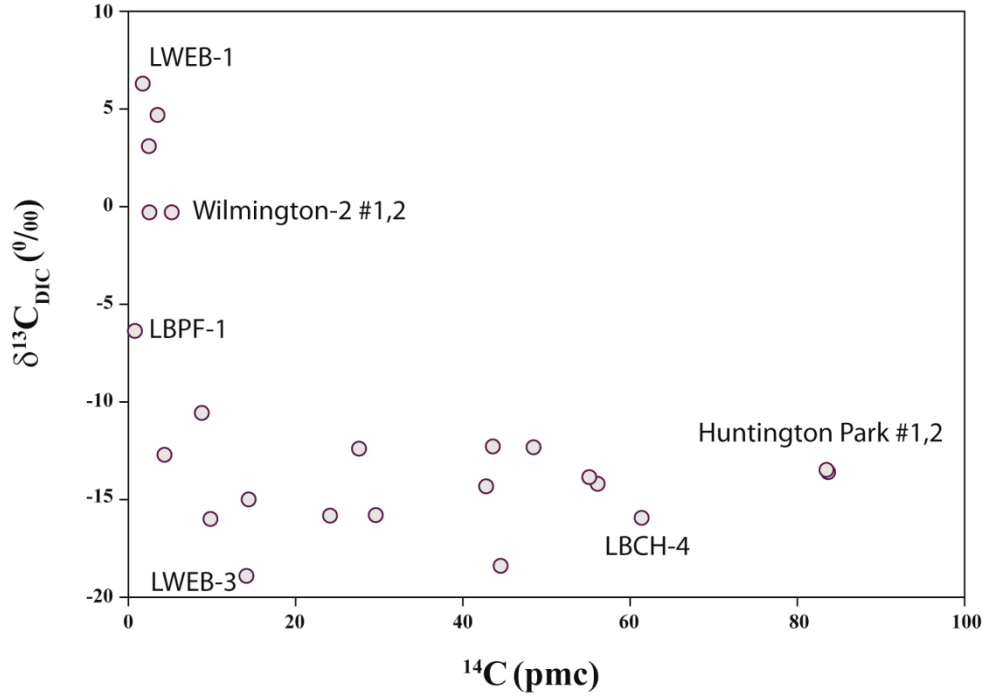

5.6. U- and Th-Series Radionuclides

The isotopic systematics of many of the naturally occurring radionuclides in the U- and Th-series decay series are invaluable in investigating aquifer behavior. Specifically, U, Th, Ra, and Rn are all ubiquitous in groundwater and are represented by multiple isotopes with very different half-lives such that groundwater processes can be studied over a large range in time-scales. Within aquifer host minerals, these radionuclides are generally expected to be in secular equilibrium. However, these same radionuclides may exhibit strong fractionations with the surrounding groundwaters. Such disequilibria can be used, for example, to obtain information of radionuclide release from aquifer host rocks, groundwater flow rates, or age dates.

5.6.1. Specific Activities of ^{238}U, ^{230}Th and ^{232}Th in Well Cuttings

The specific activity of ^{238}U ($t_{½}$ = 4.47 Gyr) from select well cuttings varied between 0.46 and 0.73 dpm g^{-1} (2.22 dpm = 1 pCi), while the $^{234}U/^{238}U$ activity ratios varied between 0.99 and 1.02 (Table 4). Within one sigma, ^{234}U ($t_{½}$ = 2.5 Gyr) and ^{238}U are in secular equilibrium with one another, which indicates that the alpha recoil loss [59] of ^{234}U is generally negligible in these samples. In contrast, the activity of ^{230}Th ($t_{½}$ = 73 kyr) was considerably greater than that of ^{238}U in host rock, thus recoil and/or long-term weathering reactions can provide an additional source of ^{230}Th [21,60]. The $^{232}Th/^{238}U$ activity ratios varied between 1.30 and 2.25, a range considerably higher than the average crustal value [61].

Table 4. Solid-phase activities of ^{238}U, ^{230}Th, ^{232}Th, and $^{234}U/^{238}U$ activity ratios (AR).

Well ID	^{238}U [a]	^{230}Th	^{232}Th	$^{234}U/^{238}U$
	(dpm g^{-1})	(dpm g^{-1})	(dpm g^{-1})	AR
LWEB, Harbor	0.47	0.72 ± 0.06	0.84 ± 0.06	1.01 ± 0.01
LWEB, Bent Spring	0.49	0.66 ± 0.06	0.84 ± 0.06	1.00 ± 0.01
LWEB, Upper Wilmington	0.46	0.60 ± 0.06	0.60 ± 0.06	0.99 ± 0.02
LWEB, Upper Wilmington	0.42	0.60 ± 0.06	0.90 ± 0.06	1.02 ± 0.01
LBPC, Pliocene A	0.56	0.72 ± 0.06	1.26 ± 0.09	0.99 ± 0.01
LWEB, Pliocene A	0.73	1.02 ± 0.06	1.44 ± 0.09	1.02 ±0.01
LBPC, Pliocene B	0.6	0.90 ± 0.06	0.90 ± 0.06	1.01 ± 0.01

Note: [a] Analytical error < 3%.

5.7. Concentrations and Activity Ratios of ^{222}Rn and Ra Isotopes

Ra isotopes can provide unique information regarding the production of U/Th series radionuclides in groundwater and reveal where significant transformations in adsorption or parent element distribution can occur along a groundwater flow path [62,63]. Values for Ra partitioning coefficients and retardation factors can also be obtained from the Ra isotopes but only by assuming that ^{222}Rn provides a reasonable proxy for the recoil production rates of radium.

The concentrations of ^{222}Rn ($t_{½}$ = 3.825 days) ranged from 142,000 dpm m^{-3} (LWEB-2) to 442,000 dpm m^{-3} (370-AJ) (average ^{222}Rn = 260,000 dpm m^{-3}), which are expectedly the highest values observed as compared to other members of U- and Th-series radionuclides reported here (Table 5). The large ^{222}Rn concentrations are the result of radon's inert character as a noble gas and its resulting inability to participate in any scavenging reactions. The concentration of ^{226}Ra ($t_{½}$ = 1600 years) varied between 29 dpm m^{-3} (Wilmington-2#3) and 1632 dpm m^{-3} (Wilmington-2#5) (average ^{226}Ra = 257 dpm m^{-3}), which is ~2–4 orders of magnitude lower than the ^{222}Rn activities. Rn-222 is a direct measure of ^{226}Ra (direct radiogenic parent of ^{222}Rn) in the host rocks as well as a measure of the relative emanation efficiency from the host rock [64]. A plot of ^{226}Ra activity as a function of Cl^- concentration is shown in Figure 7. Elevated Ra follows an increase in Cl^- and is attributed to solubilization of chloride complexes and/or through displacement from clays by ion exchange and desorption reactions.

Figure 7. Ra-226 activity (dpm m^{-3}) *versus* Cl^- concentration.

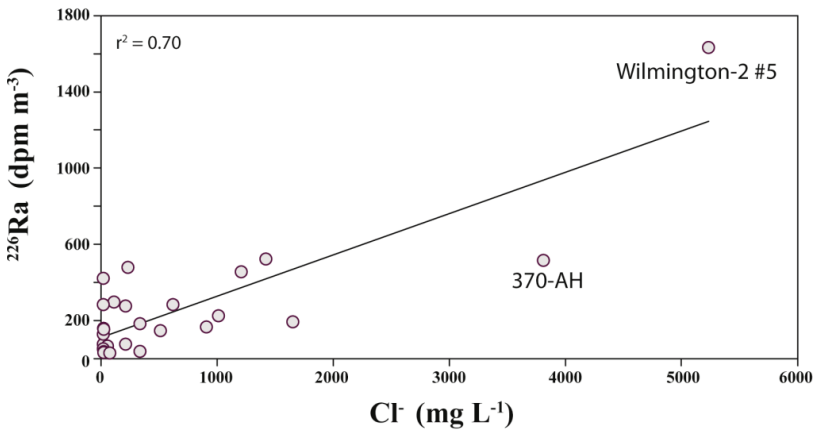

Table 5. Activities (dpm m^{-3}) of dissolved ^{222}Rn and four Ra isotopes in select wells from within the study area.

Well ID	^{222}Rn	^{223}Ra	^{224}Ra	^{228}Ra	^{226}Ra
	(dpm m^{-3})	(dpm m^{-3})	(dpm m^{-3})	(dpm m^{-3})	(dpm m^{-3})
Huntington Park #1	-	147.4	2,138.8	457 ± 25	421 ± 9
Huntington Park #2	-	44.1	1,720.4	306 ± 24	159 ± 7
Carson-1 #1	-	26.2	844.6	172 ± 15	76 ± 4
Carson-1 #2	-	35.6	2,270.7	311 ± 19	128 ± 5
Carson-1 #3	-	56.5	1,976.2	353 ± 23	154 ± 6.7
Carson-1 #4	-	109.8	3,310.2	694 ± 32	296 ± 8
Wilmington-1 #1	-	3.8	111.9	199 ± 16	76 ± 4
Wilmington-1 #2	-	11	296.6	511 ± 26	183 ± 6
Wilmington-1 #3	-	9.1	284.4	452 ± 19	166 ± 5
Wilmington-1 #4	-	73.4	1,392.2	825 ± 35	455 ± 9
Wilmington-1 #5	-	16	466.9	654 ± 30	479 ± 10
Wilmington-2 #1	-	14.7	792.2	173 ± 17	66 ± 4
Wilmington-2 #2	-	23.4	2,903.1	177 ± 17	145 ± 6
Wilmington-2 #3	-	4.9	1,813.5	378 ± 18	29 ± 1
Wilmington-2 #4	-	4.3	2,254.6	553 ± 27	225 ± 7
Wilmington-2 #5	-	204.5	3,918.8	2,716 ± 85	1,632 ± 18
LWEB-1	244,000 ± 39,000	3.4	170	84 ± 9	51.6 ± 5.0
LWEB-2	142,000 ± 47,000	4.1	115	-	-
LWEB-3	242,000 ± 47,000	13.5	277	83 ± 10	36.7 ± 4.4
LWEB-4	202,000 ± 23,000	60.6	1,285	581 ± 17	275 ± 7
LWEB-5	195,000 ± 36,000	55.9	1,301	826 ± 21	282 ± 7
LBCH-1	217,000 ± 11,000	2.9	95	53.6 ± 9.1	31.1 ± 4.2
LBCH-2	418,000 ± 27,000	9.5	152	55.2 ± 8.6	29.2 ± 4.0
LBCH-3	336,000 ± 75,000	18	690	-	-
LBCH-4	388,000 ± 39,000	151.4	11,351	-	-
370-AJ	442,000 ± 39,000	52.9	765	1,269 ± 24	522 ± 9
370-AH	347,000 ± 58,000	49.2	2,976	2,944 ± 58	515 ± 10
LBPC-1	160,000 ± 24,000	22.2	294	826 ± 21	282 ± 7
LBPC-2	223,000 ± 46,000	10	138	86 ± 12	38 ± 4.6
LBPF-1	172,000 ± 20,000	24.5	1,022	631 ± 23	192 ± 6.5
LBPF-2	173,000 ± 11,000	54.5	4,489	-	-

The concentration of ^{223}Ra ($t_{½}$ = 11.4 days) varied between 2.9 dpm m^{-3} (LBCH-1) and 204.5 dpm m^{-3} (Wilmington 2#5) (mean ^{223}Ra = 42 dpm m^{-3}), while the concentrations of ^{224}Ra ($t_{½}$ = 3.66 days) and ^{228}Ra ($t_{½}$ = 5.75 years) varied between 95 dpm m^{-3} (LBCH-1) and 11,351 dpm m^{-3} (LBCH-4) (mean ^{224}Ra = 1665) dpm m^{-3} and 54 dpm m^{-3} (LBCH-1) and 2944 dpm m^{-3} (370-AH) (mean ^{228}Ra = 606 dpm m^{-3}), respectively. The $^{223}Ra/^{226}Ra$ activity ratio (AR) varied between 0.02 and 0.37 (Table 6), with a mean value of 0.18, a value substantially higher than the expected value of 0.046. Because ^{223}Ra and ^{226}Ra are both generated after three α decays, groundwater should have a $^{223}Ra/^{226}Ra$ activity ratio similar to the host rock ($^{235}U/^{238}U$) activity ratio of 0.046. Higher $^{223}Ra/^{226}Ra$ activity

ratio may be observed in groundwater after a recharge or precipitation event, as ^{226}Ra, due to its longer half-life, will not yet have reached a steady state concentration [16,65,66].

Table 6. Dissolved activity ratios (AR) of ^{228}Ra/^{226}Ra, ^{224}Ra/^{228}Ra, ^{224}Ra/^{223}Ra, ^{224}Ra/^{222}Rn, and ^{223}Ra/^{226}Ra, as well as the model-derived parameters: Ω, k_1, k_2, and R_f in select wells.

Well ID	^{228}Ra/^{226}Ra	^{224}Ra/^{228}Ra	^{224}Ra/^{223}Ra	^{224}Ra/^{222}Rn	^{223}Ra/^{226}Ra	Ω_{224}	Ω_{228}	k_1	k_2 (min^{-1})	R_f
	AR	AR	AR	AR (× 10^{-4})	AR	(× 10^{-4})	(× 10^{-4})	(min^{-1})	(× 10^{-4})	(× 10^{3})
LWEB-1	1.61 ± 0.23	2.04 ± 0.23	50.7 ± 5.7	7.0 ± 1.2	0.065 ± 0.009	4.9	2.4	0.53	1.3	4.1
LWEB-2			28.1 ± 3.1	8.1 ± 2.7	-	5.4	-	-	-	
LWEB-3	2.25 ± 0.38	3.34 ± 0.43	20.5 ± 2.3	11.4 ± 2.3	0.367 ± 0.058	8.8	2.6	0.21	0.56	3.8
LWEB-4	2.11 ± 0.08	2.21 ± 0.13	21.2 ± 2.4	63.8 ± 8.1	0.220 ± 0.023	50	23	0.05	1.1	0.5
LWEB-5	2.93 ± 0.10	1.57 ± 0.09	23.3 ± 2.6	66.7 ± 12.8	0.198419	57	36	0.06	2.3	0.3
LBCH-1	1.72 ± 0.38	1.78 ± 0.32	32.5 ± 3.6	4.4 ± 0.3	0.094 ± 0.016	2.9	1.7	1	1.7	5.9
LBCH-2	1.89 ± 0.39	2.76 ± 0.45	16.0 ± 1.8	3.7 ± 0.3	0.325 ± 0.055	2.4	0.88	0.85	0.74	11.5
LBCH-3	-	-	38.2 ± 4.3	20.5 ± 4.7	-	-	-	-	-	
LBCH-4	-	-	74.9 ± 8.4	293 ± 33	-	-	-	-	-	
370-AJ	2.43 ± 0.06	0.60 ± 0.03	14.5 ± 1.6	17.3 ± 1.7	0.101 ± 0.010	15	25	-	-	
370-AH	5.72 ± 0.16	1.01 ± 0.05	60.5 ± 6.8	86 ± 15	0.096 ± 0.010	73	72	1.7	121	0.1
LBPC-1	2.93 ± 0.10	0.36 ± 0.02	13.3 ± 1.5	18.4 ± 2.9	0.079 ± 0.008	18	52	-	-	
LBPC-2	2.26 ± 0.42	1.61 ± 0.24	13.9 ± 1.6	6.20 ± 1.3	0.262 ± 0.041	3.5	2.2	1	2.1	4.8
LBPF-1	-	-	41.7 ± 4.7	59.5 ± 7.5	0.127 ± 0.013	41	26	0.08	2.1	0.4
LBPF-2	-	-	82.4 ± 9.2	259 ± 21	-	204	-	0.006	-	

Notes: Ω = Ratio of the activity of a radionuclide in solution (λN_d), to its production rate, P; k_1 = first order adsorption rate constant; k_2 = first order desorption rate constant; R_f = Retardation Factor, calculated from k_1/k_2.

The ^{224}Ra/^{228}Ra activity ratios provide a measure of the adsorption and desorption rate constants for radium [15,21]. Within host rocks that are in secular equilibrium, ^{224}Ra/^{228}Ra = 1. The ^{224}Ra/^{228}Ra activity ratios in the groundwater samples (Table 6) varied between 0.36 (LBPC-1) and 3.34 (LWEB-2). While in general the fresh groundwater ^{224}Ra/^{228}Ra ARs fall in a reasonably narrow range (0.5–2.0; [15,60,67]), but much higher values have also been observed [61]. Typically, higher ^{224}Ra/^{228}Ra ARs occur in groundwaters where steady state conditions have not yet been reached or in transitional coastal groundwater systems that are variably affected by seawater mixing [38]. In these groundwater samples (e.g., LBCH-2, LWEB-1,4,3), observed elevated ^{224}Ra/^{228}Ra ARs may identify waters that have recently been mixed with seawater.

Due to their short and similar half-lives ($t_{½}$ = <4 days), the activities of ^{224}Ra and ^{222}Rn are expected to be in steady state in most groundwater. From the host rock ^{232}Th/^{238}U activity ratio, ^{224}Ra/^{222}Rn activity ratios can be used to calculate recoil and sorption rate constants [21]. The observed ^{224}Ra/^{222}Rn activity ratios (Table 6) varied between 1.34 × 10^{-5} to 3.9 × 10^{-4} (average = 1.25 × 10^{-4}) and agree well with other reported values (0.2–4.4 × 10^{-4}; [15,60,67]). The measured range in ^{224}Ra/^{222}Rn activity ratios reflects the natural variability of these radionuclides in this groundwater system. The activity ratio of the two longest lived Ra isotopes, ^{228}Ra/^{226}Ra, provides a measure of the relative recoil rates of radionuclides from two decay series [21]. The observed

$^{228}Ra/^{226}Ra$ activity ratios (Table 6) ranged between 1.1 and 5.7 (average = 2.3). Because ^{226}Ra is the product of three α decays, while ^{228}Ra is produced by one single α decay, ^{226}Ra may be more mobile than ^{228}Ra, resulting in lower $^{228}Ra/^{226}Ra$ activity ratios. Differences in the activity ratios can be attributed to variations in the distribution of U and Th in host rocks.

5.8. Adsorption-Desorption Rate Constants and Retardation Factors

The production rates for Ra isotopes were calculated using ^{222}Rn as the recoil flux monitor and is based on the relation [15]:

$$F_i = F_r\ (Q_i/Q_r)\ \varepsilon \quad (6)$$

where F_i and F_r are the recoil supply rates of Ra isotopes (^{224}Ra and ^{228}Ra) and ^{222}Rn to the groundwater respectively; Q_i and Q_r are the production rates of Ra isotopes and ^{222}Rn in the aquifer solids; and ε is the rate of recoil supply of ^{224}Ra and ^{228}Ra relative to the ^{222}Rn recoil supply. The term ε depends on where the radionuclide is positioned in the decay series, the α particle energy released during its production, and the scavenging capability of its immediate radiogenic parent. The value of ε can vary from a steady state value of ~1.5, if all the ^{226}Ra recoiled into the groundwater remains in solution, to 0.86 if all the recoiled ^{226}Ra is adsorbed onto the aquifer grain surfaces [15]. For the derivation of F_i and F_r, we assumed a ε value of 1.0.

The calculated values of Ω_{224}, Ω_{228}, k_1, k_2, and R_f are given in Table 6. The adsorption rate constants (k_1) calculated based on the ^{224}Ra and ^{228}Ra concentrations varied between 0.006 to 1.70 min^{-1}, with an average value of 0.55 min^{-1} and co-varied positively ($R = 0.71$, $n = 7$) with Na^+ concentration if one excludes the three highest Na^+ values (LBPF-1,2, Wilmington-2#5). This observation is intriguing, as one might expect an inverse correlation, as higher Na^+ would imply more Na^+ available for exchange, and thus, longer Ra residence time (or smaller k_1 values). More studies need to be conducted to validate this observation. The corresponding residence times, calculated for an irreversible adsorption model ($1/k_1$) ranged from 0.59 to 20.0 min (average = 6.62 min). The desorption rate (k_2) constant varied between 0.56 and 121 × 10^{-4} min^{-1}, with a mean value of 14.8 × 10^{-4} min^{-1}. The corresponding average residence time with respect to desorption was expectedly much greater. Faster sorption (k_1) of Ra injected into the water and slower desorption (k_2) from the host rock has been previously documented [15,17,18,67]. This range in values is in contrast with the values reported for subsurface brines, where k_1 and k_2 values are typically comparable [16,68]. As k_1 is always much greater than k_2 for these groundwater samples, the ratio k_1/k_2 can be used as a measure of the retardation factor, R_f [15], which here ranged from 0.1 to 11.5 × 10^3 (average = 3.5 × 10^3). Such R_f values are on the same order of magnitude as has been reported for other groundwater systems [15,16,60,67].

6. Conclusions

Stable- and radio-isotopes, as well as a complementary suite of water quality parameters, were utilized to assess groundwater properties from select wells in the Los Angeles Basin–Dominguez Gap area. Groundwater resources in this region have been extensively developed and managed since the late 1800s. In the study area, groundwater resides in multiple aquifer systems that are complexly

mixed with seawater, non-native water that is used to stave off saltwater intrusion, and oil-field related brine waters. Elevated Cl^- concentrations are observed in some nearshore wells (LBPF-2, Wilmington-2 #5) and in the Dominguez Gap area. The $\delta^{18}O$ composition observed in select wells provides a measure of saltwater and oil-field brine mixing. Tritium data from these wells reveal that recent (less than 50 years old) groundwater was present only in a few select wells in the Upper and Lower aquifer systems close to the Dominguez Gap area (Wilmington-1 #4, Wilmington-1 #5, and Wilmington-2 #5) where the seawater barrier injection wells may introduce additional ^3H. The $\delta^{13}C_{DIC}$ composition in groundwater ranged from −18.9‰ to + 6.3‰ and provides an indication of the evolution of this groundwater system; some well water exhibited considerably lower $\delta^{13}C_{DIC}$ values and in the absence of SO_4^{2-} may reflect a contribution of enhanced ^{13}C from microbial methanogenesis under anoxic conditions. Lastly, $\delta^{18}O$ (−9.77‰ to −0.42‰) and deuterium (−3.65‰ to −77.5‰) in these well waters provide information on the likely quantification of water balance and interaction within adjacent groundwaters.

From a series of well cuttings, aquifer host rock ^{234}U and ^{238}U are expectedly in secular equilibrium. In contrast, U- and Th-series radionuclides exhibit strong fractionation in groundwaters from select wells. Such radiogenic disequilibria are used to assess fundamental aquifer properties, such as the retardation factor R_f and adsorption/desorption rate constants, $k_1$and k_2, respectively. While we cannot quantify a relative groundwater age from the Ra isotopes alone, the calculated adsorption rate constant (k_1) is markedly higher than the desorption rate constant (k_2), which implies that the residence time of dissolved Ra must be very short (average ~7 min).

In combination, this suite of isotopic and elemental tracers can provide valuable information on complex groundwater mixing scenarios and provenance, which are useful to assess groundwater vulnerability to current and future external stressors, such as groundwater withdrawals, contamination, and sea level rise.

Acknowledgements

We thank John Haines of the USGS Coastal and Marine Geology (CM&G) Program for continued support in coastal groundwater studies. Nancy Prouty, Renee Takesue, and Christopher Conaway provided thoughtful reviews of an earlier version of this manuscript. The authors are also thankful for the four constructive reviews that greatly improved the manuscript. The use of trade, product, or firm names in this publication is for descriptive purposes only and does not imply endorsement by the U.S. government.

References

1. Mendenhall, W.D. *Development of Underground Waters in the Eastern Coastal Plain Region of Southern California*; Water-Supply Paper 137; U.S. Geological Survey: Reston, VA, USA, 1905.
2. California Department of Water Resources. *Planned Utilization of the Groundwater Basins of the Coastal Plain of Los Angeles Country, Appendix A: Ground Water Geology*; Bulletin 104; California Department of Water Resources: Sacramento, CA, USA, 1961.

3. Los Angeles County Department of Public Works Web Page. Seawater Barriers. Available online: http://dpw.lacounty.gov/wrd/Barriers/ (accessed on 1 March 2013).
4. Reichard, E.G.; Land, M.; Crawford, S.M.; Johnson, T.; Everett, R.R.; Kulshan, T.V.; Ponti, D.J.; Halford, K.L.; Johnson, T.A.; Paybins, K.S.; *et al*. *Geohydrology, Geochemistry, and Ground-Water Simulation-Optimization of the Central and West Coast Basins, Los Angeles County, California*; Water-Resources Investigations Report 03-4065; U.S. Geological Survey: Reston, VA, USA, 2003.
5. Land, M.; Everett, R.R.; Crawford, S.M. *Geologic, Hydrologic, and Water-Quality Data from Multiple-Well Monitoring Sites in the Central and West Coast Basins, Los Angeles County, California*; Open-File Report 01-277; U.S. Geological Survey: Reston, VA, USA, 2002.
6. Land, M.; Reichard, E.G.; Crawford, S.M.; Everett, R.R.; Newhouse, M.W.; Williams, C.F. *Ground-Water Quality of Coastal Aquifer Systems in the West Coast Basin, Los Angeles County, California, 1999–2002*; Scientific Investigations Report 2004–5067; U.S. Geological Survey: Reston, VA, USA, 2004.
7. Clark, I.; Fritz, P. *Environmental Isotopes in Hydrogeology*; Lewis Press: Boca Raton, FL, USA, 1997.
8. Kendall, C.; McDonnell, J.J. *Isotope Tracers in Catchment Hydrology*; Elsevier Science: Amsterdam, The Netherlands, 1998.
9. Hem, J.D. *Study and Interpretation of the Chemical Characteristics of Natural Water*, 4th ed.; Water-Supply Paper 2254; U.S. Geological Survey: Reston, VA, USA, 1992.
10. Gat, J.R.; Gonfiantini, R. *Stable Isotope Hydrology—Deuterium and Oxygen-18 in the Water Cycle*; International Atomic Energy Agency: Vienna, Austria, 1981.
11. Kendall, C.; Mast, M.A.; Rice, K.C. Tracing Watershed Weathering Reactions with $\delta^{13}C$. In *Water-Rock Interactions*, Proceedings of the 7th International Symposium, Park City, UT, USA, 13–18 July 1993; Kharaka, Y.K., Maest, A.S., Eds.; Balkema: Rotterdam, The Netherlands, 1993; pp. 569–572.
12. Rozanski, K.; Araguas-Araguas, L.; Gonfiantini, R. Isotopic patterns in modern global precipitation, in climate change in Continental Isotopic Records. *Geophys. Monogr*. **1993**, *78*, 1–36.
13. Izbicki, J.A., Danskin, W.R., Mendez, G.O. *Chemistry and Isotopic Composition of Groundwater along a Section near the Newmark Area, San Bernardino County, California*; Water-Resources Investigations Report 97-4179; U.S. Geological Survey: Reston, VA, USA, 1998.
14. Szabo, Z.; Rice, D.E.; Plummer, L.N.; Busenberg, E.; Drenkard, S.; Schlosser, P. Age dating of shallow groundwater with chlorofluorocarbons, tritium/helium 3, and flow path analysis, southern New Jersey coastal plain. *Water Resour. Res.* **1996**, *32*, 1023–1038.
15. Krishnaswami, S.; Graustein, W.C.; Turekian, K.K.; Dowd, J.F. Radium, thorium, and radioactive lead isotopes in groundwaters: Application to the *in-situ* determination of adsorption-desorption rate constants and retardation factors. *Water Resour. Res.* **1982**, *18*, 1633–1675.

16. Krishnaswami, S.; Bhushan, R.; Baskaran, M. Radium isotopes and ^{222}Rn in shallow brines, Kharaghoda (India). *Chem. Geol.* **1991**, *87*, 125–136.
17. Copenhaver, S.A.; Krishnaswami, S.; Turekian, K.K.; Shaw, H. ^{238}U and ^{232}Th series nuclides in groundwater from the J-13 well at the Nevada test site: Implications for ion retardation. *Geophys. Res. Let.* **1992**, *19*, 1383–1386.
18. Copenhaver, S.A.; Krishnaswami, S.; Turekian, K.K.; Epler, N.; Cochran, J.K. Retardation of ^{238}U and ^{232}Th decay chain radionuclides in Long Island and Connecticut aquifers. *Geochim. Cosmochim. Acta* **1993**, *57*, 597–603.
19. Hussain, N. Supply rates of natural U-Th series radionuclides from aquifer solids into groundwater. *Geophys. Res. Let*. **1995**, *22*, 1521–1524.
20. Ku, T.-L.; Luo, S.; Leslie, B.W.; Hammond, D.E. Decay-series disequilibria applied to the study of rock-water interaction and geothermal systems. In *Uranium-series Disequilibrium*; Ivanovich, M., Harmon, R.S., Eds.; Clarendon Press: Oxford, England, 1992; pp. 631–688.
21. Porcelli, D.; Swarzenski, P.W. The behavior of U- and Th-series nuclides in groundwater. *Rev. Mineral. Geochem.* **2003**, *52*, 317–361.
22. Olsen, C.R.; Cutshall, N.H.; Larsen, I.L. Pollutant-particle associations and dynamics in coastal marine environments: A review. *Mar. Chem.* **1982**, *11*, 501–533.
23. Dickson, B.L. Radium isotopes in saline seepages, south-western Yilgarn, Western Australia. *Geochim. Cosmochim. Acta* **1985**, *49*, 361–368.
24. Dickson, B.L.; Wheller, G.E. Uranium-series disequilibrium exploration geology. In *Uranium-Series Disequilibrium: Applications to Earth, Marine, and Environmental Sciences*; Ivanovich, M., Harmon, R.S., Eds.; Clarendon Press: Oxford, UK, 1992; pp. 704–730.
25. Rama; Moore, W.S. Mechanisms of transport of U-Th series radioisotopes from solids into groundwater. *Geochim. Cosmochim. Acta* **1984**, *48*, 395–399.
26. Poland, J.F.; Piper, A.N. *Groundwater Geology of the Coastal Zone, Long Beach-Santa Ana Area, California*; Water-Supply Paper 1109; U.S. Geological Survey: Reston, VA, USA, 1956.
27. Yerkes, R.F.; McCulloh, T.H.; Schoellhamer, J.E.; Vedder, J.G. *Geology of the Los Angeles Basin, California: An Introduction*; Professional Paper 420-A; U.S. Geological Survey: Reston, VA, USA, 1965.
28. Davis, T.L.; Namson, J.; Yerkes, R.F. A cross section of the Los Angeles area: Seismically active fold and thrust belt, the 1987 Whittier Narrows earthquake and earthquake hazard. *Geophys. Res.* **1989**, *94*, 9644–9664.
29. Wright, T.L. Structural geology and tectonic evolution of the Los Angeles Basin, California. In *Active Margin Basins*; Memoir 52; Biddle, K.T., Eds.; American Association of Petroleum Geologists: Tulsa, OK, USA, 1991; pp. 35–134.
30. Ponti, D.J.; Ehman, K.D.; Edwards, B.D.; Tinsley, J.C., III; Hildenbrand, T.; Hillhouse, J.W.; Hanson, R.T.; McDougall, K.; Powell, C.L., II; Wan, E.; *et al. A 3-Dimensional Model of Water-Bearing Sequences in the Dominguez Gap Region, Long Beach, California*; Open-File Report 2007-1013; U.S. Geological Survey: Reston, VA, USA, 2007.

31. Nishikawa, T.; Siade, A.J.; Reichard, E.G.; Ponti, D.J.; Canales, A.G.; Johnson, T.A. Stratigraphic controls on seawater intrusion and implications for groundwater management, Dominguez Gap area of Los Angeles, California, USA. *Hydrol. J.* **2009**, *17*, 1699–1725.
32. Woodring, W.P.; Bramlette, M.N.; Kew, W.S.W. *Geology and Paleontology of Pales Verdes Hills, California*; Professional Paper 207; U.S. Geological Survey: Reston, VA, USA, 1946.
33. Epstein, S.; Mayeda, T. Variation of O^{18} content of water from natural sources. *Geochim. Cosmochim. Acta* **1953**, *4*, 213–224.
34. Coplen, T.B.; Wildman, J.D.; Chen, J. Improvements in the gaseous hydrogen-water equilibration technique for hydrogen isotope ratio analysis. *Anal. Chem.* **1991**, *63*, 910–912.
35. Burnett, W.C.; Taniguchi, M.; Oberdorfer, J.A. Assessment of submarine groundwater discharge into the coastal zone. *J. Sea Res.* **2001**, *46*, 109–116.
36. Burnett, W.C.; Dulaiova, H. Estimating the dynamics of groundwater input into the coastal zone via continuous radon-222 measurements. *J. Environ. Radio.* **2003**, *69*, 21–25.
37. Swarzenski, P.W.; Orem, W.G.; McPherson, B.F.; Baskaran, M.; Wan, Y. Biogeochemical transport in the Loxahatchee river estuary: The role of submarine groundwater discharge. *Mar. Chem.* **2006**, *101*, 248–265.
38. Swarzenski, P.W. U/Th series radionuclides as tracers of coastal groundwater. *Chem. Rev.* **2007**, *107*, 663–674.
39. Moore, W.S.; Arnold, R. Measurements of ^{223}Ra and ^{224}Ra in coastal waters using a delayed coincidence counter. *J. Geophys. Res.* **1996**, *101*, 1321–1329.
40. Moore, W.S. Sampling ^{228}Ra in the deep ocean. *Deep Sea Res. Oceanogr. Abstr.* **1976**, *23*, 647–651.
41. Drever, J.I. *The Geochemistry of Natural Waters*, 2nd ed.; Prentice Hall: Upper Saddle River, NJ, USA, 1988.
42. Back, W.; Hanshaw, B.B.; Pyler, T.E.; Plummer, L.N.; Weide, E. Geochemical significance of groundwater discharge in Caleta Xel Ha, Quintana Roo, Mexico. *Water Resour. Res.* **1979**, *15*, 1521–1535.
43. Ponti, D. U.S. Geological Survey, Menlo Park, CA, USA. Personal communication, September 2012.
44. Izbicki, J.A. *Source, Movement, and Age of Groundwater in a Coastal California Aquifer*; Fact Sheet FS126-96; U.S. Geological Survey: Reston, VA, USA, 1996.
45. Michel, R.L. *Tritium Deposition in the Continental United States, 1953–1989*; Water-Resources Investigations Report 89-4072; U.S. Geological Survey: Reston, VA, USA, 1989.
46. Craig, H. Isotopic variations in meteoric waters. *Science* **1961**, *133*, 1702–1803.
47. Dansgaard, W. Stable isotopes in precipitation. *Tellus* **1964**, *16*, 436–468.
48. Williams, A.E.; Rodoni, D.P. Regional isotope effects and application to hydrologic investigations in southwestern California. *Water Resour. Res*. **1997**, *33*, 1721–1729.
49. Taylor, C.B. On the isotopic composition of dissolved inorganic carbon in rivers and shallow groundwater: A diagrammatic approach to process identification and a more realistic model of the open system. *Radiocarbon* **1997**, *39*, 251–268.

50. Claypool, G.E.; Kaplan, I.R. The origin and distribution of methane in marine sediments. In *Natural Gases in Marine Sediments*; Kaplan, I.R., Ed.; Springer: Berlin, Germany, 1974; pp. 99–139.
51. Grossman, E.L. Stable carbon isotopes as indicators of microbial activity in aquifers. In *Manual of Environmental Microbiology*; Hurst, C.J., Ed.; American Society for Microbiology: Washington, DC, USA, 1997; pp. 565–576.
52. Hellings, L.; van den Driessche, K.; Baeyens, W.; Keppens, E.; Dehairs, F. Origin and fate of dissolved inorganic carbon in interstitial waters of two freshwater intertidal areas: A case study of the Scheldt estuary, Belgium. *Biogeochemistry* **2000**, *51*, 141–160.
53. Landmeyer, J.E.; Vroblesky, D.A.; Chapelle, F.H. Stable carbon isotope evidence of biodegradation zonation in a shallow jet-fuel contaminated aquifer. *Environ. Sci. Technol.* **1996**, *30*, 1120–1128.
54. Conrad, M.E.; Daley, P.F.; Fischer, M.L.; Buchanan, B.B.; Kashgarian, M. Combined ^{14}C and $\delta^{13}C$ monitoring of *in situ* biodegradation of petroleum hydrocarbons. *Environ. Sci. Technol.* **1997**, *31*, 1463–1469.
55. Marfia, A.M.; Krishnamurthy, R.V.; Atekwana, E.A.; Panton, W.F. Isotopic and geochemical evolution of ground and surface waters in a karst dominated geologic setting: A case study from Belize, Central America. *Appl. Geochem.* **2004**, *19*, 937–946.
56. Nascimento, C.; Atekwana, E.A.; Krishnamurthy, K.V. Concentrations and isotope ratios of dissolved inorganic carbon in denitrifying environments. *Geophys. Res. Lett.* **1997**, *24*, 1511–1514.
57. Rosenthal, E.; Vinokurov, A.; Magaritz, M.; Moshkovitz, S. Anthropogenically induced salinization of groundwater: A case study from the coastal plain aquifer of Israel. *Contamin. Hydrol.* **1992**, *11*, 149–171.
58. Plummer, L.N.; Parkhurst, D.L.; Thorstenson, D.C. Development of reaction models for ground-water systems. *Geochim. Cosmochim. Acta* **1983**, *47*, 665–686.
59. Kigoshi, K. Alpha recoil ^{234}Th: Dissolution in water and the $^{234}U/^{238}U$ disequilibrium in nature. *Science* **1971**, *173*, 47–48.
60. Tricca, A.; Wasserburg, G.J.; Porcelli, D.; Baskaran, M. The transport of U- and Th-series nuclides in a sandy confined aquifer. *Geochim. Cosmochim Acta* **2001**, *65*, 1187–1121.
61. Turekian, K.K.; Wedepohl, K.H. Distribution of the elements in some major units of the earth's crust. *GSA Bull.* **1961**, *72*, 175–192.
62. Swarzenski, P.W.; Reich, C.D.; Spechler, R.M.; Kindinger, J.L.; Moore, W.S. Using multiple geochemical tracers to characterize the hydrogeology of the submarine spring off Crescent Beach, Florida. *Chem. Geol.* **2001**, *179*, 187–202.
63. Krishnaswami, S.; Seidemann, D.E. Comparative study of ^{222}Rn, ^{40}Ar, ^{39}Ar, and ^{37}Ar leakage from rocks and minerals—Implications for the role of nanopores in gas transport through natural silicates. *Geochim. Cosmochim. Acta* **1988**, *52*, 655–658.
64. Rama; Moore, W.S. Submicronic porosity in common minerals and emanation of radon. *Nucl. Geophys.* **1990**, *4*, 467–473.
65. Davidson, M.R.; Dickson, B.L. A porous flow model for steady state transport of radium in groundwater. *Water Resour. Res.* **1986**, *22*, 34–44.

66. Martin, P.; Akber, R.A. Radium isotopes as indicators of adsorption–desorption interactions and barite formation in groundwater. *J. Environ. Radioact.* **1999**, *46*, 271–286.
67. Luo, S.; Ku, T.-L.; Roback, R.; Murrell, M.; McLing, T.L. *In-situ* radionuclide transport and preferential groundwater flows at INEEL (Idaho): Decay-series disequilibrium studies. *Geochim. Cosmochim. Acta* **2000**, *64*, 867–881.
68. Hammond, D.E.; Zukin, J.G.; Ku, T.-L. The kinetics of radioisotope exchange between brine and rock in a geothermal system. *J. Geophys. Res.* **1988**, *93*, 13175–13186.

Submarine Groundwater Discharge at a Single Spot Location: Evaluation of Different Detection Approaches

Michael Schubert, Jan Scholten, Axel Schmidt, Jean François Comanducci, Mai Khanh Pham, Ulf Mallast and Kay Knoeller

Abstract: Submarine groundwater discharge (SGD) into the ocean is of general interest because it acts as vehicle for the transport of dissolved contaminants and/or nutrients into the coastal sea and because it may be accompanied by the loss of significant volumes of freshwater. Due to the large-scale and long-term nature of the related hydrological processes, environmental tracers are required for SGD investigation. The water parameters of electrical conductivity and temperature, the naturally occurring radionuclides of radon and radium as well as the stable water isotopes ^{18}O and ^{2}H have proven in previous studies their general suitability for the detection and quantification of SGD. However, individual hydrogeological settings require a site-specific application of this "tool box". This study evaluates and compares the applicability of the abovementioned tracers for investigating SGD from a distinct submarine source in a karst environment at Cabbé, southern France. The specific advantages and disadvantages of each individual parameter under the given hydrogeological conditions are discussed. Radon appeared to be the most suitable environmental tracer in the site specific context. The water temperature was less reliable due to the little temperature difference between seawater and groundwater and since the diurnal variation of the air temperature masks potential SGD signals. Radium isotopes are less applicable in the studied region due to the lack of a well-developed subterranean estuary. The stable water isotopes showed results consistent with the salinity and radon data; however, the significantly higher effort required for stable isotope analyses is disadvantageous. A multi-temporal thermal remote sensing approach proved to be a powerful tool for initial SGD surveying.

Reprinted from *Water*. Cite as: Schubert, M.; Scholten, J.; Schmidt, A.; Comanducci, J.F.; Pham, M.K.; Mallast, U.; Knoeller, K. Submarine Groundwater Discharge at a Single Spot Location: Evaluation of Different Detection Approaches. *Water* **2014**, *6*, 584-601.

1. Introduction

Along the coastlines worldwide, terrestrial waters discharge continuously into the coastal sea. A key role in the related water budget is played by submarine groundwater discharge (SGD), *i.e.*, "the flow of water through the continental margin from the seabed to the coastal ocean, occurring regardless of fluid composition or driving force with scale lengths of meters to kilometres" [1].

Due to two general facts SGD is of major interest for coastal water resources management: (1) it provides transport for contaminants and/or nutrients, thereby potentially threatening marine ecosystem health; (2) it may cause a loss of substantial volumes of freshwater to the ocean. With regard to the first, several studies have shown that dissolved material transport associated with SGD can be of the same order of magnitude as material transport associated with river discharge and surface water runoff [2,3]. With regard to the second it can be stated, that particularly spots of focussed SGD

have the so far unexploited potential to be used as important freshwater sources in arid climate zones and/or other areas that are characterized by water scarcity (e.g., islands in the Mediterranean Sea). The overall water resources management context of SGD is not only of relevance in the coastal ocean but also linked to the phenomenon offshore fresh groundwater reserves as comprehensively discussed by Post *et al.* [4].

In comparison to the investigation of river water discharge into the sea, which allows straightforward quantification of discharge rates and material budgets, the localization and investigation of SGD is more complex. Besides the difficulty that SGD can occur as both, diffuse seeps across wide patches of sea floor and focussed flow emerging from a distinct submarine spring, it is the high temporal variability that complicates the localisation of SGD areas and the assessment of the associated environmental impacts. The main drivers causing temporal fluctuations in SGD are (1) seasonal and long-term, changes in the inland hydraulic head; (2) tidal-driven, *i.e.*, diurnal changes in pressure gradients; and (3) short-term non-cyclical wave or current-induced pressure gradients [5].

A considerable number of scientific studies during the last two decades have investigated occurrences of SGD in different environmental settings [3,6–14]. These studies revealed that in-depth understanding of SGD and related processes demands approaches that apply environmental tracers, *i.e.*, naturally-occurring hydrochemical indicators or dissolved tracers that show substantial gradients at the groundwater/seawater interface.

Indicators that are frequently used in this regard include the water parameters specific electrical conductivity (EC)/salinity and the naturally-occurring radioactive noble gas radon. The two parameters show the advantage of straightforward on-site detectability [10,15]. The radionuclide radon-222 (^{222}Rn, hereinafter referred to as radon) is of particular suitability in the given context, since it is short-lived (half-life 3.82 d) and chemically inert, which makes it a preferable dissolved tracer in the field of hydrological sciences [13,16–20].

Besides the two on-site detectable parameters EC and radon, the four naturally-occurring radium isotopes ^{226}Ra, ^{228}Ra, ^{223}Ra, and ^{224}Ra are widely used as environmental tracers for the investigation of groundwater/seawater water interaction and coastal water mixing [21,22]. While radium is mainly particle-bound in freshwater (*i.e.*, not in solution), it desorbs from the mineral matrix if the groundwater salinity rises as is the case in the mixing zone between seawater and freshwater, the so-called "subterranean estuary" [23]. Because the four radium isotopes cover a wide range of half-lives (^{223}Ra: $t_{1/2}$ = 11.4 days; ^{224}Ra: $t_{1/2}$ = 3.7 days; ^{228}Ra: $t_{1/2}$ = 5.75 years; ^{226}Ra: $t_{1/2}$ = 1600 years) mixing processes of discharging groundwater with seawater can be investigated on different spatial and temporal scales.

Also suitable as SGD indicators are the isotopic signatures of δ^{18}O and δ^{2}H, which differ in general significantly between groundwater and surface water bodies [24,25]. Both isotopes can be used as tracers for describing mixing ratios between waters masses of different origin [26].

The presented study was carried out at Cabbé within the Bay of Roquebrune close to Monaco (Figure 1). The site is characterized by focussed groundwater discharge from a major karst aquifer at a distinct submarine spring into the Mediterranean Sea. Cabbé was chosen as study site because it

represents an archetypal and easily accessible site representative for coastal zones that are dominated by karst aquifers (as in large parts of the northern Mediterranean).

Figure 1. Small-scale site morphology; the white circle highlights the vertical submarine cave structure. Ropes were used for supporting probes and sampling tubes.

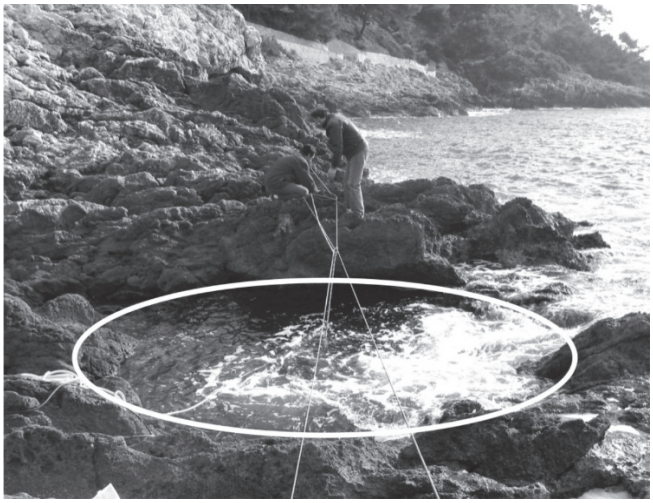

In karst environments large portions of the occurring precipitation recharge the local aquifer directly without large temporal delay, which in turn discharges mainly as focussed SGD into the sea. Zektser *et al.* [27] estimated a SGD flux to the Mediterranean Sea of about 68 km³/a, which corresponds to one third of the overall river discharge to the Mediterranean Sea. At the Cote d´Azur, France, between Nice and Menton over 50 sites of focussed SGD have been localized, which, based on local hydrogeological water mass balances, discharge in total about 18.9×10^6 m^3a^{-1} of freshwater to the sea [28]. However, the significance of this focused SGD for chemical input to the coastal sea remains so far unclear.

The objective of this study was to evaluate and compare the informative value of the abovementioned parameters under the specific conditions of a typically focussed SGD from a submarine karst spring. The investigated tracers included the stable isotopes of water (^2H and ^{18}O), naturally-occurring radioactive isotopes (^{222}Rn, $^{228, 226, 224, 223}Ra$) as well as physical (temperature) and chemical water parameters (salinity). Temporal and spatial patterns of all tracers were recorded over a 24 h period at Cabbé and along a 1.75 km transect located within the Bay of Roquebrune. In addition, the applicability of a multi-temporal thermal remote sensing approach [29] was evaluated for supporting the tracer results (and *vice versa*).

2. Methods

2.1. Site Setting

The submarine spring Cabbé is located in the north-western Mediterranean Sea about 5 km NE of Monaco (Figure 2). It is part of a group of several submarine springs mainly occurring along the coast between Nice and Menton, southern France [30]. At Cabbé groundwater discharges in a water

depth of about 4 m from the base of a vertical submarine cave with a diameter of approximately 3 m (Figure 1). The cave is surrounded by limestone forming a vertical hole that is constantly inundated by seawater. It is hydraulically connected to a major karst aquifer. Groundwater residence times in this karst aquifer were estimated to be between eight to nine days [30] (*cf.* Section 3.1.6). The yearly average temperature in the region is ~15 °C with an average of 770 mm of precipitation.

Figure 2. Regional setting of the site and the measured transect (**A**) within the Mediterranean Sea; (**B**) in geographical relation to Monaco.

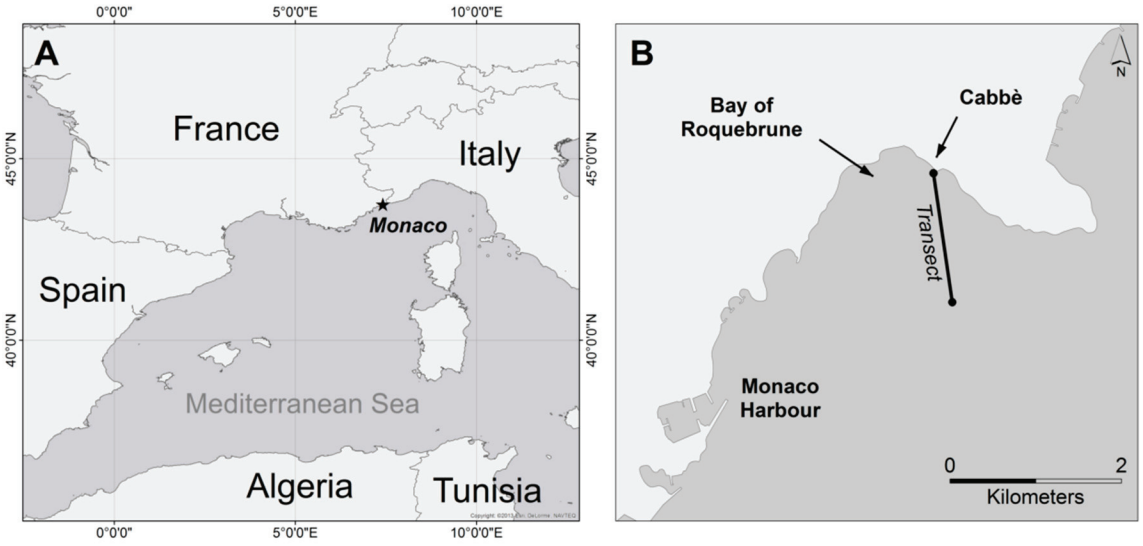

Geologically the area is part of the SE front of a subalpine range called "Arc de Nice", which consists of a series of south-verging folds and thrusts involving Mesozoic and Palaeogene sediments. The sediments consist of marls, clays, dolomites and limestones. Important aquifers with deep karstic circulation are associated with the latter. Coastal and submarine groundwater discharge spots are generally situated at the contact between the Jurassic limestone and the Cretaceous marls and clays.

2.2. Materials and Methods

At the base of the submarine vertical cave, *i.e.*, at the submarine spring, the parameters temperature, salinity, radon concentration, and water depth were monitored using automated detection equipment. All instruments were working properly from about 16:00 on the first day of the 24 h monitoring campaign and measured continuously for 24 h. A recording gap occurred on the second day between 03:00 and 05:00 due to technical difficulties. In addition to the recording of 24 h time series, discrete water samples were taken every 60 min for stable isotope analyses. Four discrete samples for radium analyses were obtained on the second day covering a period between low and high tide.

Additionally to the time-series measurements at the submarine spring, a survey was undertaken along a 1750 m transect within the Bay of Roquebrune starting at the submarine cave Cabbé. Along the transect the parameters salinity, temperature and radon concentration were monitored continuously while cruising with a speed of about 5 km/h. For stable isotopes and radium measurements discrete samples were taken along the transect.

For the measurement of conductivity/salinity, temperature, and water depth a CTD probe (YSI Inc., Yellow Springs, OH, USA) was used. At the spring the CTD was lowered into the cave with ropes (*cf*. Figure 1) and fixed close to the bottom of the vertical cave structure. The recorded water depth was used for monitoring the tidal cycle and for assessing the water turbulence within the cave (wave intensity). Along the transect the CTD was dragged behind the boat in a water depth of about 2 m for temperature and salinity recording. All CTD data were recorded in 10 second intervals. For comparison with the other monitored parameters, suitable moving average values were calculated.

For measurement of radon-in-water concentrations the portable radon-in-air monitor RAD-7 (Durridge Company, Billerica, MA, USA) was used. For radon detection, water was pumped either from the surface sea water (transect) or from the bottom part of the submarine cave. Radon was extracted from the constant water stream into a closed air loop by means of a RAD-Aqua extraction-module as described in detail by e.g., Schmidt *et al.* [15]. In order to achieve radon measurements with uncertainties of about ±10% two RAD-7s were run in parallel with a 30 min counting cycle (30 min time interval between actual readings). The radon concentration that was measured in the air loop was converted into the related radon-in-water concentration by applying the temperature and salinity dependent water/air partition coefficient $K_{a/w}$ of radon [31]. Thus a continuous time series with 30 min detection intervals was achieved.

For the analysis of radium concentrations ($^{223, 224, 226, 228}$Ra), 70 litres of water were pumped either from the bottom part of the submarine cave or from surface sea water (~2m water depth) along the transect. The water was pumped over MnO_2-fibre cartridges with a pump rate of about 1 l/min in order to scavenge the radium quantitatively [8]. The short-lived ^{223}Ra and ^{224}Ra were measured using the RaDeCC delayed coincidence counting system [32] following the procedure described in Moore [8] and Scholten *et al.* [33]. For the long-lived ^{226}Ra and ^{228}Ra measurements the MnO_2-fibres were ashed and prepared for gamma spectrometry measurements [21].

Sampling for stable water isotopes (^{2}H and ^{18}O) was carried out every 60 min from the bottom part of the submarine spring. Along the transect five discrete samples were taken at equidistant locations. All stable isotope samples were collected in 30 mL HDPE bottles and were measured using a continuous flow high temperature pyrolysis unit combined with an isotope ratio mass spectrometer (IRMS) delta plus XL Thermo Finnigan [34]. The isotopic composition of all samples was determined by the H_2O-H_2 equilibration method (for ^{2}H) with an analytical precision of ±1.0‰ and the H_2O-CO_2 equilibration method (for ^{18}O) with an analytical precision of ±0.1‰. The results of the hydrogen and oxygen isotope measurements are expressed as delta notations (δ^2H, δ^{18}O) relative to the Vienna Standard Mean Ocean Water (VSMOW).

The applied multi-temporal thermal remote sensing approach was based on eight Landsat ETM+ band 6.2 (high gain) images (path 194/row 30). All images were recorded during the hydrological summer (May-October) of the years 2000–2009 at 12:00 a.m. local time (GMT+2). Each image, which exhibits a ground sampling distance (GSD) of 30 m, was co-registered to UTM WGS 84 Zone 32N. For images recorded after the 31 May 2003, the gaps caused by SLC (scan line corrector) failure of Landsat were filled using the triangulation method implemented in the Envi 4.7 software package. Further data processing included the conversion from digital numbers to sea-surface temperatures (SST) including an atmospheric correction of each image. The applied value for water emissivity is 0.98. Values for atmospheric transmissivity, upwelling and downwelling radiances needed for the atmospheric correction of each image were obtained through the web-based Atmospheric Correction Tool that is based on MODTRAN [35]. The identification of SGD locations was based on the assumption that temperatures of discharging groundwater are less variable than ambient seawater temperatures. Hence the standard deviation of the temperature per pixel of the SST-image time-series was calculated and used as indicator [29].

3. Results and Discussion

3.1. Cabbé Submarine Spring

3.1.1. Water Turbulence and Tidal Cycle

The water turbulence was recorded because it has a strong impact on the conditions in the vertical cave, namely on (i) the degree of radon degassing from the water; (ii) the intensity of SGD/seawater mixing; and (iii) the temperature of the seawater. In particular at monitoring points that are located close to a rocky shore, as is the case at Cabbé, water turbulence must not necessarily correspond to the actual wind speed since it mainly results from the surf breaking on the rocky shore.

Figure 3 illustrates the wave intensity by showing the short-time deviation of the one minute running average water depth recorded in 10 second steps. With regard to water turbulence the 24 h monitoring period can be divided into two subsections: during the beginning of the sampling campaign, on the first day between 16:00 and 18:00, very turbulent waters were observed. Thereafter, in particular between 12:00 and 16:00 on the second day, the sea became significantly calmer. A data gap between about 03:00–05:00 occurred due to malfunction of the detection equipment.

The recorded water depths were also used for determination of the tidal cycle. The tidal cycle is a major driver for periodic changes in the SGD rate: during low tide the hydraulic gradient between land and sea is higher compared to high tide. This steeper gradient allows more groundwater to discharge from the hydraulically connected aquifer [6]. Figure 4 shows the water depth above the bottom of the submarine cave during the 24 h monitoring campaign.

Figure 3. Wave intensity shown as deviation of the water depth (WL: water depth).

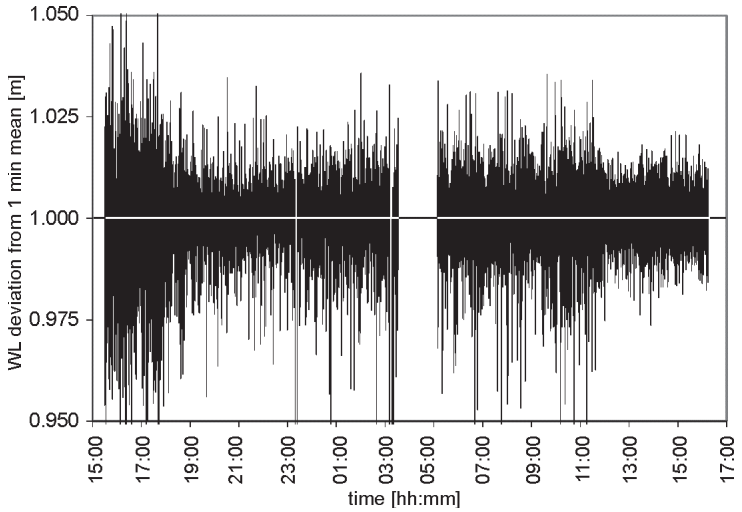

Figure 4. Water column height over the Cabbé submarine spring (*i.e.*, water depth) in 20 min intervals (white diamonds); grey points display individual 10 second readings.

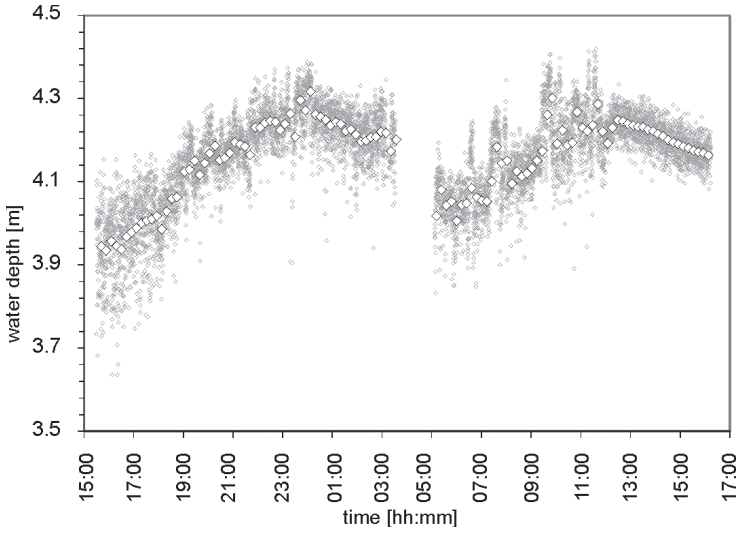

Despite the data gap, tidal periods with low tide at around 16:00 and 04:00 and high tide at around 23:00 and 11:00 can clearly be distinguished. However, even though the data show distinct flood/ebb periods, the water depths recorded during the first four hours (16:00–18:00) were considerably lower than during later ebb stages. That effect is believed to be due to two reasons: (1) strong winds coming off the land at that time pushed water out of the bay resulting in a generally decreased seawater level; (2) the water in the vertical cave, due to the high turbulence (*cf*. Figure 3), was highly enriched with air bubbles reducing the bulk water density and hence the hydrostatic pressure of the water column over the CTD (the CTD applies a pressure transducer for water depth detection). Thus, water depth readings for the period between 16:00 and 18:00 are probably too low. The changing conditions reflected in Figure 3 do affect tracer distribution behavior in the coastal sea in general. Hence the recorded tracer data show a strong dependence on the water turbulence as it will be revealed in the following.

3.1.2. Water Temperature

As illustrated in Figure 5A a distinct positive correlation between temperature and water depth was observed during the second day of the sampling campaign (calm sea). A coefficient of determination of $R^2 = 0.766$ (N = 20) was determined. This relation is caused by the changing hydrostatic pressure on the aquifer correlated to the changing tides. The discharging groundwater has a somewhat lower temperature (~17.5 °C; [30]) than the coastal sea water (~22 °C) thus leading to water temperature decrease in the cave at low tide. However, during the first hours of the campaign (rough sea; low tide) that correlation was seemingly reversed. In spite of the low water depth (and the supposedly associated increased discharge of cool groundwater) the water temperature showed the highest values recorded during the entire campaign. This observation is explained to be as a result of the rough sea (before 18:00, *cf*. Figure 3). The strong surf resulted in a substantial amount of (warm) air bubbles whirling deep in the studied water column, giving rise to a significant increase of the water temperature during that time (the outside air temperature was measured to be around 25 °C that afternoon).

In conclusion it can be stated that whereas in several other studies the water temperature could be applied as a conservative SGD tracer [36], its applicability is limited in regions where the temperature gradient between groundwater and seawater is too small to allow discrimination between diurnal fluctuations of the seawater temperature and water temperature fluctuations caused by SGD. Besides it was shown that water turbulence can have a significant influence on the seawater temperature.

3.1.3. Salinity

As shown in Figure 5B a distinct positive relation between salinity and water depth was observed during the second part of the sampling campaign (calm sea). As expected, high water depths (high tides at 23:00 and 11:00) resulted in increased salinities, an effect that can be attributed to the decreased SGD rate at high tide. However, during the period characterized by rough conditions in the beginning of the campaign (16:00–18:00) this relationship seems to be reversed. In spite of low water depths and related increased SGD rates the recorded salinities were rather comparable to the respective data recorded during the following high tides. It is most likely that the reason for this reversed relationship is the high turbulence of the water during the first hours of monitoring resulting in a more intense exchange of seawater with the discharging groundwater in the submarine cave. Even though the recorded wave heights are maximally 0.1 m, the actual breaking of the waves into the mouth of the cave caused visibly heavy turbulences in the water column of the cave resulting in the recorded inverse trend in salinity (and temperature). Another potential explanation is that seawater, which was pushed into the conduit system earlier during the rough sea conditions, discharged again at low tide after the sea started to calm down.

In terms of its applicability as SGD tracer, salinity can generally be considered more suitable than temperature. Besides the fact that it is not influenced by atmospheric conditions, the salinity gradient at the groundwater/seawater interface is much more distinct than temperature gradients. While off-shore seawaters generally show salinities of around 35 (38.06 in the Bay of Roquebrune) groundwater shows in general negligible or lower salinities (7.2 at Cabbé, see Table 1).

Figure 5. (**A**) Water depth and temperature; (**B**) Salinity; (**C**) Radon concentration; (**D**) Delta ^{2}H; and (**E**) Delta ^{18}O during the 24 h observation period. LT = low tide; HT = high tide.

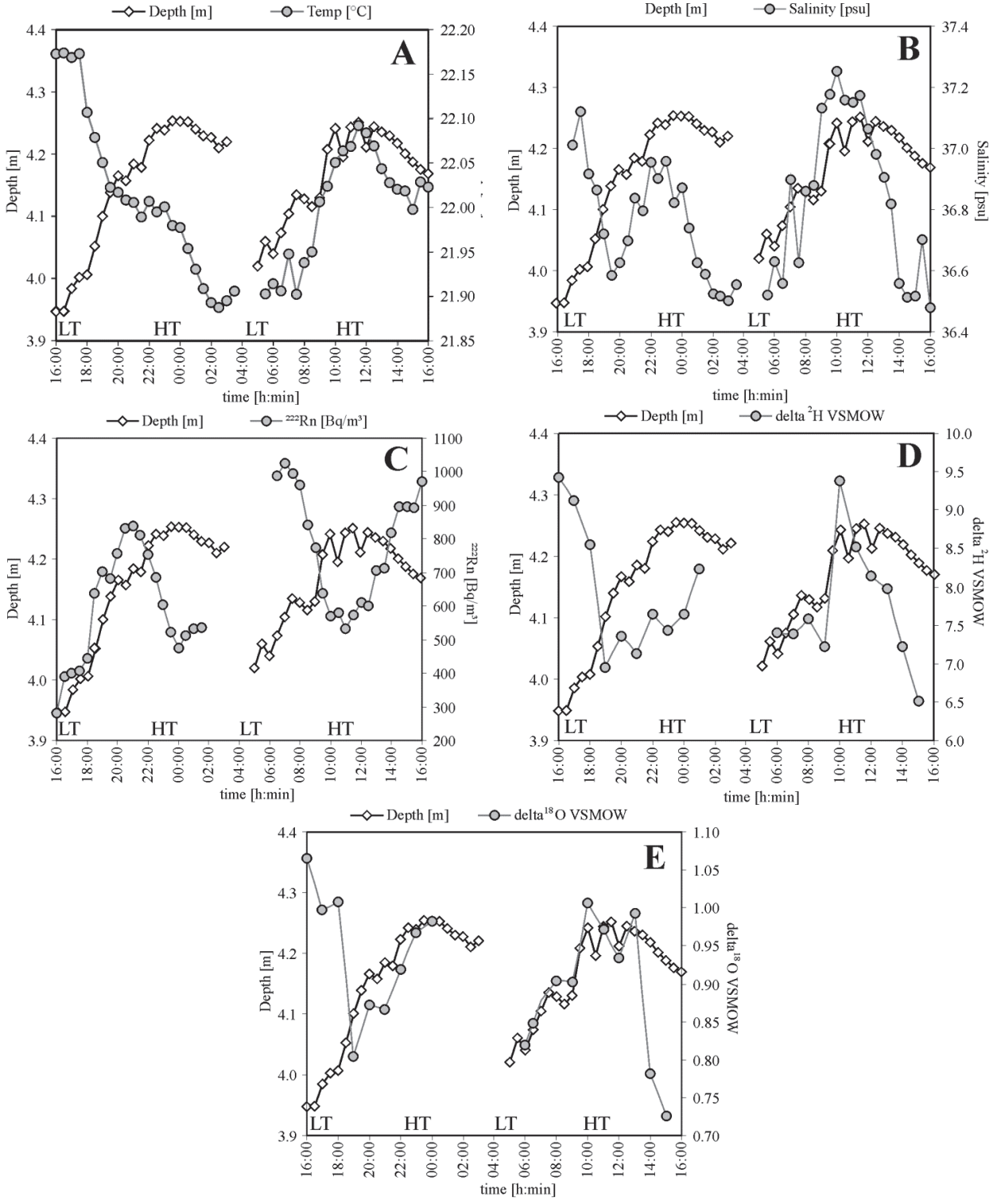

Table 1. Groundwater and off-shore seawater end-members for all applied parameters.

Parameter	Groundwater	Off-shore seawater
salinity	~7.2	38.06
^{222}Rn	28,000 Bq/m^3	<4 Bq/m^3
$\delta^{18}O$	−4.7‰ *	1.22‰
$\delta^{2}H$	−35.1‰ *	10.4‰

Note: * derived from long-term weighted annual mean rain water composition from the local GNIP station in Monte Carlo/Monaco (GNIP station code 769001).

3.1.4. Dissolved Radon Concentrations

Due to the lack of radon production, seawater shows generally a radon background of only a few Bq/m^3. Groundwater concentrations, in contrast, can reach levels of up to 20 kBq/m^3 and more. The strong gradient at the groundwater/seawater interface results in an inverse correlation between seawater depth and radon concentration in the coastal sea, *i.e.*, in high concentrations during low tides (due to intense SGD) and *vice versa* [37].

Figure 5C illustrates the radon data recorded at the base of the submarine cave. As displayed, the expected inverse correlation between radon and water depth was observed from 22:00 until the end of the monitoring campaign (calm sea). For the second day of the campaign a coefficient of determination of $R^2 = 0.624$ (N = 20) was found. At the beginning of the campaign however (rough sea), this relationship appears to be reversed. Low water depths are associated with low radon concentrations in the water column. The most likely reason for this unusual radon pattern is the high water turbulence (as mentioned above). While radon is degassing from every open water surface, this gas evasion is strongly enforced if the water is very turbulent and contains many air bubbles. (The rough sea resulted also in intense water mixing between seawater and discharging groundwater). Radon degassing is due to the water/air partition coefficient of radon which is $K_{w/a} = 0.25$ at the given temperature [31]. Comparable to the interpretation of the salinity data another potential explanation is that seawater, which was pushed into the conduit system earlier, discharged again after the sea started to calm down.

For the applicability of radon as SGD tracer it can hence generally be stated that radon reveals robust data due to its distinct gradient at the groundwater/seawater interface, due to its inert behaviour and due to its straightforward detectability on site. However, in the case of rough seas intense radon degassing may limit its applicability as a tracer.

3.1.5. Dissolved Radium Activity

At Cabbé, radium isotope concentrations do not show clear variations with tides. Also the isotope ratios determined along the transect are in the same range as observed at Cabbé (Figure 6). If SGD at Cabbé were a source of radium one would expect decreasing $^{224}Ra/^{228}Ra$ and/or $^{228}Ra/^{226}Ra$ values with increasing distance from Cabbé.

The lack of radium enrichment in the groundwater discharging at Cabbé is in contrast to several other SGD studies in the Mediterranean Sea where radium has been successfully applied as SGD tracer [38–40]. We explain the lack of radium in the discharging groundwater to be due to two main

reasons: (1) The SGD site studied is hydraulically connected to a major karst aquifer. In such oxic groundwaters radium adsorbs on mineral surfaces and therefore dissolved concentrations are very low. (2) In general radium is released from aquifer mineral surfaces in the mixing zone between seawater and groundwater (subterranean estuary) where increased salinities are present [41]. In contrast to many other settings in the Mediterranean Sea there is no well-developed subterranean estuary at Cabbé. The groundwater discharges directly into the cave without an aquifer zone where radium can be mobilized from the aquifer matrix.

Due to the specific hydrological setting, radium has to be considered less suitable for SGD investigation at Cabbé. This may also be the case for other focused SGD locations having a poorly developed subterranean estuary.

Figure 6. Radium isotope ratios at Cabbé and along the transect. (**A**) $^{224}Ra/^{228}Ra$; (**B**) $^{228}Ra/^{226}Ra$.

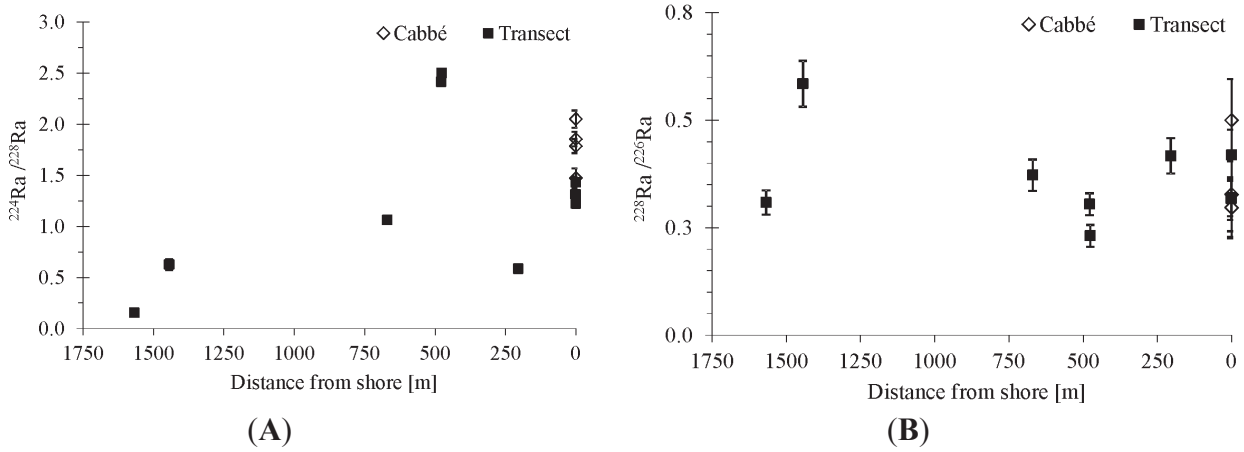

3.1.6. Stable Water Isotopes

As shown in Figure 5D,E the stable isotope signatures of the water show a distinct positive relation with the tides, *i.e.*, the water depth in the submarine cave. Only during the first hours of the observation period a seemingly inverse relationship was found (as already discussed for the other parameters).

The reason for the generally lighter isotopic signatures at low tide is the significant difference in isotopic signatures between seawater and meteoric groundwater. Lighter signatures at low tide indicate increased discharge of isotopically lighter groundwater into the sea. A shift to heavier isotope signatures can be observed at high tides since the water column is less influenced by groundwater at this stage. The inverse behaviour at the beginning of the observation period is most likely caused by intense water mixing between the near-shore seawater and the SGD fed water column in the submarine cave. The strong impacts of the water turbulence and of potentially discharging seawater that was pushed into the conduit system earlier on the stable isotope signatures during the first hours of recording are comparable to the impact on salinity and radon as discussed above.

3.2. Transect

Whereas all parameters recorded at the Cabbé SGD location (submarine spring) were discussed individually as time series, the data recorded along the transect are discussed jointly in the following.

The transect started at a distance of about 50 m from the submarine cave at Cabbé and ended *ca*. 1750 m off-shore in the Bay of Roquebrune. Figure 7 displays the continuously recorded salinity data as 20 min average values. The salinity increases from ~37 at the coastal end of the transect to ~38 at a distance of 600 m off-shore from where it remains constant with increasing distance. Although the absolute gradient is small, it can be seen that SGD has significant influence on a rather large area within the Bay of Roquebrune. It has to be mentioned that no further water influx (surface water, precipitation) occurred during the field campaign, which allows attributing the decreasing salinity solely to the SGD influence.

Figure 7. Water salinity and temperature along the transect.

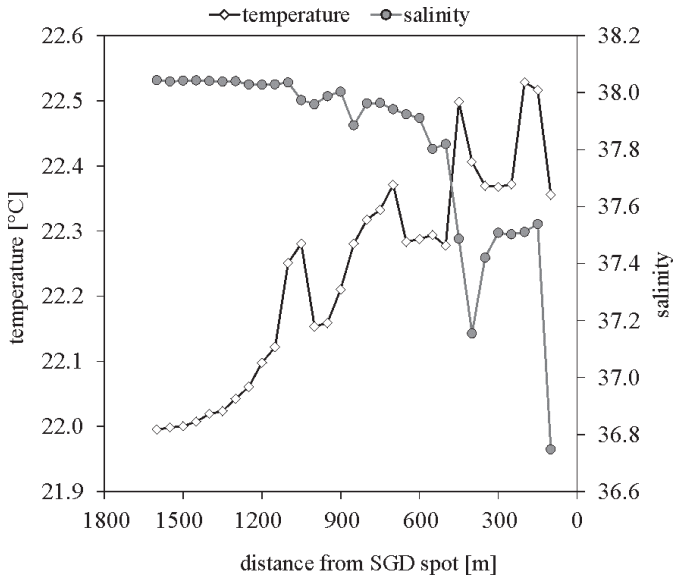

The water temperatures recorded along the transect show a rather indistinct picture with temperatures of about 22.4–22.5 °C close to the shore and later decrease towards the open ocean to a rather constant 22.0 °C. The temperatures measured close to the shore are higher than the highest temperature observed during time-series measurements at Cabbé (maximum temperature 22.0 °C). Thus the temperature variations observed along the transect are most likely not related to SGD at Cabbé. This suggests that temperature is not applicable as a parameter for SGD evaluation at the investigated site.

The stable isotope signatures for $\delta^{18}O$ and $\delta^{2}H$ display a pattern along the transect comparable to salinity (Figure 8). While $\delta^{18}O$ and $\delta^{2}H$ values are constant off-shore both isotopes show a shift to lighter signatures from around 1000 m towards the SGD location. These changes are caused by the discharging groundwater which shows significantly lighter isotopic signatures than the open sea as discussed above.

Radon shows an inverse behaviour as expected. The concentration decreases from 250 Bq/m^3 in the vicinity of the SGD spot, here clearly reflecting the SGD influence, to 4 Bq/m^3 off-shore.

Figure 8. Radon concentrations and water stable isotope signatures along the transect; (**A**) $\delta^{18}O$; (**B**) $\delta^{2}H$.

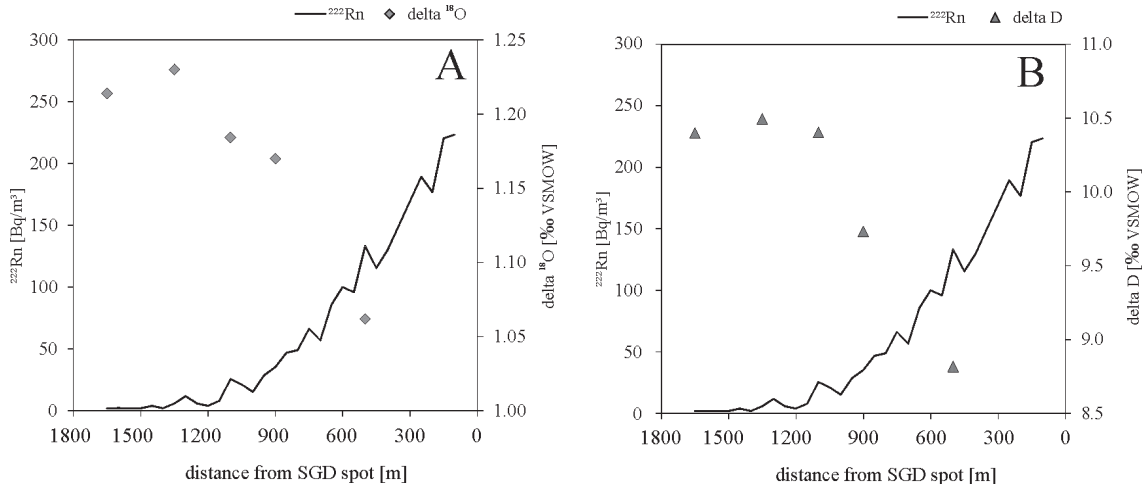

3.3. SST Evaluation

The sea surface temperature (SST) standard deviations within the Bay of Roquebrune are illustrated in Figure 9. The image shows values ranging between 1.8 and 6.0 °C. Areas with high standard deviations indicate varying influence due to e.g., seasonal temperature effects. Areas with low sea-surface temperature variability located close to the shore indicate spatially and thermally persistent groundwater inflow, which stabilizes the seawater temperature in the vicinity of the inflow location.

Figure 9. Sea Surface Temperature ("SST") standard deviation over time within the Bay of Roquebrune (note that small STD values in the proximity of the shore indicate potential Submarine Groundwater Discharge ("SGD") abundance while lower STD values offshore indicate a small SST variability only, caused by the water depth and related high heat capacity of the water column).

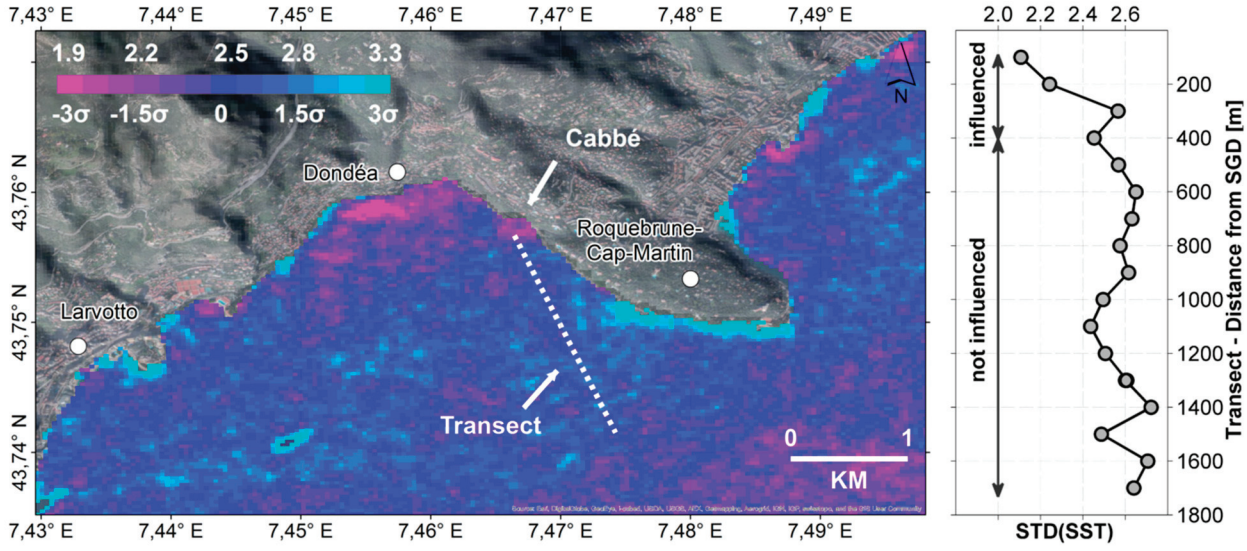

Within the Bay of Roquebrune several areas with small standard deviation values <~2 °C are visible along the coastline. The three most prominent ones are located (i) south of Dondéa; (ii) east of Roquebrune-Cap-Martin at Grimaldi and (iii) at the investigated study site at Cabbé. The latter area has a lateral extent of ~300 m and, unlike the larger area south of Dondéa, no fringe of higher SST standard deviation values in between the actual anomaly and the shoreline. This confirms that groundwater discharges at the shore at Cabbé.

Following the transect from the shore into off-shore direction the SST standard deviation values remain below ~2.3 °C up to a distance of ~200 m from Cabbé. There they increase first abruptly and rise thereafter steadily up to a distance of about 600 m off-shore. The elevated off-shore SST standard deviation values are in accordance with the salinity and radon distribution patterns, which likewise indicate decreasing influence of SGD with increasing distance from Cabbé. Hence it can be stated that, even though the satellite-based approach relies on images recorded long before the actual sampling campaign, the data proves the submarine groundwater discharge at Cabbé to be spatio-temporal constant and provides thus an independent tool for SGD investigation.

3.4. Quantification of Groundwater/Seawater Ratios at Cabbé

A simple two-component mixing equation between end-member concentrations (off-shore water and groundwater) of stable isotopes, radon and salinity was applied for quantifying the relative proportions of groundwater and seawater at Cabbé. For the seawater, end-member values measured at the end of the transect furthest distant from shore were used. Since no groundwater wells were accessible in the immediate vicinity of Cabbé, end-members for radon and salinity were obtained from a well situated directly at the beach at ~500m distance to Cabbé within the same geological/hydrogeological setting. The terrestrial $\delta^{18}O$ and $\delta^{2}H$ end-members were derived from the long-term weighted annual mean rain water composition for the closest GNIP (Global Network of Isotopes in Precipitation) station in Monaco (GNIP station code 769001). The calculation of the annual mean is based on 112 monthly isotope values obtained between 1999 and 2009 [42]. No rain samples were taken in the course of the sampling campaign since no rain had occurred during the study. Table 1 summarizes the end-members for all the parameters used to calculate the percentage of meteoric water in the water column of the Cabbé submarine cave (Figure 10). Generally the results of the SGD indicators give a consistent picture. The fraction of meteoric groundwater in the vertical cave at Cabbé varies between about 1.5%–4.5% for the radon, between 2.0% and 4.0% for the salinity, and between 3.0%–5.0% for the stable isotope data, respectively.

As it can clearly be seen in Figure 10, in particular for the second part of the campaign, the groundwater portion depends on the tidal stage. Generally high tide (HT) periods are characterized by a lower fraction of groundwater in the water column of the vertical cave than low tides (LT). An exception from that generally expected behaviour is the starting period of the campaign, which was characterized by a rough sea influencing tracer distribution behaviour.

Figure 10. Percentage of groundwater in the water in the submarine cave at Cabbé.

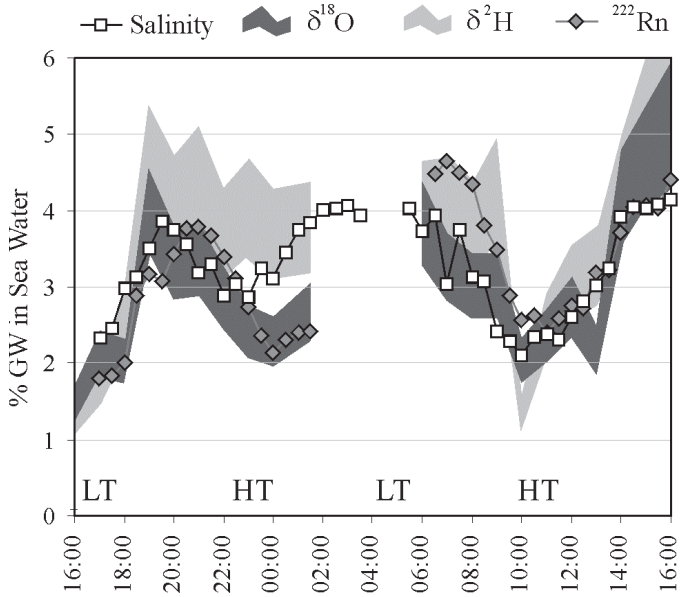

4. Conclusions

We studied the applicability and the informative value of a set of environmental tracers, which have proven in previous studies to be suitable for detecting and quantifying SGD, under the specific conditions of a focussed SGD from a submarine karst spring at Cabbé. Our results show that substantial qualitative and semi-quantitative information can be achieved by applying the easily on-site detectable parameters salinity and radon concentration (^{222}Rn). Radon can be considered as the most robust environmental tracer for SGD in the given case even though radon degassing from the water column has to be considered particularly with rough seas. The temperature of the water column can only be applied as a reliable SGD indicator if the temperature gradient between groundwater and seawater is sufficiently distinct. If it is too small as in the studied case, the diurnal variation of the air temperature masks the potential SGD signals. In our study the naturally-occurring radium isotopes ($^{228, 226, 224, 223}$Ra), were not suitable for detecting SGD, which is interpreted to be due to a poorly developed subterranean estuary inhibiting significant radium mobilization from the aquifer matrix. The stable isotopes of water (^{2}H and ^{18}O) are suitable SGD indicators. In a mass balance approach, stable isotopes, radon and salinity give comparable estimates of the groundwater fraction discharging at Cabbé. The disadvantage of using stable isotopes in comparison to salinity and radon is the significantly higher analytical effort required for stable isotope analyses. Additionally our study showed that a multi-temporal thermal remote sensing approach applying sea surface temperature (SST) patterns can be used as a powerful tool for backing up tracer results and, more importantly as a SGD pre-screening method in order to optimize on-site surveys. Further research is recommended to evaluate the applied “SGD tool box” for the investigation of offshore fresh groundwater reserves.

Conflicts of Interest

The authors declare no conflict of interest.

References

1. Moore, W.S. The effect of submarine groundwater discharge on the ocean. *Annu. Rev. Mar. Sci.* **2010**, *2*, 59–88.
2. Slomp, C.P.; van Cappellen, P. Nutrient inputs to the coastal ocean through submarine groundwater discharge: Controls and potential impact. *J. Hydrol.* **2004**, *295*, 64–86.
3. Santos, I.R.; Niencheski, F.; Burnett, W.; Peterson, R.; Chanton, J.; Andrade, L.C.; Milani, I.; Schmidt, A.; Knoeller, K. Tracing anthropogenic-driven groundwater discharge into a coastal lagoon from southern Brazil. *J. Hydrol.* **2008**, *353*, 275–293.
4. Post, V.E.A.; Groen, J.; Kooi, H.; Person, M.; Shemin Ge, S.; Edmunds, W.M. Offshore fresh groundwater reserves as a global phenomenon. *Nature* **2013**, 504, 71–78.
5. Santos, I.R.; Eyre, B.D.; Huettel, M. The driving forces of pore water and groundwater flow in permeable coastal sediments: A review. *Estuar. Coast. Shelf Sci.* **2012**, *98*, 1–15.
6. Santos, I.R.; Burnett, W.C.; Dittmar, T.; Suryaputra, I.; Chanton, J. Tidal pumping drives nutrient and dissolved organic matter dynamics in a Gulf of Mexico subterranean estuary. *Geochim. Cosmochim. Acta* **2009**, *73*, 1325–1339.
7. Peterson, R.N.; Burnett, W.C.; Taniguchi, M.; Chen, J.Y.; Santos, I.R.; Ishitobi, T. Radon and radium isotope assessment of submarine groundwater discharge in the Yellow River delta, China. *J. Geophys. Res. Oceans* **2008**, *113*, 1978–2012.
8. Moore, W.S. Fifteen years' experience in measuring ^{224}Ra and ^{223}Ra by delayed-coincidence counting. *Mar. Chem.* **2008**, *109*, 188–197.
9. Taniguchi, M.; Iwakawa, H. Submarine groundwater discharge in Osaka Bay, Japan. *Limnology* **2004**, *5*, 25–32.
10. Burnett, W.C.; Dulaiova, H. Estimating the dynamics of groundwater input into the coastal zone via continuous radon-222 measurements. *J. Environ. Radioact.* **2003**, *69*, 21–35.
11. Taniguchi, M. Tidal effects on submarine groundwater discharge into the ocean. *Geophys. Res. Lett.* **2002**, *29*, doi:10.1029/2002GL014987.
12. Corbett, D.R.; Dillon, K.; Burnett, W.C.; Chanton, J.P. Estimating the groundwater contribution into Florida Bay via natural tracers ^{222}Rn and CH_4. *Limnol. Oceanogr.* **2000**, *45*, 1546–1557.
13. Corbett, D.R.; Burnett, W.C.; Cable, P.H.; Clark, S.B. Radon tracing of groundwater input into Par Pond, Savannah River Site. *J. Hydrol.* **1997**, *203*, 209–227.
14. Lee, D.R. A device for measuring seepage flux in lakes and estuaries. *Limnol. Oceanogr.* **1977**, *22*, 140–147.
15. Schmidt, A.; Schlueter, M.; Melles, M.; Schubert, M. Continuous and discrete on-site detection of radon-222 in ground- and surface waters by means of an extraction module. *Appl. Radiat. Isotopes* **2008**, *66*, 1939–1944.
16. Schubert, M.; Brüggemann, L.; Schirmer, M.; Knoeller, K. Radon monitoring in wells as tool for the estimation of the groundwater flow rate. *Water Resourc. Res.* **2011**, *47*, doi:10.1029/2010WR009572.

17. Schmidt, A.; Gibson, J.J.; Santos, I.R.; Schubert, M.; Tattrie, K.; Weiss, H. The relevance of groundwater discharge to the overall water budget of two typical Boreal lakes in Alberta/Canada estimated from a radon mass balance. *Hydrol. Earth Syst. Sci.* **2010**, *14*, 79–89.
18. Schubert, M.; Schmidt, A.; Lopez, A.; Balcázar, M.; Paschkel, A. In-situ determination of radon in surface water bodies by means of a hydrophobic membrane tubing. *Radiat. Measur.* **2008**, *43*, 111–120.
19. Schubert, M.; Bürkin, W.; Peña, P.; Lopez, A.; Balcázar, M. On-site determination of the radon concentration in water samples: Methodical background and results from laboratory studies and a field-scale test. *Radiat. Measur.* **2006**, *41*, 492–497.
20. Schubert, M.; Paschke, A.; Bednorz, D.; Bürkin, W.; Stieglitz, T. The kinetics of the water/air phase transition of radon and its implication on detection of radon-in-water concentrations: Practical assessment of different on-site radon extraction methods. *Environ. Sci. Technol.* **2012**, *46*, 8945–8951.
21. Charette, M.A.; Buesseler, K.O.; Andrews, J.E. Utility of radium isotopes for evaluating the input and transport of groundwater-derived nitrogen to a Cape Cod estuary. *Limnol. Oceanogr.* **2001**, *46*, 465–470.
22. Charette, M.A.; Moore, W.S.; Burnett, W.C. Uranium- and Thorium-Series Nuclides as Tracers of Submarine Groundwater Discharge. In *Radioactivity in the Environment*; *Krishnaswami,* S., *Cochran,* J.K., Eds.; Elsevier: Oxford, UK, 2008.
23. Moore, W.S. The subterranean estuary: A reaction zone of ground water and sea water. *Mar. Chem.* **1999**, *65*, 111–125.
24. Craig, H. Isotopic variations in meteoric waters. *Science* **1961**, *133*, 1702–1703.
25. Epstein, S.; Mayeda, T. Variation of ^{18}O content of waters from natural sources. *Geochem. Cosmochem. Acta* **1953**, *4*, 213–224.
26. Schmidt, A.; Santos, I.R.; Burnett, W.; Niencheski, F.; Knöller, K. Groundwater sources in a permeable coastal barrier: Evidence from stable isotopes. *J. Hydrol.* **2011**, *406*, 66–72.
27. Zektser, I.S.; Dzhamalov, R.G.; Everett, L.G. *Submarine Groundwater*; CRC Press: Boca Raton, FL, USA, 2007.
28. Gilli, E. Etudes des Sources Karstiques Sous-Marines et Littorales des Alpes Maritimes Entre Menton et Nice. In *Ministre de l' Environnement, Direction Régional de l'Environnement*; DREAL PACA: Marseille, France, 1997.
29. Mallast, U.; Siebert, C.; Gloaguen, R.; Friesen, J.; Rödiger, T.; Geyer, S.; Merz, R. How to identify groundwater-caused thermal anomalies in lakes based on multi-temporal satellite data in semi-arid regions. *Hydrol. Earth Syst. Sci.* **2013**, *10*, 4901–4949.
30. Gilli, E. Détection de sources sous-marines et précision de l'impluvium par mesure des variations de salinité. L'exemple de la source de Cabbé-Massolins (Roquebrune-Cap-Martin, France). *Comptes Rendus de l'Académie des Sciences–Series IIA–Earth Planet. Sci.* **1999**, *329*, 109–116.
31. Schubert, M.; Paschke, A.; Lieberman, E.; Burnett, W.C. Air-water partitioning of ^{222}Rn and its dependence on water salinity. *Environ. Sci. Technol.* **2012**, *46*, 3905–3911.

32. Moore, W.S.; Arnold, R. Measurement of ^{223}Ra and ^{224}Ra in coastal waters using a delayed coincidence counter. *J. Geophys. Res.* **1996**, *101*, 1321–1329.
33. Scholten, J.; Pham, M.K.; Blinova, O.; Charette, M.A.; Dulaiova, H.; Eriksson, M. Preparation of Mn-fiber standards for the efficiency calibration of the delayed coincidence counting system (RaDeCC). *Mar. Chem.* **2010**, *121*, 206–214.
34. Gehre, M.; Geilmann, H.; Richter, J.; Werner, R.A.; Brand, W.A. Continuous flow ^{2}H/^{1}H and ^{18}O/^{16}O analysis of water samples with dual inlet precision. *Rapid Commun. Mass Spectrom.* **2004**, *18*, 2650–2660.
35. Barsi, J.A.; Barker, J.L.; Schott, J.R. An Atmospheric Correction Parameter Calculator for a Single Thermal Band Earth-Sensing Instrument. In Proceedings of IGARSS03, Centre de Congres Pierre Baudis, Toulouse, France, 21–25 July 2003.
36. Johnson, A.G.; Glenn, C.R.; Burnett, W.C.; Peterson, R.N.; Lucey, P.G. Aerial infrared imaging reveals large nutrient-rich groundwater inputs to the ocean. *Geophys. Res. Lett.* **2008**, *35*, L15606.
37. Tsabaris, C.; Scholten, J.; Karageorgis, A.P.; Comanducci, J.F.; Georgopoulos, D.; Wee Kwong, L.L.; Patiris, D.L.; Papathanassiou, E. Underwater *in situ* measurements of radionuclides in selected submarine groundwater springs, Mediterranean Sea. *Radiat. Protect. Dosim.* **2010**, *142*, 273–281.
38. Ferrarin, C.; Rapaglia, J.; Zaggia, L.; Umgiesser, G.; Zuppi, G.M. Coincident application of a mass balance of radium and a hydrodynamic model for the seasonal quantification of groundwater flux into the Venice Lagoon, Italy. *Mar. Chem.* **2008**, *112*, 179–188.
39. Garcia-Solsona, E.; Garcia-Orellana, J.; Masque, P.; Rodellas, V.; Mejias, M.; Ballesteros, B.; Dominguez, J.A. Groundwater and nutrient discharge through karstic coastal springs (Castello, Spain). *Biogeosciences* **2010**, *7*, 2625–2638.
40. Rapaglia, J.; Koukoulas, S.; Zaggia, L.; Lichter, M.; Manfé, G.; Vafeidis, A.T. Quantification of submarine groundwater discharge and optimal radium sampling distribution in the Lesina Lagoon, Italy. *J. Mar. Syst.* **2012**, *91*, 11–19.
41. Gonneea, M.E.; Morris, P.J.; Dulaiova, H.; Charette, M.A. New perspectives on radium behavior within a subterranean estuary. *Mar. Chem.* **2008**, *109*, 250–267.
42. IAEA/WMO. Global Network of Isotopes in Precipitation. The GNIP Database 2014. Available online: http://www.iaea.org/water (accessed on 26 February 2014).

Section 3: *Investigations Using Natural Tracers in Combination with Applied Tracers*

Use of Natural and Applied Tracers to Guide Targeted Remediation Efforts in an Acid Mine Drainage System, Colorado Rockies, USA

Rory Cowie, Mark W. Williams, Mike Wireman and Robert L. Runkel

Abstract: Stream water quality in areas of the western United States continues to be degraded by acid mine drainage (AMD), a legacy of hard-rock mining. The Rico-Argentine Mine in southwestern Colorado consists of complex multiple-level mine workings connected to a drainage tunnel discharging AMD to passive treatment ponds that discharge to the Dolores River. The mine workings are excavated into the hillslope on either side of a tributary stream with workings passing directly under the stream channel. There is a need to define hydrologic connections between surface water, groundwater, and mine workings to understand the source of both water and contaminants in the drainage tunnel discharge. Source identification will allow targeted remediation strategies to be developed. To identify hydrologic connections we employed a combination of natural and applied tracers including isotopes, ionic tracers, and fluorescent dyes. Stable water isotopes ($\delta^{18}O/\delta D$) show a well-mixed hydrological system, while tritium levels in mine waters indicate a fast flow-through system with mean residence times of years not decades or longer. Addition of multiple independent tracers indicated that water is traveling through mine workings with minimal obstructions. The results from a simultaneous salt and dye tracer application demonstrated that both tracer types can be successfully used in acidic mine water conditions.

Reprinted from *Water*. Cite as: Cowie, R.; Williams, M.W.; Wireman, M.; Runkel, R.L. Use of Natural and Applied Tracers to Guide Targeted Remediation Efforts in an Acid Mine Drainage System, Colorado Rockies, USA. *Water* **2014**, *6*, 745-777.

1. Introduction

Acidic, metal-rich drainage from abandoned hard-rock mines can produce both acute and chronic environmental problems [1]. The legacy of past hard-rock mining in the United States includes more than 200,000 abandoned or inactive mines [2] with thousands of abandoned mines located near headwater regions of the Rocky Mountains of Colorado [3]. Watersheds in mineralized regions often receive drainage from a complex distribution of mine systems [4], which are gravity driven and often discharge at low points adjacent to surface waters. The combination of low pH and high concentrations of metals associated with the acid mine drainage (AMD) can then create severe toxicological effects on local and downstream aquatic ecosystems [5]. Traditionally, an end of the pipe (e.g., at the mine discharge point) treatment strategy has been employed to handle AMD prior to mixing with local surface waters. However, this strategy is very expensive and treatment must occur in perpetuity, which does not represent a permanent solution to the problem. A more recent approach to controlling AMD involves developing targeted remediation strategies that address the feasibility of actually reducing or shutting off the AMD at its source [1]. Targeted remediation can be thought of as a source and pathway control measure and may refer to the source of the acid

producing minerals themselves, the source of the water that mobilizes contaminants, or both. In most mine settings it is impractical to isolate or remove the mineralized rock itself. Therefore, remediation efforts may be most successful when the source of water producing the AMD can be targeted and separated, isolated, or removed from the area of a mine most prone to AMD production.

A major challenge in using a targeted remediation approach to control AMD is that many hard-rock mine settings are located in mountainous areas of high mineralization that are commonly associated with fracturing and structurally deformed rocks. The result is high secondary porosity, which combined with the diverse spatial scales of man-made mining excavations, creates a highly complex hydrogeologic setting where water flow paths are particularly difficult to quantify [6]. Steep slopes and large amounts of snowfall add to the complexity of understanding the hydrology of these sites. In addition, many of the hard-rock mining sites in the Western U.S. have been abandoned for many decades leading to varying degrees of degradation to the originally engineered designs for mine drainage control. Information on the mine sites is often incomplete because mine maps may be unavailable, incomplete, or inaccurate. Therefore, the hydrologic connectivity of abandoned mines is often unknown or poorly understood. The complexities of flow paths in flooded mines are often comparable to flow paths found in karstic aquifers [7], where flow may be concentrated in subsurface conduits, making a Darcy's law approach inapplicable for evaluation of subsurface flow regimes in flooded mines [8]. A reasonable approach to understanding the hydrology of these systems involves applying ground-water tracing techniques to abandoned mine sites that generate empirical data while measuring properties *in-situ* to minimize assumptions about hydrogeological conditions [9].

In recent years, surface water and groundwater tracing techniques have been used in a variety of complex hydrogeologic settings to aid in characterizing groundwater flow systems [10–12]. Tracers have been used in various combinations of natural tracers, injected tracers, and chemical perturbations to identify and quantify transport processes in mountain streams impacted by AMD [13–15]. Fluorescent dyes are often used as an applied tracer [16–18], with the use of fluorescent dye to trace groundwater dating back to at least 1877 when sodium fluorescein (uranine) was used to evaluate the connection between the Danube River and the Aach spring [19]. Fluorescent dyes are commonly chosen as applied tracers for groundwater studies in areas with low clay content, and recent studies have found dye tracers to work well in both karst and fractured crystalline rock settings [8]. However, the use of such dyes is problematic in AMD waters, because below a pH of 6 the sorptivity of uranine increases and its fluorescence intensity diminishes [20]; Smart and Laidlaw [16] demonstrated that the fluorescence of uranine can be reduced by as much as 50% below a pH of 5. An additional difficulty in dye tracer application in groundwater and mine systems is accurately quantifying the mixing reservoir. The reservoir represents all waters (mine pools and inflows of surface or groundwater) that the tracer could mix with between the injection point and the sampling point and will influence the mass of tracer applied in order to produce appropriate dye concentrations in collected samples [9]. If the mixing reservoir is overestimated then resulting dye concentrations may become toxic or exceed the dynamic range of the instruments, whereas an underestimated reservoir will result in low dye concentrations, possibly below analytical detection. Therefore, a multiple tracer approach is often recommended for complex hydrologic settings with

limited access points and unknown flow-through times, especially when field-work time and logistical support are limited [9,21,22].

The Rico-Argentine Mine Site near Rico, Colorado (USA) provides an opportunity for the use of natural and applied tracers to understand the hydrological connectivity of a perturbed system where AMD is produced. The mine consists of multiple levels of underground workings that are interconnected by a series of tunnels that pass directly underneath a tributary creek, resulting in potential pathways for hydrologic connections between the mine and surface waters. Additionally, the mine complex is connected to a series of long drainage tunnels, which transport AMD from the mine to a discharge point adjacent to the Dolores River, a relatively pristine headwater ecosystem. At present, the AMD passively flows through a series of degraded water treatment ponds before entering the river.

The objective of this paper is to use multiple natural and applied tracers to quantitatively and qualitatively address the hydrologic connections between local inputs from precipitation, surface waters, and groundwater to interior mine workings, and resultant mine discharges. As recommended by Wolkersdorfer [9], the paper first highlights the use of synoptic and time series analyses of naturally occurring isotopic and geochemical tracers to develop a conceptual understanding of the hydrogeology of the mine system. Secondly, applied tracers (salts and fluorescent dyes) were introduced, either simultaneously or at separate discrete locations, to provide a comparative analysis of tracer approaches in an AMD setting. To expand on previous research by Naurath *et al.* [23], this study aims to further investigate the effectiveness of uranine as a tracer in acid mine waters by performing a dual tracer application with uranine and lithium salt.

The results of this study will help determine the feasibility of reducing the volume of water and/or the load of contaminants that discharge from the Rico-Argentine mine. Reducing the flow of water into and through the mine workings, reducing the mobilization of contaminants within the mine, and/or isolating high-concentration contaminant source water for limited smaller-scale treatment, may create alternative targeted remediation strategies for managing the AMD discharge that are not currently available.

2. Methods

2.1. Site Description

The historic Rico-Argentine mines are located in the San Juan Mountains of southwestern Colorado, USA (Figure 1a) and are situated along Silver Creek (Figure 1b), about 2.5 kilometers (km) northeast of the Town of Rico (Figure 1c). The mines were built to access sulfide replacement deposits associated with hydrothermal mineralization of faults in the Pennsylvania-age Hermosa formation. The mines were active from the 1860's until the 1970's with silver, zinc, and lead as the primary mining products. The mines consist of extensive underground mine workings in the ridge southeast of Silver Creek that were historically accessed by a number of entrances at and above the elevation of Silver Creek. There are also at least 7 levels (30 m of vertical separation between each) below the surface elevation of Silver Creek with historical maps indicating several levels of the mine tunnels pass directly under Silver Creek and connect to mine workings on the northwest of Silver Creek. The proximity of the mine workings adjacent to, and below, Silver Creek was hypothesized

as supporting a possible hydrologic pathway (in either direction) between surface waters in the creek and the subsurface mine workings. The mine workings on the northwest side of Silver Creek are connected to the SE crosscut, which connects to the St. Louis Tunnel (Figure 1c). The crosscut and the St. Louis Tunnel extend approximately 2500 m from the mine workings to the portal adjacent to the Dolores River. The SE crosscut and the St. Louis Tunnel connect to the Rico-Argentine mine at the 500 Level (name is a reference to being about 500 ft (152 m) below Silver Creek) and were built primarily to de-water or drain the upper mine workings using gravity flow. Water with elevated levels of metals including zinc and cadmium currently discharge from the St. Louis Tunnel and flow through a series of passive treatment ponds, eventually entering the Dolores River from the pond system outfall (Figure 1b).

For safety reasons, mine access at the time of study was limited to just a few locations in the vicinity of Silver Creek. The first accessible tunnel on the southeast side of the creek was the Argentine Tunnel, located a few hundred feet upslope of the Blaine Tunnel (Figure 1b). The Argentine Tunnel was accessible for 183 m before becoming unsafe to access, at which point samples were collected from a stagnant mine pool. The mine pool was believed to have drained to lower level mine workings, as the water was not flowing out the tunnel to the surface. The second access point was the Blaine Tunnel, with a portal just 12 m from Silver Creek on the Southeast side. At the time of the study, water was flowing into the back of the Blaine tunnel, presumable as drainage from above workings (*i.e.*, those accessed by the Argentine Tunnel), resulting in about 1 m of water on the tunnel floor behind a cofferdam located 244 m back from the tunnel portal. Water levels behind the cofferdam were relatively stable (fluctuated < 5 cm over a 6 week period) suggesting that inflows were proportionate to water movement out of the tunnel towards the lower level workings that went under Silver Creek. Samples were collected in the Blaine tunnel from both the inflow and the pooled water behind the cofferdam.

The third access point was a short tunnel on the northwest side of Silver Creek, directly across Silver Creek from the Blaine portal, which accessed the vertical 517 Shaft approximately 50 m from the portal along Silver Creek. Historical mine maps indicated that the 517 Shaft extended vertically to at least the 500 level and that several of the tunnels under Silver Creek intersected the shaft at multiple levels (Figure 1d). The water level in the 517 Shaft was approximately 146 m below the elevation of the shaft collar, which corresponds to the elevation of the SE Crosscut and St. Louis Tunnel. Water samples were collected from the shaft using a bailer and mechanical pulley system located at the collar. The final access point to sample mine water was the St. Louis Tunnel portal. The portal had collapsed preventing underground access so samples were collected at first emergence from the collapse.

Figure 1. (**a**) Map of State of Colorado with location of Town of Rico located in the San Juan Mountains of southwestern Colorado; (**b**) Site map of Rico-Argentine mine complex and Silver Creek. Silver Creek sampling location numbers refer to the distance downstream (m) from the tracer injection point; (**c**) Overview map of entire Rico-Argentine mine complex in relation to the Town of Rico and the Dolores River. Yellow box shows location of mine complex and represents extent of figure 1b. Location and extent of the subsurface workings are overlain on top of aerial imagery to demonstrate how mine workings near Silver Creek are connected to the St. Louis Portal; (**d**) Vertical view of mine workings in relation to Silver Creek and access points. The 200 and 300 levels pass directly under Silver Creek.

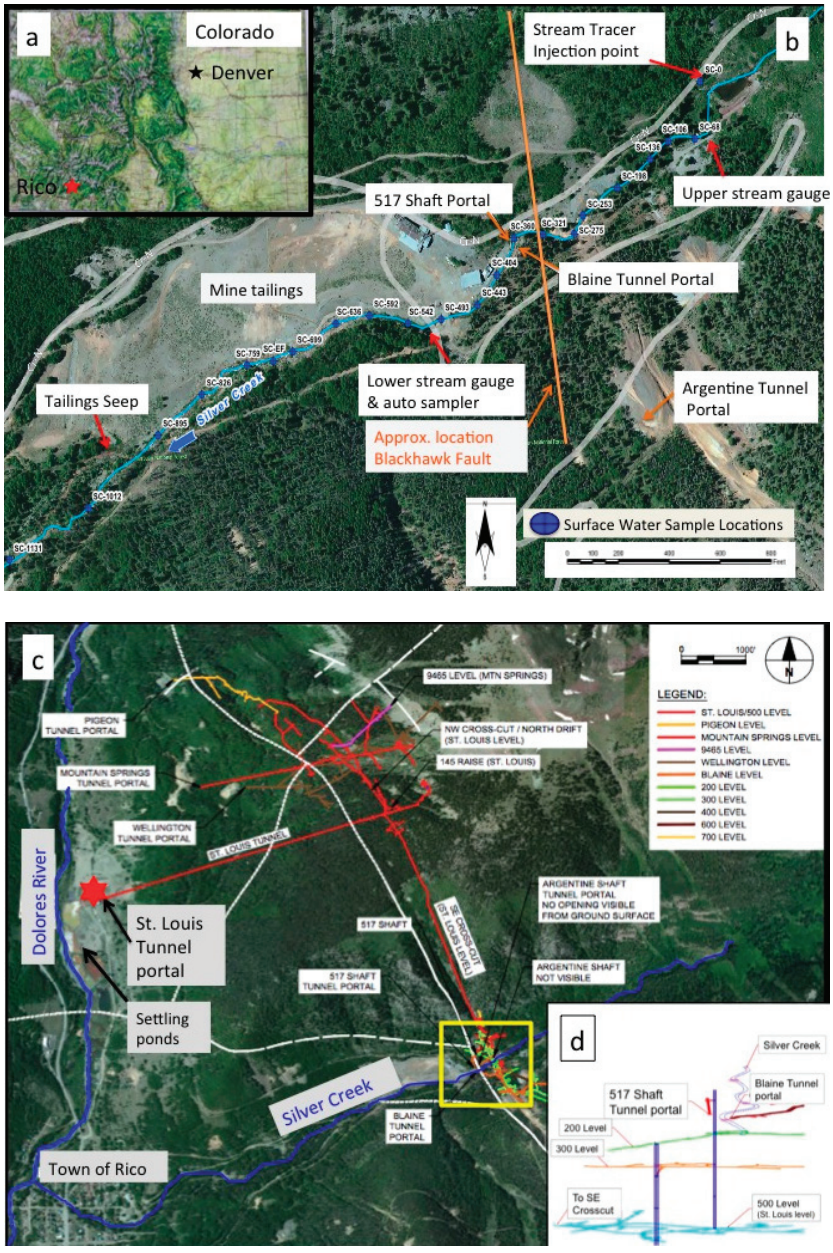

2.2. Study Design

The study was designed to understand the hydrologic connections between surface water, groundwater, and mine water associated with the Rico-Argentine mine. The tracer study was performed in October 2011, when surface water flows were at low-flow conditions, to try and minimize event based influences (rain and snowmelt) on the prevailing hydrologic conditions. Much of the southwestern USA, including the San Juan Mountains, can be characterized by bimodal precipitation patterns, *i.e.*, spring snowmelt and summer monsoon rains [24]. Previous mine drainage studies in the region have demonstrated that consistent low-flow conditions are most attainable in late summer (August–October) after monsoon rains have subsided and prior to freezing conditions during the winter months [15,25,26]. To quantitatively and qualitatively assess individual components of the hydrologic system, a series of independent environmental and applied tracers were applied and/or sampled at discrete locations within the study area. All tracers used in the study are summarized in Table 1.

To broadly understand how inputs to the system (precipitation) contribute to the surface and mine waters, the naturally occurring stable ($\delta^{18}O/\delta D$) and radioactive (^{3}H) water isotopes were measured in precipitation and at all other sampling locations. The stable isotopes provide information on source water contributions whereas the radioactive isotopes provide insight on mean residence time of waters in the mine system. The second objective of the study was to determine if Silver Creek is losing water to the mine workings. Silver Creek flow was measured using several different measurement techniques to evaluate the presence, magnitude, and timing of stream flows on Silver Creek around the area of the Rico-Argentine mine. Additionally, the mine waters (517 Shaft and St. Louis Tunnel) and mine tailings seep were analyzed for detection of tracers used in Silver Creek to look for direct hydrologic connections between the creek and the mine waters. The third objective was to determine the hydrologic connection between the Blaine tunnel mine water and mine water in the 517 Shaft. The approach was a slug injection (Table 1) into the Blaine tunnel mine pool and sampling for the breakthrough of that tracer in the 517 Shaft. The surface water in Silver Creek was concurrently monitored for Blaine tunnel tracer to check for movement of Blaine mine water towards surface flows. Finally, the study addressed the hydrologic connection between the mine water in the 517 Shaft and mine water discharging from the St. Louis Tunnel. The approach involved simultaneous slug additions of two independent tracers (Lithium salt and uranine dye; Table 1) in the 517 Shaft, which were analyzed for in samples continuously collected at the St. Louis Tunnel portal. A dual tracer approach was chosen at this location to have unique data sets to compare tracer functionality in an AMD setting.

Table 1. Summary of natural and applied tracers including the amount of tracer used and the application method. Silver Creek locations are marked in Figure 1b. Detection limits for stable isotopes reported as twice the precision. (TU, tritium units)

Tracer	Amount of tracer applied	Detection Limit	Type of Application; Location; Date	Sampling Location; Date	Objective
Oxygen (^{18}O)	NA	0.056 (‰)	Natural, Local Precipitation, 2011	All	Source water identification
Deuterium (^{2}H)	NA	0.296 (‰)	Natural, Local Precipitation, 2011	All	Source water identification
Tritium (^{3}H)	NA	0.3 (TU)	Natural, Local Precipitation, 2011	All	Source water identification; water apparent age
Sulfate (SO_4^-)	NA	0.0022 (mg/L)	Naturally occurring in mine impacted waters	Silver Creek (0–1131 m)	Hydrologic connectivity; mine water ↔ surface water
Sodium Bromide (NaBr)	75 kg NaBr	0.0031 (mg/L)	Constant injection (from 189 L reservoir); Silver Creek (0); 5 October to 7 October 2011	Silver Creek (0–1131 m)	Identify changes in streamflow
Lithium (LiOH)	9 kg LiOH	0.0108 (mg/L)	Slug injection (227 L); 517 Shaft; 4 October 2011	St. Louis Tunnel portal; 4 October to 16 November 2011	Hydrologic connectivity; mine → drainage tunnel
Sodium Fluoride (NaF)	6 kg NaF	0.0057 (mg/L)	Slug injection (30 L); Blaine Tunnel; 5 October 2011	517 Shaft; 5 October to 6 November 2011	Hydrologic connectivity; mine ↔ mine
Sodium Chloride (NaCl)	1.4 Kg NaCl per slug	0.0017 (mg/L)	Slug injections (8 L); Silver Creek (0,198,220, 384, 493,530); 3 October to 7 October 2011	Silver Creek (106, 321, 493, 636); 3 October to 7 October 2011	Estimate streamflow above and below mine workings
Rhodamine WT (liquid)	1.2 L	0.006 (ppb)	Constant injection (from 189 L reservoir); Silver Creek (0); 5 October to 7 October 2011	Silver Creek (443), Tailings Seep, 517 Shaft; 4 October to 11 November 2011	Hydrologic connectivity; Silver Creek ↔ mine, tailings seep
Uranine (Sodium Fluorescein)	13.63 kg	0.002 (ppb)	Slug injection (227 L); 517 Shaft; 4 October 2011	St. Louis Tunnel Portal; 4 October to 11 November 2011	Hydrologic connectivity; mine → drainage tunnel

2.3. Natural Tracers and Synoptic Sampling

Representative water samples were collected from along the study reach on Silver Creek, from the St. Louis Tunnel portal, and from the Dolores River above and below the mine treatment ponds. Prior to any disturbance from tracer applications, additional samples were collected from all mine locations described above and from a seep below the mine tailings pile along Silver Creek to establish background conditions (Figure 1b). Local snow and rain precipitation were analyzed for isotopes to characterize sources and timing of inputs to local surface water, groundwater, and mine water. The snow was a depth integrated sample collected adjacent to the mine complex in April 2011 to represent maximum snow accumulation prior to the study while rain samples were collected as weekly composites from five rain gauges located in the San Juan Mountains (within 50 km radius). Surface water and mine water samples were collected at several different times between April and October 2011 to examine both short-term (*i.e.*, daily) and seasonal variations at different locations. All samples were analyzed for water isotopes including oxygen-18 (^{18}O), deuterium (^{2}H or D), and tritium (^{3}H). Water samples were also analyzed for total and dissolved metals and solute chemistry to identify and distinguish the many contributions to metal load in Silver Creek and the St. Louis tunnel.

Water samples for D and ^{18}O analysis were collected unfiltered in clean 25-mL borosilicate bottles with no-headspace lids to avoid any evaporation or fractionation. The D and ^{18}O analyses were performed at the Kiowa Environmental Chemistry Laboratory in Boulder, Colorado, using an Picarro L1102-i Isotopic Liquid Wavelength- Scanned Cavity Ring Down Spectroscopy (WS-CRDS), a time-based measurement using near-infrared laser to quantify spectral features of molecules in a gas ratio of the sample to the Vienna Standard Mean Ocean Water (V-SMOW) standard, as shown for ^{18}O:

$$\delta^{18}O = \frac{\left(\frac{18_O}{16_O}\right)_{Sample} - \left(\frac{18_O}{16_O}\right)_{vsmow}}{\left(\frac{18_O}{16_O}\right)_{vsmow}} \times 1000\ ‰ \quad (1)$$

The 1−σ precision of $\delta^{18}O$ was ± 0.028 ‰ and of D was ± 0.148 ‰.

Water samples to be analyzed for tritium were collected as grab samples in high-density polyethylene (HDPE) bottles and stored at 4°C until analysis. The tritium samples were analyzed at the USGS Tritium Laboratory in Menlo Park, California, by electrolytic enrichment and Liquid Scintillation Counting. Distilled sample water was reduced electrolytically in electrolysis cells to 10 mL from an initial 200 mL in a cooling bath. The detection limit is reported as twice the precision. Tritium results reported in tritium units (TU) where 1 TU = 1 tritium atom per 10^{18} hydrogen atoms.

Water samples collected during synoptic sampling from along the study reach on Silver Creek, within the mine workings, and at the St. Louis Tunnel portal were analyzed for total and dissolved metals, select anions, and hardness. Onsite processing included filtration and measurement of pH. Filtration was completed using 0.45 μm capsule filters. Aliquots for cation analysis were acidified to pH < 2.5 with ultrapure nitric acid. Total recoverable and dissolved cation concentrations were determined from unfiltered and filtered samples, respectively (dissolved is used herein as an operational definition that refers to the concentration of the water after filtration; some colloidal material may pass through the 0.45 μm filter). Samples were analyzed at the U.S. EPA Region 8

Laboratory operated by the Environmental Sampling Assistance Team (ESAT) contractor for total and dissolved metals analysis using EPA 200 Series methods, for anions using EPA Method 300, and hardness was calculated using EPA method 2340B.

During synoptic sampling a subset of each unfiltered sample was also sent for chemical analysis to the Kiowa Environmental Chemistry Laboratory in Boulder, Colorado, where samples were immediately filtered through pre-combusted glass fiber filters with a nominal pore size of 0.7 μm and stored in the dark at 4 °C prior to analyses. Samples were analyzed for chloride (Cl^-), nitrate (NO_3^-), sulfate (SO_4^{2-}), bromide (Br^-), and fluoride (F^-), using a Metrohm 761 Compact Ion Chromatograph. The within run precision (%RSD) was < 1.1% for all solutes. Lithium (Li^+) was analyzed on a Perkin Elmer AAnalyst 200 Atomic Absorption Spectrometer with a within run precision of 1.06%.

2.4. Applied Tracers

The usefulness of applied tracer test results is highly dependent on proper test design (particularly determination of injection and sampling locations), the nature of the tracer, the ability to detect the tracer at low concentrations, and correct interpretation of recovery data [9,18,27,28]. Results from initial synoptic sampling (in May and June 2011), along with background information on the mine complex design and local geology, were used to develop a basic understanding of the hydrogeologic setting allowing for design of the applied tracer study which was performed in October 2011. Additionally, due to the hypothesis that the entire system under investigation was hydrologically connected the study was designed to ensure that all applied tracers were distinctly and independently measureable from each other in the event that mixing of tracers occurred. A previous dye tracer study was conducted by Davis [29] at a separate mine site (the Atlantic Cable mine) in Rico, Colorado, at the confluence of Silver Creek and the Dolores River, approximately 2.5 km downstream from the Rico-Argentine mine complex (Figure 1). The results of the Davis [29] study indicated that water chemistry (metals analysis) alone was inconclusive with respect to identifying and separating mine waters from local surface waters. The study was also unsuccessful at identifying surface water and mine water interactions using Sulpho-Rhodamine B dye tracer (no dye was observed at any of the sampling points around the mine site) and suggested that Rhodamine WT (RWT) may be a more effective tracer for future mine water studies in the area. These results further support the use of a multiple, natural and applied tracer approach to better understand surface water and mine water interactions in the current study of the Rico-Argentine Mine.

2.4.1. Tracer Selection and Application

In the state of Colorado, the use of surface water or groundwater tracers at permitted mining sites must be approved by the state mining regulatory agency, which is the Division of Reclamation, Mining, and Safety (DRMS) [30]. The study was performed under the authority of the U.S. EPA Superfund Technical Assessment and Response Team and the DRMS, whom both approved the experimental design and provided technical assistance and oversight throughout the course of the study. All applied tracers were chosen based on suggestions from literature reviews and based on analytical capabilities

and on the ability to safely use at concentrations that are distinguishable above background signals. Tracer amounts were determined following guidelines presented in Wolkersdorfer [9]. For all applied tracers the minimum detection limit (Table 1) was considered along with measured background concentrations and estimated mixing reservoir size (anticipated dilution) to ensure the tracer concentrations would be clearly identifiable at the sampling point.

There were six tracers used in the study (Table 1) including 4 salts and 2 fluorescent dyes. Tracers applied to surface waters (Silver Creek) included sodium bromide (NaBr) and sodium chloride (NaCl), which were applied to quantify streamflow and are described in further detail in Section 2.5. Additionally, the fluorescent dye Rhodamine WT (RWT; CI Acid Red 388; CAS 37299-86-8; Keystone Analine Corporation # 703-010-27, Chicago, IL, USA) was applied to Silver Creek concurrently with the continuous injection of NaBr to provide a dye that could be sampled for concurrently with the NaBr at several mine sampling points. The RWT was used because it is one of the most commonly recommended dye tracers for surface water application [18] and was recommended for future use by a previous study performed at a nearby mine interacting with Silver Creek [29]. Although RWT has been reported to have some genotoxic properties [16,18,31], the dye was found to exhibit ecological toxicity at concentrations greater than 1 milligram per liter (mg/L; 1000 parts per billion (ppb)) and human toxicity at concentrations greater than 100 mg/L (100,000 ppb) [8]. Therefore, the RWT was applied to the stream at low concentrations (<30 ppb) that were detectable but created minimal visible disturbance and remained well below concentrations of concern. The continuous injection ran from 5 October to 8 October with two rounds of synoptic sampling for bromide occurring on 5 and 7 October. Samples were also collected from the mine Tailings seep and 517 Shaft and analyzed for bromide and RWT to test for presence of Silver Creek water in the in mine workings or associated tailings pile.

The remaining 3 tracers were applied as slugs directly into mine waters with sodium fluoride (NaF) applied to the Blaine tunnel mine pool whereas lithium (as LiOH) and uranine (Uranine; C.I. Acid Yellow 73; CAS 6417-85-2; Keystone Analine Corporation 801-073042 Chicago, IL, USA) were applied concurrently to the mine pool at the bottom of the 517 shaft. The ability to easily sample and accurately quantify discharge at the St. Louis Tunnel portal motivated the application of multiple tracers at this location. By calculating the mass recovery of independent tracers the effectiveness of each tracer could be addressed. The lithium tracer was chosen because of low background signal in the mine water and because several of the other most common salt tracers (NaCl, NaBr, and NaF) had been used in the study. Uranine was chosen as the second tracer because it has long been used as a subsurface tracer due to low sorptive properties [16,32–35] and for being safe in terms of human or ecological toxicity [8,18,31]. Uranine also readily undergoes photo-degradation [16], but has shown long-term stability when not affected by sunlight [30], making it most suited for subsurface tracing. Uranine has only negative functional groups, and sorbs least onto negatively-charged media and most onto positively charged surfaces [35]. Mine waters often contain metal cations, especially iron (Fe), which can precipitate as hydroxides at higher pH values [36]. Uranine may therefore undergo adsorption onto iron hydroxides and be removed from the sample through filtration [36]. Conversely, if the collected mine samples are not filtered then fluorescence intensity may be

overestimated due to scattering effects caused by increased sample turbidity. Results from the dual tracer application will therefore enable this potential complication to be addressed.

On 4 October at 12:00, a 189-L slug containing 9 kg of LiOH and 13.63 kg of uranine was injected into the 517 Shaft. The size of the mine pool (mixing reservoir) at the bottom of the 517 Shaft was unknown due to inaccessibility to the flooded lower levels of the mine. Therefore, the necessary mass of tracer was estimated using the flow rate at the St. Louis Tunnel portal (assumed mine pool discharge point), the distance between injection and sampling location, and by assuming a reasonable estimated mine water flow velocity. Additionally, background concentrations of lithium were low (0.025 mg/L) and background fluorescence in the wavelengths used to detect uranine were below detection (<0.002 ppb) at the St. Louis Tunnel portal confirming minimal background interference with tracer detection. The estimated velocity (and mass) was verified based on the authors' experience with a similar tracer test at another mine site drainage tunnel with similar distance between injection and sampling points [37]. Additionally, the mine outflow at the St. Louis Tunnel portal flowed directly into a series of passive settling ponds and not into natural waters, which eliminated concerns for high concentrations of tracers (from over estimating tracer mass) rapidly entering local surface waters in the event of incomplete mixing of the tracer slug. The slug was mixed using acidic water (pH 2.7) from the Blaine Tunnel to simulate the water found at the bottom of the 517 Shaft (pH 2.5). The slug was mixed in two new, clean 115-L plastic tubs located adjacent to the top of the shaft and then siphoned from the tubs into the shaft using 137 m of new, clean garden hose. To avoid tracer contamination all materials used to transport and mix the tracers (including applicators clothing) were left at the injection site. The slug injection took approximately 45 minutes to complete and was then chased by approximately 189,000 L of water from Silver Creek delivered by a high capacity water pump over a 30-min period.

On 5 October at 14:15, a slug containing 6 kg of NaF was added to the Blaine Tunnel mine pool behind the cofferdam. The tracer mass was estimated based on the size of the mixing reservoir at injection and sampling points (Blaine tunnel mine pool and 517 Shaft mine pool), and information on background levels of fluoride at the injection point. The tracer mass was sufficient to increase F^- concentrations to approximately three times background (from 50.2 to 143.1 mg/L) in the Blaine Tunnel. The tracer recovery point (517 Shaft) had F^- background of only 1.95 mg/L. The slug was made by dissolving NaF powder into 30 L of Blaine Tunnel water using two 20-L buckets and a stirring rod made the slug. The NaF solution was slowly poured in the mine pool about 8 m behind the cofferdam. The mine pool had an estimated minimum volume of 42,500 L, but the inflow/outflow rates were not quantifiable. After the slug injection, a 7.6 cm diaphragm water pump was used to move water from the mine pool over a visible tunnel collapse (pile of rock and debris) and toward a drainage stope that extended to the lower mine levels that intersect with the 517 Shaft. The pump was able to move between 22,700 and 36,300 liters of water past the initial visible collapse in the first 2 h after injection. However, during that period no reduction in water level was observed in the mine pool and pumping was then terminated due to freezing of equipment and unsteady pump rates, so it was not possible to calculate the rate at which the entire mine pool (containing the fluoride slug) was moved past the initial blockage.

The exact pathway of the water (and tracer) leaving the Blaine Tunnel pool is unknown, but based on existing maps it was expected that water flows down a complex series of interconnected inclines, raises, winzes, stopes, tunnels, and shafts before reaching the 500 level via the 517 Shaft. Given the myriad of potential pathways, all in varying states of structural integrity, it was difficult to determine the actual distance the water and tracers would travel. Using all available information is was estimated that the shortest possible pathway from the Blaine Tunnel mine pool to the bottom of the 517 Shaft was 200 m.

2.4.2. Tracer Sampling and Analysis

Automated samplers were placed at 3 locations; SC-493, the mine Tailings seep, and the St. Louis Tunnel portal (Figure 1). The samplers in Silver Creek and at the mine Tailings seep collected samples at 1-h intervals for the duration of the constant injection of tracers in Silver Creek and then at 4-h intervals for 3 weeks following tracer application. At the St. Louis Tunnel portal water samples were collected at 1-h intervals for the first 40 h, starting 2 h before the 517 Shaft tracer injections. A Cyclops 7 field fluorometer from Turner Designs, Inc. (Sunnyvale, CA, USA), confirmed that the peak of the uranine slug occurred within the first 36 h, so sample collection was reduced to 4-h intervals on 7 October and continued for 6 weeks.

At the 517 Shaft, water samples were collected at a depth of 7.6 m below the water surface, which was 137 m below the collar of the shaft. Samples were collected manually using a stainless steel bailer lowered to the same depth for each sample using a calibrated cable reel and motorized pulley system. Samples were collected at 1-h intervals for the first 36 h after tracer injections were made in the Blaine Tunnel and then daily for 2 weeks. The last sample was collected in the 517 Shaft 690 h after tracer was injected in the Blaine Tunnel.

To provide real time confirmation of tracer emergence, the Cyclops-7 field fluorometer from Turner Designs Inc. was used to make *in-situ* field measurements for the presence of the two fluorescent dyes, RWT and uranine. The field fluorometer was calibrated for both dyes using a 4-point calibration with standards of 0, 1, 100, and 400 ppb solutions. The standards were prepared in the laboratory by diluting the purchased dye concentrates using water collected directly from the mine site at locations where the dyes were to be applied or measured. The RWT was mixed using water from Silver Creek (pH 8.2) and the uranine was mixed using water from the St. Louis Tunnel portal (pH 7.4). The manufacturer stated that the instrument's dynamic range for detection of uranine dye was 0 to 500 ppb so calibration from 0 to 400 ppb was considered sufficient for the intended use of the field fluorometer. The field fluorometer was used to qualitatively provide a rapid assessment of samples for presence/absence of the dye of interest to constrain the number of field samples that would be sent to the laboratory for analysis. At the Kiowa Laboratory, a Fluoromax 2 (F2) spectrophotometer was used to analyze water samples for the concentrations of the two fluorescent dyes. The presence of each dye was analyzed using a single excitation and a single emission value and a record of the spectrum for a 100 ppb standard for both dyes was created to determine the appropriate excitation/emission values to use for analyzing the dye tracers. The RWT dye was run with 550/580 nm excitation/emission and the uranine was run with 492/512 nm excitation/emission. The excitation and emission values for both dyes were within the expected variability [19] of values

previously reported for fluorescence analysis of these dyes [8,18,23]. For RWT, a 5-point calibration curve was developed using standards between 1 and 400 ppb concentration. For uranine, a 12-point calibration curve was developed with concentrations ranging from 1 to 1000 ppb. Dye concentrations were plotted against emissions values to generate calibration curves. Interestingly, for the uranine, F2 emissions peaked with the 500 ppb standard and then became inversely related to concentrations over 500 ppb. As reported in Käss [19] the intensity of the fluorescence likely decreased as a consequence of its individual light absorption and due to retrograde dissociation. To compensate for the decrease in emissions for high concentration samples, the standard power calibration curve (dye concentration in ppb (C) = $10^{-13} \times E^{2.1558}$; where E = measured emission (nm); $R^2 = 0.99$, N = 6) was used to calculate dye concentrations in samples with concentrations < 500 ppb and a second linear equation (dye concentration in ppb (C) = $-10^{-4} \times E + 2948$; where E = measured emission (nm); $R^2 = 0.9$, N = 6) was used to estimate dye concentrations in samples with concentrations > 500 ppb. The inflection point of 500 ppb was chosen from visual interpretation of emission/concentration plot. Additionally, when the standard curve was applied to all F2 emission results there was a false double peak in calculated uranine concentrations in the St. Louis Tunnel samples. Fortunately, the sample with the lowest uranine concentration (between the 2 false peaks) had the highest measured concentration of lithium (the second concurrently applied tracer) confirming a simultaneous arrival of the peak concentration of both tracers. The two false peaks were also at concentrations just below 500 ppb, further confirming that at concentrations over 500 ppb the F2 was unable to accurately quantify the amount of fluorescing compounds in the sample.

The fluorescence intensity of dyes is known to have a variable response to changes in pH [16,18,20,21,23,29,34,35]. To test for the effects of acidification on fluorescence, high concentration (400 ppb) standards of both uranine and RWT were acidified to a pH of 2.5 for 24 h and then filtered. The result was a 77% reduction in uranine emissions and an 11% reduction in RWT emissions. The reduction in uranine fluorescence agrees with previous research documenting considerable decrease in fluorescence intensity (up to 90% at pH 3) due to reversible ion exchange reactions caused by the acidic conditions [16,18,21]. However, as reported by Käss [18], the pH effects were reversible; when the standards were re-neutralized to the slightly alkaline conditions of the original standards (pH 8.2 and 7.4 for RWT and uranine, respectively) there was full recovery of the dye fluorescence emissions for both uranine and RWT. Although the uranine dye reaches maximum fluorescence under alkaline conditions ($pH \geq 9$) [16,18,23], the dye standards (for calibration and pH response measurements) were made with the actual mine water at the sampling location, so the above mentioned results should be representative of the range of pH the dye will be exposed to in the study.

2.5. Measuring Streamflow and Mine Discharge

There are many challenges to measuring streamflow in mountains including bed surface roughness, difficult to constrain channel dimensions, and steep stream gradients with varying degrees of hyporheic zone storage [38,39]. Furthermore, Marchand *et al.* [40] suggest that conventional current meter measurements of discharge do not properly account for hydraulic conditions commonly found in high-gradient, shallow streams of mountain catchments. Therefore a number of streamflow

measurement techniques were used to determine the magnitude and timing of flows in Silver Creek, and to evaluate potential flow losses from Silver Creek to mine workings underlying and on either side of the creek. The measurements would also identify any major inflows to Silver Creek in the vicinity of the mine. Quantification of streamflow was performed during both high flow (spring snowmelt) and low flow (fall base flow) to understand stream dynamics across the full range of the hydrograph. For this paper, only the low flow discharge will be discussed in detail, as applied tracer studies were performed during base flow.

Silver Creek flow was measured at two locations: an existing rectangular concrete weir structure with attached gauge house located upstream of the Blackhawk fault and mine workings (SC-68; Figure 1b), and at the downstream side of a road culvert just below the mine workings (SC-493; Figure 1b). Stage-discharge relationships (rating curves) were developed by correlating data from pressure transducers (stage) with discharge measurements made using an electromagnetic flow meter. Pressure transducers recorded stage every 15 min from June to August and October to November and discharge measurements were collected periodically to capture the full range of the stream hydrograph. Pressure transducers were removed in August to prevent vandalism and were re-installed in the same locations prior to the start of tracer tests in October.

Slug additions of sodium chloride (NaCl) were made to develop point estimates of streamflow at select locations above and below the mine workings along Silver Creek. Transport of the slug to a downstream observation point was monitored by a portable sonde that recorded specific conductance at 4-s intervals. Several grab samples were collected from the stream during slug tests and analyzed for Cl^- concentrations, which were matched with corresponding observations of specific conductance to develop a chloride-specific conductance relationship. The relationship was then used to convert the observed increases in specific conductance to chloride concentrations with the resultant profiles integrated to provide estimates of streamflow (Q, L/s) (1) following Kilpatrick and Cobb [41]:

$$Q = \frac{C}{V} \tag{2}$$

where C is the mass of Cl added (in kg) (C = 0.59 × mass of NaCl) and V is the time integral of the Cl concentration (above background) at the monitoring site. The units of V are (mg/L) per second. The third approach for quantifying streamflow in Silver Creek consisted of a continuous sodium bromide (NaBr) injection to provide streamflow estimates via the tracer dilution method [41] and document any potential areas of flow loss. Once the bromide tracer concentration reached a plateau synoptic sampling provided a spatial snapshot of bromide concentration and was used to determine a flow regime. In gaining streams, dilution of bromide with respect to distance is indicative of increased streamflow. Losing or constant flow streams, in contrast, will exhibit steady bromide concentrations with distance, as water leaving the stream does not affect the in-stream concentration.

Discharge was also measured at the St. Louis tunnel portal. Flow was directed through a 9-inch (22.86 cm) Parshall flume and stage heights were measured at 3 mm resolution at 15-min intervals with an ultrasonic automated water level detector that was installed on 12 May 2011. Flow estimates (L/s) were then determined using the flume's standardized stage-discharge relationship. Due to limited access to the interior portions of the mine, flow could not be directly measured along tracer flow paths in the mine workings.

3. Results and Discussion

3.1. Silver Creek: Streamflow and Hydrologic Connectivity to Mine

The multiple techniques used to quantify Silver Creek streamflow across the study site found that flow varied between 19.8 and 56.6 L/s during the October tracer study. Unfortunately, the high gradient mountain stream combined with unsteady streamflow (caused by two small precipitation events) produced unavoidable challenges in accurately quantifying streamflow. During the study period the discharge records from stage-discharge relationships at SC-68 (above the mine) and SC-493 (below the mine) produced "cross-over" where the largest instantaneous flow was at the upstream location during some periods of the study and at the downstream location at other times. Therefore, the two locations of measured discharge alone were inconclusive on determining if Silver Creek was only gaining or only losing water as it moved past the mine complex, and suggest that both inflows and outflows may be occurring within the study reach. The slug addition techniques also produced varying results ranging from 7% to 29% loss across the study reach during the sampling event with loss rates being smaller after precipitation events. The precipitation events likely masked some of the streamflow losses by adding small but influential surface water inflows along the study reach. The constantly injected RWT and Br^- tracers were analyzed by two separate synoptic sampling events, both following precipitation events, and the Br^- profiles on both sweeps suggested a gaining stream at the upstream end of the study reach (above the mine workings) and the potential for flow loss downstream of the mine workings between SC-542 and SC-759. To summarize, Silver Creek likely has some net flow loss along the study reach but high gradient stream channel and the precipitation events made it difficult to accurately quantify streamflow variations during the study period.

Concurrent with the continuous injection of Br^- and RWT, the 517 Shaft and the mine Tailing seep were sampled for the presence of the injected tracers to identify if water leaving Silver Creek (as identified by discharge calculations) was interacting with the mine system or Tailings pile on the northern side of the creek. The Br and RWT tracers injected into Silver Creek were not detected at elevated concentrations in the mine workings or discharges from the Tailings seep and St. Louis Tunnel portal. At the seep Br^- concentrations remained below detection (<0.003 mg/L) for the duration of the sampling. There was no detectable increase in RWT concentrations, which remained below detection (0.006 ppb) throughout the sampling period. In the 517 Shaft, background concentrations of Br (0.046, $\sigma = 0.037$ mg/L) were detected both before and during the tracer study, but concentrations remained at background levels with no evidence of an increase or breakthrough slug emerging at the 517 Shaft. There was no detection of RWT before or during the tracer study.

The results fail to confirm a hydrologic connection from Silver Creek to the Tailings seep or the mine workings directly connected with the 517 Shaft. However, results prevent positive confirmation or rejection of minor flows from Silver Creek through the mine to the 517 Shaft during low-flow conditions. One logistical constraint in the tracer design was that the RWT concentrations in Silver Creek were maintained at very low concentrations (range 16 to 28 ppb) to avoid any potential negative (toxicological or visual) impacts. Additionally, the in-stream Br^- concentrations were kept at a measureable but conservative concentration (4.73, $\sigma = 0.7$ mg/L) to ensure that there were no

potentially toxic effects to aquatic life. The low concentrations of stream tracers, combined with the large volumes of mine waters, made it unlikely for the tracers to be detected, especially if additional dilutions from ground water were considered. A second challenge to identifying stream tracers in the mine, was that the length of the sampling window. Tracer recovery sampling in the mine was limited by personnel availability and seasonal access, which only continued for approximately 30 days after the tracer injections. Therefore tracers may not have arrived at the sampling locations during the sampling window. Third, it is possible that some Silver Creek water (containing the applied tracers) reached the subsurface mine workings but underwent dilution from mixing with other groundwater or mine water prior to arrival at the sampling point, causing dilution to background concentrations. The use of low concentrations of tracers in Silver Creek to minimize adverse environmental impacts was likely the ultimate limiting factor preventing positive confirmation or rejection of hydrologic connection between Silver Creek and the sampled mine water locations.

3.2. Natural Tracers

3.2.1. Water Quality

Water quality varied widely across all sampling sites, with the highest concentration of contaminants generally associated with the mine pools and lowest concentrations in Silver Creek and the St. Louis Tunnel portal. The pH of samples ranged from a high of 8.7 (± 0.19 (1SD), N = 17) in Silver Creek to a low of 2.38 (± 0.06 (1SD), N = 5) in the Blaine Tunnel mine pool (Figure 2). Dissolved aluminum and zinc concentrations were highest in the mine workings to the southeast of Silver Creek and decreased prior to exiting the St. Louis Tunnel portal. Aluminum ranged from a high concentration of 654 mg/L in the Argentine Tunnel to less than 0.1 mg/L at the St. Louis Tunnel portal (Figure 3). Similarly, zinc concentrations were highest in the Argentine Tunnel pool at 24,600 mg/L and decreased to 3.8 mg/L at the St. Louis Tunnel portal. Solute loading analysis was not performed as flow rates from the Argentine Tunnel, Blaine Tunnel, and 517 Shaft mine sites were not measured during the study.

During the tracer experiment water quality along Silver Creek was synoptically sampled at the same locations as were used for the stream tracer study (Figure 1b). Sulfate (SO_4^{2-}), generally considered a conservative tracer in AMD settings [27], was measured at all sampling points and showed a measureable increase from under 10 mg/L above SC-198 to over 50 mg/L at SC-1131 the furthest downstream sampling point (Figure 4). Dissolved zinc concentrations were measured at nine of the sampling points and increased from under 0.005 mg/L upstream of the mines to 570 mg/L at SC-1131. Both sulfate and zinc concentrations had the largest increases in the 200 m upstream of the mine entrances (at approximately 400 m) and then remained relatively constant until increasing again beyond 800 m.

Figure 2. Box plot of pH in the mine workings along with that of the St. Louis Tunnel portal and tailings seep discharges and of surface waters in Silver Creek.

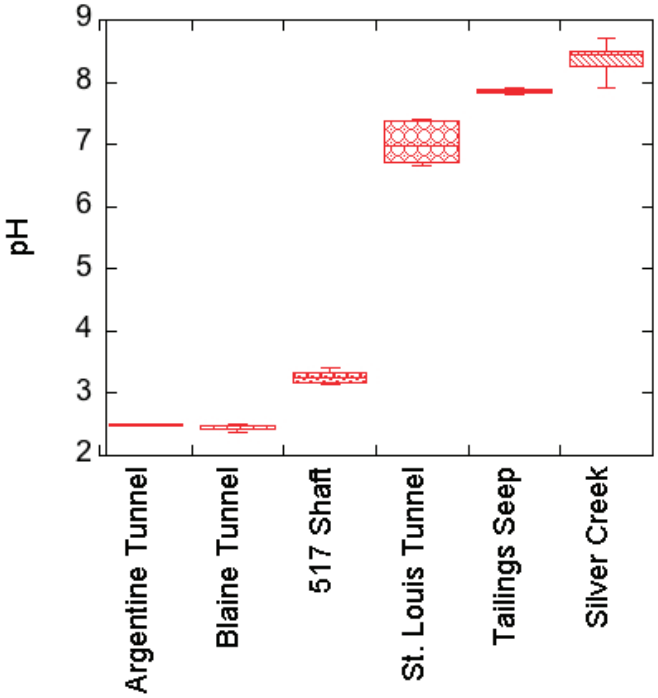

Figure 3. Dissolved zinc and total dissolved aluminum concentrations in mine workings. The mine workings are listed from left to right in the direction of hydrologic flow towards the discharge point at the St. Louis Tunnel portal.

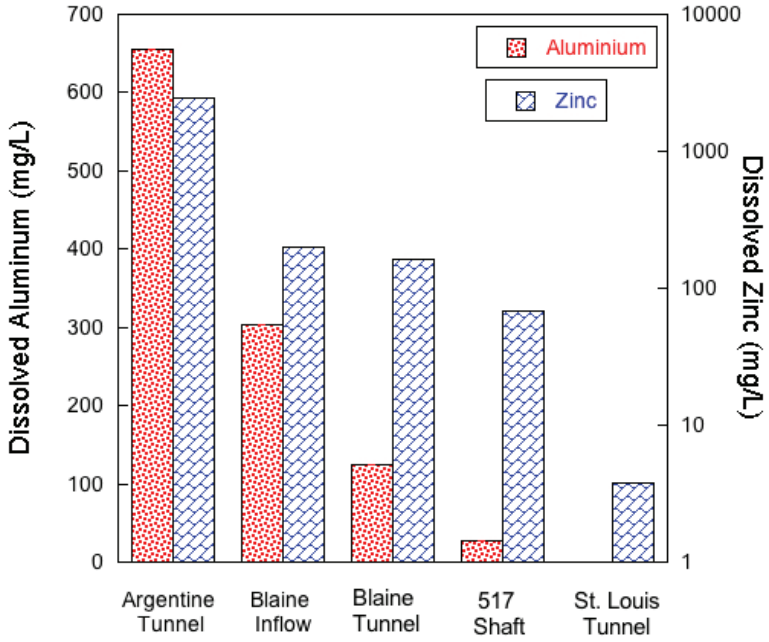

Figure 4. Sulfate and dissolved zinc concentrations in Silver Creek from synoptic sampling during base flow conditions on 7 October 2011. Stream locations are in m downstream from the location of the stream tracer injections with the stream crossing the mine workings at approximately 400 m. There are known inflows to Silver Creek from seepage below the mine tailings entering between SC-895 and SC-1131 in Figure 1.

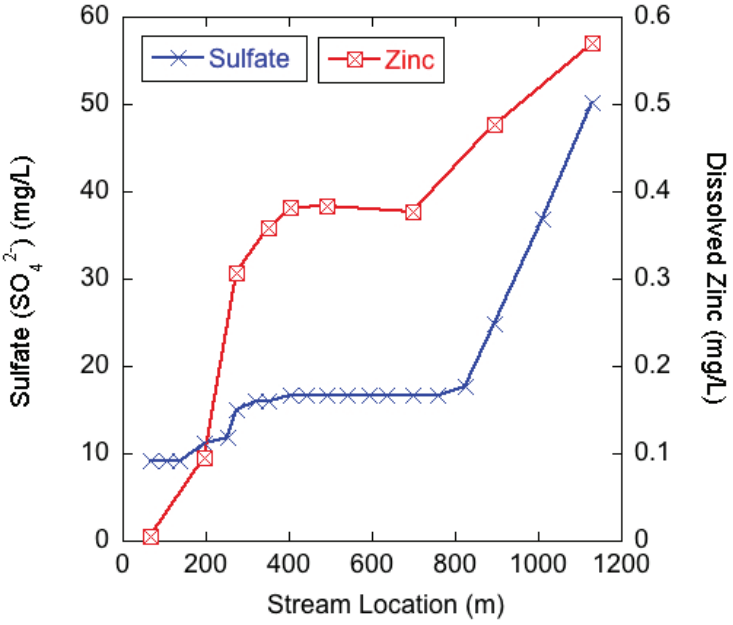

Silver Creek chemistry suggests that mining activities impact Silver Creek and the sources of AMD products (sulfate and zinc) are occurring in similar locations. The sulfate and mining-associated metal concentrations begin to increase in Silver Creek in the vicinity of the Rico-Argentine mines and indicate that even though there is a potential net loss of flow in the reach, there may be small inputs of mine water or other inflows that influence the stream chemistry. The first considerable increases in stream solutes occur between 200 and 300 m, which is upstream of the primary mine entrances (Figure 1b), but within the area of historical mining operations. Due to mining activities, there are considerable amounts of mine debris (mill tailings and mine waste rock) scattered along the banks of the stream channel starting at approximately 100 m (Figure 1b). Given the variable discharge (gains and losses) measured along the study reach it is likely that the Silver Creek waters are undergoing hyporheic zone mixing in areas where solute laden mine wastes are present. As a result, contaminated sediments in the hyporheic zone may be representing a long-lasting supply of contaminants to hyporheic pore water [42]. A second source of solutes is slow percolation of highly concentrated AMD water in the Blaine Tunnel mine pool into the subsurface and eventual movement towards the stream channel, which would likely occur at or just downstream of the Blaine Tunnel portal between 350 and 400 m. The relatively consistent solute concentrations between 400 and 700 m is likely because previous mine cleanup work at this site included capping the mine tailing pile (Figure 1) and reinforcing the bank between the tailings pile and Silver Creek to reduce erosion of the tailings pile into Silver Creek. As a result, the amount of surface water and hyporheic zone mixing may be decreasing along this segment creating less opportunity for mining-associated sulfate and zinc to enter Silver Creek. The increase in AMD contaminants to Silver Creek at locations below

the mine entrances (below SC-826) are likely from diffuse inflows from the tailings pile seep which are visually present between SC-895 and SC-1131 in Figure 1.

The results in Figures 3 and 4 therefore suggest that, when excluding the contributions from the large mine tailings pile, the sulfide deposits sourcing the AMD may be most prevalent in the mine workings and shallow subsurface on the southeastern side of Silver Creek between 200 and 400 m. As suggested by Nordstrom [6] this shallow acidic groundwater can then be mobilized by infiltration of meteoric waters, resulting in movement towards surface waters (or further into the mine complex). To elaborate, the high metals concentrations found in the mine waters to the southeast of Silver Creek may be partially explained by the mines artificial lowering of the local water table. The mine drainage tunnels were built to help dewater the mine workings but as a consequence the mine workings also exposed large amounts of sulfide minerals to air, which increased oxidation reactions. Therefore, the combined exposure to air and water (from seasonal meteoric infiltration and shallow groundwater flow) in the mine workings adjacent to, and above, Silver Creek has created an ideal situation for AMD production that is impacting the water quality in Silver Creek and at the St. Louis Tunnel.

3.2.2. Isotopes

Stable isotope results from all samples including precipitation, surface water, and mine water were plotted as the δD–δ^{18}O relationship (Figure 5A). The δ^{18}O value for snow of approximately −20‰ and the mean rain value of −5‰ are characteristic values for the Colorado Rocky Mountains for winter and summer precipitation [43]. Empirical results have shown that δD/δ^{18}O values in precipitation co-vary and are generally described by the relationship [44]:

$$\delta D = 8\delta^{18} \quad (3)$$

which is defined as the Global Meteoric Water Line (GMWL). The Local Meteoric Water line (LMWL) has a similar slope and y-intercept:

$$\delta D = 7.8\delta^{18} \quad (4)$$

Figure 5. (**A**) Plot of δ18O *vs.* δD for precipitation, surface waters, and mine waters. The St. Louis Tunnel, 517 shaft, Blaine tunnel, Tailings seep, and Silver Creek are the arithmetic mean from all samples collected. The Local Meteoric Water Line (LMWL) is plotted in black; (**B**) Seasonal variations of δ18O *vs.* δD for surface waters and mine waters in 2011. The LMWL is plotted with a second water line (WL1; red dash), representing samples from the Tailings seep and the Blaine Tunnel and a third water line (WL2; blue dot) representing samples from Silver Creek and the St. Louis Tunnel. The symbol shapes correspond to similar sites in (A) and (B), while colors represent similar dates for different sites in (B).

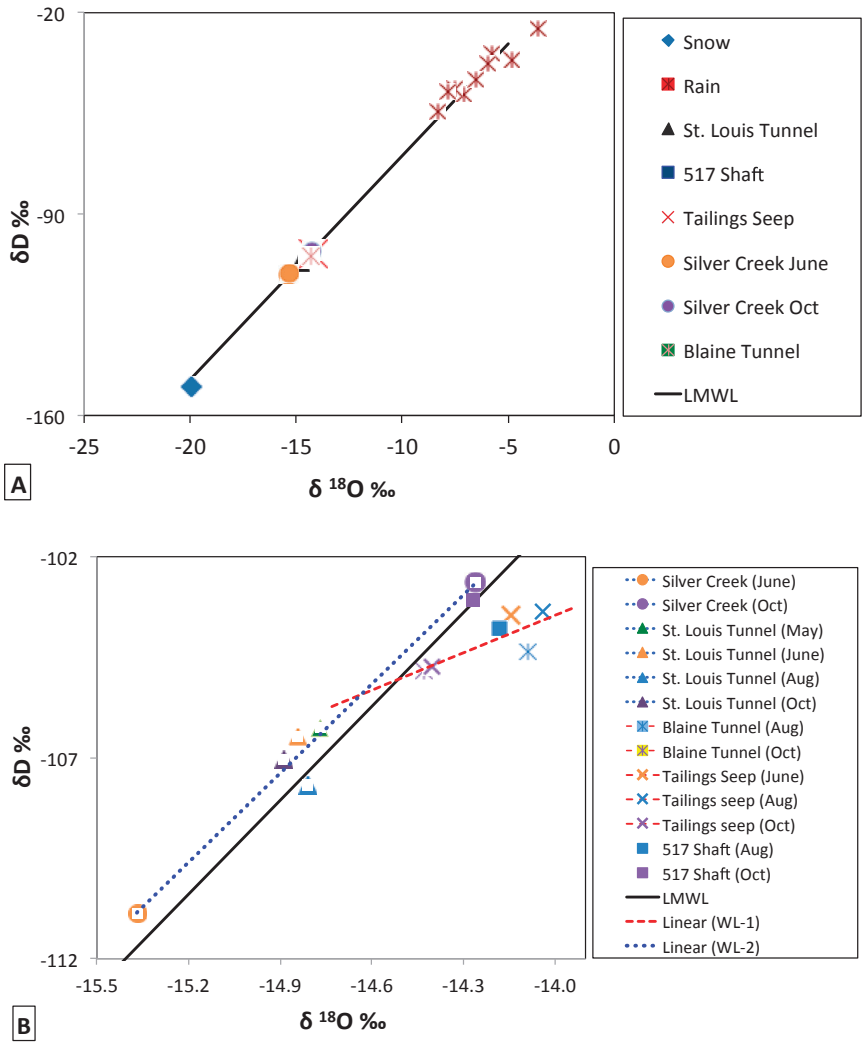

The similar values in slope between the LMWL (7.8) and the GWML (8.0) suggest an absence of complex kinetic fractionation processes affecting the δD–δ^{18}O relationship of precipitation (inputs) in the local hydrologic system [45]. All surface water and mine water samples fell on a mixing line between the snow and rain inputs, suggesting that they were a mixture of the two precipitation types with δ^{18}O values between −14‰ and −15‰.

To better observe the variations in surface waters and subsurface waters (relative to the LMWL) the δD–δ^{18}O relationship was examined at a finer resolution (Figure 5B). The isotopic concentration of Silver Creek had the greatest seasonal variation with waters more depleted in δD and δ^{18}O in June

as a result of snow melt and more enriched in δD and $\delta^{18}O$ in October from summer rains and/or groundwater contributions. All of the samples collected in or near the mine (Tailings seep, Blaine Tunnel, 517 Shaft) had an isotopic composition similar to Silver Creek in October, indicating that stream water during baseflow was of similar origin to the water moving through both the upper mine and the seep. Additionally, there was little variation in isotopic signature of the Tailings seep, which did not follow variations observed in Silver Creek, indicating that water exiting the Tailings seep was coming from a well-mixed source distinct from Silver Creek waters. However, the samples from the Tailings seep and the Blaine Tunnel all plot below the LMWL with a decreased slope and y-intercept:

$$\delta D = 3.1\delta^{18} \quad (5)$$

This linear relationship is represented by WL-1 in figure 5b and the decreased slope suggests that an evaporation trend occurred at these locations since recharge [45,46]. Conversely, samples from the St. Louis Tunnel and Silver Creek express the following δD–$\delta^{18}O$ relationship:

$$\delta D = 7.4\delta^{18} \quad (6)$$

The linear relationship is represented by WL-2 in figure 5B, and the similar slope between WL-2 (7.4) and LMWL (7.8) again suggests an absence of fractionation processes affecting those water sources since meteoric recharge. The two samples from the 517 Shaft plot close to, and slightly below, the LWML indicative of a mixture of predominantly unfractionated waters (since recharge) with a lesser amount of fractionated waters (*i.e.*, from the Blaine Tunnel). These results therefore suggest that the waters with evidence of evaporation (Tailings seep and Blaine Tunnel) are distinct from local precipitation (LMWL), surface water (Silver Creek), and the dominant source of water exiting the mine system (St. Louis Tunnel).

Figure 5B also indicates that the water discharging from the St. Louis Tunnel had similar isotopic concentration in May, June, and October, indicating the water was also predominantly from a well-mixed groundwater source with limited seasonal variation. The St. Louis Tunnel samples were also consistently more depleted than the samples from the 517 Shaft and Blaine Tunnel, indicating that water flowing downgradient from the 517 Shaft was mixing with water that has a distinctly different isotopic signature (more depleted) before emerging at the portal.

The stable isotope analysis provides initial insight into the hydrologic connectivity of the system, but due to the limited range (magnitude) of isotopic variability across all sites, is insufficient as a stand-alone tool for identifying the sources and relative contributions of water contributing to the AMD.

Tritium values from 21 rain and snow samples collected in the San Juan Mountain region between January 2010 and October of 2011 had a mean value of 6.2 TU with the 25th and 75th percentiles of samples being 4.6 and 6.5 TU respectively (Figure 6). The narrow range of tritium in incoming precipitation provided a strong estimate of the current meteoric inputs of tritium to the local hydrologic system under investigation. For comparison the annual mean tritium concentration in precipitation in Colorado was only 7.5 TU in 1999 [37], suggesting that tritium levels in meteoric waters have only decreased by about 1 TU in the decade preceding the current study. The tritium data provide insight as to the mean residence time of "old" *versus* "new" groundwater in the study. Tritium ($t_{1/2}$ = 12.43 years) is naturally present only in minute quantities but was produced in large

quantities during thermonuclear weapons testing from 1952 to 1963 [47]. As a consequence, without consideration for complex mixing scenarios, water with a tritium value <1 TU may be considered "old" water recharged prior to 1952 while higher values would represent "new" water being wholly or partially recharged since 1952. Additionally, if a tritium concentration is greater than the current meteoric recharge it can be considered to have some portion of water that precipitated with a "bomb spike" signal in the decades following weapons testing. No samples had <1 TU while all mine water and surface water tritium concentrations were near or within the range of recent precipitation suggesting that those waters were derived predominantly from recent (within a few years) meteoric recharge. The Argentine Tunnel sample, along with the Silver Creek and the Dolores River samples, had slightly elevated tritium concentrations relative to the current (2010–2011) meteoric inputs, suggesting that the water in those locations may have had slightly longer mean residence times than the waters emerging at the Tailings seep and moving through the mine to the St. Louis Tunnel. The tritium results provide only a qualitative estimate of water residence times, but suggest that the mean residence times of the mine waters are not distinctly different from residence times of the local and regional surface waters.

Figure 6. Tritium (^{3}H) values from recent (2010–2011) regional precipitation (blue), surface waters (green and pink), and mine waters (orange). The blue precipitation bar represents the mean value of all samples while the red error bar represents the 25th and 75th percentiles.

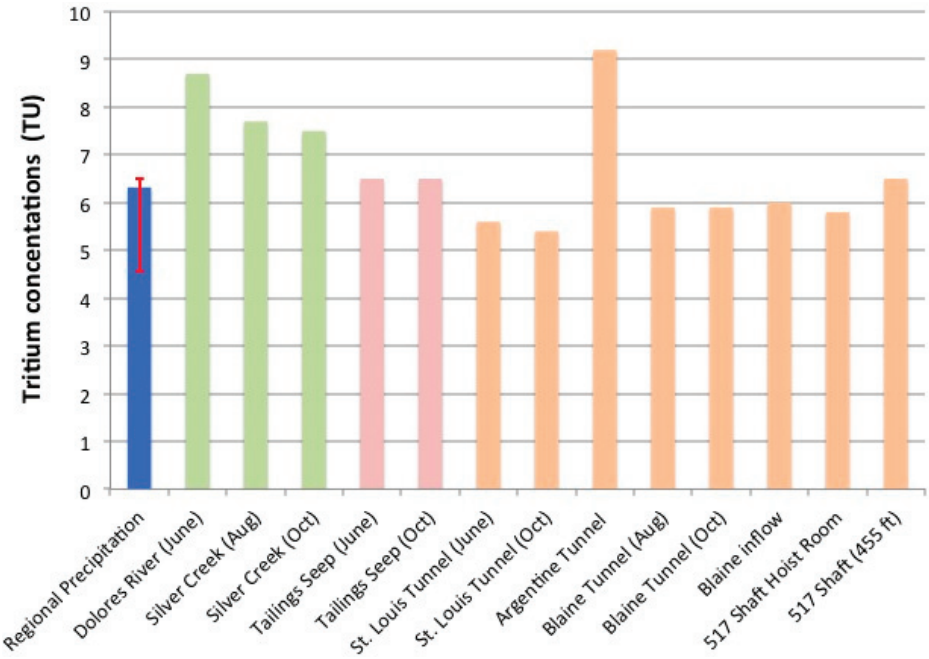

3.3. Applied Tracers

3.3.1. Blaine Tunnel to 517 Shaft

The first hydrologic connection to be investigated with applied tracers was the movement of water from the Blaine Tunnel to the 517 Shaft and the interior mine workings. There was no practical way

to quantify the volume of water entering the 517 Shaft from the Blaine Tunnel area, thus quantification of tracer mass recovery was not possible. Additionally, it was estimated that only between 50% and 85% of the mine pool water (containing the fluoride tracer slug) was successfully pumped over the first debris blockage towards the drainage stope exiting the Blaine Tunnel making it unclear what percentage of the initial tracer was moved out of the Blaine Tunnel mine pool via pumping. However, positive detection of the tracer provided a qualitative assessment of hydrologic connectivity between the Blaine Tunnel and the 517 Shaft area of the mine. Figure 7 displays a time series plot of fluoride and chloride concentrations in the 517 Shaft starting on 5 October at 14:00 when the fluoride slug was added to the Blaine Tunnel behind the cofferdam. Chloride concentrations remained relatively steady (2.11, $\sigma = 0.08$ mg/L) over the first 48 h, indicating that the changes in fluoride concentrations were occurring independently from any changes in the mine water chemistry caused by previous hydrological alterations such as the water chase applied to the 517 Shaft during the uranine/lithium tracer application. Interestingly, the chloride concentrations did decrease to a mean of 1.78 ($\sigma = 0.05$) mg/L for approximately 96 h (approximately hour 48 to 144 in Figure 7), which corresponds to the period when the highest fluoride concentrations were measured in the 517 Shaft. Given that background chloride concentration was lower in the Blaine Tunnel (1.54 mg/L) than in the 517 Shaft (2.14 mg/L) it is reasonable to suggest that the Blaine Tunnel water (which was partially moved out of the Blaine Tunnel by pumping) arrived at the 517 Shaft at an increased rate relative to background flow rates creating increases and decreases in fluoride and chloride concentrations respectively.

Figure 7. Fluoride (F^-) concentrations measured in the 517 Shaft. Background chloride (Cl^-) concentrations are plotted over the same time period. Time (x-axis) plotted as log scale.

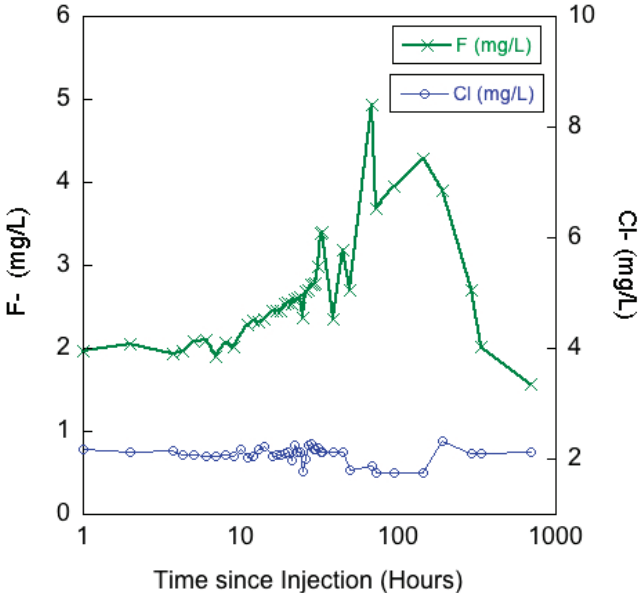

The initial fluoride concentration in the 517 Shaft (1.95 mg/L) indicated that there was a measureable background presence of fluoride in the system. However, the fluoride concentrations began to show a steady increase above background concentrations beginning 10 h after injection, and more than doubled to reach a peak concentration of 4.94 (mg/L) 68 h after the slug injection.

The fluoride concentration then began to fall sharply approximately 8 days after the tracer injection. Given an approximate minimum distance from the Blaine Tunnel cofferdam to the base of the 517 Shaft of 200 m, the velocity of the advection front (maximal velocity) was 0.34 m/min while the average velocity of the peak fluoride concentration was just 0.05 m/min. When compared to results reported by Wolkersdorfer [9], the average velocity is considerably slower than the range of 0.3 to 1.6 m/min reported as 95% confidence interval of 42 tracer tests. From a qualitative standpoint the results suggest that the hydrologic flow paths between the Blaine Tunnel and 517 Shaft may have major obstructions and/or the water is moving slower than has been most commonly observed in previously studied mine water environments. Additionally, there is diffusion in the system because there was not a distinct breakthrough curve. One anticipated possibility is one or several obstructions at points along the tunnel/stopes that causes the water to interact with rock and sediment. The collapsed portion of the adit over which water was pumped immediately after tracer injection is one likely obstruction. As mentioned in the methods, the tracer recovery at the 517 Shaft was achieved by sampling from a mine pool of unknown volume and flow-through rates. Additionally, the precise volume and rate of water moved out of the Blaine Tunnel mine pool (injection point) was not quantified due to pumping inefficiencies and unsafe access to drainage points. The flow path of the tracer between the Blaine Tunnel and the 517 Shaft was also likely diverse (multiple interconnected tunnels, stopes, and inclines present) making quantification of tracer travel distance difficult. Therefore the tracer breakthrough rates should be considered in a qualitative manner and no quantitative transport model (e.g., [9,18,27]) was used to evaluate solute transport and dispersion.

During the Blaine Tunnel tracer injection, water samples were also collected from SC-493 (about 120 m downstream from the Blaine Tunnel adit, Figure 1b) to determine if a detectable amount of water was flowing from the Blaine Tunnel, through the subsurface, to Silver Creek. The fluoride concentrations at SC-443 after the Blaine tunnel injection remained relatively steady (0.104, $\sigma = 0.018$ mg/L) with intermittent but not sustained increases, which neither confirms nor rejects the hypothesis that water contained in the Blaine Tunnel may be directly entering Silver Creek in the vicinity of the portal.

The original tracer design included pairing a third fluorescent dye (PTSA; 1,3,6,8-Pyrenetetrasulfonic Acid Tretrasodium salt; CAS # 59592-10-0) with the fluoride salt tracer applied to the Blaine tunnel. This dye tracer has a fluorescence emission peak that is distinct from both uranine and RWT so it could be used in a multiple tracer situation when tracer mixing is possible. Additionally, the Cyclops 7 field fluorometer from Turner Designs has a submersible sensor specifically designed for detection of PTSA. However, knowing that there were potentially multiple blockages (rock collapses in-filled with sediments or AMD derived precipitates) the dye tracer was not used and thus still available for additional future studies. This is important because if a tracer is used and full recovery cannot be confirmed then that tracer would not be desirable for future use in the same location for reasons of cross contamination.

3.3.2. 517 Shaft to St. Louis Tunnel Portal

The arrival time for both uranine and lithium at the St. Louis Tunnel portal was at 03:00 on 5 October, 15 h after injection (Figure 8). After arrival, the concentration of both tracers increased

rapidly with uranine reaching a peak concentration of 2900 ppb at 08:00, and the lithium tracer reaching a peak concentration of 0.258 mg/L at 09:00 on 5 October, representing 20 and 21 h to peak concentration, respectively. There was no clear increase in discharge as a result of the water chase (189,000 L in 30 min ≈ 105 L/s) added to the 517 Shaft immediately following tracer injections. The fast times for the advection front of the tracer movement from the 517 Shaft to the St. Louis Tunnel portal suggest that in general the tunnel has few obstructions and water moves through it relatively quickly as channel flow.

Figure 8 also displays field fluorometer data, which confirms the timing of tracer arrival and subsequent rapid increase in uranine concentration. Unfortunately, the upper limit of calibration for the field fluorometer was 400 ppb for this experiment so the instrument was unable to record the peak concentrations of the tracer breakthrough. The field instrument was then able to pick up the recession limb of the uranine slug. The general performance of the instrument was quantified by determining that the instrument tracked the laboratory analyses well, though with a near linear 45% reduction in concentration ($r^2 = 0.99$) when sample concentrations were below 400 ppb. According to the information provided by the manufacturer of the field fluorometer, the uranine probe was designed to analyze samples using excitation/emission values of 485/540 nm, which is shifted from the 492/512 nm values used for laboratory analysis. Therefore the field fluorometer may have failed to accurately capture the uranine fluorescence peak, resulting in consistently lower measured concentrations of uranine dye in the St. Louis Tunnel samples.

Figure 8. Time series of hourly discharge (**top**) and tracer break through curves (**bottom**) for lithium and uranine at the St. Louis Tunnel portal. Time 0 represents 12:00 on 4 October.

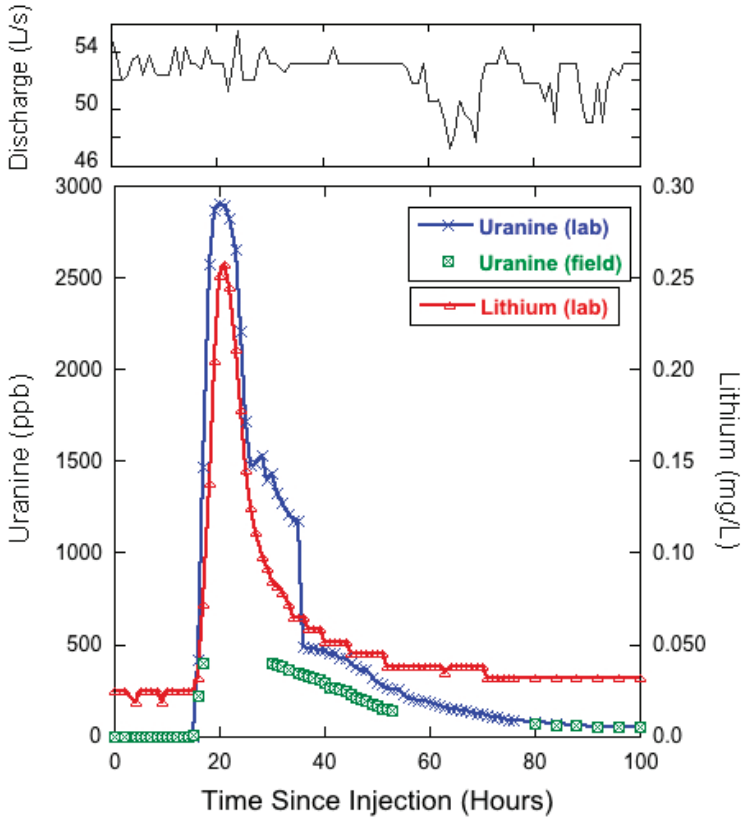

Given an estimated tunnel distance of 2591 m between the 517 Shaft and the St. Louis Tunnel portal, the average velocity of the advection front (maximal flow velocity) was 2.87 m/min while the mean velocity of the lithium and uranine peaks were 2.16 m/min and 2.06 m/min, respectively. Although time elapsed between tracer injection and passage of maximal-concentration provides a good approximation of the mean velocity, it is recognized that the true effective flow velocity occurs after the passage of maximal-concentration and cannot be calculated from the breakthrough curve alone [18]. However, when a steep and narrow breakthrough curve occurs, as observed in Figure 8, the correct time for calculating effective flow velocity is only insignificantly larger than the time of passage of maximal-concentration and the difference can be practically neglected [18]. Therefore, the approximated effective flow velocity was used, and when compared to results presented by Wolkersdorfer [9] the effective flow velocity is considerably faster than the range of 0.3 to 1.6 m/min reported as 95% confidence interval of 42 mine tracer tests. The results suggest this system differs from those reviewed by Wolkersdorfer [9], or that the water chase applied behind tracer injection may have artificially increased the velocity of tracers as they moved from the 517 Shaft towards the St. Louis Tunnel. Interestingly, the discharge at the St. Louis Tunnel portal did not show a clear increase or pulse in discharge upon tracer arrival (Figure 8). Hourly mean discharges between 01:00 and 24:00 on 5 October (the breakthrough period) fluctuated between 51 L/s and 54 L/s relative to the mean of 52 L/s (σ = 26 L/s) over the first 100 h of tracer recovery. As a result, the artificial influence of the water chase on tracer velocity was not directly quantifiable, making the estimated effective flow velocity a qualitative estimate and influencing the decision not to use an established model for solute transport simulation.

The final sample, collected 6 weeks after the tracer injection, showed that lithium concentrations had returned to background levels (approximately 0.025 mg/L) while uranine concentrations were still slightly elevated (≈1.8 ppb) relative to background (<0.002 ppb). The results indicate that 6 weeks after the tracer injection the lithium tracer was no longer moving though the system at concentrations greater than background, while the fluorescent dye tracer was still arriving at the portal in detectable quantities. However, as of the last discharge measurement on 16 November, cumulative flow and concentration data were used to calculate 74% and 109% recovery of lithium and uranine respectively. This result conflicts the final instantaneous concentrations by suggesting that all of the uranine was recovered while some of the lithium remained in the mine workings, either through sorption or ending up in an immobile fluid region that was disconnected from the main discharge conduit. Assuming the mine waters flow through a karst-like conduit system, the immobile fluid regions could be conceptually described as resulting from vortices and eddies produced by conduit surface irregularities [48].

Given that the St. Louis Tunnel discharge (Figure 8) showed considerable albeit irregular fluctuations (min/max hourly discharges were 42.3 and 57.7 L/s) over the 6-week tracer recovery period, it is reasonable to suggest that short-term variations in measured discharge may have created uncertainty in quantifying tracer recovery. For short projects, such as this study, uncertainties in cumulative flow can be upwards of 14% in a low gradient flow system if conditions are non-ideal [49]. The St. Louis tunnel discharge was measured directly downstream from the collapsed adit, with flow emerging though piles of mine timber and debris before being channelized and directed through

a flume for quantification. There was no way to completely eliminate turbulence in the flow prior to reaching the flume, which resulted in continuous small scale (≈1–2 cm) water surface undulations representing 5%–10% variability in total depth of flow at the flume. The variability in depth likely created uncertainties in calculated flow and in the quantification of tracer recovery. Additionally, there is inherent difficulty in calculating mass recovery of a fluorescent dye because the analytical results are an indirect measurement of the dye itself. Variable dye concentrations produce different intensities of fluorescence, which is then converted back to a mass of dye based on calibration curves that do not have perfect fit with standards. Therefore a reasonable degree of error should be expected when calculating mass recovery and results from this experiment are likely within that range. Given that uranine concentrations remained slightly elevated at the end of the study period, it was not possible to have recovered the entire tracer mass. Uranine concentrations on the final day of sampling suggested that discharge from the St. Louis Tunnel portal was only producing approximately 8.16 g of uranine per day, only 0.08% (per day) of the total mass of tracer added.

A second major concern with interpreting fluorescent dye results in a mine tracer study was the effect of low pH waters on the fluorescence properties of the dyes. The results of laboratory acidification tests (described in methods) agreed with previous work [16,18,21,23] by showing that the uranine dye had its fluorescence (spectral signature) reduced when exposed to low pH waters. However, results from the laboratory investigation showed that uranine fluorescence recovered when acidic conditions were re-neutralized to the pH values observed in samples collected at the St. Louis Tunnel portal (pH 7.34), which were likely maintained by reversible ion exchange reactions [18,23]. The study results therefore support previous recommendations from Naurath *et al.* [23] that uranine can be successfully used in mine tracer studies when samples analyzed for tracer recovery are alkaline.

A final consideration for uranine recovery was the influence of mine water iron (Fe) concentrations. The total recoverable Fe was approximately 66 mg/L in the 517 Shaft and only 4 mg/L at the St. Louis Tunnel portal during the study indicating that a significant portion of the iron precipitated as iron hydroxides between the uranine tracer injection and recovery locations. The Fe hydroxides can negatively influence uranine recovery rates due to dye adsorption on the hydroxide surfaces and subsequent loss by filtration [36] or settling of precipitates into immobile fluid regions of the conduit. All of the samples were filtered prior to fluorescence analysis to eliminate any fluorescence intensity overestimates due to increased turbidity in the sample. However, Naurath *et al.* [23] reported that good recovery can be expected in mine waters up to 100 mg/L of Fe, so it is concluded that the Fe levels in the mine waters emerging at the St. Louis Tunnel portal were not high enough to interfere with uranine results, as supported by the high recovery amounts reported previously.

3.4. The St. Louis Tunnel Portal Discharge

Mean daily discharge at the St. Louis Tunnel portal from May to November 2011 ranged from 36 to 57 L/s with the peak discharge occurring on 21 September (Figure 9). Daily discharge from the St. Louis Tunnel portal is plotted with the daily flows in Silver Creek at the downstream stream gauge site (SC-493, Figure 1). Although the Silver Creek discharge record does not begin until 17 June, it is clear that the discharge record depicts a typical snowmelt hydrograph for Silver Creek

with discharge peaking in late spring (May or June) and returning to near base flow in August. For comparison, the discharge of the Dolores River at Rico (USGS station 09165000) [50] had a similar snowmelt hydrograph for 2011 with peak discharge occurring on 7 June, just 10 days before the discharge record began on Silver Creek. However, at the St. Louis Tunnel portal, there is no characteristic snowmelt pulse in the discharge. Rather, the hydrograph there has a more consistent flow over time, with peak discharge occurring more than 3 months after peak discharge was recorded in the local surface waters. This observation could be explained by a regional groundwater pulse signal, which suggests that a large portion of the St. Louis Tunnel discharge is coming from or driven by a more regional (*i.e.*, watershed aquifer scale) groundwater reservoir.

The increase in pH and subsequent decrease in dissolved metals concentrations between the mine workings and the St. Louis Tunnel portal also suggest dilution and perhaps titration of acidity by non-AMD groundwater between the locations. The pH and metals concentrations support the notion of increasing dilution as mine waters move downgradient from the Argentine Tunnel (above the Blaine) to the Blaine Tunnel to the 517 Shaft to the St. Louis Tunnel portal, suggesting that the workings to the south of Silver Creek may be the primary source of AMD and that mine water at the 500 level becomes diluted as it moves northeast towards the SE crosscut and the St. Louis Tunnel.

Figure 9. Mean daily discharge from the St. Louis Tunnel portal and from Silver Creek. Silver Creek discharge was not measured between 27 August and 3 October 2011 as pressure transducers had been removed from the gauging stations during this period.

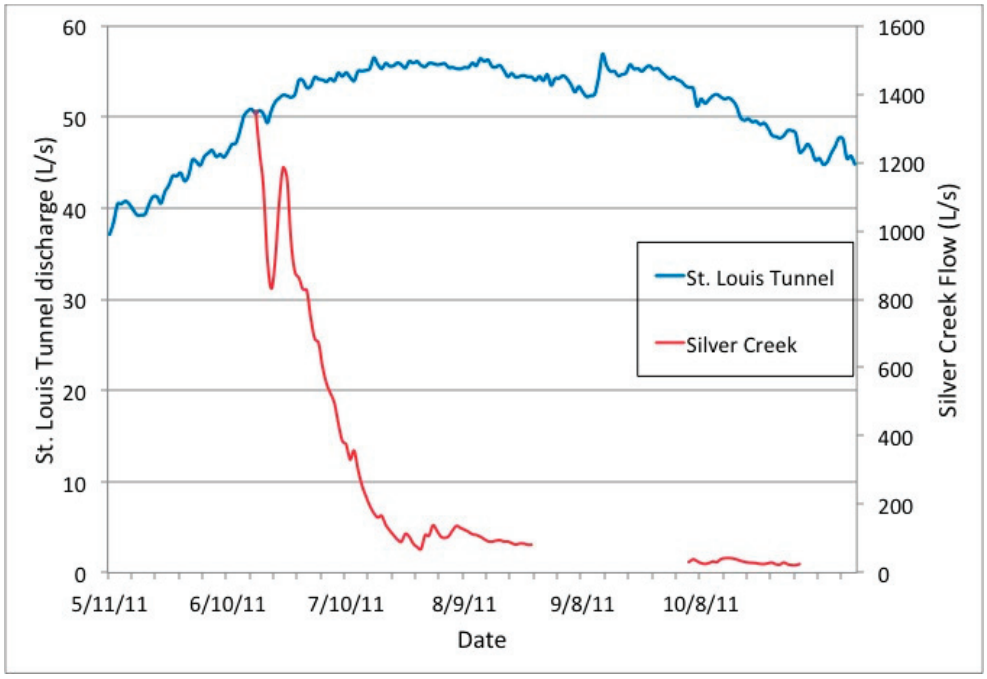

Dilution along the drainage tunnels by considerable amounts of well-mixed non-AMD groundwater is further supported by stable isotope results, which indicate a steady, low variability signal at the St. Louis Tunnel portal and greater seasonal variability at the upper mine workings (Blaine Tunnel and 517 Shaft). The potential for considerable amounts of non-AMD water entering the system along the St. Louis Tunnel may also be explained by the regional hydrogeology.

The drainage tunnel extends several thousand feet into the Rico dome, which is comprised of a thick series of interbedded sandstone, arkose, shale, limestone and dolomite of the Pennsylvania age Hermosa formation [51]. One of the units of this formation is the Leadville Limestone, which is locally 75 m thick and the top of the unit exhibits widespread karst and related erosional features [52]. The Leadville Limestone is also overlain by a sequence of clastic and calcareous sedimentary rocks up to 1000 m thick [52]. The widespread limestone and sedimentary units may therefore support a large regional aquifer. As a result, the St. Louis tunnel may likely be intercepting significant amounts of groundwater (with low levels of mineralization relative to mine waters) moving through the regional aquifer, leading to a dilution of the AMD water prior to emergence at the St. Louis Tunnel portal. The delay in peak discharge from the St. Louis Tunnel relative to the local surface waters would then be explained as being driven by the regional groundwater pulse which can lag seasonal surface or near-surface water runoff in mountain watersheds [53].

3.5. Targeted Remediation

Targeted remediation refers to controlling the source of water (*i.e.*, inflow of groundwater or surface water) into underground workings or open pits and/or controlling the outflow of mine drainage from the workings [1]. From the hydrologic characteristics identified by the multiple tracer approach there are several options for future remediation. Results suggest that there is some degree of hydrologic connectivity between the mine complex and Silver Creek, but it appears that even with the creek being a no-change or losing reach across the mine complex that creek waters are not contributing large amounts of source waters to the underlying mine workings. Therefore, it does not seem necessary to artificially control streamflow in Silver Creek. Conversely, if the study found significant contributions from Silver Creek, then targeted remediation options may have included activities such as lining the stream channel with an impervious membrane or re-routing the stream channel to minimize water exchange in the vicinity of the mine.

The most likely sources of water to the mine are therefore from localized (hillslope scale) meteoric recharge into near surface mine workings to the southeast of Silver Creek. Results suggest that these inputs are seasonally variable with the greatest inputs likely deriving from snowmelt, which is highly spatially and temporally variable in mountain settings [54,55]. The variability of input, combined with the highly variable nature of surface or near-surface mine entrance points (*i.e.*, driven by different rates of portal collapses) make it too expensive and difficult to control the most prevalent source waters. Additionally, most of the degraded mine entrance points are on steep slopes with limited access, so additional environmental impact would occur if the entrances were to be adequately shut off.

The study results further suggest that the mine discharge at the St. Louis Tunnel portal is coming from a combination of highly mineralized (and low pH) AMD waters and less mineralized, well-mixed (from stable isotope results) groundwater. The tracers suggest that the highly mineralized waters are moving in a south to north direction, or from the hillslope containing the Argentine/Blaine Tunnels under Silver Creek towards the 517 Shaft area of the mine and along the deep drainage tunnels to the St. Louis Tunnel portal. The remaining question is at what location does the highly mineralized acidic mine water mix with clean, non-mine-impacted groundwater? By untangling

the “under-ground plumbing” in these instances, a source-control approach can be used to collect and segregate the mineralized AMD water, before it can mix with and contaminate larger volumes of naturally occurring groundwater flows [1].

A next step would be to perform rehabilitation of the mine workings associated with the Argentine and Blaine Tunnels to increase safe access and provide confirmation and quantification of sources and mixing points. It would also help to know the volume of mineralized AMD water leaving the mine complex via the SE crosscut prior to any additional inflows occurring along the drainage tunnels. If the contaminated water is significantly less than the volume of water exiting the St. Louis Tunnel then active treatment of the lower volume of water may be the most economically viable option. Currently, *in-situ* treatment to neutralize the acidity (≈3 pH) of mine water in the 517 Shaft is being performed. The results of this treatment are pending but if the water quality of the St. Louis Tunnel discharge is improved then smaller scale on-site treatment of mine waters in this area may provide the most feasible targeted remediation option.

Other targeted remediation options may include bulkheads to prevent the flow of contaminated waters from ever reaching the St. Louis Tunnel portal. This requires an in-depth understanding of both the structural integrity of host bedrock and regional groundwater elevations before mining and theoretically after bulkhead installation. Installation of a bulkhead is therefore only acceptable if the compounded waters do not back up and reemerge at unintended or uncontrollable locations.

5. Conclusions

Naturally occurring stable- and radio- isotope tracers, artificial salt and dye tracers, and synoptic sampling of water quality parameters were utilized to understand the hydrologic connectivity of the Rico-Argentine mine complex. Historical mining activities have led to the production of AMD at this location and accurate hydrological characterization may enable targeted remediation to reduce or eliminate the contaminated discharge. The natural tracer results suggest that the mine hydrology is driven by recharge of recent meteoric waters while the mine discharge appears to be dominated by a well-mixed groundwater signal. The synoptic sampling of water quality suggests that the most highly contaminated mine water resides in the upper mine workings located in the hillside to the southeast of Silver Creek and are diluted prior to discharging at the St. Louis Tunnel. Tracers applied to Silver Creek indicated that the creek may be losing some water in the vicinity of the mine, but were unable to confirm or reject that Silver Creek was directly contributing water to the mine. Tracers applied directly to the mine workings indicated that mine water was moving in a south to north direction from the workings on the Blaine Tunnel side of Silver Creek to the 517 Shaft area and then draining to the St. Louis Tunnel portal. The concurrent application of a lithium salt and uranine dye tracer to the mine workings produced similar results suggesting that both type of tracers can be successfully used in acidic mine water conditions. However, it was concluded that mass recovery of the uranine dye tracer was more difficult than mass recovery of the lithium tracer because fluorescent dye mass is indirectly measured via fluorescence signal creating greater uncertainty in recovery calculations.

In combination, this suite of natural and applied tracers can provide useful information on complex hydrologic conditions that produce AMD at abandoned hardrock mine sites. The resulting

hydrologic characterization of the mine sites may ultimately reduce the impacts of AMD by supporting targeted remediation efforts.

Acknowledgments

The authors of this study would like to thank three anonymous reviewers and Jeff Writer (USGS) for greatly improving the quality of this manuscript. In addition the authors thank the following partners: The U.S. EPA Region 8 Superfund Emergency Response Program; The USGS Toxic Substance Hydrology Program; The Colorado Division of Reclamation, Mining, and Safety; Jan Christner at URS Corporation; Anderson Engineering Company Inc.; The Kiowa Environmental Laboratory of the NWT LTER program at the Institute of Arctic and Alpine Research, Boulder, CO; The Mountain Studies Institute Silverton, CO; and numerous individuals who assisted in field sampling and laboratory analysis for this project. The use of trade, product, or firm names in this publication is for descriptive purposes only and does not imply endorsement by the U.S. government.

Conflicts of Interest

The authors declare no conflict of interest.

References

1. Wireman, M.; Stover, B. Hard-rock mining and water resources. *Ground Water* **2011**, *49*, 310–316.
2. *National Hardrock Mining Framework*; U.S. EPA 833-B-97-003; U.S. EPA Office of Water: Washington, DC, USA, 1997.
3. Riebsame, W. *Atlas of the New West: Portrait of a Changing Region*; W.W. Norton & Company: New York, NY, USA, 1997; p. 192.
4. Kimball, B.A.; Runkel, R.L.; Walton-Day, K.; Bencala, K.E. Assessment of metal loads in watersheds affected by acid mine drainage by using tracer injection and synoptic sampling: Cement Creek, Colorado, USA. *Appl. Geochem.* **2002**, *17*, 1183–1207.
5. Jarvis, A.P.; Younger, P.L. Dominating chemical factors in mine water induced impoverishment of the invertebrate fauna of two streams in the Durham coalfield, UK. *Chem. Ecol.* **1997**, *13*, 249–270.
6. Nordstrom, D.K. Acid rock drainage and climate change. *J. Geochem. Explor.* **2009**, *100*, 97–104.
7. Wolkersdorfer, C. Mine water tracing. In *Mine Water Hydrogeology and Geochemistry*; Younger, P.L., Robins, N.S., Eds.; Geological Society: London, UK, 2002; pp. 47–60.
8. Field, M.S.; Wilhelm, R.G.; Quinlan, J.F.; Aley, T.J. An assessment of the potential adverse properties of fluorescent tracer dyes used for groundwater tracing. *Environ. Monit. Assess.* **1995**, *38*, 75–96.
9. Wolkersdofer, C. *Water Management at Abandoned Flooded Underground Mines—Fundamentals, Tracer Tests, Modeling, Water Treatment*; Springer: Heidelberg, Germany, 2008; p. 466.

10. Alvarado, J.A.C.; Purtschert, R.; Barbecot, F.; Chabault, C.; Ruedi, J.; Schneider, V.; Aeschbach-Hertig, W.; Kipfer, R.; Loosli, H.H. Constraining the age distribution of highly mixed groundwater using 39Ar: A multiple environmental tracer ($^{3}H/^{3}He$, ^{85}Kr, ^{39}Ar, and ^{14}C) study in the semiconfined Fontainebleau Sands Aquifer (France). *Water Resour. Res.* **2007**, *43*, 1–16.
11. Troldborg, L.; Jensen, K.H.; Engesgaard, P.; Refsgaard, J.C.; Hinsby, K. Using environmental tracers in modeling flow in a complex shallow aquifer system. *J. Hydrol. Eng.* **2008**, *13*, 1037–1084.
12. Lavastre, V.; La Salle, C.; Michelot, J.; Giannesini, S.; Benedetti, L.; Lancelot, J.; Lavielle, B.; Massault, M.; Thomas, B.; Gilabert, E.; *et al*. Establishing constraints on groundwater ages with 36Cl, 14C, 3H, and noble gases: A case study in the eastern Paris basin, France. *Appl. Geochem.* **2010**, *25*, 123–142.
13. McKnight, D.M.; Bencala, K.E. The chemistry of Iron, Aluminum, and dissolved organic material in three acidic, metal-enriched, mountain streams, as controlled by watershed and in-stream processes. *Water Resour. Res.* **1990**, *26*, 3087–3100.
14. Bencala, E.; McKnight, D.M.; Zellweger, G.W. Evaluation of natural tracers in an acidic and metal-rich stream. *Water Resour. Res*. **1987**, *23*, 827–836.
15. Runkel, R.L.; Walton-Day, K.; Kimball, B.A.; Verplanck, P.L.; Nimick, D.A. Estimating instream constituent loads using replicate synoptic sampling, Peru Creek, Colorado. *J. Hydrol.* **2013**, *489*, 26–41.
16. Smart, P.L.; Laidlaw, I.M.S. An evaluation of some fluorescent dyes used for water tracing. *Water Resour. Res.* **1977**, *13*, 15–33.
17. Smart, P.L. Applications of Fluorescent Dyes in the planning and hydrologic appraisal of sanitary landfills. *Q. J. Eng. Geol.* **1985**, *18*, 275–286.
18. Käß, W. *Tracing Technique in Geohydrology*; Balkema: Rotterdam, the Netherlands, 1998; p. 581.
19. Knop, A. Über die hydrographischen Beziehungen zwischen der Donau und der Aachquelle im badischen Oberlande. In *Neues Jahrbuch Fur Mineralogie, Geologie und Paläontologie*; Leonhard, K.C.; Bronn, H.G.; Leonhard, G.; Geinitz, H.B., Eds.; E. Schweizerbart'sche Verlagshandlung (E. Koch): Stuttgart, Germany, 1878, pp. 350–363.
20. Käß, W.A. Hydrologic tracing practice on underground contaminations. *Environ. Geol.* **1994**, *23*, 23–29.
21. Lyons, R.G. Identification and separation of water tracing dyes using pH response characteristics. *J. Hydrol.* **1993**, *152*, *13*–29.
22. Geyer, T.; Birk, S.; Licha, T.; Leidl, R.; Sauter, M. Multitracer test approach to characterize reactive transport in Karst aquifers. *Ground Water* **2007**, *45*, 36–45.
23. Naurath, L.; Weidner, C.; Rüde, T.R.; Banning, A. A new approach to quantify na-fluorescein (uranine) in acid mine waters. *Mine Water Environ.* **2011**, *30*, 231–236.
24. Bales, R.C.; Cline, D. Snow hydrology and water resources (Western United States). In *Handbook of Weather, Climate, and Water; Atmospheric Chemistry, Hydrology, and Societal Impacts*; Potter, T.D., Colman, B.R., Eds.; John While and Sons: Hoboken, NJ, USA, 2003; pp. 443–459.

25. Runkel, R.L.; Kimball, B.A.; Walton-Day, K.; Verplanck, P.L. A simulation-based approach for estimating premining water quality: Red Mountain Creek, Colorado. *Appl. Geochem.* **2007**, *22*, 1899–1918.
26. Runkel, R.L.; Bencala, K.E.; Kimball, B.A.; Walton-Day, K.; Verplanck, P.L. A comparison of pre- and post-remediation water quality, Mineral Creek, Colorado. *Hydrol. Processes* **2009**, *23*, 3319–3333.
27. Field, M.S. *The QTRACER2 Program for the Tracer-Breakthrough Curve Analysis for Tracer Tests in Karstic Aquifers and Other Hydrologic Systems*; EPA/600/R-02/001; U.S. Environmental Protection Agency—Office of Research and Development: Washington, DC, USA, 2002; p. 179.
28. Field, M.S. *Tracer-Test Planning Using the Efficient Hydrologic Tracer-Test Design (EHTD) Program*; EPA/600/R-03/034; U.S. Environmental Protection Agency—Office of Research and Development; National Center for Environmental Assessment: Washington, DC, USA, 2003; p. 175.
29. Davis, M.W. *The Use of Tracer Dyes for the Identification of a mine Flooding Problem, Rico, Dolores County, Colorado*; Colorado Geological Survey Open File Report 91-2; Colorado Geological Survey: Lakewood, CO, USA, 1994; pp. 1–20.
30. Wolkersdorfer, C.; LeBlanc, J. Regulations, legislation, and guidelines for artificial surface water and groundwater tracer tests in Canada. *Water Qual. Res. J. Can.* **2012**, *47*, 42–55.
31. Behrens, H.; Beims, U.; Dieter, H.; Dietze, G. Eikmann, T.; Grummt, T.; Hanisch, H.; Henseling, H.; Käß, W.A.; Kerndorff, H.; *et al*. Toxicological and ecotoxicological assessment of water tracers. *Hydrogeol. J.* **2001**, *9*, 321–325.
32. Flury, M.; Wai, N.N. Dyes as tracers for vadose zone hydrology. *Rev. Geophys.* **2003**, *41*, 1–33.
33. Davis, S.N.; Thompson, G.M.; Bentley, H.W.; Stiles, G. Ground-water tracers-A short review. *Ground Water* **1980**, *18*, 14–23.
34. Sabatini, D.A.; Austin, T.A. Characteristics of rhodamine WT and fluorescein as adsorbing ground-water tracers. *Ground Water* **1991**, *29*, 341–349.
35. Kasnavia, T.; Vu, D.; Sabatini, D.A. Fluorescent dye and media properties affecting sorption and tracer selection. *Ground Water* **1999**, *37*, 376–381.
36. Aldous, P.J.; Smart, P.L. Tracing groundwater movement in abandoned coal mined aquifers using fluorescent dyes. *Ground Water* **1988**, *26*, 172–178.
37. Davies, G. *Results of Ground-Water Tracing Experiments in the Nelson-Wooster-Humphrey Tunnel*; Cambrian Ground Water Co.: Oak Ridge, TN, USA, 2002; p. 14.
38. Bencala, K.E.; McKnight, D.M.; Zellweger, G.W. Characterization of transport in an acidic and metal-rich mountain stream bed on a lithium tracer injection and simulations of Transient Storage. *Water Resour. Res.* **1990**, *26*, 989–1000.
39. Jarrett, R.D. Hydrologic and Hydraulic research in mountain rivers. *Water Resour. Bull.* **1990**, *26*, 419–429.
40. Marchand, J.P.; Jarrett, R.D.; Jones, L.L. *Velocity Profile, Water-Surface Slope, and Bed-Material Size for Selected Streams in Colorado*; Open-File Report 1984-733; U.S. Geological Survey: Lakewood, CO, USA, 1984; p. 82.

41. Kilpatrick, F.A.; Cobb, E.D. *Chapter A16. Measurement of Discharge Using Tracers*; USGS Techniques of Water-Resources Investigations Reports, Book 3; U.S. Geological Survey: Reston, VA, USA, 1985.
42. Palumbo-Roe, B.; Dearden, R. The hyporheic zone composition of a mining-impacted stream: Evidence by multilevel sampling and DGT measurements. *Appl. Geochem.* **2013**, *33*, 330–345.
43. Liu, F.J.; Williams, M.W.; Caine, N. Source waters and flow paths in an alpine catchment, Colorado Front Range, United States. *Water Resour. Res.* **2004**, *40*, 1–16.
44. Michel, R.L. *Tritium Deposition in the Continental United States, 1953–1989*; Water-Resources Investigations Report 89-4072; U.S. Geological Survey: Reston, VA, USA, 1989.
45. Craig, H. Isotopic variations in meteoric waters. *Science* **1961**, *133*, 1702–1703.
46. Williams, M.W.; Knauf, M.; Caine, N.; Liu, F.J.; Verplanck, P. L. Geochemistry and source waters of rock glacier outflow, Colorado Front Range. *Permafr. Periglac.Process.* **2006**, 17, 13–33.
47. Eastoe, C.J.; Rodney, R. Isotopes as tracers of water origin in and near a regional carbonate aquifer: The Southern Sacramento Mountains, New Mexico. *Water* **2014**, *6*, 301–323.
48. Field, M.S.; Pinsky, P.F. A two-region nonequlibrium model for solute transport in solution conduits in karstic aquifers. *J. Contam. Hydrol.* **2000**, *44*, 329–351.
49. Brigand, F.G.; Lellouche, G.; Appelboom, T.W. Measuring flow in non-ideal conditions for short-term projects: Uncertainties associated with the use of stage-discharge rating curves. *J. Hydrol.* **2013**, *503*, 186–195.
50. USGS National Water Information System. Available online: http://waterdata.usgs.gov/nwis (accessed on 1 June 2012).
51. McKnight, E.T. *Geology and Ore Deposits of the Rico District, Colorado*; Professional Paper 723; U.S. Geological Survey: Reston, VA, USA, 1974; p. 100.
52. Larson, P.B. Stable isotope and fluid inclusion investigations of epithermal vein and porphyry molybdenum mineralization in the Rico Mining District, Colorado. *Econ. Geol.* **1987**, *82*, 2142–2157.
53. Hazen, J.M.; Williams, M.W.; Stover, B.; Wireman, M. Characterization of acid mine drainage using a combination of hydrometric, chemical, and isotopic analysis, Mary Murphy mine, Colorado. *Environ. Geochem. Health* **2002**, *24*, 1–22.
54. Williams, M.W.; Brown, A.D.; Melack, J.M. Biochemical modifications of snowmelt runoff in an alpine basin. In *Hydrological Interactions between Atmosphere, Soil and Vegetation*; Kienitz, G., Milly, P.C.D., van Genuchten, M.T., Rosbjerg, D., Shuttleworth, W.J., Eds.; International Association of Hydrological Sciences: Wallingford, UK, 1991; IAHS-AIHS Publication 204, pp. 457–465.
55. Caine, N. Streamflow patterns in the alpine environment of North Boulder Creek, Colorado Front Range. *Z. Geomorphol.* **1996**, *104*, 27–42.

Quantifying Reaeration Rates in Alpine Streams Using Deliberate Gas Tracer Experiments

Andrew Benson, Matthew Zane, Timothy E. Becker, Ate Visser, Stephanie H. Uriostegui, Elizabeth DeRubeis, Jean E. Moran, Bradley K. Esser and Jordan F. Clark

Abstract: Gas exchange across the air-water interface is a critical process that maintains adequate dissolved oxygen (DO) in the water column to support life. Oxygen reaeration rates can be accurately measured using deliberate gas tracers, like sulfur hexafluoride (SF_6) or xenon (Xe). Two continuous release experiments were conducted in different creeks in the Sierra Nevada of California: Sagehen Creek in September, 2009, using SF_6 and Martis Creek in August, 2012, using both SF_6 and Xe. Measuring gas loss along the creek, which was approximated with the one-dimensional advection-dispersion equation, allows for the estimation of the SF_6 or Xe reaeration coefficient (K_{SF6}, K_{Xe}), which is converted to DO reaeration (K_{DO} or K_2) using Schmidt numbers. Mean K_{SF6} for upper and lower Sagehen and Martis Creeks were, respectively, 34 day^{-1}, 37 day^{-1} and 33 day^{-1}, with corresponding K_{DO}s of 61 day^{-1}, 66 day^{-1} and 47 day^{-1}. In Martis Creek, K_{Xe} was slightly higher (21%) than K_{SF6}, but the calculated K_{DO} from SF_6 agreed with the calculated K_{DO} from Xe within about 15%; this difference may be due to bubble-enhanced gas transfer. Established empirical equations of K_{DO} using stream characteristics did a poor job predicting K_{DO} for both creeks.

Reprinted from *Water*. Cite as: Benson, A.; Zane, M.; Becker, T.E.; Visser, A.; Uriostegui, S.H.; DeRubeis, E.; Moran, J.E.; Esser, B.K.; Clark, J.F. Quantifying Reaeration Rates in Alpine Streams Using Deliberate Gas Tracer Experiments. *Water* **2014**, *6*, 1013-1027.

1. Introduction

Aquatic life requires adequate levels of dissolved oxygen (DO) for survival. Therefore, DO content is a standard monitoring tool to determine the health of fresh water systems. A major consumer of DO in aquatic systems is the microbial degradation of organic matter. A stream's ability to make up this oxygen deficit and return to its solubility equilibrium with the atmosphere is vital. This is accomplished primarily through gas exchange at the air-water interface, where oxygen is either lost or reabsorbed into the stream, due to the concentration gradient between the atmosphere and water. If levels of demand exceed reaeration into the system, a body of water will struggle to support life and may reach hypoxic conditions; in extreme cases, the surface water will become anoxic.

Reaeration coefficients vary widely due to their dependence on turbulence at the air water interface, which is poorly understood and hard to measure. Previous work has related reaeration coefficients to stream characteristics, such as mean depth, current velocity, stream channel slope and discharge (e.g., [1–5]). A number of equations have been postulated, with no one equation appropriate for every channel. The empirical equations also disagree significantly within the same channel. For instance, the equations respond differently to increasing flow: velocity-depth equations predict decreasing reaeration rates, while energy-dissipation models (utilizing channel slope and

velocity) predict increasing rates (e.g., [3]). When applied to wastewater management, an underestimation in the reaeration coefficient would result in overly restrictive regulations. With overestimation, a stream or creek will be less resilient to wastewater discharge than predicted, risking hypoxia and collapse of the aquatic ecosystem.

In addition to DO studies, high quality reaeration coefficients are needed for understanding most biogeochemical cycles within streams and other surface water bodies. Many of the gases involved in these cycles, such as CO_2, N_2O and CH_4, are greenhouse gases. They are also needed for interpreting ^{222}Rn distributions that are commonly used to investigate groundwater-surface water interactions (e.g., [6–8]). For instance, the results of the tracer experiment described here provided an estimate of the loss rate of ^{222}Rn from Martis Creek, which allowed for the quantification of the groundwater influx when combined with ^{222}Rn measurements in the stream and an estimate of the ^{222}Rn concentration in shallow groundwater [8].

Gas tracers can be used to accurately estimate a stream's reaeration coefficient through point-source injection as either a continuous release (as is the case here) or a single pulse that includes a conservative ion, dye or a second gas tracer [9–12]. Tracer concentrations are measured at specific intervals downstream from injection after the experimental reach has been flushed. Tracer loss from the water to the atmosphere can be used as a proxy for gas exchange across the interface, ultimately allowing for a calculation of reaeration rates.

Two trace gases, sulfur hexafluoride (SF_6) and the noble gas, xenon (Xe), were selected for the tracer experiments conducted in two headwater creeks in the Sierra Nevada of California. SF_6 was selected, because it has been used in numerous earlier experiments [9–11,13]. As discussed below, it is a very strong greenhouse gas and is currently regulated in California, so during the second experiment, a second gas tracer was tested to determine if it could be used as an alternative tracer for these experiments. The additional objectives of this study are to compare the reaeration rates between the two creeks and with empirical relationships, as others have done [1–5].

1.1. Study Area

The first experiment used only SF_6 and was conducted in Sagehen Creek, a headwater catchment to the Truckee River about 35 km northwest of Lake Tahoe. The second included both SF_6 and Xe and was conducted in another tributary to the Truckee River, Martis Creek, about 15 km southeast of Sagehen near the town of Truckee, CA, USA (Figure 1a). The Sagehen experiment occurred along an approximately 500-m reach of the creek in 2009, adjacent to the Sagehen Creek Field Station (SCFS). The Martis experiment occurred along an approximately 1000-m reach in 2012 (prior to the implementation of the SF_6 regulations that began 1 January 2013). SCFS is part of the University of California (UC) Natural Reserve system and is managed by UC Berkeley.

Figure 1. (**a**) The study area is located northwest of Lake Tahoe within the Sierra Nevada. Main base map from the United States Geologic Survey (USGS) 10-m National Elevation Dataset [14]. Experimental stream reaches of (**b**) Sagehen and (**c**) Martis Creeks.

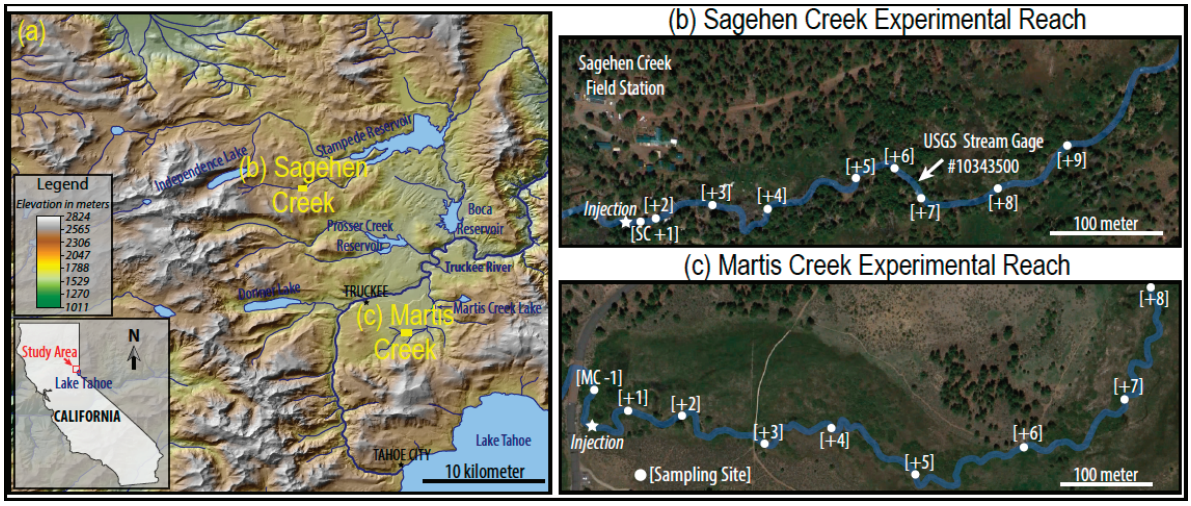

Both creeks are on the eastern side of the Sierra Nevada at elevations above 1800 m and flow through glacial till deposits (derived from andesite and granodiorite basement rocks) to the Truckee River. They are shallow (mean reach depths of *ca*. 10 cm), meandering streams with riffle and pool morphology and receive discharge perennially from shallow aquifers. At the time of the tracer experiments, the mean water temperatures were 8.3 °C (Sagehen) and 15.8 °C (Martis), though diurnal temperature fluctuations were observed. Both watersheds receive more than 80 cm of precipitation per year, most of which falls as snow between October and April. Peak and minimum discharge typically occur, respectively, during the month of May and September (as baseflow).

2. Materials and Methods

2.1. One-Dimensional Advection-Dispersion Equation

To obtain the reaeration coefficients for the gas tracers (SF_6 and Xe), dissolved gas transport was approximated using a one-dimensional (1D) advection-dispersion equation assuming first order decay of a continuously released solute in a river; gas exchange is assumed to be a first order chemical reaction. The 1D transport equation for a pollutant or tracer in a stream is written as (e.g., [11,15,16]):

$$\frac{\partial C}{\partial t} + U\frac{\partial C}{\partial x} = E_x \frac{\partial^2 C}{\partial x^2} - KC \quad (1)$$

Where C is the concentration of the dissolved gas in excess of its solubility equilibrium value (*i.e.*, $C = C_{ob} - C_{eq}$, where C_{ob} and C_{eq} are, respectively, the observed gas concentration and the solubility equilibrium value); t is time; U is the mean stream velocity; x is the distance downstream; E_x is the longitudinal dispersion coefficient; and K is the reaeration coefficient.

The concentration gradient ($\partial C/\partial x$) is small, because the tracer is being continuously released, and thus, the flux due to dispersion is negligible when compared to the flux due to advection (e.g., [15,16]). Once the stream reach has been flushed with tracer, the stream is assumed to be at a

steady state (*i.e.*, $\partial C/\partial t = 0$), and samples can be collected. With these conditions, the advection-dispersion equation can be simplified to:

$$U\frac{dC}{dx} = -KC \tag{2}$$

Solving this differential equation gives the relationship between concentration and sampling distance, x, from injection:

$$C(x) = C_0 \exp\left[(-K/U)x\right] \tag{3}$$

where C_0 is the initial concentration of gas tracer at the injection point ($x = 0$).

Injecting the SF_6 and Xe into the stream introduces a problem when calculating the appropriate initial concentration (C_0), because the injection rate is not known perfectly, especially when injecting by bubbling, as was done during the 2009 Sagehen Creek experiment. C_0 is obtained from the downstream data. Fortunately, C_0 is not needed to determine the reaeration coefficient.

To be useful for other applications and comparisons to earlier works, the reaeration coefficient for the gas tracers must be converted to analogous values for other gases, such as DO, CO_2, Rn and N_2O. This is done using Schmidt numbers (Sc_i, dimensionless ratios of the kinematic viscosity of water and the diffusion coefficient of the gas in question). The reaeration rate of SF_6 (K_{SF6}) or Xe (K_{Xe}) is related to other gases (K_i) by [1,9,17]:

$$K_i = \left(Sc_i / Sc_j\right)^{-0.5} K_j \tag{4}$$

where the Sc_i for each gas is defined at a given temperature usually using temperature relations developed by Wanninkhof *et al.* [18] and Raymond *et al.* [1] and j refers to the gas tracer.

The method used to estimate the reaeration coefficient here is significantly different from most methods reported in the literature, but similar to that used by Cook *et al.* [6]. This work uses a continuous gas tracer source of SF_6 and allows the concentration distribution to come to equilibrium. A more common approach is to use instantaneous point sources of a gas tracer paired with either a solute tracer or a second gas (e.g., [9–12]). The main advantages of using a continuous source are that the solution to the differential equation (1) is much simpler than the solution for a point source, only one gas tracer is needed and fewer samples need to be analyzed. Having a concentration in terms of distance downstream makes it easy to calculate the reaeration coefficient graphically. The slope of the line created when the log of the concentration is plotted *versus* distance is equal to $-K/U$, and the y-intercept is C_0. Most works present reaeration values normalized to a Schmidt number of 600, which is similar to CO_2 at 20 °C in seawater or oxygen at 17.5 °C (K_{DO} or K_2) in freshwater; we will also use this convention.

2.2. Tracer Injection

SF_6 and Xe were utilized as the deliberate gas tracer in these experiments for a number of reasons. SF_6 is: (1) non-reactive; (2) non-toxic [19]; (3) man-made, so the background concentrations are negligible, especially away from urban areas; (4) detectable at very low levels using gas chromatography, so little gas needs to be released; and (5) relatively inexpensive. However, SF_6

emissions are being regulated in California, because it is a strong greenhouse gas (~24,000 times stronger than CO_2 on a per molecule basis over a 100-y period [20]). Therefore, a second gas, Xe, was released during the Martis Creek experiment to evaluate its potential as a deliberate tracer for gas exchange. Xe, being a noble gas, is also non-reactive and non-toxic. The natural atmospheric concentration is low (87 ppt by volume) and well established. Xe can be measured at atmospheric abundance levels using membrane inlet mass spectrometry [21], so little gas needs to be released. While the cost per liter is similar for the two gases, Xe is not a greenhouse gas and, therefore, not regulated.

Different methods were used to inject the gas tracers during the two experiments. During the September 2009, Sagehen experiment, an injection system (Figure 2) was built and placed next to the stream. Approximately a 1:10 SF_6:N_2 mixture was created (so that the concentration would be within the calibration range of the analytical method) and released semi-continuously using a switcher valve set to switch every 30 s and bubble into the stream through a diffusion stone placed at the bottom of a small pool near mid-channel (see [13] for the details of the injection device). Injection began the evening before the collection of the first samples and continued until after the collection of the final set. The injection rate of the SF_6 mixture was 0.34 mL/min for the first three sets and then increased to 0.68 mL/min for the final set.

Based on 100% dissolution of the bubbles and the injection rate, the initial concentrations of SF_6 should have been 4.3×10^6 pmol/L for the Sagehen Creek experiment. Because the gas was being bubbled into the stream, most of it was lost to the atmosphere and only a small amount (less than 0.01%) of it actually dissolved into the stream. In the Martis Creek Experiment, tracer introduction via gas permeable silicon tubing achieved a gas introduction efficiency of 100%.

Figure 2. The diagram of the sulfur hexafluoride (SF_6) injectors used during the Sagehen Creek (top) and Martis Creek (bottom) experiments.

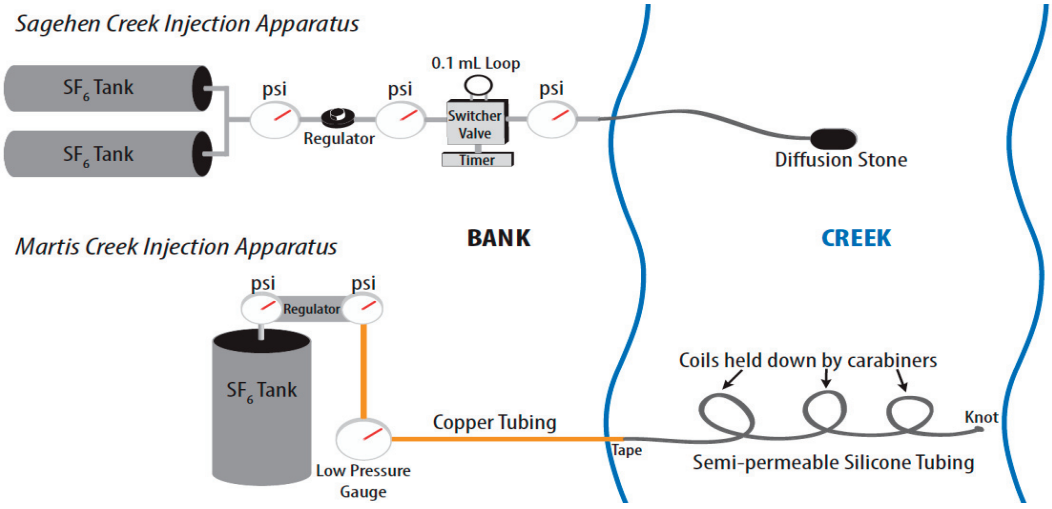

The Martis Creek injection began at 14:15 on 14 August 2012. Injection occurred through 1/8" inner diameter gas permeable silicon tubing fully submerged in the stream (Figure 2) following methods similar to those of Cook *et al.* [6] and Clark [22]. The tubing was coiled and weighted down with carabiners across the creek. The end of the tubing was knotted tightly, so that no large gas bubbles could escape (and none were observed). Copper tubing was attached to the submerged silicon

tubing and fastened to the gas tracer tank on the creek bank. Separate setups of silicone tubing were used for the SF_6 and Xe tracers with 6 m of tubing submerged for SF_6 and 11 m for Xe. The Xe pressure in the silicone tubing was set to about 2 psi using a pressure regulator. A pressure gauge in line with the copper tubing recorded a constant pressure of 15 psi over the course of the 3-day injection in the N_2-SF_6 line. Once again, a 1:10 diluted SF_6 mixture was used during this experiment.

2.3. Creek Sampling

For both SF_6 experiments, eight or nine sampling locations were selected every 15–100 m downstream of the injection apparatus (Figure 1). At each location, five samples were collected in pre-weighed 10 mL Vacutainers™ evenly distributed across the channel 5–10 cm below the air-water interface. The samples were collected by submerging the Vacutainers™, piercing the septa with a needle, until 2–5 mL of stream water were collected. During the Sagehen experiment, samples were collected during the morning, afternoon and evening of 11 September 2009. A fourth set was collected the following morning on 12 September 2009, after the injection rate was changed.

The Xe samples were collected at the same locations as the SF_6 samples during the Martis Creek experiment. Duplicate samples were collected from the center of the stream by submersing an empty 40-mL glass vial upside down and filling it at 5–10 cm below the surface. The vial was capped under water. At two downstream locations (Martis Creek (MC) + 1 and MC + 8), additional cross-section samples were collected (in duplicate) at the left and right bank and in between the banks and the center.

During the Martis Creek experiment, sampling began about 1 h after the injection started. It was interrupted by a 2-h rain event that dropped considerable water onto the field site. While this precipitation event may have changed the creek flow, stream gauging shows that the discharge was the same on Days 2 and 3, so if any changes occurred, they were short lived. The first full set was collected 18 h after injection, with six complete sets collected over the next three days. Four sets were collected on 15 August 2012 (morning, afternoon with duplicates and evening), and one set each was collected during the mornings of 16 August 2012, and 17 August 2012. Xe samples were collected on the morning of 17 August 2012. Background sampling occurred at one location upstream of the injector in Martis Creek. This paper will discuss only the 17 August 2012, data, when both gases were analyzed.

2.4. Creek Measurements

To quantify channel geometry in Sagehen Creek, stream transect data were collected at 27 locations along the creek starting approximately 41 m upstream of the injection point and continuing approximately 550 m downstream. At each transect, the stream width and the depth every 20 cm (from the north bank to the south bank) were measured. In addition, the grain size of the streambed was descriptively characterized at each depth determination (for details, see [23]). A United States Geological Survey (USGS) river gauging station located about 370 m downstream from the injection point provided continuous 15-min discharge data, which showed little variation and averaged 43 L/s during the experiment. The gauge also represents the place where the mean channel geometry changes. In the upper reach, the average measured depth, cross-sectional area and

flow velocity were, respectively, 0.11 m, 0.41 m^2 and 0.11 m/s, while below the gauge, they were, respectively, 0.15 m, 0.49 m^2 and 0.09 m/s.

The flow velocity in Martis Creek was determined by gauging with an FP111 Global Water™ flow probe at four stations (MC − 1, MC + 2, MC + 5, and MC + 8). Cross-sectional data were also measured at these stations. The average depth, cross-sectional area, flow velocity and discharge were, respectively, 0.11 m, 0.20 m^2, 0.29 m/s and 57 L/s. Flow velocity varied from a low average of 0.14 m/s at MC + 2 to a high average of 0.65 m/s at MC + 5; the average velocity at a given cross-sectional location did not vary significantly over the course of the experiment.

The channel gradient in Sagehen Creek was measured using a combination of GPS coordinates and a 1-m digital elevation model (DEM) provided by the Sagehen Creek Field Station that was created from aerial LiDAR flown in September 2005. The gradient was then calculated by dividing the measured center channel length by the difference in elevation based on the DEM and was found to be 0.0143; there was little change in slope between the upper and lower reaches. The channel slope for Martis Creek was determined in a similar fashion, but using Google Earth rather than ArcGIS and LiDAR elevations. It was determined to be 0.0145, very similar to Sagehen Creek, and it also did not vary substantially along the creek.

At Martis Creek, two deep pools along the experimental reach were sampled at three depths (top, middle and bottom) to assess vertical mixing. Little stratification was suspected, due to the stream's generally shallow depth. One pool was ~3 m downstream of MC + 4 with a maximum depth of 0.56 m; the other was ~1 m upstream of MC + 7 with a maximum depth of 0.66 m. Temperature and oxygen measurements were also made using a YSI™ 556 multi-meter (Yellow Springs, OH, USA) and averaged 16.3 °C and 15.4 °C for the two pools. This temperature difference was likely due to the typical diurnal fluctuation found in most shallow creeks rather than an indication of the groundwater discharge of cooler water.

2.5. Laboratory Analysis

SF_6 samples were processed using the modified headspace method of Clark *et al.* [24], which employs Vacutainers™. In order to minimize contamination, the containers were kept separate from the injection equipment, during the transport to, from and while at the field sites. The laboratory procedure was as follows: (1) each sample was weighed in order to calculate the volume of water collected; (2) the headspace of each vial was filled with ultra-high purity N_2 to atmospheric pressure in the lab (about 1 atm); (3) vials were agitated by gently shaking in order to allow the gasses in the headspace to become well-mixed; and (4) gases in the headspace were then fed into a gas chromatograph system via displacement with water. SF_6 standards of known concentrations (1.95 parts per billion by volume (ppbv) and 10.0 ppbv) purchased from and certified by Scott-Marrin, Inc. Riverside, CA, USA) were run every ~10 samples to ensure accurate instrument calibration. Ultra-high purity nitrogen was used to flush the system of residual SF_6 between runs. The analytical uncertainty of the Vacutainer™ method is typically better than ±5%.

Xe samples were analyzed three days after collection on 20 August 2012, using a noble gas membrane inlet mass spectrometer (NG-MIMS) [21]. The NG-MIMS system consists of a membrane inlet, a dry ice water trap, a liquid nitrogen carbon-dioxide trap, two getters, a gate valve, a turbomolecular pump and a quadrupole mass spectrometer equipped with an electron multiplier. Vials were opened, and the sample was withdrawn from the bottom of the vial through the membrane inlet for 5 min at 0.5 mL/min. The last two minutes of measurements were averaged to reduce measurement noise. Dissolved Xe concentrations are determined from measurements made every 10 seconds at mass over charge ratios of 124 and 132, by comparing against air equilibrated water (AEW) standards, with a laboratory determined uncertainty of ±8%. The linearity of the NG-MIMS was demonstrated across a wide range of noble gas concentrations [21].

3. Results and Discussion

As expected, average SF_6 and Xe concentrations at each sampling site decreased downstream (Table 1, Figures 3 and 4). The standard deviation is used as a measure of horizontal mixing. When the deviation of bank-to-bank concentrations at each sampling location stabilizes, the tracer is assumed to be well-mixed across the creek. For all sets collected during the Sagehen Creek experiment, the standard deviation of the first sample location (SC + 1) ranges from 20% to 28% of the cross-sectional mean, while, with a few exceptions, the standard deviation for the rest of the samples is generally less than 5% of the mean, equivalent to analytical uncertainty. The first sample location is close to the injector (15 m downstream), and SF_6 had yet to become well mixed across the stream. By the second sampling location (44 m downstream), it had. The first samples were collected further downstream during the Martis Creek Experiment (69 m *vs*. 15 m) and showed a lower standard deviation (<15%) across the creek. The standard deviation of Xe concentrations in the first (MC + 1) and last (MC + 8) cross-sections was 14% and 10%, respectively. The duplicate reproducibility was 9% for the Xe samples.

In Sagehen Creek, at the location immediately upstream (SC + 6) and downstream (SC + 7) of the USGS stream gauge (about 370 m downstream injector), the drop in concentrations of SF_6 is quite large over a very short distance. This drop indicates a higher reaeration rate, due to the waterfall created by the gauge, as is commonly observed at spillways [25].

Furthermore, in the large pool immediately upstream of the gauge, the concentration suddenly increased for samples from Sets 1–3. After further inspection, the increases in concentration were coincident with a method change that required the use of different standards. It is important to note that after the offset in standards was found, the fourth set was analyzed using the same method (high standard) from the top to the bottom of the reach. In this paper, only the fourth set is discussed.

Table 1. Average tracer concentrations and standard deviations (SD) at each cross-section during the 12 September 2009, Sagehen Creek (SC) and 17 August 2012, Martis Creek (MC) experiments.

Station	Distance (m)	[SF_6] (pmol/L)	SD (%)	Station	Distance (m)	[SF_6] (pmol/L)	SD (%)	[Xe] (nmol/L)	SD (%)
SC + 1	16	118	27	MC − 1		0	0.0	0.46	-
SC + 2	44	74.9	7.8	MC + 1	69	315	20	43.5	14
SC + 3	114	55.9	2.8	MC + 2	139	325	2	40.2	-
SC + 4	180	42.0	4.3	MC + 3	257	270	3	34.1	-
SC + 5	294	27.1	2.8	MC + 4	352	244	2	29.9	-
SC + 6	364	23.9	5.5	MC + 5	481	203	2	24.4	-
SC + 7	372	20.5	4.9	MC + 6	641	169	2	19.9	-
SC + 8	445	13.5	5.6	MC + 7	798	125	3	13.5	-
SC + 9	507	10.5	2.4	MC + 8	964	111	3	10.8	10

The semi-log plot of the concentration for Sagehen Creek shows that the slope ($-K/U$) for the lower reach is generally steeper than that of the upper reach (Figure 3). In fact, it is about 22% larger. Detailed analysis of the channel geometry, as noted above, revealed that the mean depth of the lower portion (0.15 m) was about 35% larger than the upper section (0.11 m).

Figure 3. Semi-log plot of SF_6 concentrations with least squares fit trend lines showing the different slopes (−K/U) for the upper and lower reaches in Sagehen Creek (red squares from 12 September 2009) and for Martis Creek (blue circles from 17 August 2012). In the equations, "x" is the distance downstream.

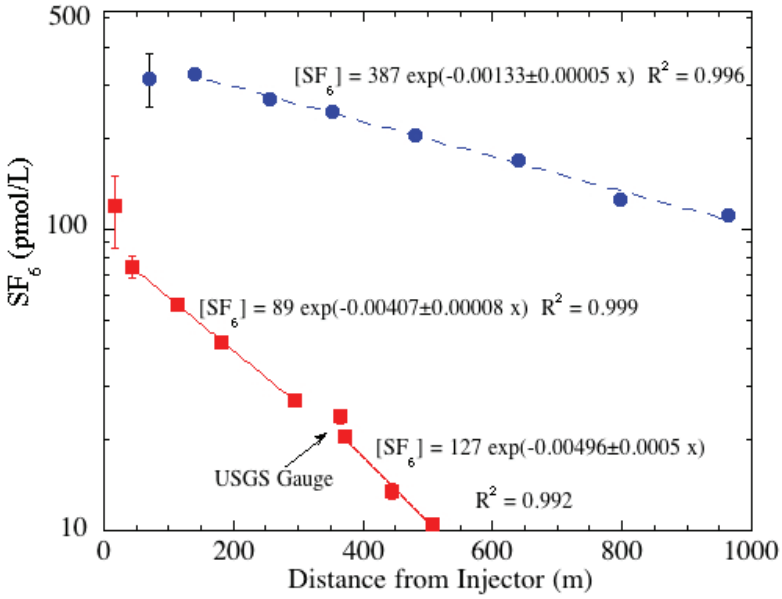

In Martis Creek, relatively more tracer degassing occurred per meter between stations MC + 6 and MC + 7 than elsewhere along the creek. A few locations of riffles with white water that accelerate gas transfer across the air-water interface were noted between these stations. A comparison of SF_6 and Xe tracers show more similarities than differences (Figure 4). Both gases show reaeration, with

SF_6 degassing at a faster rate. This is most apparent when examining the reaeration coefficient normalized for DO (Table 2).

Reaeration rates are calculated from the semi-log plot of gas concentration *versus* sampling distance (Figures 3 and 4). The slope of the exponential best-fit equals $-K/U$, where K is the reaeration rate and U is mean velocity. Table 2 presents mean stream characteristics and reaeration rates by sampling date and location.

Figure 4. Semi-log plot of SF_6 (filled blue circles) and Xe (open red squares) concentrations with trend lines for the Martis Creek 17 August 2012, sampling event. The station closest to the injector was not used for the least squares fit and that only center samples were used for calculating the Xe distribution. In the equations, "x" is the distance downstream.

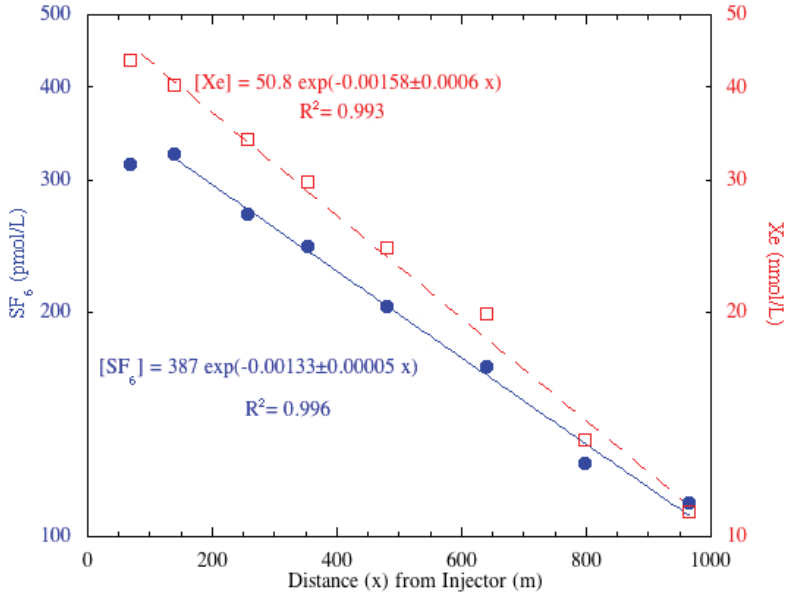

Table 2. Reaeration (K) values for the gas tracers ($K_{SF6\ or\ Xe}$) and normalized to dissolved oxygen (DO) (K_{DO}) using temperature-dependent Schmidt numbers of 1875 and 1192 for SF_6 (Sagehen and Martis Creek), 1230 for Xe (Martis Creek) and 600 for DO (Sagehen and Martis Creek) and Equation (4).

Location	Sampling Date	Tracer	Discharge (L/s)	Velocity U (m/s)	Depth (m)	$-K/U$ (m^{-1})	$K_{SF6\ or\ Xe}$ (day^{-1})	K_{DO} (day^{-1})
Sagehen-Upper	12 September 2009	SF_6	43	0.11	0.11	0.00407	34	61
Sagehen-Lower	12 September 2009	SF_6	43	0.09	0.15	0.00496	37	66
Martis Creek	17 August 2012	SF_6	57	0.29	0.11	0.00133	33	47
Martis Creek	17 August 2012	Xe	57	0.29	0.11	0.00156	40	57

For comparison, K_{DO} values for Sagehen and Martis Creeks were calculated using empirical relationships for the experimental reaches (Table 3, Figure 5). Predictive equations show a very wide range of values for K_{DO} (6 to142 day^{-1}) with a mean of 43 ± 34 day^{-1} for Sagehen Creek and (22 to 544 day^{-1}) with a mean of 117 ± 131 day^{-1} for Martis Creek. In both creeks, the Thyssen-Jeppesen [26]

relationship appears to be an outlier. Removing that relationship from the data set reduces the range and mean to 6–74 day^{-1} (35 ± 20 day^{-1}) and 22–147 day^{-1} (84 ± 48 day^{-1}), respectively, for Sagehen and Martis Creeks.

Table 3. Predictive equations for reaeration (K_{DO}) compiled by Raymond *et al.* [1] and Cox [4]. See these publications for the citations to the original papers. Please note: Raymond *et al.* [1] models calculate gas transfer velocities (m day^{-1}) rather than reaeration coefficients, so the equations listed have been converted, and only the equations that matched their metadata set with a $R^2 > 0.7$ are presented.

Reference	Predictive Equation	Sagehen Creek K_{DO} (day^{-1})	Martis Creek K_{DO} (day^{-1})
[27]	$K_{DO} = 3.93U^{0.5} H^{-1.5}$	28	58
[28]	$K_{DO} = 5.026UH^{-1.67}$	16	59
[29]	$K_{DO} = 5.35UV^{0.67} H^{-1.85}$	54	139
[30]	$K_{DO} = 5.5773U^{0.607} H^{-1.689}$	47	109
[31]	$K_{DO} = 3170\ S$	45	46
[32]	$K_{DO} = 22{,}700\ SU$	32	95
[33]	$K_{DO} = 8784S^{0.93}U^{0.734}H^{-0.42}$	74	147
[34]	$K_{DO} = 596(SU)^{0.528}Q^{-0.136}$	12	22
[35]	$K_{DO} = 23.04(1 + 0.17\ F^2)(US^{0.375})H^{-1}(1.0212)^{(T-20)}$	16	27
[36]	$K_{DO} = 23{,}000(1 + 0.17\ F)^{2.66}S^{1.13}H^{-0.6}$	142	544
[1] #1	$K_{DO} = 5037\ (SU)^{0.89}D^{-0.46}$	34	107
[1] #2	$K_{DO} = 5937\ (1-2.54\ F)(SU)^{0.89}D^{-0.42}$	37	92
[1] #7	$K_{DO} = 4725(SU)^{0.86}Q^{-0.14}\ D^{-0.34}$	48	135
	Mean and Standard Deviation *	43 ± 34	117 ± 131
SF_6 tracer		61, 66 †	47
Xe tracer			57

Notes: velocity (U, *m/s*); mean depth (H, *m*); stream gradient (S, *m/m*); Froude number (F); Temperature (T); * by removing Thyssen-Jeppesen [36], the mean and standard deviation become 35 ± 20 and 84 ± 48 for Sagehen and Martis Creeks; † for upper and lower Sagehen Creek.

Despite the fact that most predictive equations produced wildly differing reaeration rates, underestimation is better than overestimation when considering wastewater discharge to streams. Over predictions could lead to assumptions of a higher level of resiliency and less stringent and potentially dangerous management strategies. Under-predictions, on the other hand, would lead to overly precautious management, which, while inaccurate, would not threaten stream health.

Figure 5. A comparison of the field K_{DO} (filled circles) listed in Table 2 with the model predicted K_{DO} (open circles) listed in Table 3, with the exception that the Thyssen-Jeppesen [36] model values are not shown or used in the calculation of median or quartile values.

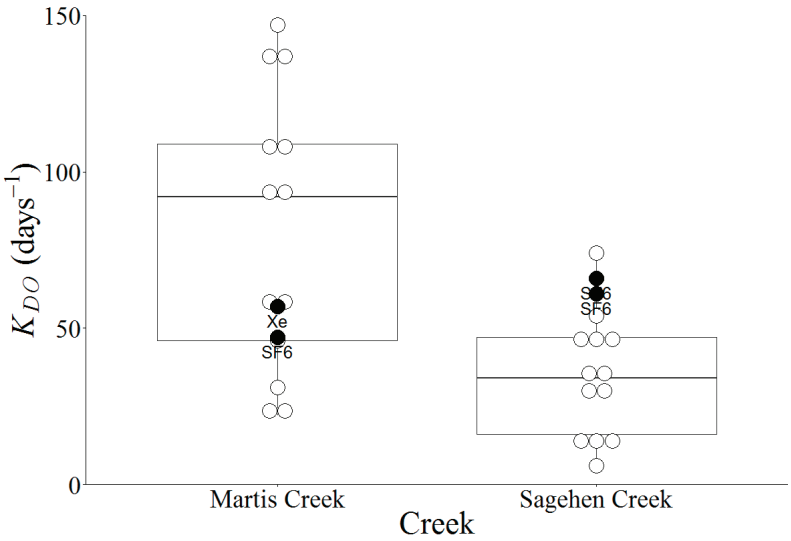

4. Implications and Conclusions

Sagehen and Martis Creeks are very similar in terms of their morphology (both have pool and riffle characteristics and similar channel slopes) and hydrology (with much of the late summer flow derived from groundwater discharge and a similar mean depth at the time of the experiments). As shown in Table 2, the discharge and current velocity in Martis Creek were higher (respectively, 57 *vs.* 43 L/s and 0.3 *vs.* 0.1 m/s). The SF_6 tracer experiments revealed that the reaeration coefficients corrected to a Schmidt number of 600 (K_{DO}) differed substantially, with Sagehen Creek (>60 day^{-1}) being larger than Martis (<50 day^{-1}). Interestingly, the results of the Xe tracer experiment (57 day^{-1}) agree better with the SF_6 result from Sagehen Creek (61–66 day^{-1}) than from Martis Creek (47 day^{-1}). This difference between the SF_6 and Xe results could be due to the bubble-enhanced gas transfer [26] that generally removes lower solubility gases faster (SF_6 is less soluble than Xe).

Most empirical formulas of reaeration rates, expressed as K_{DO}, rely on an assessment of the current velocity. The actual reaeration rate over a stretch of river or stream is directly observed as a change in tracer concentration. Established empirical formulas of K_{DO} using stream characteristics did a poor job of predicting K_{DO} for the two creeks. Although some agree with the field experiments in either Sagehen or Martis Creek, no one relationship worked well for both of them.

Dissolved oxygen is one of the most important indicators of a stream's biologic potential and health. The United States Environmental Protection Agency's criteria for dissolved oxygen are designed to protect freshwater aquatic life under "worst case conditions"; the suggested DO limit expressed as a seven-day mean minimum for cold water is 4.0 mg/L [37]. In this study, DO concentrations in Martis Creek ranged between 5 mg/L and 9 mg/L throughout the summer. Considering that minimum criteria estimations are conservative, DO content in this stream reach is sometimes close to threatening levels. This exemplifies the need for accurate measurements of

reaeration to ensure a healthy aquatic environment. Future expansion of development in the Tahoe and Truckee areas could also increase biological oxygen demand on the creek and lead to noncompliance.

With mounting concerns and subsequent regulations of greenhouse gasses, the future of SF_6 as a hydrologic tracer is in doubt. Noble gasses, such as helium and Xe, are on their way to replacing SF_6, and we demonstrate that Xe is a viable replacement option for reaeration studies, as shown by others [12]. Future SF_6 use may depend on more efficient injection methods. Traditional bubbling results in an immediate loss of most of the gas to the atmosphere, requiring more SF_6 for water tagging. The semi-permeable silicon tubing, used in the Martis Creek study, is very promising in this regard and results in very high injection efficiency.

Acknowledgments

We would like to thank Tom Gleeson (McGill University) and Andrew Manning (USGS, Denver, CO, USA) for their help with collecting samples and measuring stream transects. We are grateful to Sagehen Creek Field Station; especially, station manager Jeff Brown, for technical and logistical assistance. Gina Lee helped with some concepts and GIS. We are also grateful for the time and effort of the two anonymous reviewers. Their comments helped to improve the paper substantially. Financial support for this project was provided by the California Energy Commission Public Interest Energy Research (PIER) Project PIR-08-010, the WateReuse Research Foundation project WRF 09-11, the State of California Groundwater Ambient Monitoring & Assessment (GAMA) Special Studies Program, and the Lawrence Livermore National Laboratory Lawrence (LLNL) Scholar Program. Parts of this project were performed by LLNL under Contract DE-AC52-07NA27344.

Conflicts of Interest

The authors declare no conflict of interest.

References

1. Raymond, P.A.; Zappa, C.J.; Butman, D.; Bott, T.L.; Potter, J.; Mulholland, P.; Laursen, A.E.; McDowell, W.H.; Newbold, D. Scaling the gas transfer velocity and hydraulic geometry in streams and small rivers. *Limnol. Oceanogr. Fluids Environ.* **2012**, *2*, 41–53.
2. Moog, D.B.; Jirka, G.H. Analysis of Reaeration Equations Using Mean Multiplicative Error. In: *Air-Water Gas Transfer*; Jähne, B., Monahan, E.C., Eds.; AEON Verlag & Studio: Hanau, Germany, 1995; pp. 101–111.
3. St. John, J.P.; Gallagher, T.W.; Paquin, P.R. The Sensitivity of the Dissolved Oxygen Balance to Predictive Reaeration Equations. In *Gas Transfer at Water Surfaces*; Brutsaert, W., Jirka, G.H., Eds.; D. Reidel Publishing Company: Dordrect, The Netherland, 1984; pp. 577–588.
4. Cox, B.A. A review of dissolved oxygen modelling techniques for lowland rivers. *Sci. Total Environ.* **2003**, *314*, 303–334.

5. Haider, H.; Ali, W.; Haydar, S. Evaluation of various relationships of reaeration rate coefficient for modeling dissolved oxygen in a river with extreme flow variations in Pakistan. *Hydrol. Process.* **2013**, *27*, 3949–3963.
6. Cook, P.G.; Lamontagne, S.; Berhane, D.; Clark, J.F. Quantifying groundwater discharge to Cockburn River, southeastern Australia, using dissolved gas tracers ^{222}Rn and SF_6. *Water Resour. Res.* **2006**, *42*, 12.
7. Cartwright, I.; Hofmann, H.; Sirianos, M.A.; Weaver, T.R.; Simmons, C.T. Geochemical and ^{222}Rn constraints on baseflow to the Murray River, Australia, and timescales for the decay of low-salinity groundwater lenses. *J. Hydrol.* **2011**, *405*, 333–343.
8. DeRubeis, E.A. Radon as a Tracer of Groundwater-Surface Water Interaction in Martis Valley. Master's Thesis, California State University, East Bay, CA, USA, 4 October 2013.
9. Wanninkhof, R.; Mulholland, P.J.; Elwood, J.W. Gas exchange rates for a first-order stream determined with deliberate and natural tracers. *Water Resour. Res.* **1990**, *26*, 1621–1630.
10. Clark, J.F.; Wanninkhof, R.; Schlosser, P.; Simpson, H.J. Gas-exchange rates in the tidal Hudson River using a dual tracer technique. *Tellus Ser. B Chem. Phys. Meteorol.* **1994**, *46*, 274–285.
11. Hibbs, D.E.; Parkhill, K.L.; Gulliver, J.S. Sulfur hexafluoride gas tracer studies in streams. *J. Environ. Eng. Asce* **1998**, *124*, 752–760.
12. Reid, S.E.; Mackinnon, P.A.; Elliot, T. Direct measurements of reaeration rates using noble gas tracers in the River Lagan, Northern Ireland. *Water Environ. J.* **2007**, *21*, 182–191.
13. Clark, J.F.; Hudson, G.B.; Avisar, D. Gas transport below artificial recharge ponds: Insights from dissolved noble gases and a dual gas (SF_6 and ^3He) tracer experiment. *Environ. Sci. Technol.* **2005**, *39*, 3939–3945.
14. Gesch, D.B. The National Elevation Dataset. In *Digital Elevation Model Technologies and Applications: The DEM Users Manual*, 2nd ed.; Maune, D., Ed.; American Society for Photogrammetry and Remote Sensing: Bethesda, MD, USA, 2007; pp. 99–118.
15. Rutherford, J.C. *River Mixing*; Wiley: New York, NY, USA, 1994; p. 347.
16. Thomann, R.V.; Mueller, J.A. *Principles of Surface Water Qality Modeling and Control*; Harper & Row: New York City, NY, USA, 1987; p. 644.
17. Jähne, B.; Heinz, G.; Dietrich, W. Measurement of the diffusion coefficients of sparingly soluble gases in water. *J. Geophys. Res. Oceans* **1987**, *92*, 10767–10776.
18. Wanninkhof, R. Relationship between wind-speed and gas-exchange over the ocean. *J. Geophys. Res. Oceans* **1992**, *97*, 7373–7382.
19. Lester, D.; Greenberg, L.A. The toxicity of sulfur hexafluoride. *Arch. Ind. Hyg. Occup. Med.* **1950**, *2*, 348–349.
20. Houghton, J.T.; Filho, L.G.M.; Bruce, J.P.; Lee, H.; Callander, B.A.; Haites, E.F.; Harris, N.; Maskell, K. *Climate Change 1994: Radiative Forcing of Climate Change and an Evaluation of the IPCC 1992 IS92 Emission Scenarios*; Cambridge University Press: Cambridge, UK, 1995; p. 339.
21. Visser, A.; Singleton, M.J.; Hillegonds, D.J.; Velsko, C.A.; Moran, J.E.; Esser, B.K. A membrane inlet mass spectrometry system for noble gases at natural abundances in gas and water samples. *Rapid Commun. Mass Spectrom.* **2013**, *27*, 2472–2482.

22. Clark, J.F. Defining Transport near ASR Operations Using Sulfur Hexafluoride Gas Tracer Experiments. In *Management of Aquifer Recharge for Sustainability (4th International Symposium on Artificial Recharge of Groundwater)*; Dillon, P.J., Ed.; A.A. Balkema Publishers: Exton, PA, USA, 2002; pp. 257–260.
23. Zane, M. Reaeration of Sagehen Creek near Truckee, CA. Bachelor's Thesis, University of California, Santa Barbara, CA, USA, 11 June 2010.
24. Clark, J.F.; Hudson, G.B.; Davisson, M.L.; Woodside, G.; Herndon, R. Geochemical imaging of flow near an artificial recharge facility, Orange County, California. *Ground Water* **2004**, *42*, 167–174.
25. Rindels, A.J.; Gulliver, J.S. Oxygen Transfer at Spillways. In Proceedings of the Second International Symposium on Gas Transfer at Water Surfaces, Minneapolis, MN, USA, 11–14 September 1990; American Society of Civil Engineers: New York, NY, USA, 2001; pp. 524–533.
26. Ho, D.T.; Asher, W.E.; Bliven, L.F.; Schlosser, P.; Gordan, E.L. On mechanisms of rain-induced air-water gas exchange. *J. Geophys. Res. Oceans* **2000**, *105*, 24045–24057.
27. O'Conner, D.J.; Dobbins, W.E. Mechanisms of reaeration in natural streams. *Trans. Am. Soc. Civil Eng*. **1956**, *123*, 641–667.
28. Churchill, M.A.; Elmore, H.L.; Buckingham, R.A. Prediction os stream reaeration rates. *Int. J. Air Water Pollut.* **1962**, *6*, 467–504.
29. Owens, M.; Edwards, R.; Gibbs, J. Some reaeration studies in streams. *Int. J. Air Water Pollut.* **1964**, *8*, 469–486.
30. Bennett, J.P.; Rathburn, R.E. *Rearation in Open-Channel Flow*, *USGS Professional Paper: No. 737*; United States Geological Survey: Washington, DC, USA, 1972.
31. Tsiovoglou, E.C.; Neal, L.A. Tracer measurements of reaeration: III—Prediciting the reaeration capacity of inland streams. *J. Water Pollut. Control. Fed.* **1976**, *48*, 2669–2689.
32. Grant, R.S. *Reaeration-Coefficient Measurement of 10 Small Streams in Wisconsin Using Radioactive Tracers with a Section of the Energy Dissipation Model*; U.S. Geological Survey Water-Resources Investigations 76–96; United States Geological Survey: Madison, WI, USA, 1976.
33. Thyssen, N.; Erlandsen, M.; Jeppesen, E.; Ursin, C. Reaeration of oxygen in shallow, macrophyte ricj streams: I—Determination of the reaeration rate coefficient. *Int. Revue Ges. Hydrobiol.* **1987**, *72*, 405–429.
34. Melching, C.S.; Flores, H.E. Reaeration equations derived from US Geological Survey database. *J. Envirn. Eng.* **1999**, *125*, 407–414.
35. Parkhurst, J.D.; Pomeroy, R.D. Oxygen absorption of streams—State of the art. *J. Sanit. Eng. Div. ASCE* **1972**, *98*, 101–124.
36. Thyssen, N.; Jeppesen, E. Reaeration in small water courses. *Vatten* **1980**, *36*, 231–248.
37. US Environmental Protection Agency. *Quality Criteria for Water 1986: The Gold Book*; US Environmental Protection Agency: Washington, DC, USA, 1987; p. 477.

Investigation of Groundwater Flow Variations near a Recharge Pond with Repeat Deliberate Tracer Experiments

Jordan F Clark, Sheila Morrissey, Jason Dadakis, Adam Hutchinson and Roy Herndon

Abstract: Determining hydraulic connections and travel times between recharge facilities and production wells has become increasingly important for permitting and operating managed aquifer recharge (MAR) sites, a water supply strategy that transfers surface water into aquifers for storage and later extraction. This knowledge is critical for examining water quality changes and assessing the potential for future contamination. Deliberate tracer experiments are the best method for determining travel times and identifying preferential flow paths between recharge sites over the time scales of weeks to a few years. This paper compares the results of two deliberate tracer experiments at Kraemer Basin, Orange County, CA, USA. Results from the first experiment, which was conducted in October 1998, showed that a region of highly transmissive sedimentary material extends down gradient from the basin for more than 3 km [1]. Mean groundwater velocities were determined to be approximately 2 km/year in this region based on the arrival time of the tracer center of mass. A second experiment was initiated in January 2008 to determine if travel times from this basin to monitoring and production wells changed during the past decade in response to new recharge conditions. Results indicate that flow near Kraemer Basin was stable, and travel times to most wells determined during both experiments agree within the experimental uncertainty.

Reprinted from *Water*. Cite as: Clark, J.F.; Morrissey, S.; Dadakis, J.; Hutchinson, A.; Herndon, R. Investigation of Groundwater Flow Variations near a Recharge Pond with Repeat Deliberate Tracer Experiments. *Water* **2014**, *6*, 1826-1839.

1. Introduction

Groundwater has been a primary source of potable and irrigation water for centuries. During the last 50 years, the soaring demand for freshwater has placed unprecedented stresses upon many aquifers throughout the world; many aquifers are now in overdraft. The projected growth in population combined with uncertainties associated with a changing climate will only aggravate this problem. A cost-effective advancement in groundwater/surface water management aimed at augmenting local water supplies is managed aquifer recharge (MAR), the practice of artificially recharging imported surface water, reclaimed (recycled) wastewater, or storm runoff into aquifers for storage and later extraction [2–4].

For a MAR operation to be successful, a few challenges must be overcome. First, a source of recharge water must be found. Second, facilities, which can rapidly transfer water into aquifers, must be engineered. These include injection wells and spreading basins (recharge ponds), with both requiring periodic removal of accumulated clogging material to maintain recharge rates. Third, because the available water for the recharge operation can be of lesser quality than the local groundwater supply, there is the potential to degrade the existing aquifer. The introduction of salts, pathogens, disinfection by-products, and trace organic compounds such as pharmaceuticals, is a

concern, especially when urban runoff or reclaimed wastewater is a large component of the source water for the operation [4]. Lesser quality sources can become a larger portion of the recharge water at MAR operations because the availability of higher quality water such as imported water from remote watersheds is limited and may shrink due to shifts in climate and the diversion of this water to other uses such as maintaining riparian ecosystems (*i.e.*, loss of California State Water Project supplies to the delta smelt). Even in cases where the recharge water may be of a higher quality, it may have a different geochemical character (e.g., redox state) than the ambient groundwater and the potential exists for mobilization of intrinsic constituents, such as arsenic. For these reasons, it is vital to understand the fate and transport of potential contaminants near MAR sites. Only from this understanding can cost effective and appropriate regulations be developed.

Recent water quality studies near MAR operations have shown that many potential contaminants such as dissolved organic carbon (DOC), nitrate, some pharmaceuticals, and most pathogens are naturally removed or become inactive with time and distance in the subsurface (e.g., [4–9]). These water quality improvements, known as soil-aquifer treatment (SAT), are considered one of the benefits of MAR [3,4] and are generally observed soon after recharge, near the facility.

Despite these studies, water quality concerns still remain the focus of many regulations and an obstacle for the permitting of new MAR operations that include a reuse component (*i.e.*, reclaimed wastewater). For instance, MAR operations in California, USA, must conform to the state Drinking Water Program's Groundwater Recharge Reuse Regulations, which require a subsurface retention time prior to its extraction for a potable supply that varies based on the level of pre-recharge treatment, in addition to a number of source water controls and how the travel times is being assessed [10]. The required retention time varies from two to six months and must be verified using a tracer study.

1.1. Travel Time Estimates

Development of field methodologies to evaluate flow near MAR facilities is critical for the effective management of these operations where water quality assessment is warranted. The California Drinking Water Program's Groundwater Recharge Reuse Regulations place a greater level of confidence on tracer data than on numerical models or Darcy flow calculations (see Table 2 in reference [10]). Geochemical techniques provide a fundamental approach for investigating travel times, flow paths, recharge rates, and dispersivity in groundwater. Intrinsic environmental tracers such as Tritium/^{3}He (T/^{3}He) dating (e.g., [11,12]) are ideal for examining flow over spatial scales of kilometers and temporal scales of years to decades near MAR operations [1,13,14]. Other environmental tracer dating techniques such as chlorofluorocarbons (CFCs) or sulfur hexafluoride (SF_6) are likely to be unreliable near MAR operations because non-atmospheric sources of these tracers may complicate the interpretation of apparent ages, especially when chlorinated reclaimed or potable water is being recharged (e.g., [15–17]).

Because of the typical uncertainty associated with geochemical dating techniques (generally no better than ±2 years), these methods are not well suited for examining short-term transport specified by the Recharge Reuse Regulations in the state of California [14]. Deliberate (*i.e.*, injected or applied) tracer experiments using gases such as SF_6 or noble gases (*i.e.*, He or Xe isotopes) have become acceptable methods for evaluating transport from recharge locations to wells over periods of weeks

to a few years [1,10,18,19]. There is a long history of using SF_6 as a deliberate tracer starting with atmospheric experiments and expanding into aqueous systems initially by the gas exchange and oceanographic communities [20–23]. SF_6 can also be used as an intrinsic or environmental tracer for dating water in a similar fashion as CFCs [17].

The scale of deliberate tracer experiments is defined by the quantity of water that can be "tagged" and the signal to noise ratio of the tracer being used. The three factors that often limit an experiment's scale are: (1) identification of a tracer that does not adversely impact potable aquifers; (2) the cost of tracer; and (3) the ability to introduce a sufficient amount of tracer without significantly changing the buoyancy (or density) of the tagged water. The cost of the tracer can be a particular problem when large volumes of water ($>10^5$ m^3 or >80 AF) need to be tagged, as is often the case near MAR operations. As shown by the oceanographic community (e.g., [20]), SF_6 can be used economically to tag large volumes of water.

There are cost advantages of using SF_6 over noble gas isotopes in terms of analysis; more SF_6 samples can be analyzed over a given period of time on less expensive equipment. However, it is a strong greenhouse gas and its emission is regulated in California. SF_6 is a synthetic gas used primarily in the electrical industry as a gas insulator and has been used as a tracer in the atmosphere and natural waters for more than two decades. It is an ideal tracer for the following reasons: (1) SF_6 is nontoxic [24] and permission has been granted to use it as a tracer in potable aquifers in the southwestern USA and South Australia; (2) background concentrations of SF_6 in natural waters are extremely low (<0.05 pmol/L; 1 pmol = 10^{-12} mole) because of its low solubility and low atmospheric mixing ratio (*ca*. 8 pptv in 2014); (3) it can be measured precisely in water (±5% or better) over a concentration range of eight orders of magnitude (0.01 fmol/L to 1 nmol/L) using a gas chromatograph equipped with an electron capture detector [25]; and (4) laboratory scale experiments have shown that breakthrough curves of SF_6 and bromide are identical in saturated porous media which contains either high contents of organic material or clays, demonstrating that SF_6 is not retarded (has a retardation factor of 1.0) [26,27].

SF_6 differs from ionic and dye tracers in that it is a gas and is easily lost from solution across the air—water interface to the atmosphere. It has often been used as a tracer for reaeration in surface water [21–23,28]. Thus, it is important to monitor the SF_6 concentrations in the recharge water to determine the amount of tracer lost due to gas exchange. This is especially true if the artificial recharge is taking place in a shallow river or spreading pond. Insufficient monitoring of the spatial variability of the tracer concentrations in the "spiked" surface water can lead to erroneous interpretations of travel times. Furthermore, laboratory column experiments have shown that SF_6 transport is slowed (retarded) when trapped air is contained within the porous media [29,30]. While there has been some evidence of gas tracer loss during recharge when a significant vadose zone is present, experiments conducted at three sites in California with a long history of fairly continuous recharge (OCWD, Orange County; Montebello Forebay, LA County; and El Rio, Ventura County) have shown that gas loss during percolation from spreading ponds is manageable if the tracer is introduced properly [1,13,16,18].

Fundamental questions concerning deliberate tracer experiments at MAR sites include: How general are the results? Can the results of an experiment performed several years in the past be used

in the future? These questions arise because groundwater flow and travel times, e.g., to particular wells, should reflect hydrologic conditions at the time of the experiment such as recharge rates both at the MAR operation and surrounding area, pumping rates of nearby wells, and the regional hydraulic gradient. All of these are likely to change over time scales of months to years and imply that deliberate tracer results may not be similar year to year. For instance, long-term changes in the demographics and economics of an area could lead to changes in the locations and extraction/recharge rates from facilities. Furthermore, in areas with a Mediterranean climate such as Southern California, it is likely that recharge and groundwater production are out of phase, with the wet season having more recharge and less production. This should create seasonal variations in groundwater flow that should affect travel times, especially at shorter time scales (*i.e.*, months).

In this paper, we discuss the results of two deliberate tracer experiments conducted at a spreading basin in Southern California that is operated by the Orange County Water District (OCWD), ten years apart to assess if travel times changed significantly over a decade.

1.2. Field Site

A 9-km section of the Santa Ana River (SAR) and a series of spreading basins, including Kraemer Basin and Anaheim Lake, located near Anaheim, California USA are used by the OCWD as principal recharge locations for the Orange County groundwater basin (Figures 1 and 2). For more than 75 years, OCWD has been actively replenishing and managing the groundwater basin that supplies about 70% of the total water demand of approximately 2.4 million people and has been actively managing and replenishing the local groundwater basin. Currently, it operates more than 400 hectares of surface spreading facilities and recharges approximately 3.5×10^8 m^3 (2.8×10^5 AF; 10-year average between 2000 and 2010) per year [31].

In January 2008, OCWD completed and began operating the Groundwater Replenishment System (GWRS), which is the world's largest wastewater purification system for indirect potable reuse [33]. The system produces up to 2.43×10^5 m^3 (197 AF) of high quality reclaimed water each day using a three-step advanced treatment process that consists of microfiltration, reverse osmosis, and ultraviolet light disinfection with hydrogen peroxide advanced oxidation. A variable portion of the reclaimed water is pumped about 20 km to the MAR facilities and is recharged through Kraemer and other permitted nearby basins to replenish the groundwater.

Detailed investigations of the groundwater flow were conducted in the late 1990s using a variety of techniques including $T/^3He$ dating and deliberate tracer experiments at Anaheim Lake, Kraemer Basin, and the SAR [1,34]. The January 08 SF_6 experiment was required by state regulators because of the use of Kraemer Basin for GWRS water recharge and to determine if travel times near Kraemer Basin were similar to those determined a decade earlier during the October 1998 Xe isotope tracer experiment.

Figure 1. Maps of the Orange County managed aquifer recharge (MAR) facilities. (**A**) Topographic map of the field area including the location of Orange County Water District (OCWD) recharge basins based on data from the United States Geological Survey (USGS) 10-m National Elevation Dataset [32]; (**B**) Recharge occurs from the basins and from the Santa Ana River (SAR) between the Imperial Dam and Ball Road. The first arrival times of tracers determined in 1998 are contoured (modified from [1]).

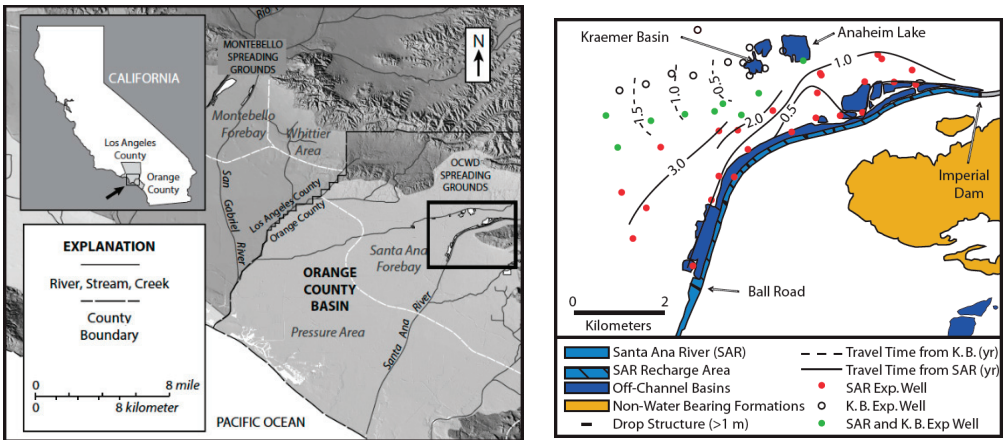

(**A**) (**B**)

2. Materials and Methods

The methodology of Clark *et al.* [1] was used during the January 2008 Kraemer Basin deliberate tracer experiment and is outlined below. At the time of the tracer injection, the basin contained approximately 1.4×10 m^5 (2000 AF) of water. The volume increased during the experiment and by the end, the pond contained about 2.1×10 m^5 (3000 AF). The study began on 17 January 2008 (defined as day 0) when 99.8% pure SF_6 gas tracer was carefully injected into Kraemer Basin over a period of about 1 hour by bubbling the tracer through a submerged diffusion stone at a rate of about 40 mL/min at two locations ~10 m offshore (Figure 2C). This injection technique was repeated twice more, on day 8 and 11. During each injection, SF_6 formed a rising bubble plume that only partially dissolved in the water column (bubbles could be seen bursting at the surface); therefore, an unknown quantity of tracer was released into the recharge water. Previously, it was estimated that less than 5% of the bubbled gas dissolves [14,18,19,34].

Because it is vital to know the initial dissolved tracer concentration, SF_6 surveys of Kraemer Basin water were conducted on days 1, 3, 5, 8, 9, 11, 12, 14, 18, and 22. During each survey, surface (~1 m below the pond's surface) and bottom (~1 m above sediment) samples were collected from five stations evenly distributed throughout the basin and marked with fixed buoys (Figure 2A,C). Approximately 2–3 mL samples were collected in Vacutainers™ in triplicate for storage and later analysis. Vacutainers™ are convenient storage and reaction containers that are commercially available. Surveys were conducted until the mean SF_6 concentration decreased to approximately the detection limit. Following the tracer injection, well samples were collected for a period of one year by personnel from OCWD in Vacutainers™ and sent to UCSB for analyses, which generally

occurred within two weeks of collection. The frequency of sampling was adjusted for each well based on the results of recent sampling.

Figure 2. Maps of the Orange County MAR facilities. (**A**) Photograph of the basin looking from the northern shore to the south towards the boat ramp. The inserted photo shows one of the fixed buoys; (**B**) Detailed map of the January 2008 field area showing the sampled wells and principle recharge areas. At the start of the experiment, neither Miller nor La Jolla Basins were recharging the aquifer. For reference, the north-south 57 freeway and the east-west 91 highway have been included. The black dashed arrows represent the northern and southern flow lines, the solid purple and dashed/dotted green contours represent, respectively, the and November 1998 and June 2008 piezometric surfaces; (**C**) Detail of Kraemer Basin at the time of the 2008 tracer injection showing where tracer was introduced and sampled.

(**A**)

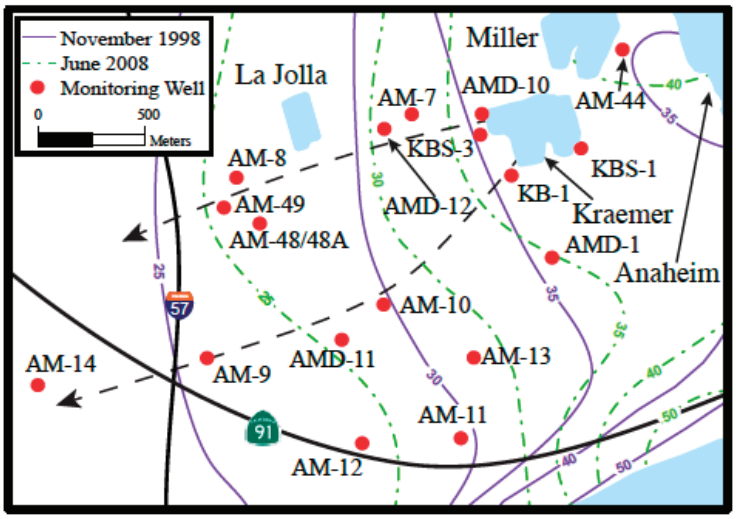

(**B**)

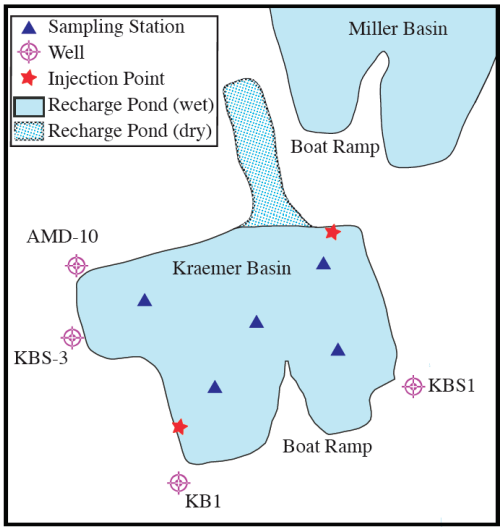

(**C**)

All SF_6 samples were analyzed using a headspace method similar to that described by [1]. In the field, pre-weighed 10 mL Vacutainers™ were partially filled (2–5 mL of water). In the laboratory, these containers were weighed (to determine the sample weight) and carefully filled with ultra-high purity nitrogen gas (so that the final pressure was equal to about 1 atmosphere). After a brief shaking to mix the headspace, this gas was injected through a column of $Mg(ClO_4)_2$ (to remove water vapor) into a small sample loop of known volume (about 1.5 mL). Subsequently, the gas in the sample loop was flushed into a gas chromatograph equipped with an electron capture detector with ultra-high purity nitrogen carrier gas. SF_6 was separated from other gases with a molecular sieve 5a column held at room temperature. The detector response was determined by running gas standards purchased from and certified by Scott-Marrin, Inc. (Riverside, CA, USA). The detection limit of this method is about 0.05 pmol/L, three orders of magnitude lower than the mean pond concentration (see below). Error on duplicate Vacutainer™ measurements was typically better than ±10% but not as good as the ±5% reported for the syringe headspace method [25].

At each well, arrival times of tracer can be determined by evaluating breakthrough curves, which are plots of concentration *versus* time. In homogenous aquifers—sand boxes, the initial and mean arrival (center of mass or COM) times of tracer at narrow-screened monitoring wells represent, respectively, the fastest and mean flow paths in the aquifer. In heterogeneous aquifers with preferential flow paths tracer breakthrough curves are more complicated, often showing multiple peaks [1,14]. Tailing is also evident on breakthrough curves and can represent the tracer reaching the well by slower flow paths, back diffusion out of lower permeability strata, non-ideal tracer input function, or retardation, which in the case of gas tracers can be due to trapped gas [29,30]. As discussed by Becker *et al.* [35], sampling biases can result in moderate and hard to quantify travel time errors. These biases are often caused by infrequent sampling due to budget limitation.

3. Results and Discussion

Mean basin concentrations of SF_6 tracer determined for each survey ranged between about 0.4 pmol/L (day 22) and 120 pmol/L (day 9); the daily infiltration rate varied between 1.7 m^3/s (day 20) and 2.2 m^3/s (days 6 and 7) and averaged 1.95 ± 0.15 m^3/s (68.9 ± 5.3 cfs). The basin concentrations were the highest following the injections and decreased exponentially due to recharge and gas loss across the air-water interface (Figure 3). The rate of loss was slightly greater during the first week than during the second, most likely due to the progressive deepening of the basin as it was filling with recharge water. This would increase the mean residence time of water in the basin and decrease the gas exchange loss.

Figure 3. SF_6 concentrations in Kraemer Basin during the injections and subsequent monitoring periods. Injections occurred on days 0, 8, and 11; estimated basin concentrations are plotted for these days. The dashed line represents the 14-day flow weighted mean concentration (66 pmol/L) during the defined injection period.

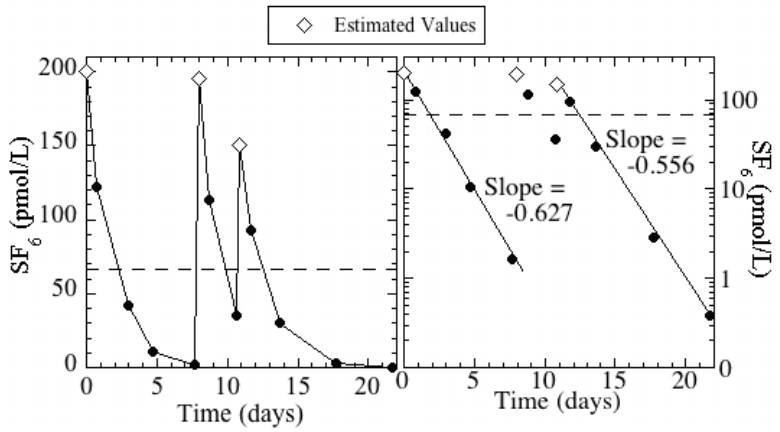

The tracer injection period was defined as the first 14 days (between January 17 and 31) when 96% of the total mass injected percolated into the ground and the flow-weighted mean SF_6 concentration was 66 pmol/L. It is important to note that the basin concentration decreased below 10% of the mean for 2 days (days 6 and 7) in the middle of the injection period (Figure 3). This complexity in the basin concentration is apparent in the breakthrough at monitoring well KBS-3/1, which displays two peaks (Figure 4B).

Although the water level contours represent different seasons and therefore different water use times in terms of the domestic landscape irrigation cycle, they are sub-parallel indicating that the location of recharge and pumping remained similar between experiments (Figure 2B). However, the hydraulic gradient west-southwest of Kraemer Basin was ~50% steeper in November 1998 (~0.0064) than June 2008 (~0.0042). Furthermore, the absolute elevation of the piezometric surface was about 5 m higher in June. These changes most likely reflect seasonality rather than long-term use patterns. The June survey occurred near the beginning of heavy domestic landscape irrigation while the November survey reflects water levels at the end of this irrigation period.

Groundwater samples were collected at 28 monitoring points (at 17 well sites, three of which were multi-level: AMD-10, AMD-11, AMD-12; Figure 2B), with sufficient frequency to construct tracer breakthrough curves (Figure 4). Tracer was detected at twelve wells down gradient (to the west) of Kraemer Basin (Table 1). As was observed during the October 1998 Xe isotope tracer study [1,33], detections progress systematically to the west along two flow paths that follow the local hydraulic gradient: the northern path of KBS-3/1, AM-7, AMD-12/1, AM-48, and AM-8; and the southern path of KBS-1/1, KB-1, AMD-11/1, AM-10, AM-9, and AM-14 (Figure 2B). The one exception is the tracer's first arrival was essentially the same at the deeper screened AMD-11/1 and AM-10 even though AMD-11/1 was more distant. This implies that depth as well as distance is important when considering travel times and that the first arrival is a difficult parameter to interpret. Interestingly, the arrival of the COM followed the distance trend with it arriving at AM-10 prior to AMD-11/1.

Figure 4. Breakthrough curves at representative wells. Wells found along, respectively, the southern (**A**, **C**, **E**) and northern (**B**, **D**, **F**) flow paths are displayed on the left and right. The mean pond concentration was 66 pmol/L and non-detections (<0.05 pmol/L) have been plotted as "0 pmol/L". Please note that the scale on the y-axes (concentration) differs.

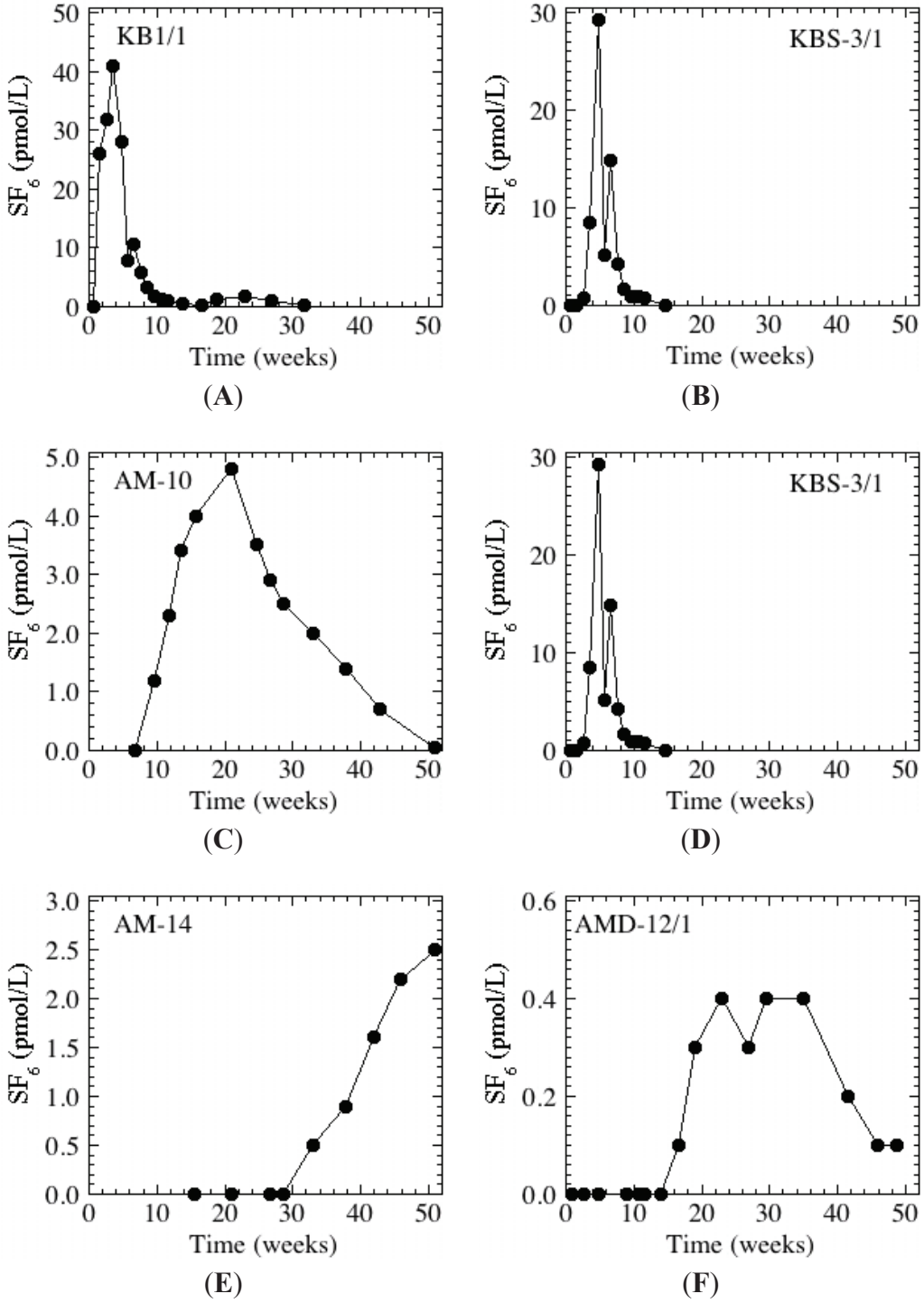

Table 1. Summary of travel times during the Oct-98 ^{136}Xe and Jan-08 SF_6 tracer experiments from Kraemer Basin. The Oct-98 Xe isotope data is from [33]. The distance was measured from the basin's shoreline directly to the well. This is the shortest distance and does not necessarily represent the flow path length. Travel times are in weeks.

Well	Distance (m)	Screen Interval (m msl)*	Jan-08 SF_6			Oct-98 ^{136}Xe		
			First Detect	Peak	COM	First Detect	Peak	COM
Northern Flow Path								
KBS-3/1	<100	44 to 41	2.7	4.7	5.6	<1.4	<1.4	†
AM-7	130	1 to −4	10.6	22.9	25.4	8.3	15.1	15.3
AMD-12/1	525	−36 to −42	16.6	22.9	30.5	—	—	—
AM-48	1250	−20 to −29	<16.6	18.7	25.7	—	—	—
AM-8	1250	−26 to −31	20.9	—	37.1 †	17.7	23.0	38.3
Southern Flow Path								
KBS-1/1	<100	4 to 1	<1.6	<1.6	†	1.4	1.4	—
KB1	<100	13 to 7	1.6	3.6	6.0	2.6	2.3	3.7
AM-10	1000	−3 to −8	6.6	20.9	23.8	15.1	23.0	28.4
AMD-11/1	1260	−91 to −97	6.7	29.1	>28*	—	—	—
AM-9	1840	−26 to −31	15.7	26.6	33.8	26.4	39.7	50.6
AM-14	2630	−32 to −38	37.7	37.7	†	45.8	—	67.9

Notes: * Depth is measured relative to mean sea level (msl). The ground surface elevation of Kraemer Basin is about 68 m and the basin floor has an elevation of about 53 m. During the tracer injection period, the surface of the water increased from about 57 m to 59 m; † Incomplete breakthrough, center of mass (COM) travel time is a minimum or could not be calculated.

At relatively shallow wells (<65 m to the screen top) near the basin (KB-1, KBS-1, KBS-3), tracer was first detected <1 to 3 weeks after the beginning of the injection period. This was not the case at another nearby well, AMD-10, where the tracer was never detected in the five zones sampled, which have screen tops between 90 and 285 m below ground surface. This is in agreement with the October 1998 experiment [1,33], which showed that these zones are hydraulically connected with Anaheim Lake (Figures 1 and 2B), a recharge basin up gradient (to the east) of Kraemer Basin, once again indicating the importance of depth to the flow field.

The influence of depth is best explained by the complicated local hydrostratigraphy. The water recharged from the basins is not flowing through a sand box, rather it flows through conductive layer between confining and semi-confining layers [1,33,36]. This complicated hydrostratigraphy also helps to explain the reversal of arrival time (first *vs.* COM) at AM-10 and AMD-11/1 and points to a potential problem of using a tracer with a large signal to noise ratio. There is no doubt that the first arrival time is poorly defined: the arrival is defined by the first detection of the tracer and therefore is defined by which tracer is being used and how good the analytical system is. Therefore the signal to noise ratio of the tracer is vital for determining this arrival time and not the local hydrology. It may make sense in the future to define this arrival time with C/C_0, where C_0 could be either the initial concentration in the recharge water or the local peak concentration. We believe that the former

makes more sense because in is likely that the local peak concentration cannot capture unless continuous sampling is employed.

The travel times of the leading edge of the tracer arrival, which is defined by the first detection, were very similar (within three weeks) at six of the nine wells monitored during both the 2008 and 1998 experiments (Figure 5A; Table 1). The mean observed velocity of the leading edge was about 60 m/week (3 km/year). The exceptions were the three most distant wells along the southern flow path, AM-9, AM-10, and AM-14. During the 2008 experiment, the tracer arrival was traveling about 50% faster and, therefore, earlier detections were observed at these wells.

Figure 5. Comparison between the arrival times and distance from the January 2008 and October 1998 tracer experiments. (**A**) First arrival and (**B**) COM. Note the change of scale on the x-axis. During the January 2008 experiment, COM arrivals could not be calculated at all wells because of incomplete breakthroughs (see Table 1).

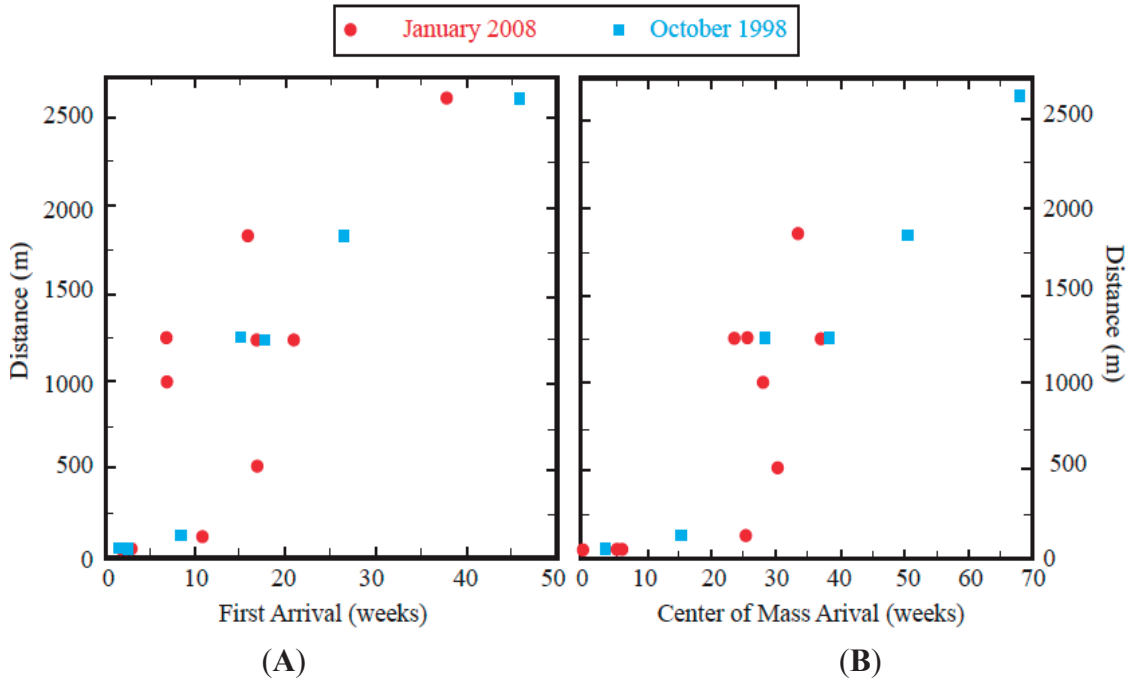

Monitoring wells AM-8, AM-48, AM-48A, and AM-49 are located along the northern flow path approximately the same distance down gradient. However, the screen depth of these wells differs. Tracer was not detected at the relatively shallow wells, AM-48A and AM-49 (screen depths between 20 and 30 m msl) while it was detected at the deep wells, AM-8 and AM-48 (screen depths between −20 and −31 m msl). This implies that the tracer had migrated vertically downward beneath the water table and was traveling through deep layers, with the shallow layers recharged by other sources, such as the nearby La Jolla Basin (Figure 2B). The movement of the COM was also very similar during two experiments (Figure 5B) and traveled with a velocity of about 40 m/week (2 km/year).

4. Conclusions

The results of the two deliberate tracer experiments conducted a decade apart were very similar despite differences in the local piezometric surface. The arrival times at nine of the twelve wells

were nearly identical once the experimental uncertainty (*i.e.*, frequency of sampling) is considered. Apparently the hydraulic gradients near Kraemer Basin had not changed significantly between experiments. This may be partly due to the fact that both experiments were conducted during similar times of high recharge at Kraemer Basin and reduced seasonal pumping in the winter-spring study period. As seen near other MAR facilities, vertical flow is important and must be considered when evaluating travel time information.

Acknowledgments

We would like to thank Alex Cervantes, David Field, Brian Okey, Nira Yamachika, Gary Yoshiba, and many others at Orange County Water District (OCWD) for hosting this research and providing assistance over many years. Daniel Petersen assisted with the field and laboratory work at Universoty of California Santa Barbara. Tim Becker helped draft some of the figures. The comments and suggestions of the two anonymous reviewers improved the manuscript considerably. Funding was provided by OCWD.

Author Contributions

All authors contributed equally to this paper.

Conflicts of Interest

The authors declare no conflict of interest.

References

1. Clark, J.F.; Hudson, G.B.; Davisson, M.L.; Woodside, G.; Herndon, R. Geochemical imaging of flow near an artificial recharge facility, Orange County, CA. *Ground Water* **2004**, *42*, 167–174.
2. Bouwer, H. Artificial recharge of groundwater: Hydrogeology and engineering. *Hydrogeol. J.* **2002**, *10*, 121–142.
3. Dillon, P. Future management of aquifer recharge. *Hydrogeol. J.* **2005**, *13*, 313–316.
4. National Research Council. *Prospects for Managed Underground Storage of Recoverable Water*; National Academy Press: Washington, DC, USA, 2007.
5. Yates, M.V.; Yates, S.R. A comparison of geostatistical methods for estimating virus inactivation rates in ground water. *Water Res.* **1987**, *21*, 1119–1125.
6. Fox, P.K.; Narayanaswamy, A.; Genz, A.; Drewes, J.E. Water quality transformations during soil aquifer treatment at the Mesa Northwest Water Reclamation Plant, USA. *Water Sci. Technol.* **2001**, *43*, 343–350.
7. Drewes, J.E.; Heberer, T.; Rauch, T.; Reddersen, K. Fate of pharmaceuticals during groundwater recharge. *Groundw. Monit. Remediat.* **2002**, *23*, 64–72.
8. Hiscock, K.M.; Grischeck, T. Attenuation of groundwater pollution by bank filtration. *J. Hydrol.* **2002**, *266*, 139–144.

9. Fox, P.K.; Makam, R. Surface area and travel time relationships in aquifer treatment systems. *Water Environ. Res.* **2009**, *81*, 2337–2343.
10. Johnson, T.A. Groundwater recharge using recycled municipal wastewater in Los Angeles County and the California Department of Public Health's draft regulations on aquifer retention time. *Ground Water* **2009**, *47*, 496–499.
11. Schlosser, P.; Stute, M.; Dörr, H.; Sonntag, C.; Münnich, K.O. Tritium/^{3}He dating of shallow groundwater. *Earth Planet. Sci. Lett.* **1988**, *89*, 353–362.
12. Solomon, D.K.; Cook, P.G. ^{3}H and ^{3}He. In *Environmental Tracers in Subsurface Hydrology*; Cook, P.G., Herczeg, A.L., Eds.; Kluwer Academic Publishers: Boston, MA, USA, 2000; pp. 397–424.
13. Massman, G.; Sültenfuss, J.; Knappe, A.; Dünnbier, U.; Taute, T.; Pekdeger, A. Investigation of groundwater residence times during bank filtration in Berlin: A multi-tracer approach. *Hydrol. Process.* **2008**, *22*, 788–801.
14. McDermott, J.A.; Avisar, D.; Johnson, T.A.; Clark, J.F. Groundwater travel times near spreading ponds: Inferences from geochemical and physical approaches. *J. Hydrol. Eng. ASCE* **2008**, *13*, 1021–1028.
15. Schultz, T.R.; Randall, J.H.; Wilson, L.G.; Davis, S.N. Tracing sewage effluent recharge—Tucson, Arizona. *Ground Water* **1976**, *14*, 463–470.
16. Clark, J.F.; Smethie, W.M., Jr.; Simpson, H.J. Chlorofluorocarbons in the Hudson estuary during summer months. *Water Resour. Res.* **1995**, *31*, 2553–2560.
17. Busenberg, E.; Plummer, L.N. Dating young groundwater with sulfur hexafluoride: Natural and anthropogenic sources of sulfur hexafluoride. *Water Resour. Res.* **2000**, *36*, 3011–3030.
18. Gamlin, J.D.; Clark, J.F.; Woodside, G.; Herndon, R. Large-scale tracing of ground water with sulfur hexafluoride. *J. Environ. Eng. ASCE* **2001**, *127*, 171–174.
19. Clark, J.F.; Hudson, G.B.; Avisar, D. Gas transport below artificial recharge ponds: Insights from dissolved noble gases and a dual gas (SF_6 and ^{3}He) tracer experiment. *Environ. Sci. Technol.* **2005**, *39*, 3939–3945.
20. Ledwell, J.R.; Watson, A.J.; Law, C.S. Evidence for slow mixing across the pycnocline from an open-ocean tracer-release experiment. *Nature* **1993**, *364*, 701–703.
21. Wanninkhof, R.; Ledwell, J.R.; Broecker, W.S. Gas exchange-wind speed relationship measured with sulfur hexafluoride on a lake. *Science* **1985**, *227*, 1224–1226.
22. Clark, J.F.; Wanninkhof, R.; Schlosser, P.; Simpson, H.J. Gas-exchange rates in the tidal Hudson River using a dual tracer technique. *Tellus Ser. B Chem. Phys. Meteorol.* **1994**, *46*, 274–285.
23. Hibbs, D.E.; Parkhill, K.L.; Gulliver, J.S. Sulfur hexafluoride gas tracer studies in streams. *J. Environ. Eng. ASCE* **1998**, *124*, 752–760.
24. Lester, D.; Greenberg, L.A. The toxicity of sulfur hexafluoride. *Arch. Ind. Hyd. Occup. Med.* **1950**, *2*, 348–349.
25. Wanninkhof, R.; Ledwell, J.R.; Watson, A.J. Analysis of sulfur hexafluoride in seawater. *J. Geophys. Res*. **1991**, *96*, 8733–8740.

26. Wilson, R.D.; Mackay, D.M. The use of sulfur hexafluoride as a conservative tracer in saturated sandy media. *Ground Water* **1993**, *31*, 719–724.
27. Wilson, R.D.; Mackay, D.M. SF_6 as a conservative tracer in saturated media with high intragranular porosity or high organic carbon content. *Ground Water* **1996**, *34*, 241–249.
28. Wanninkhof, R.; Mulholland, P.J.; Elwood, J.W. Gas exchange rates for a first-order stream determined with deliberate and natural tracers. *Water Resour. Res.* **1990**, *26*, 1621–1630.
29. Fry, V.A.; Istok, J.D.; Semprini, L.; O'Reilly, K.T.; Buscheck, T.E. Retardation of dissolved oxygen due to a trapped gas phase in porous media. *Ground Water* **1995**, *33*, 391–398.
30. Vulava, V.M.; Perry, E.B.; Romanek, C.S.; Seaman, J.C. Dissolved gases as partitioning tracers for determination of hydrogeological parameters. *Environ. Sci. Technol.* **2002**, *36*, 254–262.
31. 2009-10 Report on Groundwater Recharge in Orange County Groundwater Basin. Available online: http://www.ocwd.com/Portals/0/Pdf/09-10AnnualRechargeReport_All.pdf (accessed on 9 June 2014).
32. Gesch, D.B. The National Elevation Dataset. In *Digital Elevation Model Technologies and Applications: The DEM Users Manual*, 2nd ed.; Maune, D., Ed.; American Society for Photogrammetry and Remote Sensing: Bethesda, MD, USA, 2007; pp. 99–118.
33. Groundwater Replenishment System. Available online: www.gwrsystem.com (accessed on 5 April 2011).
34. Davisson, M.L.; Hudson, G.B.; Clark, J.F.; Woodside, G.; Herndon, R. Final report on isotope tracer investigations in the forebay of the Orange County groundwater basin. Lawrence Livermore Nation Laboratory UCRL-TR-201735, 2004. Available online: https://e-reports-ext.llnl.gov/pdf/303507.pdf (accessed on 14 April 2008).
35. Becker, T.E.; Clark, J.F.; Johnson, T.A. Heat ^{10}B-enriched boric acid, and bromide as recycled groundwater tracers for Managed Aquifer Recharge: A case study. *J. Hydrol. Eng. ASCE*, submitted.
36. Thomson, A.F.B.; Carle, S.F.; Rosenberg, N.D.; Maxwell, R.M. Analysis of groundwater migration from artificial recharge in a large urban aquifer: A simulation perspective. *Water Resour. Res.* **1999**, *35*, 2981–2998.

MDPI AG
Klybeckstrasse 64
4057 Basel, Switzerland
Tel. +41 61 683 77 34
Fax +41 61 302 89 18
http://www.mdpi.com/

Water Editorial Office
E-mail: water@mdpi.com
http://www.mdpi.com/journal/water

MDPI • Basel • Beijing
ISBN 978-3-906980-92-8
www.mdpi.com